NOVA SCHOOL OF SCIENCE & TECHNOLOGY

DEPARTAMENT OF MECHANICAL AND INDUSTRIAL ENGINEERING

INVESTIGATION ON WELDING OF HIGH ENTROPY ALLOYS IN SIMILAR AND DISSIMILAR COMBINATIONS.

João Carlos Galveias Lopes

Master in Mechanical Engineering

DOCTORATE IN MECHANICAL ENGINEERING

NOVA university Lisbon

October, 2024

DEPARTAMENT OF MECHANICAL AND INDUSTRIAL ENGINEERING

INVESTIGATION ON WELDING OF HIGH ENTROPY ALLOYS IN SIMILAR AND DISSIMILAR COMBINATIONS.

JOÃO CARLOS GALVEIAS LOPES

Master in Mechanical Engineering

Supervisor: João Pedro de Sousa Oliveira,
Full professor, NOVA School of Science and Technology, NOVA University of Lisbon.

Co-supervisor: Norman Zhou,
Full professor, University of Waterloo.

Examination committee:

Chair: Telmo Jorge Gomes dos Santos,
Full professor, NOVA School of Science and Technology, NOVA University of Lisbon.

Rapporteurs: Maria de Fátima Reis Vaz,
Full professor, Instituto Superior Técnico, University of Lisbon.

António Manuel de Bastos Pereira,
Full professor, University of Aveiro.

Supervisor: João Pedro de Sousa Oliveira,
Full professor, NOVA School of Science and Technology, NOVA University of Lisbon.

Members: Joel Oliveira Correia Vasco,
Coordinator professor, Polytechnic University of Leiria.

Telmo Jorge Gomes dos Santos,
Full professor, NOVA School of Science and Technology, NOVA University of Lisbon.

DOCTORATE IN MECHANICAL ENGINEERING

NOVA university Lisbon
October, 2024

INVESTIGATION ON WELDING OF HIGH ENTROPY ALLOYS IN SIMILAR AND DISSIMILAR COMBINATIONS.

Copyright © João Carlos Galveias Lopes, NOVA School of Science and Technology, NOVA University Lisbon.

The NOVA School of Science and Technology and the NOVA University Lisbon have the right, perpetual and without geographical boundaries, to file and publish this dissertation through printed copies reproduced on paper or on digital form, or by any other means known or that may be invented, and to disseminate through scientific repositories and admit its copying and distribution for non-commercial, educational or research purposes, as long as credit is given to the author and editor.

To my family.

ACKNOWLEDGEMENTS

I would like to start this text by acknowledging the Portuguese Foundation for Science and Technology (FCT) for funding my PhD scholarship and UNIDEMI for allowing me to work in its premises. Without it, my pursual of doctoral studies would never have started. With this, now that I'm close to finishing my thesis, I completely understand why the process of being awarded a PhD scholarship is hard and competitive and, thus, I must thank firstly to the man who helped me in obtaining this achievement.

Thus, I express my deepest gratitude to my supervisor, Prof. João Pedro Oliveira, whose expertise and guidance were invaluable in shaping this the progress of my work. With him I learned and developed important skills, both personally and professionally, and had access to all the materials I would require for carrying out this work. Without his insightful feedback on my manuscripts, this research would not have reached its full potential. I am also thankful to him, for constantly keeping me on the edge and demonstrating, through a consecutive sequence of acts, not words, that the way we look at challenges can de-escalate them to a manageable size. Finally, and most importantly, he taught me that an important talent that must be mastered is to partition life from work. I'm exceptionally proud to have had the opportunity of working with him.

I am also grateful to my co-supervisor Prof. Norman Zhou, who embraced me in his research team at the Centre for Advanced Materials Joining, in Waterloo (Canada) and gave me the opportunity to explore new perspectives in my research. With him, I understood that a good researcher is not shaped by his achievements, money or equipment, but by the team he gets to work with and how willing he is to make the effort to pursue a determined topic, however enigmatic and disperse it may be.

For the weekly meetings, availability and friendship, I also acknowledge Prof. Peng Peng, my appointed co-supervisor while in Waterloo, with whom I learned how reunions can be conducted to efficiently conclude them in time. Amidst many other features his open-minded way of thinking made him one of the best persons with whom I got to work with.

Aside from Canada, I part of the work was conducted in Germany, at Deutsches Elektronen-Synchrotron (DESY) and Karlsruhe Institute of Technology (KIT), where the more advanced characterization techniques were available. As such, my gratitude extends to Dr.

Norbert Schell, Dr. Emad Maawad, Delphine Chassaing and Dr. Torben Boll. Besides this, I also thank Prof. Rajiv Mishra, Prof. Priyanka Agrawal and Prof. Ana Baptista for supplying all the data I couldn't retrieve myself.

I am also grateful to the members of my pre-thesis defense committee, Prof. António Bastos and Prof. José Xavier and Prof. Rui Martins, for their constructive feedback on the first version of my thesis.

On a different tone, I devote my sincere thanks to the friendships I developed and strengthened during the course of my thesis. For collaborating with people with similar ambitions in a plenitude of topics helps to diffuse tension in the office and develop the most interesting ideas one can come across. In these terms, I thank my friends from UNIDEMI, Samrudha Kokare, Filipa Cunha, André Ramalho, Douglas Serrati, Igor Felice and Adriana Alves, with whom I got the pleasant opportunity of working in the same office, thus wishing them the best in their own endeavors and congratulating them for successfully finishing our 5 Km "Marathon".

For being present from the very start of my PhD and including me right away without even giving it a thought, I also thank Dr. Jiajia Shen's friendship with a warm embrace and acknowledge all her efforts in producing relevant research. Alas, I also extend my sincere gratitude to Rui Gonçalves, whom I respect for his many aptitudes and wish him the best in his PhD studies and subsequent future.

A special thanks to my hard-working friends in CENIMAT, Dr. Jaivindra Singh, Liu Lei, Nithin Reddy, Davi Alves, Dr. Giovani Ribamar and Isaque Moura. For the discussions and help granted throughout days.

Important to mention as well, are the young engineers I helped in co-supervising during the execution of their master thesis. I'm proud that all of them are now pursuing their own lines of work. Pedro Dias, Daniela Afonso, Pedro Rocha, António Alvarez, Margarida Varela, Diogo Martins, Alexandre Candeias, Carolina Coelho, Filipe Ribeiro and Miguel Pinto, thank you for being a part of my PhD.

During my stay at Waterloo, many lasting friendships were also made. Although with an ocean separating us, I believe that we shall meet again on many occasions. Thus, I shall never forget Kaping Zhang, Tetsuya Oyamada, Shasvat Rathod, Shadab Sarmast, Jihui Yan, Xiaoye Zao, Ali Gathei, Hanwen Yang, Shasvat Rathod and Muhammad Shehryar Khana and Arko Roychoudhury. Thank for being there.

For their friendship and emotional support, I must thank my close friends Diogo Machado, Grigore Savva, Tiago Pedro and Vanda Espírito Santo, for their constant friendship and precious memories shared in our get-togethers.

Finaly, I thank and dedicate this document to my family. Without them none of this would have been possible. Thanks for your patience, for sheltering me, for the hundreds of kilometers to take me to the airport (and then making the way back), for your strength and for your help through the hardest of times. For this I am grateful from the bottom of my heart.

Thank you all.

“When the snows fall and the white winds blow, the lone wolf dies but the pack survives.”

George R.R. Martin, A Game of Thrones.

RESUMO

O conceito de ligas de alta entropia tem a capacidade de revolucionar a produção de aplicações de engenharia ao fornecer novos métodos para o desenvolvimento de ligas metálicas. Tal é possível através da possibilidade de gerar novas composições capazes de garantir às ligas propriedades específicas com foco nos requisitos de um dado produto/estrutura.

No entanto, é necessário gerar conhecimento referente ao processamento destas ligas, uma vez que não só estarão expostas às condições operacionais de uma determinada finalidade, mas também às condições impostas por todas as etapas de fabrico necessárias ao desenvolvimento de um produto.

É desta forma, que os processos de soldadura por fusão se apresentam como métodos promissores para o desenvolvimento de ligas de alta entropia, uma vez que envolvem a exposição destes materiais a altas temperaturas, capazes de alterar massivamente a sua microestrutura e, como tal, a suas propriedades. Pressupondo, assim, explorar a relação entre o processamento, microestrutura e propriedades destas ligas avançadas.

Deste modo, o presente trabalho foca-se no estudo de juntas soldadas em ligas de alta entropia bem conhecidas na literatura, nomeadamente nos sistemas CoCrFeMnNi, AlCoCrFeNi, FeMnCoCr, FeCuCoMnNi e CoCrNiAlTi. Esta investigação é posta em prática por forma a investigar a viabilidade destes materiais avançados em aplicações de engenharia e enfrentar quaisquer desafios que possam ocorrer durante a sua produção.

Palavras-chave: Ligas de alta entropia; Soldadura por arco elétrico com elétrodo de tungsténio; Difração de raio-X através de radiação de sincrotrão; Microestrutura; Caracterização de propriedades; Simulação termodinâmica; Inoculantes.

ABSTRACT

By providing new ways of discovering new alloy compositions, the high entropy alloy concept has the ability to revolutionize the way engineering applications are produced. Such is possible by developing materials based on the requirements of a determined purpose, that is, with specific properties in visage.

Nevertheless, it is necessary to generate knowledge regarding the processability of such novel alloys, provided that they will not only be exposed to operational conditions, but also to the conditions imposed by all manufacturing stages necessary for the development of a product.

It is in this line of thought that fusion welding processes present themselves as promising methods for the development of high entropy alloys, as they involve the exposure of these materials to high temperatures, capable of massively altering their microstructure and, consequently, its properties. Such presupposes exploring the relationship between the processing, microstructure and properties of these advanced alloys.

With this in mind, the present work focuses on the weldability of well-known HEA systems, namely the CoCrFeMnNi, AlCoCrFeNi, FeMnCoCr, FeCuCoMnNi and the CoCrNiAlTi systems. Such is done to pursuit the feasibility of these advanced materials in key engineering applications and to address any challenges that may occur during their production.

Keywords: High entropy alloys; Gas tungsten arc welding; Synchrotron X-ray diffraction; Microstructure; Mechanical testing; Thermodynamic simulations, Inoculants.

CONTENTS

1 Introduction _____ *1*

1.1 Motivation and objective _____ 1

1.2 Major findings and publications in international peer-reviewed indexed journals _____ 2

1.3 Document organization _____ 4

2 Literature Review _____ *6*

2.1 Chapter Introduction _____ 6

2.2 High entropy alloy design and definition _____ 6

2.3 Welding technologies _____ 11

2.4 Gas tungsten arc welding _____ 12

2.5 Welded joint characterization for the improvement of HEAs _____ 14

2.6 Current progress on welding of HEAs _____ 21

2.6.1 $Fe_{50}Mn_{30}Co_{10}Cr_{10}$ HEA _____ 23

2.6.2 AlCoCrFeNi HEA _____ 24

2.6.3 $CoCu_xFeMnNi$ (x=20,30) HEA _____ 24

2.6.4 $Co_{29.7}Cr_{29.7}Ni_{35.4}Al_4Ti_{1.2}$ HEA _____ 25

2.6.5 CoCrFeMnNi HEA _____ 25

3 Materials and Methods _____ *27*

3.1 Chapter introduction _____ 27

3.2 Computer numerical control platform utilized for GTAW _____ 28

3.3 GTAW experiments _____ 30

3.4 Microscopy techniques _____ 31

3.5 Synchrotron X-ray diffraction _____ 32

3.6 Thermodynamic calculations _____ 36

3.7 Mechanical characterization _____ 37

4 Results and Discussion _____ *39*

4.1 Chapter introduction _____ 39

4.2 Microstructure evolution and mechanical performance of Gas tungsten arc welded $Fe_{50}Mn_{30}Co_{10}Cr_{10}$ HEA _____ 39

4.2.1 Sections highlights 39
4.2.2 In-situ x-ray diffraction analysis during tensile testing of the $Fe_{50}Mn_{30}Co_{10}Cr_{10}$ HEA 39
4.2.3 Gas tungsten arc welding of the dual-phase $Fe_{50}Mn_{30}Co_{10}Cr_{10}$ HEA 61
4.2.4 Analyzing the weldability of a Fe-based shape memory alloy 89
4.2.5 Dissimilar gas tungsten arc welding between the dual-phase $Fe_{50}Mn_{30}Co_{10}Cr_{10}$ HEA and a Fe-based SMA 118
4.2.6 Section summary 128

4.3 Microstructure evolution and mechanical performance of a gas tungsten arc welded AlCoCrFeNi HEA 129

4.3.1 Section highlights 129
4.3.2 Role of TiB_2 inoculation particles during welding of a AlCoCrFeNi high entropy alloy 129
4.3.3 Dissimilar gas tungsten arc welding between the AlCoCrFeNi HEA and 316L stainless steel 157
4.3.4 Section summary 175

4.4 Microstructure and mechanical performance comparison between gas tungsten arc welded $CoCu_{20}FeMnNi$ and the $CoCu_{30}FeMnNi$ HEAs 176

4.4.1 Section highlights 176
4.4.2 Microstructural characterization of the joints and CalPhaD analysis 176
4.4.3 Synchrotron X-ray diffraction of the welded joints 186
4.4.4 Electrochemical characterization of the joints 191
4.4.5 Mechanical properties assessment via microhardness mapping and tensile testing 193
4.4.6 Section summary and conclusions 198

4.5 Microstructure and mechanical performance analysis on a gas tungsten arc welded CoCrNiAlTi HEA 200

4.5.1 Section highlights 200
4.5.2 Microstructural analysis 200
4.5.3 Thermodynamic Calculations 211
4.5.4 Synchrotron x-ray diffraction 218
4.5.5 Mechanical properties of the welded joints 221
4.5.6 Section summary and conclusions 226

4.6 Microstructure and mechanical performance analysis of the CoCrFeMnNi HEA 227

4.6.1 Section highlights 227
4.6.2 In-situ microstructural evolution during tensile loading of CoCrFeMnNi high entropy alloy welded joint probed by high energy synchrotron X-ray diffraction 227
4.6.3 Dissimilar laser welding of an as-rolled CoCrFeMnNi high entropy alloy to Inconel 718 superalloy 237
4.6.4 Section summary 249

5 Conclusions and future work 251

LIST OF FIGURES

Figure 1 – Vast compositional space for high entropy alloy development. _____ 8
Figure 2 – Gas tungsten arc welding operating in straight polarity. _____ 13
Figure 3 - Schematic representation of a welded joint. _____ 14
Figure 4 – Schematic representation of constitutional undercooling: (a) one-dimensional solidification process of an alloy, (b) corresponding phase diagram and (c) temperature variation with increasing distance to the S/L interface (Adapted from [32,35]). _____ 17
Figure 5 – (a) Effect of constituitional supercolling on solidification mode and (b) effect of G an R on the morphology and size of microstrucuture during solidification (Adapted from [32]). _____ 19
Figure 6 – Variation in solidification mode across the fusion zone (From [32]). _____ 20
Figure 7 - Evolution of the number of publications on welding of high entropy alloys over time. _____ 22
Figure 8 - Percentual distribution of the number of papers by welding technique. _____ 22
Figure 9 - Welding platform: a) 3D view of the welding platform assembly; b) detailed 3D view of the fixture; c) actual welding platform. _____ 29
Figure 10 - Experimental setup utilized for synchrotron X-ray diffraction, not to scale. _____ 32
Figure 11 – Simplified interface for integration of diffraction data. _____ 33
Figure 12 –Microstructure evaluation and mechanical behavior of the DP-HEA: a) EBSD IPF and b) EBSD phase maps; c) Engineering and true stress/strain curves describing the macroscopic tensile behavior of the DP-HEA, along with the strain hardening rate, which is further detailed in d); e) fracture surface and f) its corresponding detailed view. _____ 40
Figure 13 – a) Full azimuthal integration of the diffraction patterns obtained during tensile testing alongside with b) the corresponding colormap which evidences peak broadening and intensity changes with the increasing load (# corresponds to 2^{nd} reflections). _____ 42
Figure 14 – Evolution of ε-HCP phase fraction obtained via Rietveld refinement (using MAUD [87]) with an R_{wp} below 5% and c/a ratio evolution throughout the tensile test calculated using single peak analysis considering the (1 0 -1 0) and (1 0 -1 3) diffraction peaks, highlighting the variations occurring at the microstructural level on the DP-HEA. _____ 43
Figure 15 – Normalized integrated intensity evolution during tensile test along TD and LD. (a) shows the evolution of γ-FCC (1 1 1), (2 0 0) and (3 1 1) diffraction peaks; (b) details the evolution of ε-HCP (1 0 -1 0) and (1 0 -1 1) diffraction peaks. Here, the (0 0 0 2) peak evolution is only shown for reference in the TD; (c) shows the evolution of ε-HCP (1 0 -1 2) and (1 0 -1 3) diffraction peaks. _____ 45
Figure 16 – Color maps corresponding to the stage I and IV of the tensile test on the: a) (1 0 -1 0) and b) (1 0 -1 2) diffraction peaks. This serves to evidence the different behavior exhibited by each peak upon the increase of stress and visible only by 1^{o} cake integration of the diffraction patterns. _____ 48
Figure 17 - Lattice strain evolution during tensile testing along TD and LD. (a) shows the evolution of γ-FCC (1 1 1), (2 0 0) and (3 1 1) diffraction peaks; (b) shows the evolution of ε-HCP (1 0 -1 0) and (1 0 -1 1) diffraction peaks. Here the (0 0 0 2) peak evolution is only shown for reference in the TD; (c) shows the evolution of ε-HCP (1 0 -1 2) and (1 0 -1 3) diffraction peaks. _____ 50

Figure 18 - Dislocation density evolution on the γ-FCC and ε-HCP phases, throughout the in-situ tensile experiment. _____ *52*
Figure 19 – (a) Load partitioning between the γ-FCC and ε-HCP phases. (b) Estimation of the yield strength of the DP-HEA based on the γ-FCC phase, which is the first phase to yield (σ0 is the lattice friction stress, σD is the strengthening contribution from dislocations, σSF corresponds to the influence of staking faults and σGB represents the strengthening effect of grain boundaries). _____ *53*
Figure 20 – Schematic representation of the loading stages undertaken by the DP-HEA, highlighting the stress thresholds for the activation of the multiple strain accommodation mechanisms developed upon tensile stress. _____ *56*
Figure 21 – Microstructure of the $Fe_{50}Mn_{30}Co_{10}Cr_{10}$ HEA welded joint: (a) Macrograph detailing the joint cross section, indicating the BM to HAZ interface and the fusion boundary; (b) BM, where a parent γ-FCC grain is highlighted with a yellow dashed line, while the ε-HCP laths are also shown; (c) BM to HAZ interface; (d) FZ; (e) EDS mapping of the BM to HAZ interface. The red dots in b) and d) detail locations where EDS point analysis was performed. The yellow box c) details the location for EDS mapping. _____ *62*
Figure 22 – Weld microstructure analysis: (a) IPF map and (b) Phase map. _____ *64*
Figure 23 – High-resolution EBSD analysis of the BM and FZ. The IPF maps in (a) and (d), phase maps in (b) and (e), and KAM maps in (c) and (f) provide valuable insights into the crystallographic orientation, phase distribution, and deformation within the samples. _____ *68*
*Figure 24 – Representative SXRD patterns from the BM and FZ. The diffraction peaks corresponding to the γ-FCC and the ε-HCP phases are identified on the top. Lower intensity reflections corresponding to manganese oxides (*****) and 2nd harmonic reflections (**#**), the latter resulting from the beamline setup, are also identified.* _____ *69*
Figure 25 – SXRD mapping: (a) colormap exhibiting the variation of the diffraction peaks after full azimuthal integration; (b) 3D depiction highlighting the diffraction peaks within the 6.9-7.8 2ϑ range. _____ *70*
Figure 26 – Evolution of (a) peak intensity and (b) full width at half maximum along the welded joint. _____ *71*
Figure 27 – Distribution of microstrain on the (a) γ-FCC and the (b) ε-HCP phases along the full extension of the weld _____ *75*
Figure 28 – Evolution of 2ϑ angle obtained by integrating in 1-degree segments along the azimuthal angle on representative zones of the: (a) BM, (b) HAZ and (c) FZ. On each region, peak fitting was performed on: the (311) peak of the γ-FCC (d), e) and f)) and on the (10-13) peak of the ε-HCP phase (g), h) and i)). _____ *76*
Figure 29 - Scheil calculations performed considering the nominal composition of the HEA base material. ____ *79*
Figure 30 - Partition coefficients of the matrix γ-FCC phase during solidification, calculated from the data obtained from the calculations obtained with the Scheil-Gulliver method. _____ *80*
Figure 31 - Analysis of (a) Gibbs energy of the γ-FCC, ε-HCP and Liquid phases and (b) difference between the Gibbs energy curves of the ε-HCP and Liquid phases and the matrix γ-FCC phase. _____ *82*
Figure 32 – Microhardness evaluation of the welded joint: a) mapping of the variation of hardness along the full extension of the weld superimposed with optical microscopical results and b) representative hardness evolution taken from the middle line of the map. _____ *83*
Figure 33 - Tensile test behavior comparison between the BM and the welded joints. _____ *85*
Figure 34 - Stress-strain behavior of: (a) representative points located in the BM, HAZ and FZ obtained with DIC during tensile testing of the welded joints and (b) welded joint and the DIC average response. _____ *86*

Figure 35 – Fracture surface after tensile testing inspected by SEM: a) Overall Overview and b) detailed view of the fracture surface. _____ *87*
Figure 36 – Microstructural analysis of the welded joint: (a) Overview of the joint as obtained by optical microcopy; (b) Scanning electron microscopy of the transition from the BM to the FZ highlighting the several regions generated during welding; (c) Close-up view of the transition from the BM to the FZ by optical microscopy; (d) Close-up view of the FZ by SEM. _____ *92*
Figure 37 – Electron Backscatter Diffraction Inverse Pole Figure map parallel to the Z axis: (a) cross section of the welded joint; (b) Detailed view of the fusion boundary. _____ *94*
*Figure 38 – (a) representative bright field TEM image of the BM; (b) SAED pattern highlighting the γ-FCC matrix; (c) SAED pattern indicating the presence of an annealing twin alongside the γ-FCC matrix; (d) TEM image detailing the presence of stacking faults within the annealing twin, and (e) SAED pattern of the annealing twin showcasing streaking due to the presence of stacking faults.*_____ *96*
Figure 39 - (a) representative bright field TEM image of the FZ; (b) detail of VC precipitates near the sub-grain boundaries, and (c) corresponding EDS map of Vanadium; (d) detail of Fe-rich precipitates scattered withing the sub-grains and corresponding EDS maps in (e) alongside the (f) EDS line results marked in (d). The transition from one sub-grain to another was inspected using SAED as in (g) upper sub-grain; (h) boundary between sub-grains and (i) lower sub-grain. _____ *97*
Figure 40 – Synchrotron X-ray diffraction patterns taken form (a) the full extension of the weld, highlighting the matrix γ-FCC phase; representative diffraction patterns of: (b) BM, (c) HAZ, (d) FZ, with corresponding phase identification. Low intensity 2nd harmonic diffraction peaks were left unidentified because they do not correspond to any structure present on the alloy. _____ *98*
Figure 41 – Distribution of (a) peak intensity, and (b) FWHM per diffraction peak along the welded joint. ___ *100*
Figure 42 – Comparison between the microstrain of the BM and the: (a) HAZ, (b) columnar region of the FZ and (c) equiaxed region of the FZ. _____ *102*
*Figure 43 – Electrochemical characterization of the welded joint in terms of: (a) polarization curves alongside with the (b) corresponding open circuit potential; (c) Bode plot and corresponding (d) Nyquist plot, obtained on the BM; (e) Bode plot and corresponding (f) Nyquist plot, obtained in the FZ.*_____ *105*
Figure 44 –Microhardness distribution of the Fe-SMA welded joint: (a) colormap and (b) evolution at mid height of the weld (marked by the black arrow and dashed line). _____ *107*
Figure 45 – Representative stress-strain curves of the (a) base material and (b) welded joint, taken from the multiple tensile tests performed on the samples (three in each condition). _____ *108*
*Figure 46 – Depiction of the strain distribution during tensile testing in the as-welded condition, using digital image correlation: (a) corresponds to the evolution until fracture, while in (b) the last stage before fracture is depicted on a different scale. The regions marked in (b) are utilized to plot the local tensile behavior in Figure 47.*_____ *109*
Figure 47 - DIC results for the BM, HAZ and two region (columnar and equiaxed) zones of the FZ. _____ *110*
Figure 48 – Representative fracture surface of the welded samples. _____ *111*
*Figure 49 – Load/unload cycling tests performed on: (a) BM and (b) welded samples.*_____ *112*
Figure 50 - Results from cycling tests: (a) Irrecoverable strain; (b) maximum stress at 6% strain and (c) absorbed energy. _____ *114*

Figure 51 – Microstructural features and their influence on microhardness on the joint: (a) Optical microscopy of the welded joint and (b) EBSD IPF of the FZ highlighting grain orientation; (c) microhardness distribution across the full extension of the joint and detailed view of the HAZ close to the (d) SMA and (e) the HEA BMs. Closer visualization of the transition from the HAZ to the FZ can be seen in (f) highlighting a PMZ and in the (g) highlighting the transition from the HEA side of the joint. _____ *120*
*Figure 52 – Advanced characterization of the FZ using TEM and APT: (a) atomic arrangements corresponding to γ-FCC and ε-HCP phases; (b) VC precipitate and corresponding composition maps in (c) and (e); APT tips revealing compositional homogeneity within the FZ.*_____ *121*
*Figure 53 – Synchrotron x-ray diffraction throughout the welded joint: (a) Intensity distribution map of the (2 0 0) peak and (b) Interplanar spacing map. The diffraction patterns taken from the regions marked in (a) correspond to those presented in Figure 54 and Figure 55.*_____ *122*
Figure 54 – Representative diffraction patterns from the (a) the SMA BM, (b) the HEA BM, (c) the HAZ from the SMA side and (d) the HAZ from the HEA side of the joint. _____ *123*
Figure 55 – (a) Superimposition of the diffraction pattern taken from the FZ, namely closer to each of the BMs and at its bulk. (b) Detailed view of the low intensity diffraction peaks corresponding to phases with lower fraction within the FZ. _____ *124*
Figure 56 – (a) Representative mechanical response to tensile stress of the welded joints, the SMA and the HEA BMs; (b) DIC results showcasing local strain distribution before fracture;(c) DIC point analysis obtained during tensile testing. _____ *125*
Figure 57 – (a) Fracture surface of the gas tungsten arc welded dissimilar joint. (b) Depiction of the fractured tensile specimen marking the analyzed region. _____ *126*
Figure 58 - Macrostructure of the GTAW AlCoCrFeNi HEA joints: (a) and (c) correspond to the optical micrographs of the non-inoculated and inoculated joints, respectively, while (b) and (d) comprise the superposition of the EBSD IQ map of the IPF map and the non-inoculated and inoculated materials, respectively. _____ *130*
Figure 59 – (a) Initial condition of the AlCoCrFeNi HEA BM showcasing large primary FCC grains and the eutectic (FCC + B2 BCC) constituents observed by SEM and (b) corresponding EDS maps. The points marked in (a) correspond to the EDS point analysis results exhibited in Table 10. In (c) a representative synchrotron X-ray diffraction pattern indicates the presence of more (nanometric) phases in the BM. _____ *133*
Figure 60 – Phase diagrams calculated considering: a) nominal composition and b) real composition (L stands for Liquid phase). The Scheil solidification curves of both compositions are shown in c). _____ *136*
Figure 61 – Representative synchrotron X-ray diffraction pattern from the HAZ. (# stands for the low intensity 2nd harmonic diffraction peaks that do not correspond to any structure present on the alloy) _____ *138*
Figure 62 – Detailed optical micrograph view of the microstructure features at the HAZ/FZ boundary: (a) fusion boundary of the non-inoculated joints and (b) fusion boundary of the TiB_2 inoculated samples. _____ *140*
Figure 63 – Microstructural differences between both types of samples: (a) optical microscopy and (b) EBSD of the non-inoculated samples; (c) optical microscopy, detailed view of the eutectic constituent (d) and (e) EBSD of the TiB_2 inoculated samples. _____ *143*
Figure 64 – EDS maps of non-inoculated (a) and inoculated (b) joints. For b) a Ti map was added to track the changes induced in the FZ composition due to partial dissolution of the TiB_2 particles. A detailed view of the Cr

map of the inoculated FZ is displayed in (c) marking the points where EDS scans were performed. The EDS point results are shown in (d). _____ *145*
Figure 65 – CalPhaD-based analysis of the phases formed during solidification using the Scheil-Gulliver method. The curve in (a) highlights the solidification path of the inoculated sample. Additionally, (b) shows the evolution of o the composition in the liquid phase is shown for the non-inoculated and the TiB_2-inoculated compositions. _____ *146*
Figure 66 – Representative synchrotron x-ray diffraction patterns in: a) non-inoculated sample and b) in the TiB_2-inoculated case. (# stands for the low intensity 2nd harmonic diffraction peaks that do not correspond to any structure present on the alloy) _____ *149*
Figure 67 – Microhardness distribution along the welded joint: a) microhardness map of the non-inoculated samples; b) microhardness map of the inoculated sample and c) microhardness distribution comparison at half height as indicated by the red and black arrow. _____ *151*
Figure 68 – Representative tensile test results, showcasing the macroscopic mechanical properties of BM and welded joints. _____ *152*
Figure 69 – DIC point analysis obtained during tensile testing of: a) non-inoculated and d) TiB_2-inoculated samples. Additionally, b) and e) exhibit the local strain distribution right before fracture of each sample. The fracture surfaces of the non-inoculated and inoculated samples are displayed in c) and f), accordingly. _____ *153*
Figure 70 – Optical microscopy of the cross-section of the dissimilar weld: (a) Macrograph highlighting the FZ and the two BMs; and (b) EDS maps displaying an overall perspective of the elemental distribution throughout the joint (c) Collage of IPF EBSD maps of the dissimilar welded joint, highlighting the variation in grain orientation and morphology throughout the joint. (FB corresponds to the fusion boundary). _____ *157*
Figure 71 – Representative EBSD maps of the BMs: (a) AlCoCrFeNi HEA and (b) 316L SS. _____ *159*
Figure 72 - EDS maps of the AlCoCrFeNi HEA. _____ *160*
Figure 73 – Microstructural features at the fusion boundary: a) EBSD maps obtained on the AlCoCrFeNi side and b) 316L SS side. SEM micrographs highlighting the sharp microstructural differences, i.e., grain size and morphology variations, can be observed in c) for the AlCoCrFeNi side and d) for the 316L SS side of the weld. 161
Figure 74 – EDS mapping at the fusion boundary near the: a) AlCoCrFeNi HEA and b) 316L SS BMs. _____ *162*
Figure 75 – EBSD maps obtained (a) near the AlCoCrFeNi HEA, (b) at the bulk and (c) near the 316L SS side of the FZ, alongside (d), (e) and (f) and (g) representing the composition at obtained at each of these regions utilizing APT, respectively. The EDS maps in (h), (i) and (j) highlight the composition of each examined regions. _____ *163*
Figure 76 – Synchrotron X-ray diffraction analysis of the welded joint: (a) superimposition of full azimuthal integrated diffraction over the full extent of the joint (major peaks from the FCC and BCC B2 phases are marked on the left side of the map). Representative synchrotron X-ray diffraction scans were obtained from: (b) AlCoCrFeNi HEA BM; (c) 316L SS BM; (d) FZ near the AlCoCrFeNi HEA and (e) FZ near the 316L SS BM. Peaks coming from 2nd harmonic reflections, due to P07b/PETRA III beamline conditions, were left unidentified. __ *165*
Figure 77- CalPHaD-based simulation of the phases that may develop during solidification: (a) variation of Liquidus, solidus and eutectic temperatures with an increasing amount of 316L SS; (b) Scheil-Gulliver solidification curves corresponding to the FZ and the compositions of 50% and 60% of the mixture of 316L SS; and (c) partition coefficient evolution of the FZ. _____ *168*
Figure 78 – Microhardness map of the dissimilar welding joint, highlighting the differences arising from the varying microstructure. _____ *170*

Figure 79 – Representative mechanical response to tensile stress of: (a) the welded joints; (b) 316L SS base material and (c) AlCoCrFeNi HEA base material. _____ *171*
Figure 80 - Digital image correlation results exhibiting: (a) the local strain distribution before fracture and (b) point analysis obtained during tensile testing; and fracture surface after failure of the sample. _____ *173*
Figure 81 - Representative electron backscatter IPF macroscopic images of the welded joints of: (a) CoCu20FeMnNi; (b) CoCu30FeMnNi. _____ *177*
Figure 82 – EBSD phase maps highlighting the initial condition of the (a) CoCu20FeMnNi and (b) CoCu30FeMnNi HEAs, alongside with the corresponding elemental distribution in (c) for the CoCu20FeMnNi and (d) for the CoCu30FeMnNi BMs. _____ *178*
Figure 83 – One axis equilibrium performed to evaluate the phase formation in equilibrium conditions. The calculations were computed using TCHEA5 databases. _____ *179*
Figure 84 – Microstructural analysis at the fusion boundary, highlighting the optical microscopy image of the (a) CoCu20FeMnNi HEA and (b) CoCu30FeMnNi HEA and corresponding EBSD IPF and phase maps in (c) and (e) for the CoCu20FeMnNi, and phase maps in (d) and (f) for the CoCu30FeMnNi HEA. _____ *181*
Figure 85 – (a) Simulation of the non-equilibrium solidification using Scheil-Gulliver method, and (b) partition coefficient of the elements throughout solidification. _____ *183*
Figure 86 - Microstructural analysis of the fusion zone on the (a) $CoCu_{20}$FeMnNi and (b) $CoCu_{30}$FeMnNi HEAs in the as-welded condition, and corresponding EDS line scans (c) and (d). _____ *186*
Figure 87 – Representative synchrotron X-ray diffraction patterns, from both HEAs welded joints on the: (a) BM, (b) HAZ, and (c) FZ. _____ *188*
Figure 88 - Interplanar spacing distribution corresponding to the different phases identified throughout the microstructure of $CoCu_{20}$FeMnNi (a) and $CoCu_{30}$FeMnNi (b) welded HEAs. _____ *191*
Figure 89 – Comparison between the polarization curves of the $CoCu_x$FeMnNi (x=20,30) BMs alongside with the corresponding FZs. _____ *192*
Figure 90 – EIS measurements of the welded joints: (a) and (b) are the Bode and Nyquist diagrams of the CoCu20FeMnNi BM, respectively, while (c) and (d) are the Bode and Nyquist diagrams of its corresponding FZ; (e) and (f) correspond to the Bode and Nyquist diagrams of the CoCu30FeMnNi BM and (g) and (h) are the Bode and Nyquist diagrams of the CoCu30FeMnNi FZ. _____ *193*
Figure 91 – Microhardness distribution along the (a) $CoCu_{20}$FeMnNi and (b) $CoCu_{30}$FeMnNi welded HEAs. Comparison of the hardness variation taken from the middle line of the map is displayed in (c). _____ *195*
Figure 92 – (a) Representative stress-strain curves obtained from both HEAs in the as-welded and base material conditions. Digital image correlation images taken prior to fracture of the (b) $CoCu_{20}$FeMnNi and (c) $CoCu_{30}$FeMnNi welded HEAs, highlighting the FZ as the softest and weakest point of the joint. _____ *197*
Figure 93 - Fracture surfaces of welded specimens: (a) $CoCu_{20}$FeMnNi and (b) $CoCu_{30}$FeMnNi welded joints and corresponding detailed views in (c) and (d), respectively. _____ *198*
Figure 94 - Microstructural features of the GTAW Cr29.7Co29.7Ni35.4Al4Ti1.2 MPEA joint: a) Overall perspective indicating the BM, HAZ and FZ regions; b) BM; c) Transition from the HAZ to the FZ; d) FZ; e) Detailed view of the BM, highlighting the presence of TiN inclusions, as indicated by black arrows, and annealing twins marked with red dashed lines; f) Detailed view of the PMZ (Partially Melted Zone); (g) Detailed view of the HAZ, indicating similar features to those identified in e). _____ *201*
Figure 95 – Analysis of a region comprising the BM, HAZ and FZ: (a) SEM micrograph and (b) EBSD map. ___ *204*

Figure 96 – Pole figures displaying the crystallographic texture on the (a) [001], (b) [101] and (c) [111] directions of the base material; (d) [001], (e) [101] and (f) [111] directions of the grain refined region near the interface of the Heat affected zone with the fusion zone and (g) [001], (h) [101] and (i) [111] directions of the fusion zone. All pole figures are presented on the same scale for a direct comparison. _____ *207*
Figure 97 - Analysis of the region comprising the FZ: (a) SEM micrograph and (b) corresponding EBSD and (c) KAM maps; (d) EDS line scan results performed across the joint to evaluate the possibility for macrosegregation. _____ *208*
Figure 98 - EDS mapping of the FZ: (a) Inspected region and elemental distribution of (b) Al, (c) Ti, (d) Cr, (e) Co and (f) Ni. _____ *209*
Figure 99 – Intermetallic phase present within grain boundaries: (a) Morphology at the grain boundary; (b) Elemental map and (c) Line scan taken in the region indicated by the red line in (a). _____ *211*
Figure 100 – Comparison between the non-equilibrium Scheil-Gulliver thermodynamical calculations performed using Thermo-Calc (TCHEA5 database) and Pandat (PanHEA2022 database), to interpret the molten pool solidification. _____ *212*
Figure 101 – Comparison between the elemental partition on the matrix γ phase throughout solidification, calculated with (a) Thermo-Calc, using the TCHEA5 database and (b) Panda, using the PanHEA2022 database. _____ *214*
Figure 102 - One axis equilibrium calculation performed on the nominal composition of the MPEA, to evaluate the phase formation in equilibrium conditions. The calculations were computed using TCHEA5 and PanHEA2022 databases. _____ *216*
Figure 103 - Understanding the microstructure of the fusion zone using Thermo-Calc software (TCHEA5 database): (a) equilibrium calculations performed on specific compositions retrieved from Scheil-Gulliver simulations and (b) representation of a dendrite and the material that surrounds it, to highligh the microstrcutural differences form the dendrites and the interdedritic material. _____ *217*
Figure 104 – Synchrotron X-ray data of the Cr29.7Co29.7Ni35.4Al4Ti1.2 MPEA welded joint: (a) Overall superimposition of the diffraction patters highlighting the different regions of the welded joint, namely: (b) Base material, (c) Fusion Zone and (d) Heat affected zone (# corresponds to 2nd harmonic reflections). _____ *220*
Figure 105 - Microhardness measurements: (A) Microhardness map across the welded joint); (B) representative line scan obtained at the joint mid height. _____ *222*
Figure 106 – Comparison of the tensile behavior of the welded $Cr_{29.7}Co_{29.7}Ni_{35.4}Al_4Ti_{1.2}$ *MPEA and the BM.* ___ *223*
Figure 107 – Weld tensile behavior probed by DIC: (A) Sample condition before loading and (B) Strain partitioning evolution throughout the test. The symbols marked in the underformed material (blue collored snapshot of b) correspond to the locations of the welded joint which were used to obtain the representative stress-strain behaviors of the BM, HAZ and FZ detailed in Figure 108. _____ *224*
Figure 108 – Stress-strain behavior of representative points located in the BM, HAZ and FZ obtained with DIC during tensile testing of the welded joints. between the analyzed points (marked in Figure 107 (B) sample undeformed condition). Locations of these regions was previously indicated in Figure 107. The insert details the macroscopic mechanical response of the welded joint (black curve) and the DIC average response (orange curve). _____ *225*
Figure 109 - Fractography of the welded sample: (A) Overview of a fractured sample; (B) Close-up highlighting a ductile-like morphology of the surface; (C) Detail of the dimples in the ductile region of the fracture surface. *226*

Figure 110 – Depiction of the experimental procedure and conditions: (a) Optical micrograph of the welded joint complementing a graphical explanation of the SXRD in-situ tensile test; (b) Debye-Scherrer rings captured by the 2D detector during one scan of the welded joint; (c) mechanical performance of the welded joint under tensile stress; (d) Representative diffraction patterns of the BM and FZ prior to loading. _____ *228*
Figure 111 – (a) Normalized integrated intensity variation of the (3 1 1) diffraction reflection obtained throughout the full extension of the weld, at different loading stages. The joint regions (BM, HAZ and FZ) are marked considering the 0 MPa loading condition. Data obtained using full azimuthal integrated data. (b) Schematic representation of the cross-section evolution during tensile testing. _____ *230*
Figure 112 – Lattice strain evolution, measured on the LD and TD, throughout the in-situ tensile test. The diffraction reflections (a) (2 0 0) and (b) (3 1 1), were chosen due to their exclusive availability in the LD of the FZ. The value of d_0 was set to be the value for d-spacing obtained in the BM at the 0 MPa stage serving as the baseline for comparison. _____ *231*
Figure 113 – Region-specific lattice strain evolution during tensile loading along LD and TD with regard to strain. The results shown in (a) and (b) correspond to the BM, (c) and (d) correspond to the HAZ and (e) and (f) correspond to the FZ. Note that in the FZ, the only visible reflections correspond to the (2 0 0) and (3 1 1) planes on the LD, such being due to the large grain size characteristic of this region and the solidification conditions imposed during welding. _____ *233*
Figure 114 – (a) Initial and (b) last stages of the tensile test probed by SXRD, highlighting, qualitatively, prevalent grain orientations on the BM, HAZ and FZ, obtained by integration of 1-degree segments on the full azimuthal range. (c) corresponds to the obtained lattice strain on each of the segments, quantitatively indicating the amount of localized lattice strain handled by each of the regions. _____ *236*
Figure 115 – Microstructure of the welded joint: a) SEM macrograph of the welded joint and corresponding EBSD IPF maps of the transition from the HAZ to the BM (b) and transition from the FZ to the HAZ (c) and detailed view of the HAZ (d); e) SEM micrograph of the BM; f) EDS maps the along the full extension of the welded joint. Additional detailed view and corresponding EDS maps of: g) NbC precipitates on the Inconel 718 BM and h) Cr-Mn oxides on the Cantor HEA BM. _____ *240*
Figure 116 – Phase identification and distribution across the welded joint: a) Superimposition of the SXRD patterns along the whole extension of the weld; b) representative SXRD pattern of the FZ; c) CalPhaD-predicted phase distribution at the top of the joint, which is located in d), alongside with the e) phase distribution prediction at the middle of the joint. _____ *242*
Figure 117 – (a) FWHM variation of the (3 1 1) diffraction peak measured on the 0 ^{o} and 90 ^{o} azimuthal angles along the welded joint. b) Comparison between the diffraction data obtained on the FZ and both BM, obtained by integrating in 1^o segments along the azimuthal angle. _____ *245*
Figure 118 - a) Microhardness distribution along the welded joint and b) corresponding microhardness distribution measured at mid height. _____ *246*
Figure 119 –a) Representative stress-strain curve of the welded joint tensile and macroscopic view of the fracture surface (b); c) and d) are representative stress-strain curves for the rolled CoCrFeMnNi and annealed Inconel 718 BMs, respectively. e) and f) corresponding to detailed views of the macroscopic fracture surface shown in b). _____ *248*

LIST OF TABLES

Table 1 – Welded joint summary. _____ *27*
Table 2 - Welded joint summary (continuation). _____ *28*
Table 3 – Parameters utilized for welding. _____ *30*
Table 4 – List of etchants and corresponding composition, utilized to observe the microstructure of each welded joint. _____ *31*
Table 5 - Young's modulus and for different lattice planes of the constituent phases in the DP-HEA. _____ *49*
Table 6 – Compositional measurements, as obtained by point EDS, in the BM and the FZ. _____ *63*
Table 7 – Phase fraction distribution along the weld microstructure, calculated using ImageJ on a representative location of each region. _____ *65*
Table 8 – Quantification of the microhardness distribution throughout the welded joint microstructure. ____ *107*
Table 9 – Compositional comparison of the AlCoCrFeNi HEA base material. _____ *134*
Table 10 – EDS single point analysis results. The scanned regions are marked in Figure 59 (a). _____ *135*
Table 11 – Compositional measurements in FZ obtained by EDS. _____ *164*
Table 12 – Compositions utilized for Scheil-Gulliver calculations (all values in at. %). _____ *167*
Table 13 - Lattice parameter in the HAZ and FZ (rounded to the fourth decimal case) _____ *189*
Table 14 – Average grain size measurements ordered taking the proximity to the FZ in consideration. _____ *205*
Table 15 – Average chemical composition of Inconel 718 and CoCrFeMnNi BMs and the FZ, obtained via EDS, considering the elements detailed in Figure 115. _____ *241*
Table 16 - Summary of the welded joint mechanical properties of both BM and dissimilar welded joint. ____ *246*

List of Abbreviations and Symbols

Abbreviations:

AC	Alternate current
BCC	Body centered cubic
BM	Base material
CalPHaD	Calculation of phase diagrams
CNC	Computer numerical control
DCEN	Direct current electrode negative
DCEP	Direct current electrode positive
DIC	Digital image correlation
DP-HEA	Dual phase high entropy alloy
EBSD	Electron backscatter diffraction
FB	Fusion boundary
FCC	Face centered cubic
Fe-SMA	Fe-based shape memory alloy
FWHM	Ful width at half maximum
FZ	Fusion zone
HEA	High entropy alloy
IPF	Inverse pole figure
GTAW	Gas tungsten arc welding
HAZ	Heat affected zone
HCP	Hexagonal close-packed
HI	Heat input
KAM	Kernel average misorientation
LEA	Low entropy alloy
LD	Load direction
MEA	Medium entropy alloy

OM	Optical microscopy
PMZ	Partially melted zone
QI	Quality index
SEM	Scanning electron microscopy
SMA	Shape memory alloy
SS 316L	Stainless steel 316L
SXRD	Synchrotron X-ray diffraction
S/L	Refers to the Solidus/Liquid interface
TD	Transverse direction
TRIP	Transformation induced plasticity
TWIP	Twinning induced plasticity
UTS	Ultimate tensile strength

Symbols:

b	Burgers vector
C	Composition of an alloy
c	Molar fraction
D	Crystallite size
$\mathbf{D_L}$	Diffusion coefficient in the liquid
d	Interplanar spacing, not to be confused with mean grain size, also d.
d	Mean grain size, not to be confused with interplanar spacing, also d.
G	Temperature gradient, not to be confused with the shear modulus, also G.
G	Shear modulus, not to be confused with the temperature gradient, also G.
K	Partition coefficient
$\mathbf{K_{sf}}$	Strengthening coefficient
$\mathbf{L_{sf}}$	Stacking fault interspacing
M	Taylor factor

$\mathbf{n}$	Number of elements
$\mathbf{P_{sf}}$	Stacking fault probability
R	Gas constant, not to be confused with the growth rate, also R.
R	Growth rate, not to be confused with the gas constant, also R.
$\mathbf{T_L}$	Liquidus temperature
$\mathbf{T_m}$	Melting temperature
$\mathbf{T_S}$	Solidus temperature
v	Welding speed
ΔG	Gibbs free energy of a system
ΔH	Enthalpy of mixing of a system
ΔT	Variation in solidification temperature
ΔS	Entropy of mixing of a system
δ	Length of the solute-rich region next to the S/L interface,
ε	Lattice strain
$\mathbf{\langle\varepsilon\rangle^2}$	Microstrain
θ	Theta angle
λ	Wavelength
ρ	Dislocation density
$\mathbf{\sigma_0}$	Strengthening contribution from lattice friction stress
$\mathbf{\sigma_D}$	Strengthening contribution from dislocations
$\mathbf{\sigma_{GB}}$	Strengthening contribution from the grain boundaries
$\mathbf{\sigma_{sf}}$	Strengthening contribution from the stacking faults
$\mathbf{\sigma_y}$	Yield strength
φ	Azimuthal angle

1

INTRODUCTION

1.1 Motivation and objective

Often used to this day is the conventional approach for alloy design, where small quantities of alloying elements are added to a principal constituent to grant it specific characteristics. However, in recent years, new ideas on this topic led to the discovery of a new class of materials named high entropy alloys (HEAs).

On this regard, HEAs differ from the traditional approach of producing new metals, by allowing large quantities of each element into its composition, rendering them not to be established as alloying components, but as principal elements themselves.

With this in mind, many techniques have been employed for the development of HEAs throughout the years, which are mainly based on thermodynamics. However, HEAs can also be designed with specific characteristics in visage, by taking a mechanistic alloy development pathway, which is pursued as the focus of the present document, via welding technologies.

As such, welding technologies envelope several categories of well-established processing methods that are often used in the modern industrial world to permanently join several components into a singular part. Amidst these categories fusion-based welding processes stand out as they render the final condition of a material to be massively distinct from its initial form, by causing several changes in the microstructure either through solidification or solid-state processes. As such, it is possible to obtain research-based data through the correlation between processing, microstructure and properties on HEAs welded joints for further advancement of these materials and, thus, widening the horizon regarding HEAs and expanding their potential in engineering applications.

In light of this, the main objective of this thesis is to provide fundamental knowledge on the how fusion based welding processes of these advanced materials and, thus, to offer a relevant input of information for their further development and assimilation in the modern-day world.

1.2 Major findings and publications in international peer-reviewed indexed journals

With regard to the major findings acquired thorough this work, it can be stated that these derive from the several HEAs that were successfully welded in similar and dissimilar combinations.

In general, all welds are microstructurally accessed, either via optical microscopy (OM), synchrotron X-ray diffraction and SEM based techniques such as EBSD. Correlation with the mechanical performance via microhardness mapping and tensile testing was also accessed. Furthermore, thermodynamic calculations were performed to evaluate the solidification path undertaken during the welding process. Overall, the findings regarding each of these welds were fully discussed and are ready to fulfil the main purpose of this thesis, which is to supply the overall knowledge in this topic with results that increase knowledge on these advanced alloys.

During the progress of this work, eights scientific papers were published in international indexed (ISI/Scopus) journals, as bellow:

Published scientific papers:

- *J.G. Lopes*, P. Agrawal, J. Shen, N. Schell, R. S. Mishra, J.P. Oliveira. **Evolution of microstructure and mechanical properties in gas tungsten arc welded dual-phase $Fe_{50}Mn_{30}Co_{10}Cr_{10}$ high entropy alloy**, Materials Science and Engineering: A. (2023). https://doi.org/10.1016/j.msea.2023.145233.

- *J.G. Lopes*, P. Rocha, D.A. Santana; J. Shen; E. Maawad; N. Scheel; F.G. Coury; J.P. Oliveira. **Impact of Arc-Based Welding on the Microstructure Evolution and Mechanical Properties in Newly Developed $Cr_{29.7}Co_{29.7}Ni_{35.4}Al_4Ti_{1.2}$ Multi-Principal Element Alloy**. Advanced Engineering Materials (2023). https://doi.org/10.1002/adem.202300109.

- *J.G. Lopes*, D. Martins, K. Zhang, B. Li, B. Wang, X. Wang, N. Schell, E. Ghafoori, A.C. Baptista, J.P. Oliveira. **Unveiling the microstructure evolution and mechanical properties in a gas tungsten arc-welded Fe–Mn–Si–Cr–Ni shape memory alloy**. Journal of Material Sciences (2024). https://doi.org/10.1007/s10853-024-09606-4.

- *J.G. Lopes*, A. Candeias, P. Agrawal, J. Shen, N. Schell, R.S. Mishra, J.P. Oliveira, **Role of TiB_2 inoculation particles during welding of a AlCoCrFeNi high entropy alloy**, Journal of Alloys and Compounds (2024). https://doi.org/10.1016/J.JALLCOM.2024.174694.

- P. Dias, *J.G. Lopes**, T. Curado, E. Maawad, N. Schell, H.S. Kim, J.P. Oliveira, **In-situ microstructural evolution during tensile loading of CoCrFeMnNi high entropy alloy welded joint probed by high energy synchrotron X-ray diffraction**, Science and Technology of Welding and Joining (2024). https://doi.org/10.1177/13621718241259349.

- *J.G. Lopes*, J. Shen, E. Maawad, N. Schell, R. S. Mishra, J. P. Oliveira. **Time-resolved evolution of the deformation mechanisms in a TRIP/TWIP $Fe_{50}Mn_{30}Co_{10}Cr_{10}$ high entropy during tensile loading probed with synchrotron X-ray diffraction**, International Journal of Plasticity (2024). https://doi.org/10.1016/j.ijplas.2024.104048.

- D. Afonso, *J.G. Lopes**, Y. T. Choi, R. E. Kim, N. Schell, N. Zhou, H. S. Kim, J. P. Oliveira. **Dissimilar laser welding of an as-rolled CoCrFeMnNi high entropy alloy to Inconel 718 superalloy**, Optics & Laser Technology (2025). https://doi.org/10.1016/j.optlastec.2024.111427.

- *J.G. Lopes*, M. Varela, S. H. Shim, N. Schell, E. Maawad, S. I. Hong, A.C. Baptista, J.P. Oliveira. **Gas tungsten arc welding of a multiphase CoCuxFeMnNi (x=20,30) high entropy alloy system: microstructural differences and their consequences on mechanical performance**, Intermetallics (2024). https://doi.org/10.1016/j.intermet.2024.108439.

* - corresponding author.

1.3 Document organization

This thesis is segmented into five chapters. Their description is as follows.

Chapter 1 - Introduction: This chapter aims to introduce the research topic of this thesis. It also details the motivation and objectives behind this work.

Chapter 2 – Literature review: This chapter provides an overview of the state of the art regarding welding of HEAs, including definitions. It starts by introducing HEAs definition and design techniques. Then an overview of the GTAW process is presented alongside the premise of welded joint characterization for the improvement and development of HEAs. Then a literature review on the topic of welding HEAs is given, finalizing with the current state of the knowledge regarding the HEAs that compose the core of this thesis.

Chapter 3 – Material and Methods: In this chapter the methodologies adopted for characterization of the welded joint are highlighted. A short overview of all the welded joints, alongside welding platform development, synchrotron x-ray diffraction characterization, thermodynamical calculation and sequent mechanical analysis is shown.

Chapter 4 – Results and Discussion: In this chapter the results obtained from the analysis HEA are exhibited and discussed.

This chapter starts with an in-situ synchrotron X-ray diffraction study during tensile loading on the base material. Then, the similar weldability of the FeMnCoCr HEA joints, obtained via GTAW are presented and discussed. A study on the weldability of a Fe-based shape memory alloy (SMA) is also presented, which stands as the basis for the full characterization of dissimilar welds between FeMnCoCr HEA and the Fe-based SMA.

Furthermore, an effort to refine the microstructure on AlCoCrMnNi HEA similar welding joints is performed via inoculation with TiB_2 particles, which are then compared to similar welded joints of the same HEA. Dissimilar welding between the AlCoCrMnNi HEA and Stainless steel is also presented.

Next, two HEAs belonging to the $CoCu_xFeMnNi$ system are analyzed. Both welded joints obtained from each HEA are analyzed and compared in terms of microstructure and mechanical performance.

Subsequently, the CoCrFeAlTi HEA is a new alloy that was based on a CoCrNi matrix, which is one of the toughest materials known. Here, the similar weldability of the CoCrFeAlTi MPEA is thoroughly discussed.

On a different approach, an in-situ synchrotron X-ray diffraction study during tensile loading on the welded joints the CoCrFeMnNi HEA is shown. To the best of the authors knowledge this is the first study concerning in-situ testing of a welded joint. Then, the dissimilar weldability between the CoCrFeMnNi HEA and Inconel 718 is presented and discussed.

Chapter 5 – Conclusions and future work: An overall conclusion regarding the presented results and future work possibilities are provided.

2

LITERATURE REVIEW

2.1 Chapter Introduction

In this chapter, a state of the art on the topic of welding high entropy alloys is provided. Such is especially important to lay the foundation required to enlighten the potential contained within this research topic.

Given this, starting with the definition of high entropy alloys, the path leading towards the relevant point of investigating welding processes, namely gas tungsten arc welding, on these advanced materials is followed. This is done in an effort to magnify the microstructural and mechanical findings that will be discussed throughout the document.

In summary, a state-of-the-art regarding welding high entropy alloys reveals that, although being in its early stages, research on this topic is invaluable for the development of new and existing HEAs. Such is the premise on which this thesis is founded and can be accomplished via standard and advanced metallurgical characterization techniques, that may serve as valid inputs for the advancement of the body of knowledge regarding HEAs.

2.2 High entropy alloy design and definition

The first mentions in the literature related to the attempt of discovering new metallic alloys through the mixture of different elements was carried by Franz Carl Achard [1], in 1788. However, without knowledge of modern metallurgical concepts, the topic of discovering new alloys by mixing several elements in various compositions was left untouched until much later, in 2004 [2,3].

Consequently, the fundamental alloy development strategy of adding small amounts of secondary constituents to a dominant element has remained intact over the centuries. Such can be especially noticed in the nomenclature given to titanium alloys, aluminum alloys, nickel superalloys, etc. (outside some exceptions like steels and brasses) and presents itself as the prime example of this effective, albeit limited, alloy production approach [4].

Nevertheless, with the turn of the XXI century, new thoughts on alloy development research have revolutionized the way new metallic combinations are developed, yielding

advanced materials capable of being exploited and customized for case-specific purposes. Such materials are presently known as high entropy alloys, multi-component alloys, compositionally complex alloys and multiprincipal-element alloys. All these refer to the same new class of materials, although reasoning with distinct definitions [5].

Still, being the most commonly found in the literature, the high entropy alloy name, which was coined by Yeh et al. [4], states that stable solid solutions can be created from at least five elements in concentrations ranging from 5–35 at.%. On a more entropy-based definition, the imposition for the number of elements relates to the Boltzmann's entropy formula expressed in Equation 1 [3].

$$\Delta S = - R \cdot \sum_{i}^{n} c_i \cdot \ln(c_i) \quad (1)$$

Where, ΔS is the entropy of mixing, R is the gas constant, c_i is the is the molar fraction of the i^{th} element of constituent elements and n refers to the number of elements. Where the case of an equiatomic alloy $c_i = c_n$ and the Equation 1 becomes:

$$\Delta S = R \cdot \ln(n) \quad (2)$$

As such, depending on the number of elements, three different classes of alloys can be defined, as follows:

- Low entropy alloys (LEAs), with $\Delta S < 0.69 \cdot R$;
- Medium entropy alloys (MEAs), $0.69 \cdot R < \Delta S < 1.61 \cdot R$;
- High entropy alloys (HEAs), $\Delta S > 1.61 \cdot R$.

Where MEAs would resemble to some extent HEAs, being capable of showcasing interesting properties upon compositional tunning, and LEAs correspond to traditional alloys, such as steels [6].

Apart from that, granted that such requirements are met in a HEA, the means for the entropic contribution, at the melting temperature (T_m), are attained to overcome the enthalpic factor (ΔH) on the overall Gibbs free energy (ΔG) of a system (see Equation 3). In this way the conditions to prevent the formation of intermetallic compounds and other possibly detrimental phases on the alloy are met (depending on their ΔH), thus contributing to the formation of a single-phase alloy.

$$\Delta G = \Delta H - T_m \cdot \Delta S \quad (3)$$

Nevertheless, such criterion cannot simply predict single-phase solid solution, as other factors come into play. For example, as more and more elements are added to a system, the number of possible phases (including binary or ternary intermetallic compounds) that can be formed, also increase leading to the formation of not only a single phase but perhaps to more phases within the alloy. However, such challenges could be mitigated by the increasing entropy in the system, nevertheless, outside the theoretical space, other difficulties, such as uneven elemental distribution and additional defects on the lattices, can arise impacting the overall phase stability of the newly developed alloy. Thus, the necessity for development of other nomenclatures throughout the years.

Still, such consideration allows for the exploration of the compositional space beyond the traditional design concept of a single element as the main component in an alloy, driving potential combinations for HEAs away from the vertices of the diagram displayed in Figure 1. There each corner corresponds to a specific element and as moving away from them, different compositions with small addition of other elements are achieved. Such elemental combinations may correspond to conventional alloys, however when moving towards the vast and unexplored compositional space, novel alloy compositions can be discovered aiding in the interpretation and giving form and of the concept of HEAs.

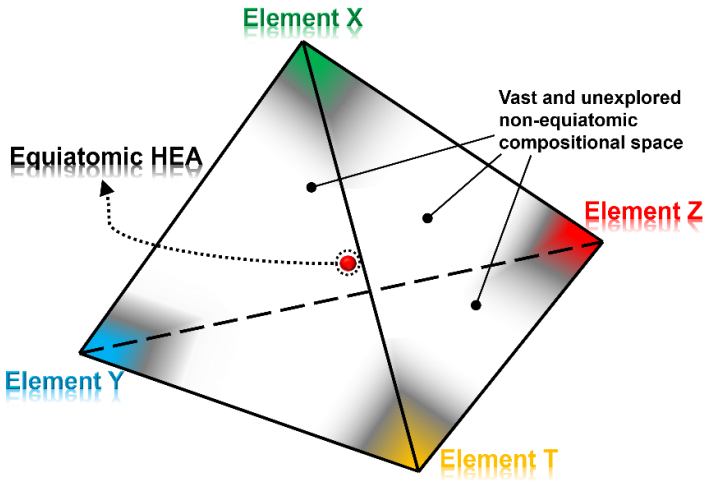


Figure 1 – Vast compositional space for high entropy alloy development.

Furthermore, granted that these requirements for the development of an HEA are met, four core effects of HEAs were identified to occur. First, we have the “high entropy effect”, which is associated with configurational entropy that stabilizes the formation of simple solid-

state phases and was debated in the last paragraph. Then, there is the “lattice distortion effect”, that occurs due to the lack of a dominant element, which causes atoms of different sizes to occupy random positions of the crystal structure, promoting its distortion and hindering dislocation movement. In this case, depending on the selected atoms distribution, different phases can nucleate [7], thus being a valid method to favor a phase in detriment of another. However, this can prove to be a difficult task as, per example, in the CoCrFeMnNi HEA, the atomic size of the atoms that compose it is quite similar. Thirdly, the “sluggish diffusion effect”, which constrains atomic diffusion, inhibiting phase transformations that require such phenomenon. As such higher recrystallization temperatures can be attained causing nano-precipitates and secondary phases to precipitate after long periods. Finally, the “cocktail effect”, that relates to the properties of the HEAs that cannot be attributed independently to any of the elements that are a part of it.

However, as discussed next, HEAs are not secluded to only these effects, since additional and enhanced HEAs can be obtained envisaging other routes.

As such, beyond this initial definition the scientific focus over the years turned not to the theoretical definition of HEAs, but rather to the development of new HEA systems. In his work, George, E. P. et al. [5] identified three alternatives for obtaining of a new HEA system: the experimental pathway, the thermodynamic pathway and the mechanistic pathway.

The experimental pathway follows the traditional, yet effective, manner of finding, producing and characterizing an alloy or many of its variants in simultaneous. Such can either be possible from the bulk production of a sample composed of a single composition or from the manufacture of compositionally graded samples, followed by their consequent characterization. This approach can be beneficial in finding potential compositions and rejecting unviable ones, thus playing an important role in exploring the high entropy alloy landscape. That is, provided that a reliable mechanical and microstructural characterization are successfully performed.

On a more theoretical basis, there is the thermodynamic pathway [8]. This method bases itself on the CalPhaD methodology, which stands for “calculation of phase diagrams”, and envisages the prediction of the phases that can nucleate in an alloy in accordance with temperature. It does so through polynomial equations, known as Redlich–Kistler functions,

obtained via fitting of theoretical and experimental data that allow to describe the Gibbs–Helmholtz free-energy of every phase. For such, however, these functions must be coherently gathered for each phase in an assigned database, which more often than ever can be incomplete, as many unpredicted precipitates can developed in real-life situations. Although having proved itself to be a very valuable source of knowledge, as in [9,10] ,other challenges arise, since it is solely based on thermodynamics, meaning that it may not predict the formation of transient or metastable phases, such as martensite or bainite.

Outside the scope of these two alloy development approaches, the mechanistic pathway presents itself as an alternative route that seeks to tailor an alloy's response over the stability of its phases. That is, engineering an alloy based on their application and consequent working conditions, by taking advantage of specific strengthening mechanisms, such as deformation twinning [11], precipitation strengthening [9] and martensitic transformation [12]. Such can be achieved by composition tuning the projected alloy, to control and adapt, for example its stacking-fault energy, which is the reigning mechanism responsible for twinning or martensite nucleation amongst other phenomena. Thus, this mechanistic alloy design not only focuses on obtaining particular deformation mechanisms, but also in identifying thermodynamic parameters that reign over them, so that the response to given solicitation can be optimized. However, while in the pursuit of alloys with specific effects and characteristics, it deviates for the original HEA definition, in the sense that less than five alloying elements can be used, as well as lower elemental quantities than 5%, to achieve new HEAs with optimal properties. Such is the case of the [12] and the [13], thus asserting that the entropy is not the governing factor behind the formation of these novel alloys, as other key thermodynamic parameters may favor the HEAs performance during their effective lifespan in a given application.

From all these different HEA design ideas, the inception of HEAs occurred in 2004, with the seminal works of Cantor [2] and Yeh [3]. As such, as many other HEA systems can be uncharted, there are infinite application prospects to which these advanced alloys can be utilized in, leaving to the imagination of the alloy development researcher the possible utilization of such material. Such applications are already the research focus of many scientists. These range

from resistance to corrosive environments [14,15], performance at high [16,17] or cryogenic temperatures [18,19] or resistance to static [20,21] or dynamic forms of loading [22,23].

However, following the line of thought of alloy design discussed above to achieve such a potential in a HEA, there is also the point of testing a material, upon its development, under well-established processing techniques. Such envisages the evaluation of their usability in key engineering applications, otherwise rendering them ineffective.

2.3 Welding technologies

Considering the abovementioned statement and to ensure the viability of these alloys to be used in in the modern world, their weldability is an important issue that must be addressed. This is especially important since any engineering alloy may require welding to either produce complex structures or to couple its properties to those from another material, in a dissimilar manner [24].

Such welding processes when compared with other joining methods, such as bolting or riveting, offer significant advantages given its ability to create strong and permanent joints. For example, unlike mechanical fasteners, welding fuses materials at the molecular level, resulting in a continuous joint with superior strength and durability. Such allows for the handling of higher loads, making welded structures lightweight and efficient. Another key advantage of welding is its ability to provide leak-proof and airtight joints, which is critical in pressure vessels and pipelines. Additionally, modern advancements in automated welding techniques, like robotic welding, have improved its productivity, consistency and precision, making it a cost-effective option in mass production and large-scale industrial projects.

In this regard, welding processes comprise many different technologies that can be divided into two groups: solid-state and fusion-based processes.

Starting with the solid-state based welding processes, these are grounded on plastic deformation, attrition and diffusion mechanisms. The microstructure of the obtained welds will, therefore, be a product of both temperature and deformation imposed onto the workpieces. Additionally, by avoiding the high temperatures necessary for fusion, these approaches allow to avoid the precipitation of undesired phases, residual stresses and distortions that are prone to occur upon cooling, during solidification.

On the other hand, there are fusion-based welding processes. These present themselves as reliable and valid solutions for research in HEAs, as they are based on melting and solidification of metal and are responsible for achieving strong bonds. Additionally, fusion-based welding has proved itself to be reliable under many aggressive environments once parameters optimization has been conducted [25–31]. With this in mind, amongst the many available fusion-based welding methods, gas tungsten arc welding stands as a relatively low-cost processing method capable of producing defect-free and highly performant joints [32]. Such processing technique is the core of this document and is going to be discussed in the next section.

2.4 Gas tungsten arc welding

Gas tungsten arc welding (GTAW), also known as Tungsten inert gas (TIG) in accordance with ISO 4063 [33], is a processing method capable of generating permanent bonds between separate parts, by increasing the temperature at their interface above the melting point. This occurs through the striking of an electric arc initiated by passage of electrical current between the metal, which is connected to one of the terminals of the power source, and a non-consumable electrode which is held on the welding torch that is connected to the other terminal. This non-consumable electrode is mainly composed of tungsten given that it can withstand high temperatures with practically no degradation.

Also connected to the torch is a gas cylinder that is responsible for supplying a shielding gas that shrouds the electric arc allowing for its ionization, and ensures that no oxidation nor overheating can damage the resulting joint and the torch.

Several parameter combinations can be changed in order to maximize the properties of a weld. These are for example: current intensity, shielding gas flow and type, tungsten electrode thickness and distance from tip of the electrode to the metal part; and can be changed accordingly with the operation conditions imposed of the weld technician or machine. However, attention to other special parameters must also be kept in mind, as they can influence the composition (either at the surface or in bulk) and, thus, the microstructure and the mechanical behavior of the final joint. These are the polarity and the type of shielding gas.

There are three different polarities in GTAW: “Direct Current Electrode Positive” (DCEP), “Direct Current Electrode Negative” (DCEN), and alternating current (AC).

In DCEP, the tungsten electrode is connected to the positive terminal of the power source. Such is also known as reverse polarity, where most of the energy in the form of heat is applied to the electrode rather than the metal, consequently resulting in a shallow weld (often water cooled and large diameter electrodes are used to counteract this fact). In this case, the heavy positive ions from the shielding gas travel towards the surface of the joint, generating an oxide free clean surface.

Nevertheless, to produce welds with deeper penetration, DCEN is often used. Here the tungsten electrode is connected to the negative terminal of the power source, which causes the electrons to travel from the electrode to the metal. This results in more power density as the energy necessary to emit one electron from the tungsten electrode (known as work function) is released upon impact on the surface of the metal, thus generating heat more efficiently. This approach is also known as straight polarity and is depicted in Figure 2.

Finally, there is the alternative current option, which grants the joints to an intermediate action between both the DCEN and DCEP alternatives.

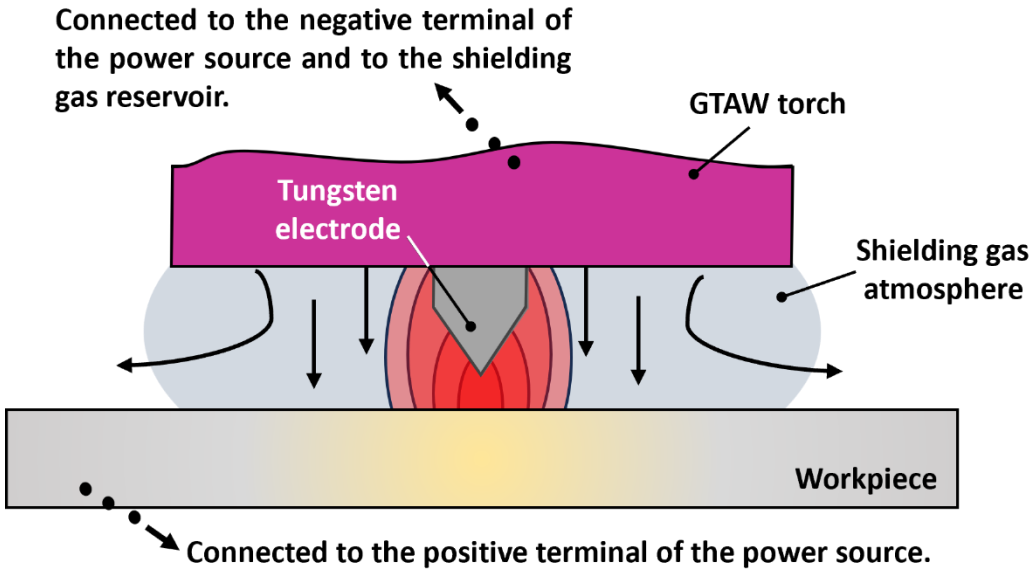


Figure 2 – Gas tungsten arc welding operating in straight polarity.

Then, there is the matter of shielding gas. Commonly used gases are Argon or Helium, which are inert in their nature. Main differences between both are the energetic potential required to ionize each of these gases, where Argon requires 15.7 eV and Helium 24.5 eV and the fact that Argon is heavier, thus, having more resistance to cross draft and thus granting a

better shielding effect, making Argon the most cost-efficient option [32]. However, beyond the usage of inert gases, there is also the option for including non-inert gases, such as CO_2 or O_2 in the mixture envisaging a chemical reaction to favor the weld properties, in which case the acronym TIG would become TAG (for Tungsten active gas).

Accordingly with the workpiece material, the microstructure of the obtained joint will depend on the amount of energy that is applied to the solid BM in order to melt it. Such quantity is known as the heat input, HI [kJ/mm] and directly dependent on the physical phenomena associated to each welding process. Particularly in GTAW, it can be calculated using Equation 4 [34].

$$HI = \eta \cdot \frac{V \cdot I}{v} \tag{4}$$

Where η is the efficiency of power transferred to the workpiece, I corresponds to the electric current intensity [A], V is the voltage [V] and v the welding speed [mm/s].

Given this and having presented the GTAW process, there is also the matter of explaining how it can contribute to the development of HEAs. Such, of course, requires analysis through standard and advanced characterization techniques that can be employed on the weld to obtain valuable information regarding its microstructure, properties and performance. Therefore, rendering it useful for key engineering applications and offering valuable insights for the improvement and development of novel HEAs.

2.5 Welded joint characterization for the improvement of HEAs

To recognize the potential of welding in the HEAS development field, first it is necessary to understand a welded joint's microstructure and its influence in the mechanical behavior. As such, in a fusion-based weld it is practically always possible to identify three regions. These being the base material (BM), the heat affected zone (HAZ) and the fusion zone (FZ), as shown in Figure 3.

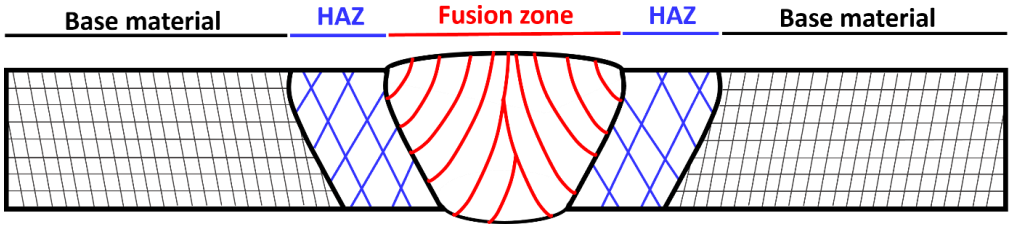


Figure 3 - Schematic representation of a welded joint.

Starting with the BM, this region corresponds to the initial condition of the metallic material. As such, it retains all the characteristics imposed on the metal prior to any welding procedure, as a consequence of its production.

Going towards the HAZ, this region is characterized by being a function of high temperatures (below its melting point) imposed by the heat input applied to the initial BM in order to melt it and, thus, obtain the joint. Here, several solid-state phenomena can take place, such as recovery, recrystallization and grain growth, which effectively cause a localized alteration of the microstructure present in the initial BM, as there are both time, temperature and microstructure dependent.

While recovery occurs at relatively low temperatures, it is a process that is mainly evident in cold worked metals. It involves the return of the physical and mechanical properties to their original state, without causing any alteration to the microstructure. However, the rate that each specific property change can be different, often occurring simultaneously with recrystallization (at higher temperatures). Such attests to the complicated nature of the recovery process, provided that some properties also depend on the microstructural features as it is the case of hardness and tensile behavior.

Considering the recrystallization process, which occurs at higher temperatures, it has its driving force allocated within the stored strain energy left during manufacturing. During this process the deformed grains tend to recrystallize into new and (relatively) strain-free grains, by releasing their internal strains as a consequence of the atom kinetics attained at elevated temperatures.

Finally, taking place at higher temperatures than recrystallization, there is the grain growth process. As the name suggests, it involves the increase in grain size and its main driving force arises from the necessity of reducing the surface energy to achieve the most stable condition of a system, with this being the one that thermodynamically minimizes its global energy. This process occurs with the migration of grain boundaries, causing larger grains to consume smaller ones, nevertheless, the presence of precipitates, such as carbide and nitride particles can inhibit such process.

Furthermore, the most changes in terms of microstructure can be seen in the FZ, which corresponds to the region that experienced complete remelting within a joint. Such region

results from the solidification of the molten pool (which is the name given to the localized portion of metal that undergoes full remelting). Here a strong microstructural distinction can be easily seen (often without etching), due to the thermal conditions experienced by the molten metal that forms it. Such conditions are a directly a consequence of the employed welding technique and impact the solidification path of the liquid, which is formed due to the high temperatures (thus influencing the final microstructure and, consequently the mechanical behavior of the joint in the process). Given this, the comprehension of noteworthy solidification concepts is necessary.

This endeavor, however, is transversal to multiple fields, often being associated with thermodynamics, i.e. phase diagrams and Gibbs free energy of a phase, and kinetics, including diffusion and fluid flow. As such, case specific phenomena occurring in each weld must be discussed independently, as multiple factors will impact the final microstructure of the corresponding FZ.

Still, as in other fusion-based process (p.e. casting), fusion-based welding is highly impacted by the solidification parameters known as the temperature gradient, G [°C/cm] and the growth rate, R [cm/s] that occur at the solid/liquid interface (S/L). In simple terms, these parameters will dictate the size and the morphology of the structures that are generated during the solidification process. However, for an easier understanding on how these two parameters can influence the final microstructure of the FZ, it is important to start by observing what occurs at the S/L vicinity during the process of solidification.

Such can be done by analyzing the one-dimensional solidification of an alloy and considering that equilibrium solidification occurs only at the S/L interface, diffusion on the solid state is negligeable and diffusion in the liquid occurs, although being limited. The latter assumption allows us to consider that a solute rich region is formed in the liquid phase close to the S/L interface. A graphical interpretation of this can be observed in Figure 4 a), where heat extraction occurs one-directionally from right to left, that is, from the high temperature liquid towards the colder solid, and the rate of advancement of the S/L interface is constant (R = constant).

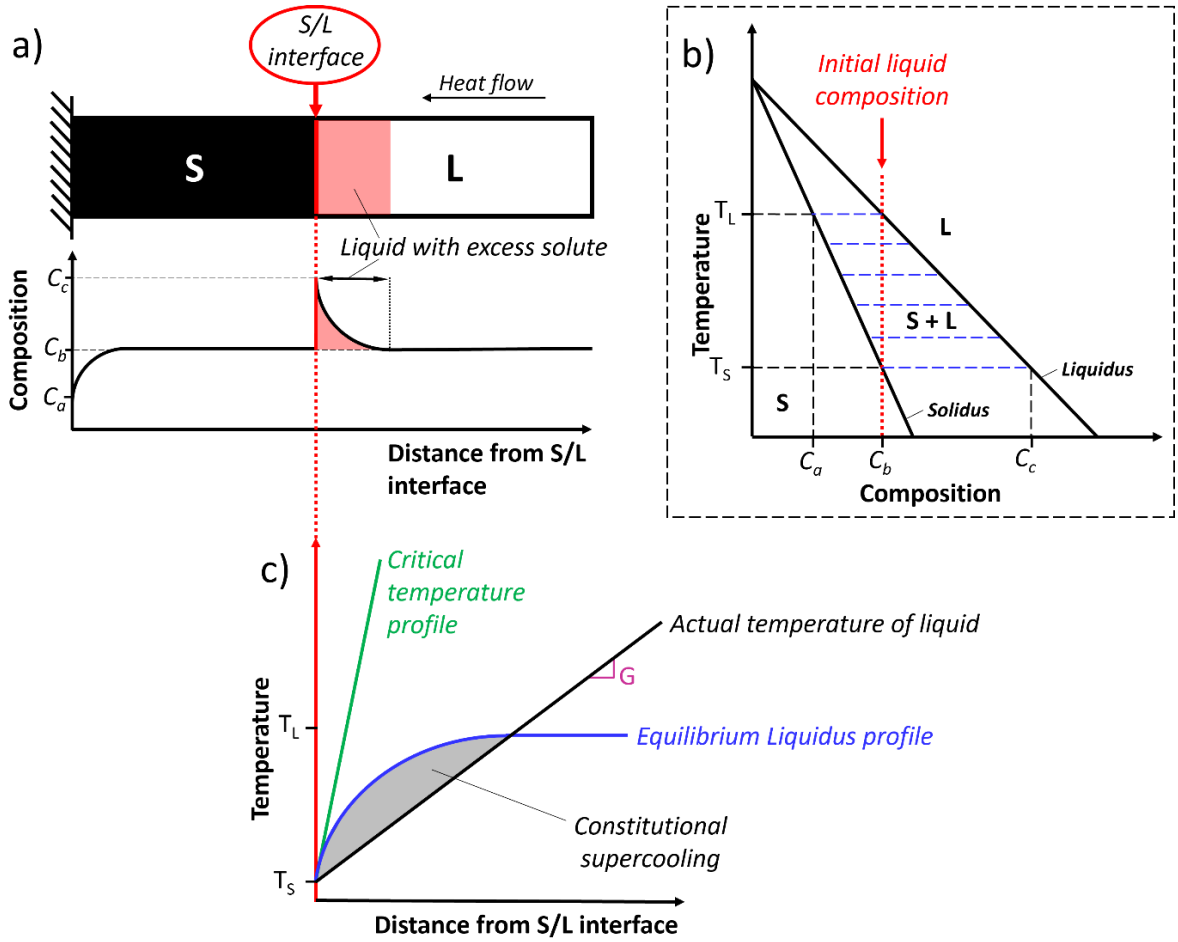


Figure 4 – Schematic representation of constitutional undercooling: (a) one-dimensional solidification process of an alloy, (b) corresponding phase diagram and (c) temperature variation with increasing distance to the S/L interface (Adapted from [32,35]).

Given this, interpretation of what occurs at the S/L interface can be made with the aid of the portion of the phase diagram available in Figure 4 b) and imagining that, initially, all material in in liquid state with a composition C_b. Upon heat extraction, the liquid reaches the temperature T_L, and the conditions to generate a solid with a composition C_a are attained. With further cooling, going from T_L to T_s, the solid cannot accommodate as much solute as the liquid can, thus all solute rejected during solidification goes into the liquid and generates a solute rich liquid region in the process. However, provided that all solid forms from the liquid and that the solute concentration in the liquid increases locally, the concentration of solute in the solid will also increase until reaching the composition C_b (at a temperature T_s) and a steady state is reached. At this point, the solidification process occurring at the S/L continues to reject solute into the liquid, which reaches its maximum concentration at C_c. Finally, once the liquid

attains the concentration C_c, it is capable of continuously forming a solid with composition C_b and continues to do so until the last solidification stage initiates. This final stage is characterized by the increase in concentration of both solid and liquid, as diffusion can no longer occur due to the lack of liquid which has totally solidified.

From this, it is also noticeable that the diffusion in the liquid phase, which can be measured from the diffusion coefficient in the liquid, D_L [cm^2/s] (corresponding to the amount of solute that diffuses across a unit of area in one second) and the variation in solidification temperature, ΔT [°C] ($\Delta T = T_L - T_s$) also play an important role in the process and are interconnected with G and R. Of special interest is the length of the solute-rich region next to the S/L interface, δ [cm], which can be estimated via the D_L/R ratio.

Furthermore, another phenomenon must be acknowledged when considering the solidification of an alloy, which is known as constitutional supercooling. Basically, this phenomenon can be interpreted as the region where both liquid and solid can coexist below the liquidus temperature of an alloy. Such occurs within the "S+L" region of the phase diagram, where the liquid phase alone is thermodynamically unstable. To further understand this, Figure 4 c) displays the variation in temperature with regard to the distance to the S/L interface. There the blue curve corresponds to the liquidus profile in equilibrium conditions, while the black line corresponds to the actual temperature profile imposed on the molten alloy, which can be assumed to be linear provided that, in this case, heat only flows one-directionally. Depending on the slope of the actual temperature profile, which corresponds to the temperature gradient ($G = \Delta T/\delta$), an area between the two temperature profiles can be identified as the constitutional supercooling region, where the liquid phase is effectively present bellow the liquidus curve. On the other hand, the green line corresponds to the G magnitude beyond which constitutional undercooling does not occur, corresponding to a value of $\Delta T/(D_L/R)$, which is equivalent to $G/R = \Delta T/D_L$.

In fact, the more constitutional supercooling (larger area) is imposed on the S/L interface the more intricate the attained microstructure will be, allowing for different solidification modes to occur, as it is the case of planar, cellular, columnar dendritic and equiaxed dendritic. This can be observed in Figure 5 a), where these solidification structures are ordered in accordance with the degree of constitutional supercooling.

With this established, Figure 5 b) summarizes the effect of the solidification parameters, that is G and R, in regard to the morphology type and size of the structures that are developed during solidification.

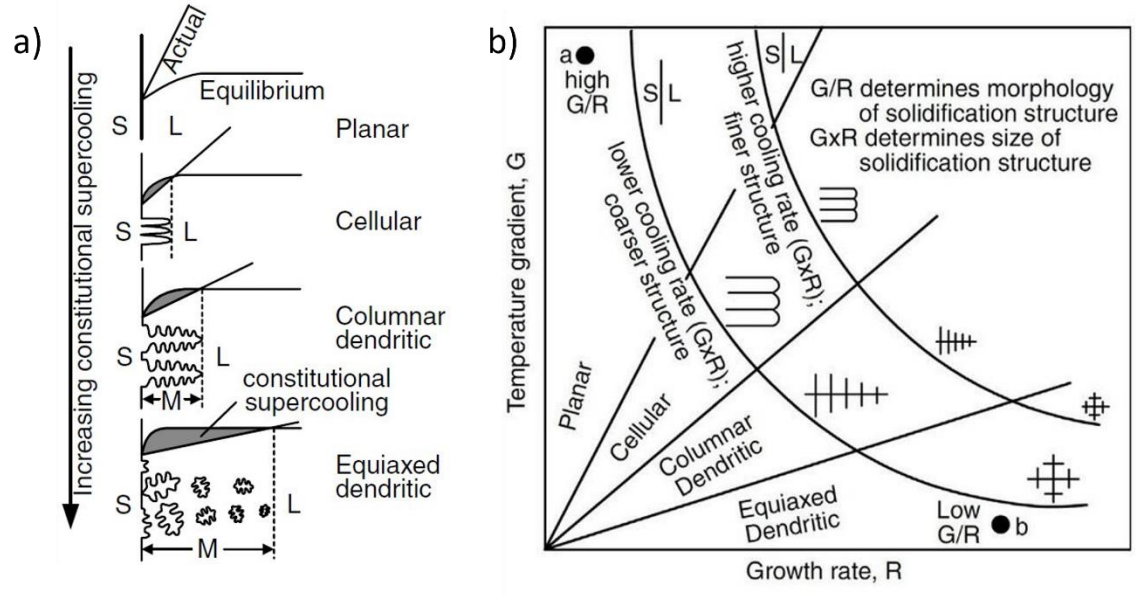


Figure 5 – (a) Effect of constituitional supercolling on solidification mode and (b) effect of G an R on the morphology and size of microstrucuture during solidification (Adapted from [32]).

Given this, qualitatively speaking, the ratio G/R yields as a result the solidification parameter that has more influence on the advancement of the S/L towards the liquid, during solidification. That is, should G be much higher than R (corresponding to a high G/R ratio), the rate at which S/L is solidifying (related to the parameter R) mainly depends on the difference temperature between two points at each boundary of the S/L (related to G). Such conditions would result in a planar solidification mode arising from the solidification process.

On the other hand, there is the product between G and R (G·R), which mainly affects the size of the solidification structures. Such calculation yields as a result the cooling rate (in °C/s) and provides the combined influence of both solidification parameters. In this case a high G·R results on a finer microstructure, while a low G·R provides a coarser size of the freshly developed solidification structures.

Nevertheless, there are other means for altering the grain structures that arise upon solidification. Such can be attained by inducing external nucleation sites within the molten

pool, via the introduction of particles that will eventually contribute to heterogeneous nucleation during the solidification process.

Aside from this basic knowledge in solidification theory, other phenomena must be accounted for when considering the solidification of the molten pool, as any fusion-based welding process stands far from this one-dimensional solidification explanation. These phenomena are epitaxial growth and competitive growth. Firstly, in the case of epitaxial growth, the newly forming grains exhibit an overall tendency to grow from the preexisting BM, retaining the same crystalline orientation as their parent grains. This process often occurs at the fusion boundary (FB). Secondly, there is the competitive growth process, where upon heat extraction the grains that have their growth direction aligned with the maximum heat extraction direction will be favored. This allows for them to become larger and at the expense of poorly oriented and newly formed grains, overall tending to occur in the bulk of the FZ and perpendicularly to the fusion boundary.

On a further note, amidst the mentioned already welding zones (BM, HAZ and FZ), other regions can be identified, as it is possible to segmentate the HAZ in smaller portions corresponding to smaller regions where the effect of a solid-state phenomenon is significantly more visible than the others, or the same on the FZ, where the microstructure can change significantly, due to the imposed cooling conditions and associated solidification parameters that vary spatially with the distance from peak temperatures. Such can be observed in Figure 6.

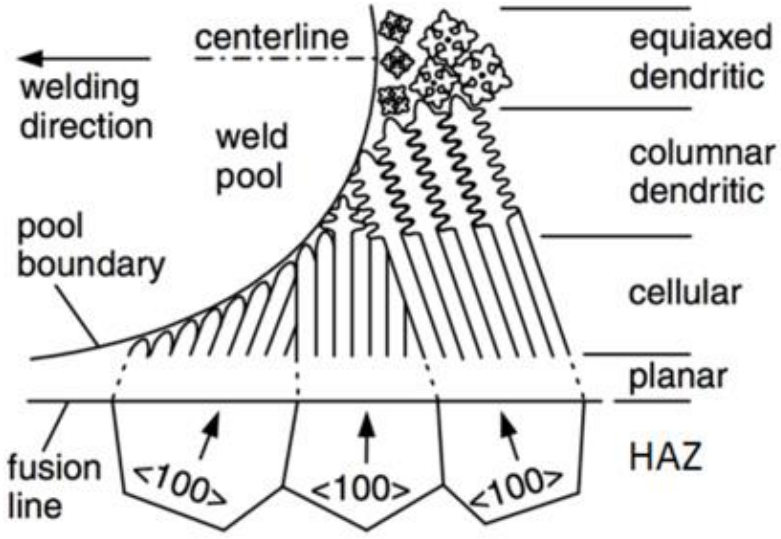


Figure 6 – Variation in solidification mode across the fusion zone (From [32]).

Beyond these regions, there is also the partially melted zone (PMZ), which often can be identified the between HAZ and the FZ, and corresponds to a region of composed of grain with partially molten and resolidified material along their grain boundaries [30].

Nevertheless, identifying all these regions and their full extension on a joint, requires experience and depends on the analysis techniques employed to characterize them [29]. Still, it is undeniable that such a variation on microstructure causes a weld to showcase different properties throughout its full extension. Such results on a microstructurally "graded" material enveloping all the phenomena associated with the welding process, including fast cooling and possible defects. This by itself fits on the experimental pathway, described earlier in the approaches for the development of HEAs, on a welding perspective. Moreover, such a perspective can also be seen as a mechanistic input for the development of HEAs, since it considers the material working conditions, where the welding parameters can be optimized to favor a specific effect on the mechanical behavior of the joint. Finally, for this purpose it is also important to follow the thermodynamic pathway and gather results to cross-check with the obtained microstructure to obtain joint with the best performance under its final working conditions.

Given this, the use of conventional and advanced characterization techniques is essential to retrieve valid and reliable information for the advancement of the knowledge regarding HEAs. This is especially relevant, given that each joint showcase es its own features, both in terms of microstructural and mechanical properties. Examples of these techniques include optical and electron microscopy, synchrotron X-ray diffraction, thermodynamic modelling and micro to macro mechanical assessment.

2.6 Current progress on welding of HEAs

Surveying the existing literature on the topic of welding HEAs, it is possible to observe that many studies have already taken place to characterize these advanced materials in terms of joining processes. Considering the data compiled in Figure 7 a), the number of publications regarding this topic can be seen increasing from the years prior to 2017 up to the present moment. Here several studies on brazing were also added to the count, although not being welding based studies, the reason being that they also account for the metallurgical understanding on HEAs.

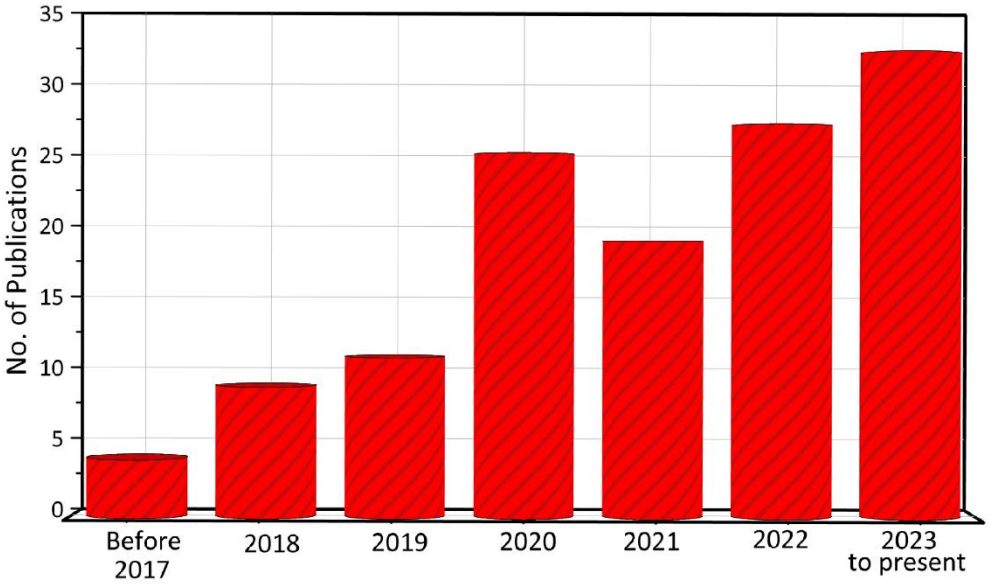


Figure 7 - Evolution of the number of publications on welding of high entropy alloys over time.

In the literature regarding welding processes on HEAs, Figure 8 showcases their percentual distribution. Overall, it can be seen that fusion-based is by far the most employed technologies to study HEAs (with a total of 54.35 %), with GTAW and laser welding imparting 18.84% and 28.26% of the total amount of studies, respectively.

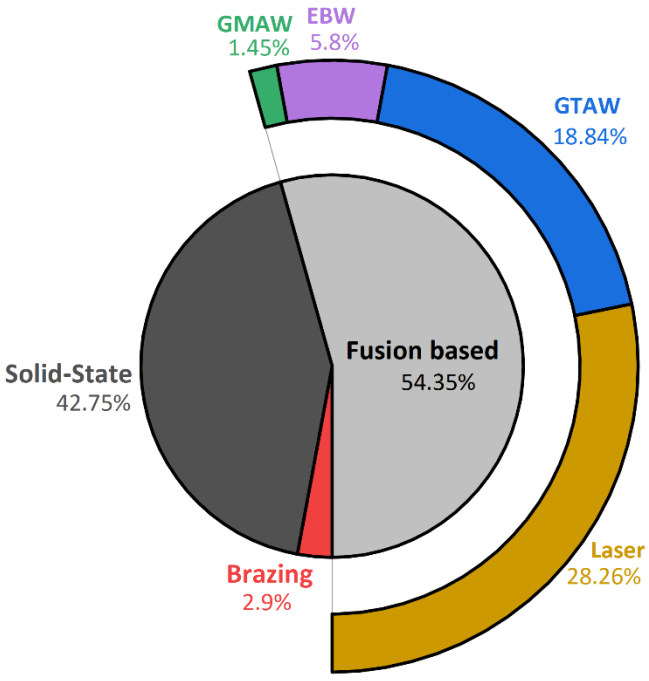


Figure 8 - Percentual distribution of the number of papers by welding technique.

Provided that there is an overall interest in evaluating HEAs amidst the scientific community, now we delve into the state of the art of the HEAs that are going to be discussed throughout this document. These are the CoCrFeMnNi, $Fe_{50}Mn_{30}Co_{10}Cr_{10}$, AlCoCrFeNi, $Co-Cu_xFeMnNi$ (x=20,30) and $Co_{29.7}Cr_{29.7}Ni_{35.4}Al_4Ti_{1.2}$ HEA systems. These were some of the most common HEAs already well established in the literature, thus deserving attention to their processability via welding processes. Furthermore, dissimilar welding in these HEAs is also a topic worthy of investigation, as their insertion in industrial applications may rely on their compatibility with other conventional materials such as stainless steels.

As such, a state of the art regarding each of the materials that were researched within the scope of this thesis is presented as follows:

2.6.1 $Fe_{50}Mn_{30}Co_{10}Cr_{10}$ HEA

From the multiple combinations that already have been discovered since the inception of HEAs, the $Fe_{50}Mn_{30}Co_{10}Cr_{10}$ alloy has interesting features that make it a competitive choice for a wide range of applications. The design concept of this HEA was first developed in 2017[36]. Although exhibiting some similarity in composition with the Cantor alloy (equiatomic FeMnCoCrNi), the absence of Ni makes it a less expensive and interesting alternative. Additionally, the transformation induced plasticity (TRIP) effect exhibited by this HEA once mechanically deformed, effectively transforms the face centered cubic phase (γ-FCC) parent phase into the metastable hexagonal closed packed (ε-HCP) phase via a martensitic transformation, granting this HEA a dual-phase (DP) constitution [10].

Such phase metastability combined with the concepts of high entropy alloy design is a systematic topic in the current literature [11–15], which can yield several different options for the improvement of the deformation behavior on a material, making it a potential alternative to conventional alloys. More specifically, in the case of the DP-HEA, the TRIP deformation mechanism coupled with dislocation slip, can provide this DP-HEA an excellent strength-ductility synergy.

Nevertheless, to prevent premature failure when in service, the processability of any alloy must be thoroughly analyzed once a promising material composition has been determined. For such, as a crucial aspect of the manufacturing process, one must combine the metallurgical and mechanical characteristics of the material with the possible manufacturing

routes to which the material might be subjected prior to its deployment for a specific application.

2.6.2 AlCoCrFeNi HEA

This HEA was developed by Lu et al. [37], in 2014, to overcome the strength/ductility paradigm and is also characterized by exhibiting two phases, an ordered $L1_2$ FCC phase and a B2 BCC phase. Such was possible by combining the ductility characteristic of the $L1_2$ FCC phase and the strength exhibited by the B2 BCC phase.

At the moment, several studies have already been conducted in the AlCoCrFeNi HEA system to prove its efficacy in various work conditions, for example by characterizing its behavior under high temperature [38,39] or cryogenic environments [40,41]. Furthermore, research on the weldability, and consequent mechanical performance, of this HEA has also been conducted in the past years [42–46]. Of special notice is the work developed by Shen et al. [28], were GTAW was utilized in this HEA system to relate the obtained microstructural features with the mechanical behavior exhibited by the joint. On a step further, the processability of this HEA system is still at its infancy and further research can be performed using inoculant particles and dissimilar welding, making it an excellent candidate for high performing engineering applications.

2.6.3 $CoCu_xFeMnNi$ (x=20,30) HEA

Another HEA system worthy of notice is the $CoCu_xFeMnNi$ system (x=20,30). The first mentions to this HEA system can be found in [47], in 2017. The difference between the two alloys mainly resides in the amount of Cu in their composition. In one hand, we have an equiatomic $CoCu_{20}FeMnNi$ alloy, while in the other hand exists a non-equiatomic $CoCu_{30}FeMnNi$ HEA. In both cases, these HEAs are characterized by possessing at least two phases in their microstructure [48]. As such, the available literature indicates that the main drive for research on these two HEAs is their mechanical performance, with the equiatomic CoCuFeMnNi being able to reach up to 2 GPa, at the cost of ductility [49–51]. Furthermore, also worthy of mention are other studies, where focus is given to the driving forces responsible for the formation of characteristic dual phase microstructure and the subsequent correlation with mechanical performance [52–54]. Nevertheless, although these topics have been addressed, the processability, namely the weldability, and the relation between the initial

condition of the materials and their post-processed state must also be analyzed. Currently, only the weldability of the equiatomic CoCuFeMnNi HEA was assessed using laser welding [55] and transient liquid phase bonding [56]. In both cases, it was demonstrated the practicality of these alloys for engineering purposes. However, the change in composition, especially the higher fraction of Cu can potentially lead to defects associated to liquation cracking. Moreover, the use of low-cost arc-based welding processing was not yet attempted for these alloys, showing a gap in the existing body of knowledge associated to the welding of HEAs at large.

2.6.4 $Co_{29.7}Cr_{29.7}Ni_{35.4}Al_4Ti_{1.2}$ HEA

Recently, a novel $Cr_{29.7}Co_{29.7}Ni_{35.4}Al_4Ti_{1.2}$ HEA was firstly developed by Santana et al. [10,57], in 2021, on the premise of introducing small quantities of alloying elements, such as Al, Ti, Mo and Nb, in a concentrated CoCrNi matrix. These alloying additions can promote the formation of new precipitate phases which eventually lead to an improvement on the material mechanical properties, they also increase the solidification interval, what can make the processing more challenging. This novel MPEA, similarly to some Ni-based alloys, is mainly composed of two primary phases: a disordered face centered cubic phase, γ, and an ordered face centered cubic phase, γ'. Owing to the excellent mechanical performance evidenced by the $Cr_{29.7}Co_{29.7}Ni_{35.4}Al_4Ti_{1.2}$ HEA, the next logical step is to address it processability. As such, in this study we evaluate the impact of GTAW on the microstructure and mechanical properties of the material to further promote the adoption of these novel engineering alloys into potential structural-related applications.

2.6.5 CoCrFeMnNi HEA

The equiatomic CoCrFeMnNi high entropy alloy (HEA) was first presented in 2004 by Cantor et al. [58]. This material has attracted significant attention since the inception of HEAs, whose concept is based on composition, microstructure and mechanical behavior customization for case-specific purposes, typically surpassing conventional engineering alloys [6,59,60].

The CoCrFeMnNi HEA is known to yield a single-phase face centered cubic (FCC) solid solution that has been thoroughly studied to unveil its behavior in a wide array of corrosion environments [61,62] and temperature regimes [63–65]. Nevertheless, research on its processability is imperative to guarantee their implementation in key engineering applications.

These advancements on CoCrFeMnNi-based HEAs research further potentialize its integration in key engineering applications.

For such, welding has been widely used to address the increasing interest in exploring the processability phenomena arising from the high temperature/pressure required to achieve strong and permanent joints in similar and dissimilar combinations [26,27,29,66–70]. Among these studies, GTAW of the CoCrFeMnNi high entropy alloy on the as-rolled condition was performed by Oliveira et al. [29] and stands as the basis of the present paper. There, the excellent weldability of the CoCrFeMnNi system was highlighted by means of advanced microstructure and mechanical characterization. This allowed to observe the transition from the base material (BM) to the fusion zone (FZ), as well as the solid-state mechanisms occurring in the heat affected zone (HAZ). Additionally, the mechanical performance of the joints was assessed by tensile testing (reaching ≈519 MPa at a ≈8.4% of strain) and microhardness mapping, showcasing a decreasing hardness transition from the BM to the FZ. Of special notice is the use of synchrotron X-ray diffraction (SXRD) to complement the electron microscopy analysis, evidencing that the actual extension of the HAZ is larger than that determined by microscopy techniques. This was related to the different microstructural features captured by each characterization technique, highlighting the potential for their combined use.

3

MATERIALS AND METHODS

3.1 Chapter introduction

In this chapter, the experimental procedure and the corresponding apparatus is described. It includes the description of a welding platform prototype developed for GTAW and python language programming for its control and for subsequent data treatment using synchrotron x-ray diffraction, which is method of unhinged potential for materials research.

Given this, as a starting point for this chapter Table 1 summarizes the successful welds were obtained in both similar and dissimilar combinations using HEAs and other engineering material such as stainless steel 316 L (SS 316L) and an Fe-based shape memory alloy (Fe-SMA).

Table 1 – Welded joint summary.

Welded joint	Similar/ Dissimilar	Condition	Comments
FeMnCoCr	Similar	**As-cast**. Slabs were cut from an ingot via wire electrical discharge machining.	Apart from the GTAW joint characterization, this HEA was also investigated with synchrotron X-ray diffraction in-situ tensile testing.
CoCrFeMnNi	Similar	**As-rolled**. 3 mm plates were cold-rolled at room temperature until a thickness reduction of ≈50%.	The GTAW joint tensile performance was analyzed via synchrotron X-ray diffraction, utilizing joints fully characterized in [29].
CrCoNiAlTi	Similar	**As-rolled**. Ingots were homogenized at 1200°C for 4h and rapidly cooled in water. After,cold-rolling was performed, until 50% reduction, followed by a recrystallization heat treatment at 1100 °C for 1h. This procedure was repeated until 20 mm diameter slabs became 2 mm thickness sheets. These were solution annealed at 1100°C for 5min and quenched in water.	---

Table 2 - Welded joint summary (continuation).

Welded joint	Similar/ Dissimilar	Condition	Comments
FeMnSiCrNi(V,C)	Similar	**As-rolled**. The material underwent hot-rolling (at 1000 °C) until reaching a thickness of 3 mm. Subsequently cold-rolling was performed to achieve a final thickness of 1.5 mm.	This material corresponds to a Fe-based SMA. GTAW was performed to investigate the phenomena associated to it before dissimilar welding with HEAs.
AlCoCrFeNi + TiB_2 inoculants	Similar	**As-cast**. Commercially pure elements were cast using vacuum induction melting. The obtained ingot was remelted multiple times to ensure good chemical homogeneity. 1.5 mm slates were cut from the ingot.	TiB_2 inoculant particles were added to the joint during GTAW, which was then compared to a GTAW similar joint.
$CoCu_xFeMnNi$ (x=20,30)	Similar	**As-cast**. Equiatomic and non-equiatomic ingots were cast by vacuum induction melting. After homogenizing at 1000 °C for 24 h, the rod-type ingots, were cut by electrical-discharge machining, to a diameter of 2 mm.	Two different HEA GTAW weld compositions were analyzed and compared.
AlCoCrFeNi + SS 316L	Dissimilar	**As-cast**. The procedure for obtaining the AlCoCrFeNi HEA was the same as above (in AlCoCrFeNi + TiB_2 inoculants). The SS 316L were commercially available, in the **as-rolled** condition.	---
FeMnCoCr + Fe-SMA	Dissimilar	**As-cast**. The procedure for obtaining the FeMnCoCr HEA was the same as above (in the FeMnCoCr similar joint). The Fe-SMA plates followed the same procedure as in the FeMnSiCrNi(V,C) similar joints, being in the **as-rolled** condition.	---

3.2 Computer numerical control platform utilized for GTAW

To achieve full penetration GTAW joints, a computer numerical control (CNC) platform was designed and assembled to allow for three-dimensional movement and control of the welding machine. The GTAW platform is displayed in Figure 9.

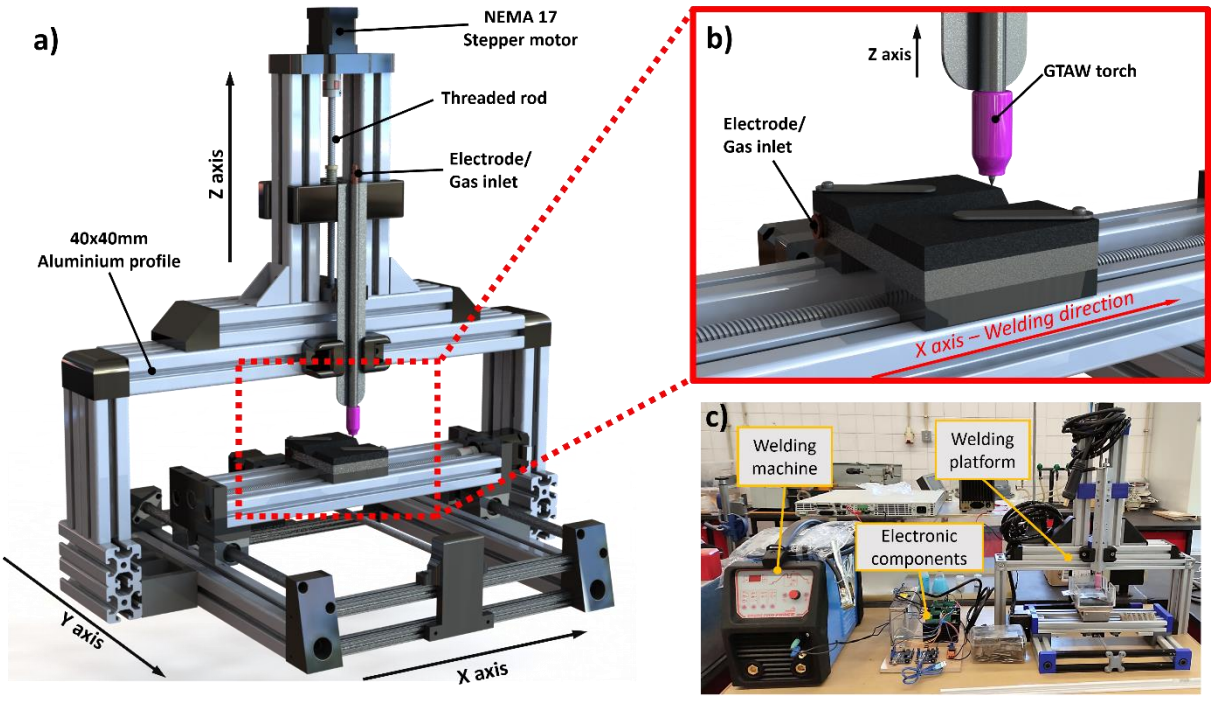


Figure 9 - Welding platform: a) 3D view of the welding platform assembly; b) detailed 3D view of the fixture; c) actual welding platform.

The overall dimensions of the welding CNC platform are, approximately, 45 × 60 × 60 mm, with its frame being composed mainly by 40 × 40 mm and 30 × 30 mm aluminum profiles, granting it to be structurally sound.

Furthermore, to avoid instability in the electric arc, the z-axis (which is where the torch is fixed) is detached from the remaining axes. This allowed for the distance between the electrode and the part to be set prior to welding and to remain consistent throughout the whole procedure. At the same time, the threaded rods that corresponded to the X and Y axes were connected to the fixture., which was custom made to allow for shielding gas to enter from underneath the workpiece and, thus, protecting the root of the weld. All the axes were controlled with NEMA 17 stepper motors, and each stepper motor was connected to a TB6600 stepper driver. These allowed to operate the motors with an Arduino UNO, with small step increments. Independently to this, another Arduino UNO was connected to a relay that would give the triggering signal to the welding machine (CITOTIG 2200 Force, from OERLIKON) in order to strike the arc.

To synchronize both Arduinos UNO, these were embedded with the open-source firmware GRBL and connected to the same computer. A python-based script was developed to control them simultaneously, using G-code. Thus, once the command was given, both the CNC platform and the welding machine would successfully accomplish a welded joint onto the workpiece, with the predetermined parameters.

3.3 GTAW experiments

Prior to welding any of the materials mentioned in Table 1, welding tests were performed in stainless steel sheets with the same thickness as the final tests. The materials were then cleaned with acetone and welded. For each case, the parameters utilized for welding are summarized in Table 3. Aside from the rods and the CrCoNiAlTi HEA plates (both with a diameter/thickness of 2 mm), all samples had a thickness of 1.5 mm. The plates to be welded had a square geometry of 30 × 30 mm.

Table 3 – Parameters utilized for welding.

Welded joint	Current [A]	Voltage [V]	Gas flow rate [L/min]	Welding speed [mm/min]	Notes
FeMnCoCr	25	≈3.8	**Face:** 8 **Root:** 5	200	---
CoCrFeMnNi	60	≈9.2	16	252	Not welded in the framework of this thesis.
CrCoNiAlTi	90	≈13.6	**Face:** 16 **Root:** 8	150	---
FeMnSiCrNi(V,C)	110	≈16	**Face:** 8 **Root:** 5	60	---
AlCoCrFeNi + TiB_2 inoculants	100	≈15.2	**Face:** 8 **Root:** 5	60	---
$CoCu_xFeMnNi$ (x=20,30)	46	≈50	15	Single spot	Rods with a diameter of ≈2 mm.
AlCoCrFeNi + SS 316 L	90	≈13.6	**Face:** 16 **Root:** 6	210	---
$Fe_{50}Mn_{30}Co_{10}Cr_{10}$ + Fe-SMA	68	≈10.3	**Face:** 16 **Root:** 6	150	---

Apart from this, all welding experiments were performed using Argon gas (99.999% pure) at a 1.5 mm distance from the workpiece to the tip of the tungsten electrode.

3.4 Microscopy techniques

For observing the microstructure of the welded joints, both optical and scanning electron microscopy techniques were employed. Optical microscopy (OM) was performed on a Leica DMI 5000 M optical inverted microscope, while a Hitachi SU8000 scanning electron microscope, equipped with a secondary electrons (SE) and a backscattered electrons (BSE) detectors, was used for the scanning electron microscopy (SEM). Electron backscatter diffraction (EBSD) maps were gathered using an FEI Nova NanoSEM 230 with EDAX Hikari Super EBSD equipment.

Nevertheless, prior to any type of microscopy technique, all samples were grinded and polished using sandpapers with progressive grits from P200 to P2500 and polished using 3 µm and 1 µm diamond suspensions. In some cases, colloidal silica was also employed. After polishing, the samples were etched accordingly to Table 4. Provided that the corrosion properties of the materials are directly correlated with the temperature, this was performed by dipping the polished samples in their corresponding solution for consecutive periods of 5s, until the microstructure was visible in the optical microscope. For the FeMnCoCr HEA, this procedure can take up to 40 min depending on the concentration of the solution.

Table 4 – List of etchants and corresponding composition, utilized to observe the microstructure of each welded joint.

Welded joint	Etchant	Composition
FeMnCoCr	Nital	1-5% Nitric acid (HNO_3) + 95-99% Ethanol (C_2H_6O)
CrCoNiAlTi	Aqua regia	25% Nitric acid (HNO_3) + 75% Hydrochloric acid (HCl)
FeMnSiCrNi(V,C)	---	85% Ethanol (C_2H_6O) + 10% Hydrochloric acid (HCl) + 5% Nitric acid (HNO_3
AlCoCrFeNi + TiB_2 inoculants	Aqua regia	25% Nitric acid (HNO_3) + 75% Hydrochloric acid (HCl)
$CoCu_x$FeMnNi (x=20,30)	Nital	1-5% Nitric acid (HNO_3) + 95-99% Ethanol (C_2H_6O)
AlCoCrFeNi + SS 316 L	Aqua regia	25% Nitric acid (HNO_3) + 75% Hydrochloric acid (HCl)
$Fe_{50}Mn_{30}Co_{10}Cr_{10}$ + Fe-SMA	---	1-5% Nitric acid (HNO_3) + 95-99% Ethanol(C_2H_6O) and 85% Ethanol (C_2H_6O) + 10% Hydrochloric acid (HCl) + 5% Nitric acid (HNO_3)

3.5 Synchrotron X-ray diffraction

Synchrotron X-ray diffraction (SXRD) is a complementary analysis technique that provides quantitative and qualitative information about the crystal structures present within a material. The way this technique works is summarized in Figure 10.

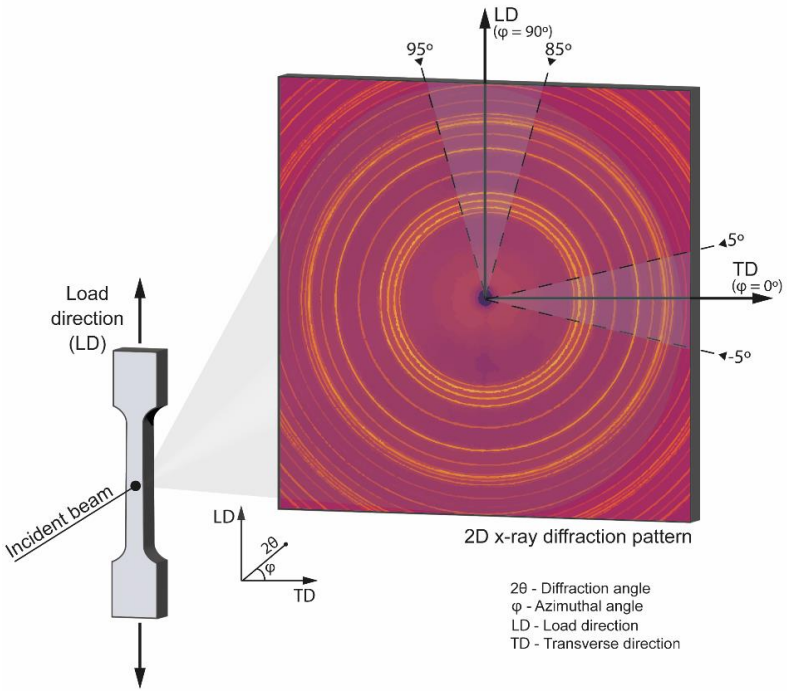


Figure 10 - Experimental setup utilized for synchrotron X-ray diffraction, not to scale.

Simply put, the samples are exposed to a high energy photon beam, of 87.1 keV (corresponding to a wavelength 0.14235 Å), which allows to work in transmission mode, meaning that information can be retrieved from the bulk of the sample. The diffracted beam is then captured by a 2D detector, which converts the data into Debbye Scherrer rings, with each ring corresponding to a diffraction peak of a determined phase present within the analyzed material.

The 2D data can then be processed using specific firmware, such as the pyFAI python package [71] or Fit2D [72], converting it into 1D diffraction patterns. This conversion can be performed by full integration along the azimuthal angle, φ [°], or in specific segments (also known as cakes) to analyze texture or microstructure evolution. In the case, of Figure 10, information form segments within the 85 to 95° and -5 to +5° ranges, can be obtained to analyze orientation-dependent microstructure in the loading direction, LD, and transverse direction,

TD, during tensile testing. Due to the large amount of data, a simplified python-based interface was developed, to simplify and ease the integration process, as most parameters were kept the same (refer to Figure 11). It is also important to mention that all tests were calibrated using a LaB6 standard from NIST.

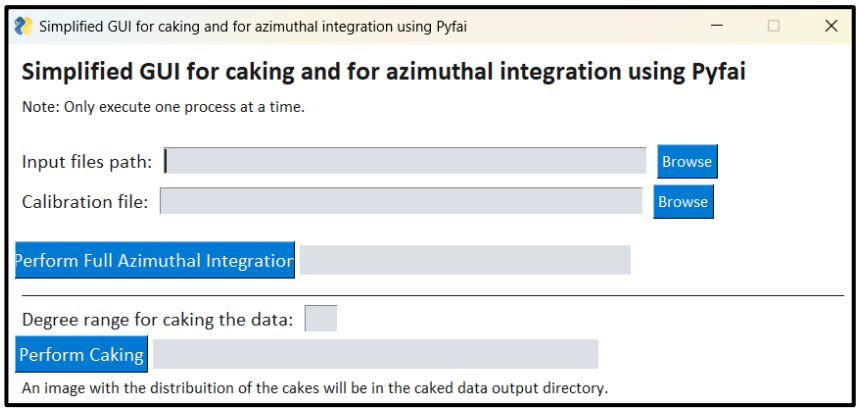


Figure 11 – Simplified interface for integration of diffraction data.

Furthermore, to acquire meaningful information, such as peak center, full width at half maximum (FWHM) and integrated peak intensity, in-house developed python scripts, were utilized to fit the diffraction data with a Voigt profile along with the neighboring background, using a Chebyshev polynomial [20,21]. The Voigt profile was chosen given its capability to accurately describe the peak shape, as the combined influence of both of its components, being described as the convolution of a Gaussian and Lorentzian functions [22,23]. The script allows for mass analysis of diffraction data in bulk, allowing to reveal phase specific peak distribution within a single joint, or throughout the full duration of an in-situ test.

From the acquired peak parameters, computation of the lattice strain, ε_j^{hkl}, can be done using Equation 5. Where d_j^{hkl} is the interplanar spacing corresponding to a given (h k l) phase reflection at a certain stage, j, should the microstructure evolution be the focus of the work. d_0^{hkl} corresponds to the interplanar spacing at the stress-free condition of the analyzed material.

$$\varepsilon_j^{hkl} = \frac{d_j^{hkl} - d_0^{hkl}}{d_0^{hkl}} \quad (5)$$

For the determination of d_j^{hkl}, Bragg's law (Equation 6) is of fundamental importance as it is a condition for constructive interference to occur, resulting in the existence of peaks on the diffraction pattern, correlating d_j^{hkl} with the 2θ value of the peak center of a given diffraction peak [73].

$$n \cdot \lambda = 2 \cdot d_j^{hkl} \cdot \sin\left(\theta_j^{hkl}\right) \quad (6)$$

Where, λ is the X-ray beam wavelength, which equals to 0.14235 Å, and θ_j^{hkl} corresponds to half of the peak center position [°], as obtained through fitting. Aside from these, the order of reflection, n, is a positive integer, which is commonly equal to 1. When such law is not fulfilled, destructive interference takes place meaning that the diffracted beam will not be in phase with each other, and no phase reflection is observable. Linear fitting of the lattice strain in the LD (in the elastic regime) of each diffraction reflection allowed to obtain its corresponding Young's modulus.

On a different approach, the dislocation density, ρ [m^{-2}] can be calculated using Equation 7 was employed, where the term $\langle \varepsilon^2 \rangle$ corresponds to the microstrain, D is the crystallite size [nm] and b is the burgers vector [nm].

$$\rho = \frac{2 \cdot \sqrt{3} \cdot \langle \varepsilon^2 \rangle}{b \cdot D} \quad (7)$$

In the case of the FeMnCoCr HEA, the available phases were FCC and HCP. Thus, for the FCC phase the magnitude of b is $\frac{\sqrt{2}}{2} \cdot a_\gamma$, where a_γ is the FCC lattice constant [74]. While for the HCP phase, b = 1/3 <11-20> is utilized to quantify basal-type dislocations and b = 1/3 <11-23> to quantify prismatic-type dislocations, with their magnitude depending on their slip plane [75].

By performing a linear fitting using the Halder-Wagner method [76,77], $\langle \varepsilon^2 \rangle$ and D were computed. This method considers θ_j^{hkl} and $FWHM_j^{hkl}$ (after subtraction the instrumental broadening obtained from the LaB_6 powder standard diffraction data), as in Equation 8.

$$FWHM_j^{hkl} = \left(FWHM_{j,measured}^{hkl} - FWHM_{instrumental}\right)^{\frac{1}{2}} \quad (8)$$

Finally, when possible, the load partitioning between the phases present within an alloy can be computed considering the law of mixtures, and the load contribution to the yield

strength, σ_y [MPa] was calculated based on the γ-FCC phase, which is the first phase to yield (thus contributing majorly to the deformation on the elastic regime), using Equation 9.

$$\sigma_y^{\gamma\text{-FCC}} = \sigma_0 + \sigma_D + \sigma_{SF} + \sigma_{GB} + \sigma_P \quad (9)$$

where σ_0 corresponds to the lattice friction stress (which is inherent from the material), σ_D is the strengthening contribution arising from dislocations, σ_{SF} corresponds to the influence of staking faults and σ_{GB} represents the strengthening effect of grain boundaries. The influence of any second phase particles in the microstructure was disregarded. Here, σ_0 was considered to be 179 MPa [78], σ_D and σ_{GB} were calculated based on [78,79] and σ_{SF} was obtained as in [80].

For calculation of the strengthening contributions arising from dislocations (σ_D), Equation 10 was utilized.

$$\sigma_D = M \cdot \alpha \cdot G \cdot b \cdot \sqrt{\rho} \quad (10)$$

Where, M stands for the Taylor factor (equal to 3.06), α is a constant for FCC metals (equal to 0.2), G is the shear modulus (which was calculated to be 64.2 GPa for the γ-FCC), b is the absolute value of the Burgers vector $b = a \cdot \frac{\sqrt{2}}{2}$, where a is the lattice parameter, and ρ corresponds to the dislocation density of the γ-FCC [78,79].

Furthermore, Equation 11 was used to calculate σ_{GB} and corresponds to the Hall Petch relationship. Here k is the Hall-Petch coefficient and d the mean grain size of the γ-FCC [78,79].

$$\sigma_{GB} = k \cdot \sqrt{d} \quad (11)$$

Considering the σ_{SF}, this component was calculated based on the method shown in [80], as in Equation 12:

$$\sigma_{SF} = \frac{k_{SF}}{L_{SF}} \quad (12)$$

Where, $L_{SF} = (d_{111})/P_{SF}$, d_{111}corresponds to the interplanar spacing of the (1 1 1) plane and P_{SF} can be calculated using Equation 13. k_{SF} is the strengthening coefficient and can be obtained by the slope of the $1/L_{SF}$ versus yield strength, in the present study the value k_{SF} = 3149 MPa.nm was utilized.

$$P_{SF} = \frac{1}{0.0517}(\varepsilon_{111} - \varepsilon_{222}) \quad (13)$$

Where ε_{111} and ε_{222} are the microstrain calculated, based on the diffraction peaks, for the (1 1 1) and (2 2 2) planes.

Finally, the strengthening contribution (σ_p) arising from the presence of MnO particles was calculated based on the Ashby-Orowan approach [81], as in Equation 14.

$$\sigma_p = 0.538 \cdot \frac{G \cdot b \cdot \sqrt{f}}{d_p} \cdot \ln\left(\frac{d_p}{2b}\right) \quad (14)$$

where, G is the shear stress, d_p corresponds to the particle size, f is the phase fraction and b is the corresponds to the burgers vector.

3.6 Thermodynamic calculations

To complement the analysis of the microstructure it is also important to analyze thermodynamically which phases that are prone to develop in a system upon solidification. This is especially relevant since all the phenomena associated with fusion-based welding processes may cause different phases to nucleate than those that are expected from an HEA system.

Such prediction is made possible via the CalPhaD methodology. This method allows not only to calculate which phases are stable at a given temperature, but it also permits to extrapolate the properties of a given phase. As mentioned, it does so by modeling individual phases as polynomials as a function of composition, temperature and pressure.

In this work, the CalPhaD-software Thermo-Calc was used to retrieve the phase information required for each weld in terms of equilibrium and non-equilibrium solidification. The software was coupled with the TCHEA 4 and TCHEA 5 databases, which hold the phase polynomials designed specifically for studying HEAs. Such allows to predict the microstructure developed during solidification.

Beyond phase equilibrium phase diagrams, special emphasis was given to Scheil-Gulliver calculations. This method considers solute redistribution during solidification of an alloy, thus allowing for a more accurate prediction of the phases that develop under non-equilibrium solidification. That is, by assuming that diffusion solely occurs in the liquid phase, where D_L is infinite, and that equilibrium solely exits at the S/L interface, it makes possible the calculation of evolution of the concentration of an alloy during all the solidification process. Such considerations yield the well-known Scheil-Gulliver equation (see Equation 15).

$$C_s = k \cdot C_0 \cdot (1 - f_s)^{k-1} \quad (15)$$

Here, C_s is the concentration of solid at a given stage during solidification, C_0 is the initial concentration of the alloy (prior to solidification), k is the partition coefficient and f_s is the fraction of solid within the solidifying alloy. Also, of interest is the concept of k which is given by the ratio between C_s and C_L (composition of the Liquid).

3.7 Mechanical characterization

To correlate the microstructure with the mechanical properties of a joint, microhardness mapping and tensile testing, coupled with Digital Image Correlation (DIC), were performed.

Microhardness tests were conducted on a Mitutoyo HM-112 Hardness Testing Machine, with the load varying accordingly with the materials to analyzed. All indentations were performed with a 10 s dwelling time and were space from each other at a distance determined from the diagonal length.

Furthermore, uniaxial tensile testing was performed on a Shimadzu tensile machine equipped with a 50 kN load cell, at a 10^{-3} s^{-1} strain rate. To ensure replicability, at least 3 welded samples were tested with the loading direction normal to the welding direction. During the experiments DIC data was gathered allowing for region specific strain distribution analysis. After tensile testing, fractography was conducted on the fractured surfaces using a Hitachi SU3800 SEM.

4

RESULTS AND DISCUSSION

4.1 Chapter introduction

In this chapter, all the results obtained from the experimental procedure displayed in Chapter 3 are exhibited and discussed.

As such, in this chapter the findings corresponding to each investigated HEA have their own corresponding section, where all the investigation performed on them is presented alongside their specific conclusions.

4.2 Microstructure evolution and mechanical performance of Gas tungsten arc welded $Fe_{50}Mn_{30}Co_{10}Cr_{10}$ HEA

4.2.1 Sections highlights

In this section the microstructure and the mechanical performance of a GTAW $Fe_{50}Mn_{30}Co_{10}Cr_{10}$ HEA are accessed. Initially, the mechanical behavior of the BM is analyzed in terms of in-situ tensile testing under synchrotron x-ray radiation. Next, similar and dissimilar welded joints performed on this HEA are analyzed. In particular, dissimilar welding with an Fe-based SMA is studied and presented for comparison with a similar welded joint obtained in this advanced Fe-based SMA.

4.2.2 In-situ x-ray diffraction analysis during tensile testing of the $Fe_{50}Mn_{30}Co_{10}Cr_{10}$ HEA[1]

4.2.2.1 Microstructure description throughout tensile loading

The initial microstructure condition and overall mechanical performance of the DP-HEA are presented in Figure 12. Observing the data contained within the EBSD inverse pole figure (IPF) and phase maps present in Figure 12 a) and b), the dual phase nature of the DP-

[1] The results discussed in this subsection were accepted for publication in the International Journal of Plasticity.

HEA is revealed, as the two phases characteristic of this HEA, austenite (γ-FCC) and martensite (ε-HCP) can be easily identified. From this technique and from the microscopy performed via OM, we can infer that the γ-FCC grains exhibit a polygonal shape, with an average grain size of 40.2 ± 10.7 µm, while plate-like ε-HCP grains can be observed amidst the DP-HEA microstructure. However, note that for EBSD and OM sample preparation, the plastic deformation and material removal processes involved in polishing may cause TRIP to occur at the surface, thus resulting in a slightly higher fraction of ε-HCP than that which is really present in the bulk of the material. Such, however, does not hinder the present discussion of the SXRD results, provided that not only do we work in transmission mode, as different samples, other than those used for EBSD and OM characterization, were tested during the experiment.

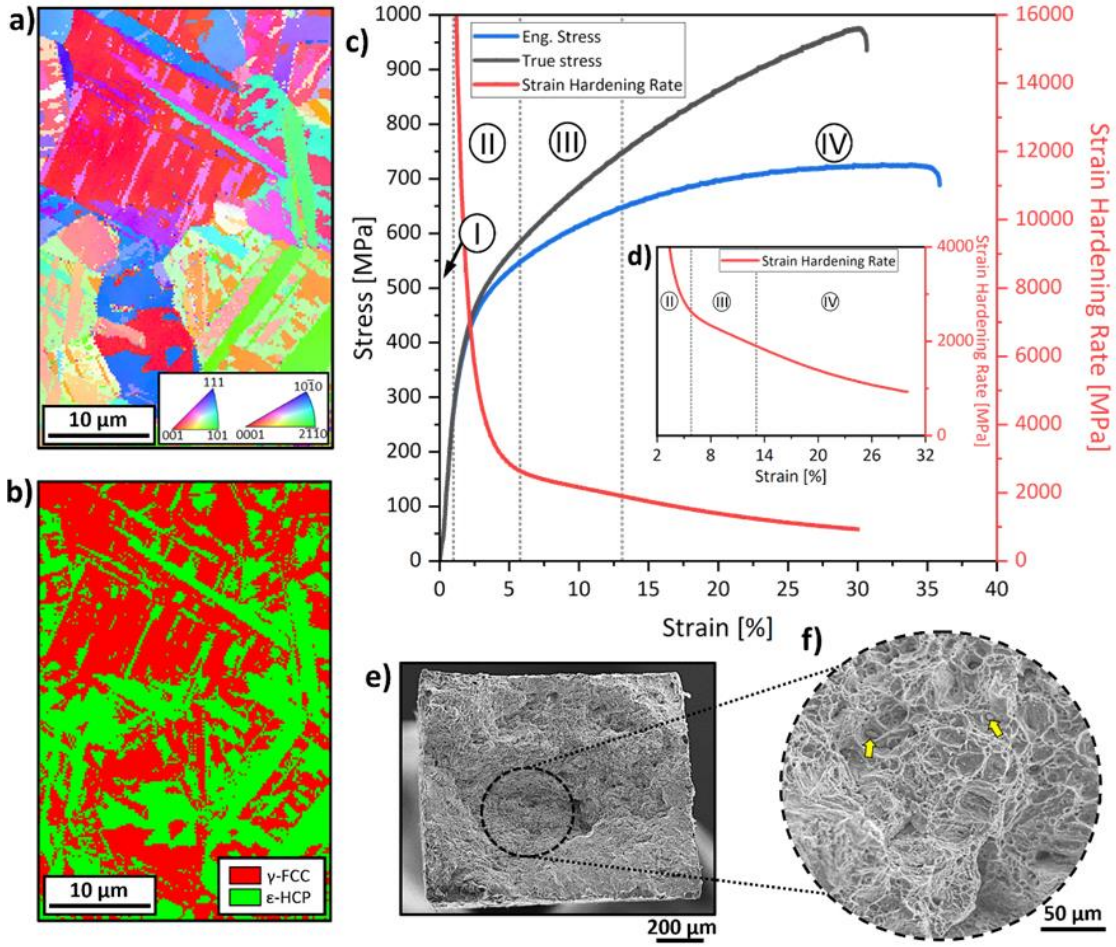


Figure 12 –Microstructure evaluation and mechanical behavior of the DP-HEA: a) EBSD IPF and b) EBSD phase maps; c) Engineering and true stress/strain curves describing the macroscopic tensile behavior of the DP-HEA, along with the strain hardening rate, which is further detailed in d); e) fracture surface and f) its corresponding detailed view.

Furthermore, the engineering and true stress-strain curves of the material are also exhibited (refer to Figure 12 c). Upon loading the alloy entered the plastic regime at ≈319 MPa, reaching an ultimate tensile strength of 726 MPa and eventually fracturing at an elongation of 36% (all engineering values). These results are comparable to those found in the literature regarding this HEA [36,82–85], indicating it is consistency with the data already available concerning the DP-HEA. However, it should be mentioned that the tensile properties of the DP-HEA are highly dependent on the initial ε-HCP phase volume fraction [36]. Thus, any (minor) differences between the tensile behavior obtained in present study and those found in the literature, can also be due to the intermittent loading process to which the sample was subjected during the in-situ tensile test to acquire the diffraction patterns at each loading stage.

Moreover, the strain hardening rate, calculated from the true stress-true strain data is displayed and further detailed in Figure 12 c) and d), respectively. From it we can identify four different stages within the tensile loading response of the DP-HEA. The first corresponds to the elastic portion of the curve, that ultimately ends with the onset plastic deformation. From that point on, a steep and continuous decrease with each increment of strain can be observed up to a true strain value of ≈6%, marking the onset of new loading stage. Finally, when reaching a true-strain level of ≈13%, the onset of a final loading stage can be marked. Although subtle, these changes occurring in the strain hardening rate account for the activation of the TRIP and TWIP effects. Such evidences that the DP-HEA becomes significantly stronger with the increasing loading and is going to be discussed further with the aid of diffraction data.

Eventually, upon failure, the fracture surface exhibited several dimples characteristic of a ductile-like fracture as observed via electron microscopy in Figure 12 (e) and (d). Also, the presence of scarcely scattered round particles can also be observed (marked with yellow arrows), corresponding to Mn oxides. These have also been identified in [25,85] and can be expected due to the high Mn content in the DP-HEA composition.

Considering this, we now turn our attention to the SXRD data results. In Figure 13, we can observe the microstructural evolution (obtained after full azimuthal integration), of the DP-HEA upon loading on a crystal structure perspective. Starting with phase identification, we can observe that diffraction peaks corresponding to γ-FCC, ε-HCP and MnO phases are present, corroborating the previous observation using optical and electron microscopy. Note that

the latter phase corresponds to lower intensity peaks that can only be properly observed by utilizing a logarithmic scale in the intensity axis due to the reduced volume fraction of MnO, which was determined to be ≈1%.

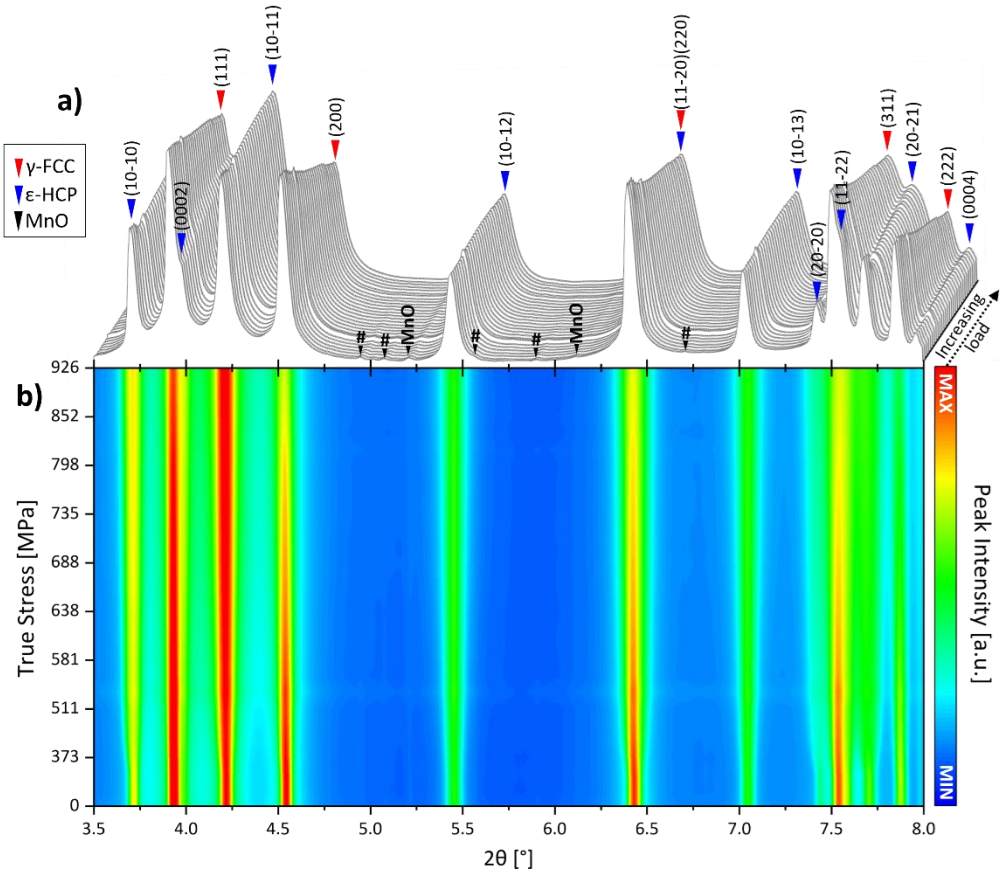


Figure 13 – a) Full azimuthal integration of the diffraction patterns obtained during tensile testing alongside with b) the corresponding colormap which evidences peak broadening and intensity changes with the increasing load (# corresponds to 2nd reflections).

Additionally, evidencing the variation of peak intensity with increasing load, the colormap of Figure 13 (b)) highlights significant changes in the evolution of different diffraction peaks with each loading step. Given this, further single peak analysis of the diffraction data was conducted to gather a deeper understanding of the microstructural changes visible with SXRD.

Regarding this microstructural evolution occurring in the DP-HEA during tensile test, we start by addressing the effect of TRIP on the DP-HEA. For this, Figure 14 highlights the continuously increasing ε-HCP phase fraction after the onset of TRIP, upon entering the plastic regime (at ≈250 MPa, which is the nearest point to the yield strength measured in Figure 12

c). From this data we can observe that prior to the tensile test the amount of ε-HCP on the DP-HEA was approximately of 33% in volume fraction, reaching nearly 77% upon fracture. It must also be emphasized that while TRIP is occurring, the mechanical behavior of the already deformed and newly formed ε-HCP phase in the alloy can be different [86]. However, it is not possible to separate the contributions of newly formed and thermally stable ε-HCP by synchrotron X-ray diffraction, thus the mechanical behavior of ε-HCP phase simultaneously considers those conditions. Given this, fluctuations on the amount of ε-HCP being formed throughout the tensile test can be observed and correlated with the evolution of the ε-HCP c/a ratio.

On this topic, the evolution of the lattice constants, which indicate the overall behavior of each phase, must first be mentioned. In the γ-FCC phase, the lattice constant, a, is 3.582 Å at the beginning of the test, exhibiting a continuous increase, up to 3.588 Å at the final loading stage. Such is coherent with the increase in interspatial distance due to the tensile loading. Additionally, in the ε-HCP case, the values of a and c are ≈2.535 Å and ≈4.100 Å, respectively, prior to the experiment, whereas the value of a tends to increase and the value of c exhibits a decreasing tendency, reaching the values of a ≈ 2.540 Å and c ≈ 4.097 Å.

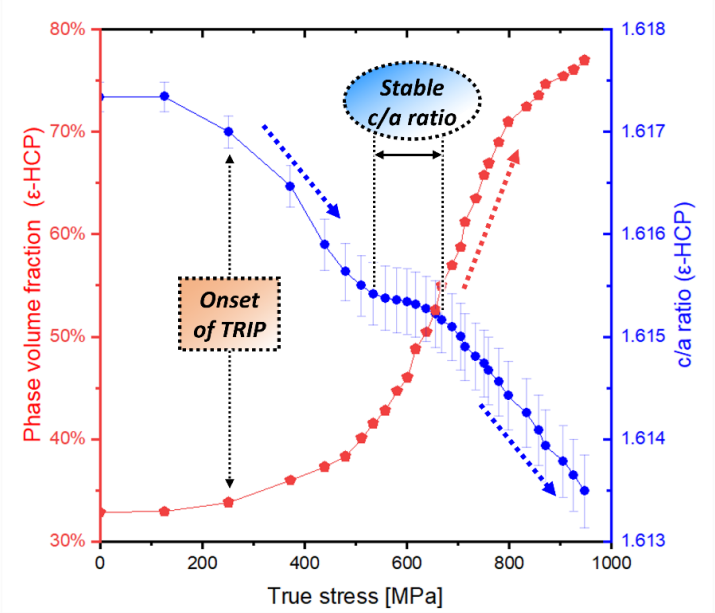


Figure 14 – Evolution of ε-HCP phase fraction obtained via Rietveld refinement (using MAUD [87]) with an R_{wp} below 5% and c/a ratio evolution throughout the tensile test calculated using single peak analysis considering the (1 0 -1 0) and (1 0 -1 3) diffraction peaks, highlighting the variations occurring at the microstructural level on the DP-HEA.

Upon the onset of TRIP, the c/a ratio decreases drastically until the stress imparted by the material reaches ≈530 MPa, where it becomes stable. At this point a massive increase in the ε-HCP phase fraction can be observed, indicating that the initial strain accommodation mechanisms occurring in the both phases reached a critical stage, where the TRIP effect becomes more prominent, and stabilization of the ε-HCP phase lattice, due to the activation of different strain accommodation processes, acted together to prevent premature failure. However, when reaching ≈655 MPa, a sharp decrease on the c/a ratio can again be observed, marking the onset of a different stage on the mechanical behavior of the DP-HEA. These strain accommodation stages are responsible for the mechanical behavior of the DP-HEA and the following sections will illustrate the changes occurring on the diffraction peaks that take place at the onset of each stage.

4.2.2.2 Evolution of integrated peak intensity and ε-HCP twinning activation

To unveil the deformation mechanisms occurring considering different grain orientations, the integrated diffraction intensities were obtained from the LD and TD integrated data at each loading step. The results can be observed in Figure 15.

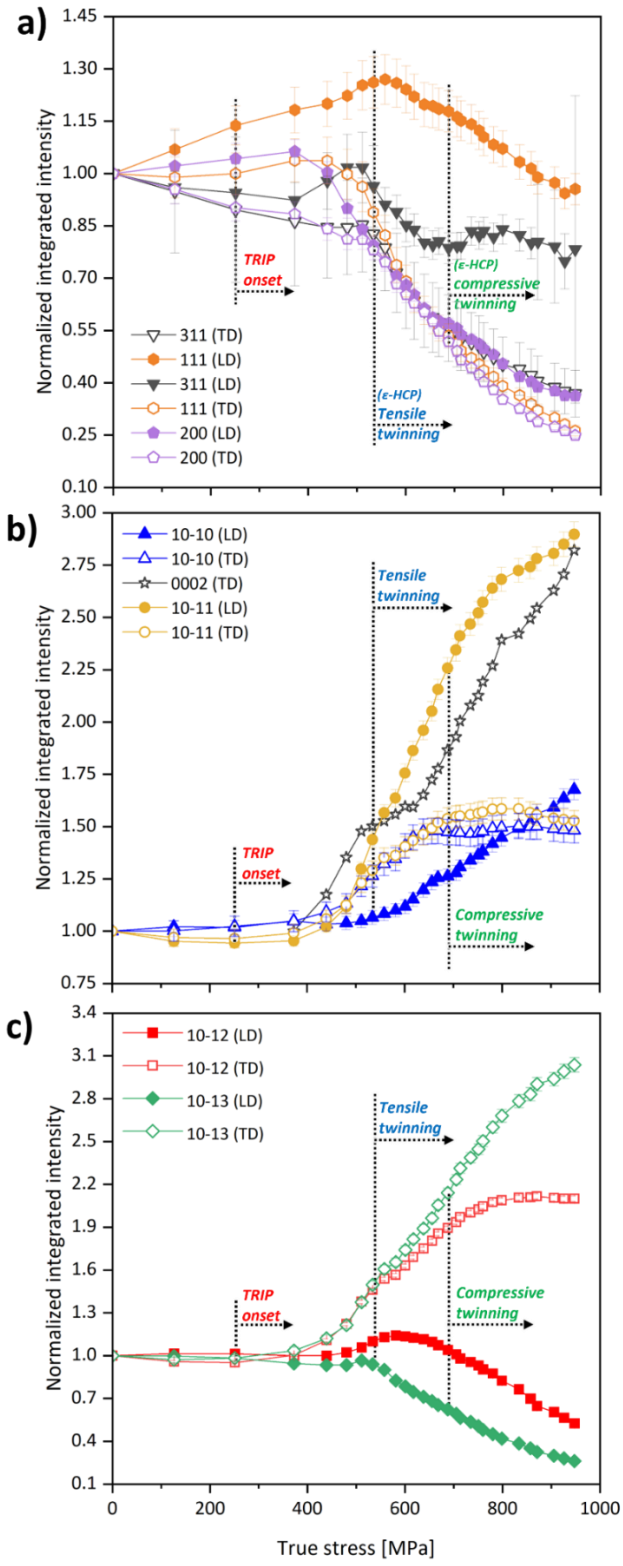


Figure 15 – Normalized integrated intensity evolution during tensile test along TD and LD. (a) shows the evolution of γ-FCC (1 1 1), (2 0 0) and (3 1 1) diffraction peaks; (b) details the evolution of ε-HCP (1 0 -1 0) and (1 0 -1 1) diffraction peaks. Here, the (0 0 0 2) peak evolution is only shown for reference in the TD; (c) shows the evolution of ε-HCP (1 0 -1 2) and (1 0 -1 3) diffraction peaks.

Starting from the γ-FCC phase (refer to Figure 15 (a)), all integrated intensities of the analyzed diffraction reflections exhibit an overall similar trend. As it is possible to observe, before reaching the yield strength, the intensity (1 1 1) and (2 0 0) planes tend to increase aligned with the LD, while a slight decrease can be observed for the (3 1 1) peak in this direction. Interestingly, the (1 1 1) intensity shows the higher intensities aligning with the LD, which is coherent with the expected preferential deformation direction of FCC materials [30]. This behavior continues to exhibit a stable behavior allowing for the γ-FCC grains to rotate, except for the (2 0 0) diffraction peaks, where upon the onset of TRIP, there is a major decrease in intensity in both directions.

Nevertheless, it is when reaching approximately a stress level of 530 MPa that the integrated intensity of all peaks evidences a sharp decrease. This agrees with the phase volume fraction results obtained from Rietveld refinement (refer to Figure 14), meaning that at this stage the TRIP effect becomes more predominant, to relax the stresses imposed by tensile loading, within the γ-FCC rich microstructure.

Considering the peak intensity evolution of the ε-HCP phase, Figure 15 (b) and (c) displays the results obtained for the (1 0 -1 0), (1 0 -1 1), (1 0 -1 2) and (1 0 -1 3) diffracting reflections. Here, the intensity results for the (0 0 0 2) plane are also shown as a reference, as this reflection only starts being noticeable at the onset of plastic deformation exhibiting an ascendant behavior on the TD and being practically non-existent on the LD (this being the reason on why this is not shown). Such behavior can be associated with the TRIP effect, as it effectively transforms the γ-FCC into ε-HCP.

Furthermore, considering the deformation mechanisms activated in the ε-HCP phase, besides the possibility for dislocation slip (discussed further ahead in this paper), literature [36,84] shows that tensile {1 0 -1 2} <1 0 -1 0> and compression {1 0 -1 1} <1 0 -1 2> twinning modes are activated during deformation, corresponding to twinning misorientation angles of, approximately, 87° and 57°, respectively. Such phenomena can be analyzed thought the peak intensity evolution during plastic deformation, where an abrupt splitting of intensity in the LD and TD evidences the inception of twinning [84,88] .

With this in mind, Figure 16 depicts color maps corresponding to stage I and IV of the tensile test on both the (1 0 -1 0) and (1 0 -1 2) diffraction peaks. Such allows us to evidence the

different behavior exhibited by each peak, during the tensile test and highlight the effect that the tensile and compression twinning mode have on peak intensity and distribution.

Examining the integrated intensities evolution, it is possible to observe that the first twinning mode to occur is the {1 0 -1 2} <1 0 -1 0> tensile twinning mode at ≈530 MPa. Such can be observed through the evolution of peak intensities on the LD and TD directions, on both the (1 0 -1 2) and (1 0 -1 3) reflections as exhibited in Figure 4 c). Such indicates the onset of the TWIP effect, where twining starts to take an important role in stress accommodation in the ε-HCP phase. It is also at this point that the (1 0 -1 1) reflection initiates a substantial increase in the LD, which, as mentioned by Fu et al. [84], can be attributed to the tensile twinning of the (1 0 -1 3) grains under the {1 0 -1 2} <1 0 -1 0> twinning mode. This is due to the fact that the lattice angle between the planes belonging to the (10-11) and (10-13) families of planes is approximately 90° and the twinning misorientation angle is ≈87°, thus increasing the possibility for the (1 0 -1 3) grains to become oriented in the [1 0 -1 1] direction.

With further loading, the compression {1 0 -1 1} <1 0 -1 2> twinning mode is activated (at approximately 655 MPa). This can be noticed by the stabilization of the intensity behavior on the (1 0 -1 2) and (1 0 -1 0) diffraction peaks on the TD. Such results are coherent with the noticeable changes in the c/a ratio. Additionally, further analysis on this twining mode, which is not so evident, can be seen in Figure 16, where the diffraction patterns corresponding to the beginning and end of the tensile test were integrated into 1^{o} azimuthal angle segments, within the 2θ ranges corresponding to the (1 0 -1 0) and (1 0 -1 2) peaks.

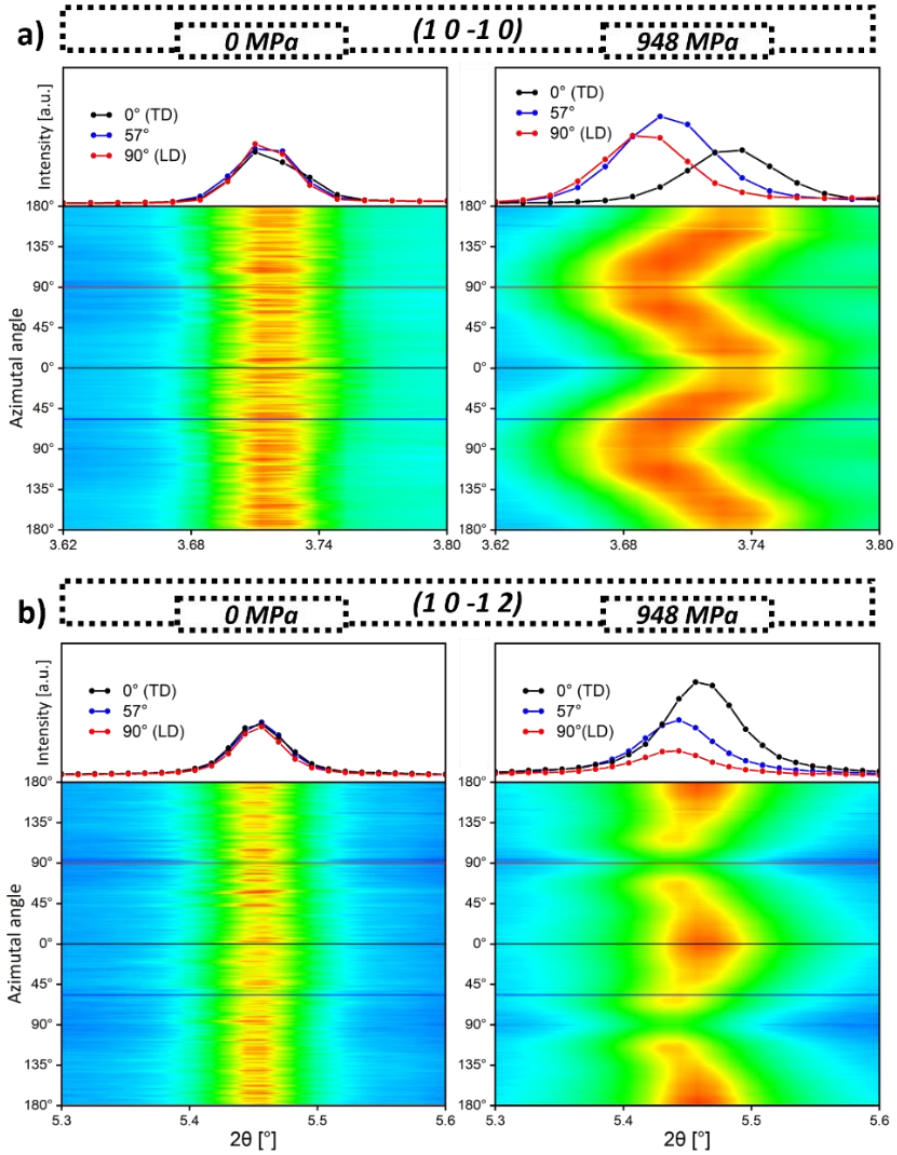


Figure 16 – Color maps corresponding to the stage I and IV of the tensile test on the: a) (1 0 -1 0) and b) (1 0 -1 2) diffraction peaks. This serves to evidence the different behavior exhibited by each peak upon the increase of stress and visible only by 1° cake integration of the diffraction patterns.

Observing closely, prior to tensile testing (at 0 MPa condition) both diffraction peaks showcase an even distribution along the azimuthal angle, regarding their 2θ angle position. Nevertheless, a very different behavior can be seen at the final stages of the experiment. While the (1 0 -1 0) peak evidence a continuous distribution, reaching lower 2θ values at 90° (corresponding to the LD), it is also possible to observe that higher intensity values are obtained at 57°. Additionally, the (1 0 -1 2) peaks exhibit higher intensity values at 0° (corresponding to the TD) and also at 57°. In the latter case the 2θ angles are higher than those in

the stress-free condition. Considering the behavior of (1 0 -1 0) diffraction reflection and the data acquired to this point it is viable to assume that the grains oriented in this direction tend to mainly exhibit dislocation slip as their main strain accommodation mechanism, finally exhibiting the compression twinning mode the last stages of the tensile test. As for the (1 0 -1 2) case, it is possible to infer that the increasing diffracted intensities due to tensile twinning result on a higher amount of (1 0 -1 2) oriented grains in the TD which tends to increase with the increasing stress, resulting in the compression of grains in this direction, which is perpendicular to loading. Such behavior then causes the compression twinning mode to activate, resulting in the higher (yet relatively lower) intensities oriented near the 57° azimuthal angle.

4.2.2.3 Lattice strain evolution upon loading

Having now established the phenomena associated with intensity changes, further information can be obtained by analyzing peak behavior in terms of their deviation from their stress-free 2θ position (at 0 MPa). Such was performed to unveil the strain effects (tensile or compression) on the LD and TD. Analyzing Figure 17 permits us to observe that, as expected, the lattice strain behavior of all crystallographic planes deviates from linearity at ≈250 MPa during the loading stage. In both γ-FCC and the ε-HCP cases, the DP-HEA exhibited a similar behavior to that expected from literature [89], where the highest magnitude for lattice strain was achieved at the final loading stages in both phases.

Additionally, for a full characterization of the lattice strain in each phase, the Young's modulus along the LD for each analyzed crystallographic plane, were calculated, and are summarized in Table 5.

Table 5 - Young's modulus and for different lattice planes of the constituent phases in the DP-HEA.

γ-FCC				
Reflection	**(1 1 1)**	**(2 0 0)**	**(3 1 1)**	
E [GPa]	240.0 ± 13.7	119.6 ± 0.5	175.5 ± 3.3	
ε-HCP				
Reflection	**(1 0 -1 0)**	**(1 0 -1 1)**	**(1 0 -1 2)**	**(1 0 -1 3)**
E [GPa]	139.2 ± 37.3	217.0 ± 50.2	324.5 ± 38.5	308.5 ±8.9

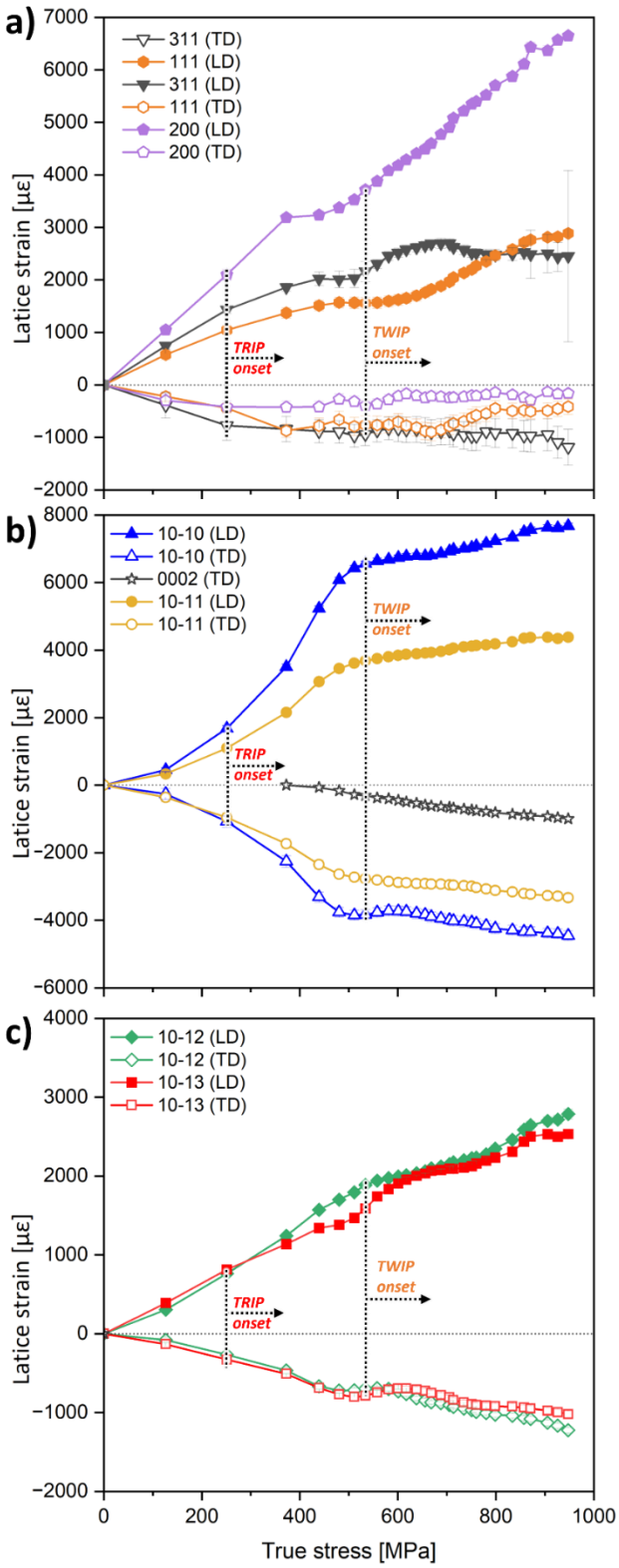


Figure 17 - Lattice strain evolution during tensile testing along TD and LD. (a) shows the evolution of γ-FCC (1 1 1), (2 0 0) and (3 1 1) diffraction peaks; (b) shows the evolution of ε-HCP (1 0 -1 0) and (1 0 -1 1) diffraction peaks. Here the (0 0 0 2) peak evolution is only shown for reference in the TD; (c) shows the evolution of ε-HCP (1 0 -1 2) and (1 0 -1 3) diffraction peaks.

Starting with the γ-FCC phase, Figure 17 (a) displays the lattice strain for the accessible diffraction peaks in both LD and TD. Comparably the largest lattice strain exhibited by the diffraction peaks can be observed in the direction of the tensile solicitation (LD). The (2 0 0) diffraction peak exhibits the largest lattice strain in LD and the lowest in TD indicating its higher ductility when compared to the other reflections, while the (1 1 1) reflections exhibited the stiffest behavior.

For the ε-HCP lattice strain, the results are displayed in Figure 17 (b) and (c). Again, the (0 0 0 2) peak is shown here as a reference, as the data retrieved from it cannot be used to fully characterize its behavior on the ε-HCP phase. As expected, the lattice strain in the LD is higher than the TD. The (1 0 -1 0) exhibits the most ductile behavior, followed by the (1 0 -1 1), (1 0 -1 2) and the (1 0 -1 3) diffraction peaks. Furthermore, as the (1 0 -1 2) and (1 0 -1 3) peaks exhibit a continuously increasing trend in their lattice strain behavior, the (1 0 -1 0) and (1 0 -1 1) reflections start to exhibit a steady behavior when reaching the ≈530 MPa threshold, at the onset of tensile twinning marked as "TWIP onset", showcasing their sensitivity to the onset of tensile twinning on the ε-HCP microstructure.

4.2.2.4 Dislocation density evolution with increasing load

With knowledge of the effect that TRIP and TWIP have on the accommodation of the imposed deformation, as seen in section 4.2.2.2, the activity of dislocation slip is still a major factor that can impact the strain accommodation on the DP-HEA. As such, assuming a direct relation between dislocation slip with dislocation density, it can be related to peak broadening [90], whereas the results obtained by the Halder-Wagner method can aid in visualizing the increase in dislocation density in both phases during loading.

Figure 18 (a) displays the dislocation density evolution on the γ-FCC phase. Here a steady increase from 1.4 x 10^{14} m^{-2} to 8.2 x 10^{14} m^{-2} can be observed throughout the experiment. Such result allows us to conclude that the main strain accommodation mechanisms occurring in the γ-FCC phase are TRIP and dislocation slip.

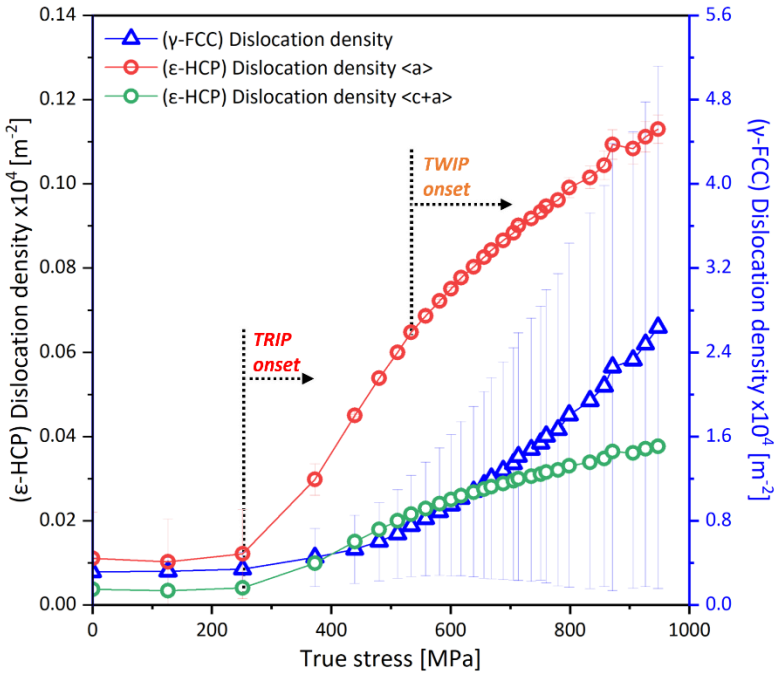


Figure 18 - Dislocation density evolution on the γ-FCC and ε-HCP phases, throughout the in-situ tensile experiment.

However, the dislocation density progression on the ε-HCP phase allows us to observe the differences in dislocation slip behavior when the TWIP mechanism is activated through tensile and compression twinning of its grains. In this phase the dislocation density shown is calculated using the b = 1/3 <1 1 -2 0> and b = 1/3 <1 1 -2 3> burgers vectors, to define <a> and <a+c> dislocations, respectively. The difference between them allows us to observe that, although both dislocation slip types may occur in simultaneous, the <a>-mode is dominant over the <a+c>-mode, which makes sense provided that strain accommodation in the c-axis of the HCP unit cell can be attained thought twinning. Such behavior can be observed at the onset of the TWIP effect (roughly 530 MPa) where the values of dislocation density tend to exhibit a slower increase when compared to the dislocation density results calculated between the onset of TRIP and the activation of TWIP.

4.2.2.5 Phase load partitioning between γ-FCC and ε-HCP

The load imparted by each phase along with their averaged contribution is plotted against the true stress-true strain curve in Figure 19 a). These results allow us to comprehend the stress partitioning occurring between both phases and their interaction to comply with

the externally imposed stresses. Overall, a good agreement between the volume averaged curve, calculated by averaging the contribution of both phases with their corresponding volume fraction, and the true stress - true strain curve was obtained.

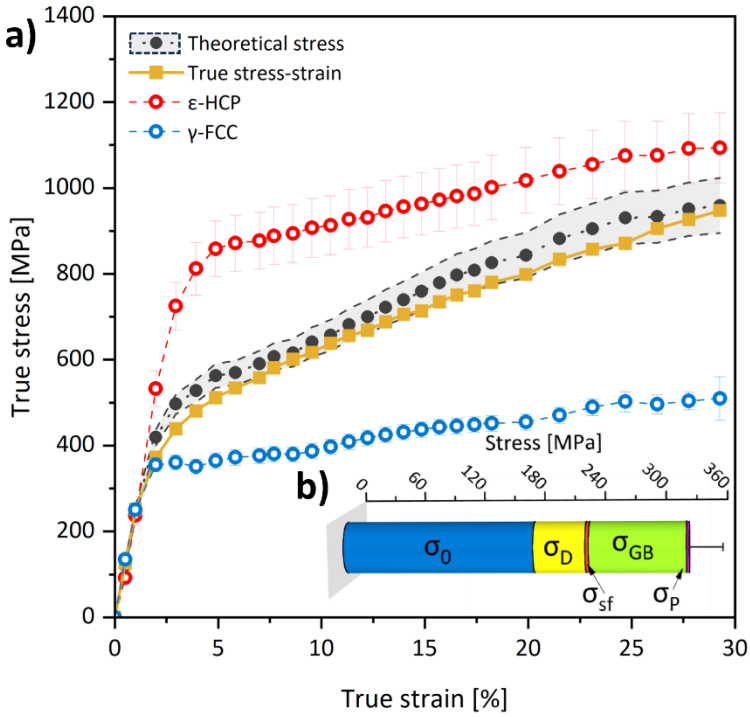


Figure 19 – (a) Load partitioning between the γ-FCC and ε-HCP phases. (b) Estimation of the yield strength of the DP-HEA based on the γ-FCC phase, which is the first phase to yield (σ_0 is the lattice friction stress, σ_D is the strengthening contribution from dislocations, σ_{SF} corresponds to the influence of staking faults and σ_{GB} represents the strengthening effect of grain boundaries).

Here it is possible to observe that both phases yield at different stages. While the γ-FCC yields within the range of ≈250 MPa to ≈355 MPa of the true stress-true strain curve, the ε-HCP phase only deviates from linearity it when surpasses the ≈480 MPa threshold. Additionally, the calculated elastic modulus for the γ-FCC and ε-HCP phase were 170 ± 4 GPa and 222 ± 47 GPa, respectively. Calculation of the Poisson ratio was also considered, where the value of 0.33 ± 0.03 was obtained for the γ-FCC and 0.35 ± 0.08 was obtained for the ε-HCP phase. It is, therefore, possible to conclude that it is the γ-FCC phase that dictates the end of stage I of the tensile test, as marked in Figure 12, meaning that once surpassing its yielding stress the TRIP effect activates, starting to actively transform the softer γ-FCC into the ε-HCP phase.

Calculation of the contributing factors to the yield strength of the γ-FCC phase was then performed to determine its yielding strength, and thus quantify the contribution factors that can contribute to the hastening/delay of the onset of stage II. In this regard, the load contribution to the γ-FCC phase yield strength was calculated based on using Equation 9. For this calculation, σ_0 was considered to be 179 MPa [78], σ_D and σ_{GB} were calculated based on [78,79] and σ_{SF} was obtained as in [80]). The results are shown in Figure 19 b). These indicate that beyond σ_0, which corresponds to the inherent strength of the DP-HEA, the grain boundary effect is the most impactful component, followed by the dislocation contribution and finally the stacking fault influence. At the same time the strengthening effect arising from the MnO particles can be considered negligeable. Overall, the summed contribution renders in a yield stress value of 321 ± 31 MPa, which is coherent with the yielding stress range of the γ-FCC phase and the measured yield stress of the DP-HEA (319 MPa, as exhibited in Figure 12 c)).

Finally, with the impact of the in-situ tensile test reported using SXRD, we now delve into the interpretation of such results to unveil the complete mechanical response of the DP-HEA.

4.2.2.6 Discussion

Before we delve into the deformation behavior of the $Fe_{50}Mn_{30}Co_{10}Cr_{10}$ HEA under tensile testing, one important notion to establish is that of strain-induced martensitic transformation. This phenomenon occurs in certain materials, such as the present HEA, when they are subjected to mechanical deformation. Such effectively transforms an austenitic phase (in this case γ-FCC) into a martensitic one (ε-HCP). The martensitic phase is characterized by a different crystal structure, when compared to the phase that gives it its origin, granting the alloy unique mechanical properties, being at the core of the TRIP effect [91].

Given the tensile nature of this study, the martensitic transformation occurring in this HEA, which exhibits both the TRIP and TWIP effects, allows for the continuous transformation of γ-FCC into ε-HCP, permitting the DP-HEA to benefit from the ductility and the strength associated with each phase.

Considering this, starting from the initial γ-FCC rich condition of the DP-HEA at 0 MPa (displayed in Figure 14) there is a highly evident presence of ε-HCP (with a total volume phase fraction of 33%). Conversely, this initial ε-HCP phase amount present within the

microstructure can be described as thermal martensite, given that it is not related with mechanical loading, but manifests from the lattice defects developed during its manufacturing [92] of such stacking faults leads to the formation of ε-HCP thin laths. Such thermally induced ε-HCP can then act as nuclei for the mechanically induced ε-HCP; thus, the initial phase volume fraction of ε-HCP is a parameter that directly influences the mechanical behavior of the alloy [25,36,93,94].

With this matter established, direct comparison between Figure 12 c) and Figure 19 a), allows us to infer on both the macroscopic and phase specific behavior of the DP-HEA throughout the tensile test. This is especially relevant regarding the yielding stress of each phase. As mentioned, the yield stress of the material reaches ≈319 MPa, nevertheless, it is clear that the more ductile γ-FCC reaches its yielding stress earlier than the harder ε-HCP, dictating the onset of the TRIP effect and the macroscopic yield stress of the DP-HEA. Minding the yielding stress, Figure 19 b) indicates that beyond the inherent strength of the alloy, the influence of the grain boundaries stands as a major contribution, followed by dislocation density and with stacking faults exhibiting a minor effect on the yielding of the DP-HEA. Beyond this point, the load imparted by the DP-HEA is then distributed by each phase, where (obeying the rule of mixtures) the ε-HCP sustains higher stress levels, while a lower amount of stress is distributed towards the γ-FCC phase. This indicates that, while granting ductility to the DP-HEA, the most critical role of the γ-FCC phase is to enable the inception of ε-HCP in the microstructure, via the TRIP effect.

Furthermore, it is with focus set on the SXRD data that the succession of events occurring upon mechanical solicitation beyond the yielding stress can be unveiled and correlated. Accordingly, as a starting point for such interpretation, we divide the mechanical behavior of the alloy into four different loading stages. Each stage beginning at the, relatively precise, onset of each microstructural response to the external loading, more specifically regarding the TRIP and TWIP effects (refer to Figure 20). For such, the stress ranges considered for marking the loading stages undertaken by the DP-HEA during tensile testing, are based on true stress values.

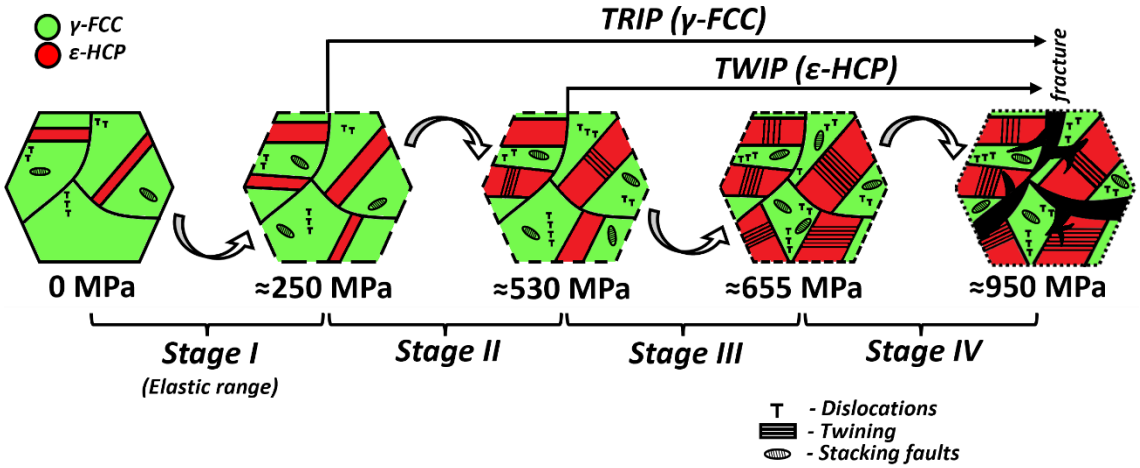


Figure 20 – Schematic representation of the loading stages undertaken by the DP-HEA, highlighting the stress thresholds for the activation of the multiple strain accommodation mechanisms developed upon tensile stress.

4.2.2.7 Stage I: from 0 MPa to ≈250 MPa

Given this, the stage I ranges from 0 MPa to the moment when the DP-HEA enters in the plastic regime. For analysis purposes we set the end of this stage at ≈250 MPa, which is the closest point to the yield stress within the elastic regime that was probed by SXRD.

This stage is mainly characterized by both phases being elastically deformed, so no influence of the TRIP or TWIP mechanisms on the mechanical response exist. The c/a ratio in this region shows a slight tendency to decrease, going from 1.6173 ± 0.0001 to 1.6170 ± 0.0002. At this stage, the ε-HCP phase volume fraction and the corresponding dislocation density are stable, and the same can be said regarding the integrated peak intensity, in both the TD and LD. Nevertheless, the integrated peak intensity on the γ-FCC, tends to exhibit a small deviation from the initial values, indicating that the grains are rotating due to the imposed elastic strain. This preferential deformation of the γ-FCC phase is related to its lower strength compared to the ε-HCP phase.

Concerning the microstrain, however, it can be noted that it increases linearly in both directions, although exhibiting different slopes, which in turn reveals the stiffness associated with specific families of planes. Such is highlighted by the Young's modulus calculated and detailed in Table 5. Therefore, for the γ-FCC phase it can be observed that the (1 1 1) is the hardest and the (2 0 0) corresponds to the softest of the crystallographic plane families. Additionally, from the analyzed peaks of the ε-HCP phase it is revealed that (1 0 -1 0) corresponds

to the softest family of planes, while the (1 0 -1 3) is the hardest. Such is coherent with the analyzed literature [74,84,95]. This is of particular interest to consider, given the anisotropic mechanical response of each family plane at later stages of loading. All things considered; this region exhibits the expected behavior of a material being deformed in the elastic range.
Moreover, the lattice strain of all peaks of both phases keeps increasing throughout the tensile test in both directions, especially in the LD (which is the direction of solicitation). Nevertheless, it is important to mention that each family of planes has its own pace and, with the increasing stress, will showcase their specific response, with this being accomplished by either TRIP, TWIP and/or dislocation slip. This way multiple mechanisms can act together to sustain the imposed loading.

Furthermore, although, at this stage, local plastic deformation can theoretically occur within the global elastic regime our SXRD analysis indicates no observable changes in phase fraction or peak parameters, likely due to the bulk analysis capabilities of this technique.

4.2.2.8 Stage II: from ≈ 250 MPa to ≈ 530 MPa

Upon the yielding of the γ-FCC phase, at ≈250 MPa, the beginning of a new stage can be marked up to the point where TWIP becomes a noticeable load bearing mechanism, via tensile twinning (at ≈530 MPa). At this stage, we can observe an increase on the ε-HCP phase volume fraction complemented with a sharp decrease on the overall hardening rate of the DP-HEA. This indicates that the activation of the TRIP effect acts as a major strain accommodating mechanism by granting the DP-HEA more strength as the stress level increases.

At this point of the tensile test, γ-FCC is still the dominant phase, thus the strain accommodation mechanisms beyond the evident TRIP effect, must also be analyzed. Evidently, in Figure 18, the dislocation density on this phase exhibits a massive increase upon yielding, indicating that dislocation slip on γ-FCC also contributes to the overall accommodation of external stresses. Observing the intensities variations, however, it can be observed that no abrupt splitting of intensities in the LD and TD occurs. This leads to the conclusion that twinning is not a strain accommodation mechanism in the γ-FCC phase, as it would be expected from its ability to generate stacking faults.

Furthermore, a decrease in c/a ratio (reaching 1.6154 ± 0.0003) is also noticeable and can be related with dislocation slip modes on the ε-HCP. As mentioned by Bu et al. [96], the

combined action of ⟨a⟩, ⟨c⟩ and ⟨a + c⟩ slip systems were observed via in-situ transmission electron microscopy in a $Fe_{50}Mn_{30}Co_{10}Cr_{10}$ HEA. This feature was attributed to a c/a ratio of 1.616 (which is lower that the ideal 1.633 value), highlighting that the reduction of the c/a ratio enhances the ⟨a + c⟩ slip activity in the DP-HEA. In the present case, the increasing dislocation density on the ε-HCP phase (refer to Figure 18) calculated using both the basal and pyramidal Burgers vectors, indicates that both ⟨a⟩ and ⟨a + c⟩ type of dislocations show an massive increase at this stage of the tensile test, with the ⟨a⟩-type being prevalent. In here, the steady evolution of integrated intensities also evidences grain rotation due to dislocation slip, owing to the lack of any sharp change in slope, which implies that deformation twinning is not the prevalent mechanism for strain accommodation.

4.2.2.9 Stage III: from ≈530 MPa to ≈655 MPa

Furthermore, the c/a ratio between ≈530 MPa and ≈655 MPa becomes stable, signaling the start of new deformation stage in the DP-HEA. The present results are in good agreement with those of Sinha et al. [17], since it is observed a stabilization of the c/a ratio when the relative volume fraction of each phase varies between 40 and 60 %, which is correspondent to a range of externally applied stress of 530 to 655 MPa.

Being depended on the lattice parameters of the ε-HCP phase, the c/a ratio is, therefore, directly related to the volume variation induced by the TRIP effect, which inherently, requires the γ-FCC atoms to adapt in order to generate the ε-HCP basal plane and, perpendicularly to it, the c-axis of HCP unit cell, which requires the displacement of atoms from the neighboring lattice. Here, the stabilization of c/a ratio can be related to activation of twinning, provided that it is only responsible for the reorientation of a portion of the lattice, not resulting on the direct alteration of the lattice constants of a phase. Nevertheless, this phenomenon ultimately exerts more stresses in the γ-FCC phase, which then causes TRIP to occur more intensively, as it can be seen through the nucleation of new ε-HCP cells that will no longer be exposed to lower levels of stress.

This way, TWIP can be observed through the tensile twinning visible in the analyzed peaks intensities, although, interestingly, not all peaks showcase this effect at this stage. Such allows us to infer that, considering the crystallographic plane stiffness, noticeable by the lattice strain in the elastic range, the most rigid planes exhibit a sharp variation in intensity

between the LD and TD (thus indicating tensile twinning), while the softer ones continue to accommodate strain via dislocation slip. This phenomenon is corroborated by the dislocation density evolution showcased by the ⟨a⟩ and ⟨a + c⟩ dislocation slip modes, where both have an evident decrease in slope, while the ⟨a⟩-type, corresponding to basal slip, still increases in a relatively higher amount. Interestingly the effects of TWIP on the diffraction peak behavior can also be noticeable in the lattice strain variation of the ε-HCP phase, where the (1 0 -1 2) and (1 0 -1 3) peaks (corresponding to the stiffer crystallographic planes) continuously increase with the increasing stress, while the slopes on the lattice strain evolution of the softest peaks, (1 0 -1 0) and (1 0 -1 1), decreases. This evidences that TWIP is prevalent over dislocation slip in the ε-HCP phase, although not inhibiting it.

Regarding the integrated intensities analyzed in the γ-FCC phase, an overall decreasing trend for all peaks is depicted. Such is related to an increasing in the ε-HCP phase fraction, which at this point exhibits a sudden increase in slope. This allows us to conclude that when reaching the ≈530 MPa threshold, both TRIP, in the γ-FCC, and TWIP, in the ε-HCP, collaborate to achieve higher strengths and strains imparted by the DP-HEA. This combined behavior has an impact on the hardening rate, as during this stage the slope of the curve is decreasing, when the stress-strain curve reaches the corresponding stress levels, as visible in Figure 12 c). This indicates that the ability for these mechanisms to accommodate the increasing stress levels is decreasing, and so is the DP-HEA's capacity for hardening.

4.2.2.10 Stage IV: from ≈655 MPa to ≈950 MPa

Finally, when the stress-strain curve reaches ≈655 MPa the hardening rate reaches a plateau. At this point the DP-HEA reaches the final last stage of the tensile test, which is marked by the onset of compression twinning.

Furthermore, the lattice strain keeps increasing at a coherent pace as the previous stage, however, the c/a ratio decreases which indicates that the ⟨a + c⟩ dislocation slip mode should become favored in supplementing the DP-HEA with strain accommodation in the ε-HCP c-axis [96]. However, although the dislocation density curves of the ε-HCP keep increasing it does so at a lower rate. Such suggests that at this moment this dislocation slip mechanism is no longer the most effective way to allow for strain to be accommodated. The

accommodation of strain is then accomplished by the increasing resolved compression stress in the TD, making it more energetically favorable [80,97].

This phenomenon can be seen in Figure 16, where the intensity of both the dislocation slip prevalent (1 0 -1 0) peak and the tensile twinning affected (1 0 -1 2) peak, become noticeably high when oriented 57° from the TD direction, at the last analyzed point of the in-situ tensile test.

Regarding the γ-FCC phase (which is now under 30% of the total phase volume fraction), the active strain accommodation mechanisms continue to be dislocation slip and the TRIP effect, according to decreasing γ-FCC volume fraction and increasing dislocation density.

Eventually, the sample fractured at ≈950 MPa, corresponding to approximately 30 % of engineering strain, marking the end of this stage and that of the in-situ tensile test.

4.2.2.11 Conclusions

In this work we contemplate the deformation behavior and microstructural evolution of a $Fe_{50}Mn_{30}Co_{10}Cr_{10}$ DP-HEA during in-situ tensile testing.

Quantitative analysis granted the analysis of the evolution of the continuously forming ε-HCP phase, upon yielding of the γ-FCC phase. Through this, mean ε-HCP volume fraction and c/a ratio evolution were assessed and calculation of diffraction peak-specific parameters were determined. Quantitative analysis was also performed to inspect the dislocation density evolution on both the major phases present in the DP-HEA.

Further investigation was conducted qualitatively, via single peak analysis. This allowed to observe the multiple mechanisms taking place to accommodate the externally imposed stress. In stage I, the DP-HEA deforms elastically until reaching the yielding stress of the soft γ-FCC phase, causing the onset of TRIP and the beginning of the stage II. This phenomenon occurs throughout the extent of the tensile test. As stress increases, strain accommodation on the ε-HCP phase causes the activation of the TWIP effect, which is noticeable by the onset of tensile twinning, visible through peak intensities. These two effects occur as dislocation slip takes place in both phases. Finally, stage IV occurs as compression twinning is activated until the eventual material fracture.

This sequence of events allowed to highlight the combination the transformative capability of γ-FCC (via TRIP) and the exceptional work hardening potential of ε-HCP (via TWIP).

4.2.3 Gas tungsten arc welding of the dual-phase $Fe_{50}Mn_{30}Co_{10}Cr_{10}$ HEA[2]

Having asserted that welding is a key manufacturing technique that will eventually be applied to HEAs, there is a need to evaluate the microstructure and property changes induced by the weld thermal cycles. Such is performed to assess the suitability of certain welding process/HEAs combinations for possible industrial applications. In this section, GTAW was used to achieve defect-free joints based on the novel TRIP and TWIP $Fe_{50}Mn_{30}Co_{10}Cr_{10}$ HEA.

4.2.3.1 Microstructural analysis

Upon visual inspection of the joints cross section, autogenous $Fe_{50}Mn_{30}Co_{10}Cr_{10}$ DP-HEA welds with full penetration were obtained, as shown in Figure 21 (a). Also, in Figure 21 (a), it is possible to observe the effect of the thermal cycle across the microstructure of the welded joint. The BM, HAZ and FZ are delimitated to further help in establishing differences in microstructure at each location within the joint.

Focus is now given to representative locations within the welded joint as observed by light optical microscopy. Analysis of the BM details the initial condition of the material prior to welding. As it can be observed in Figure 21 (b), the material is composed by two phases: austenite (γ-FCC), characterized by equiaxed grains with an average size of 27.2 ± 10.7 μm, and ε-martensite (ε-HCP) which corresponds to the needle-shaped laths within the grains. In the case of this TRIP DP-HEA, the presence of martensitic laths in the as-cast condition can be explained by the phase transformation arising from the internal strains developed during solidification and contraction of the material as it cools down from casting, causing the lattice atoms to rearrange in a different crystal structure from the parent FCC phase [98].

Adjacent to the BM exists the HAZ. Figure 21 (c) portraits the transition from the BM to the HAZ clearly exhibiting a grain size variation upon entering in the latter region. The temperature and permanence time at temperatures where solid-state transformations can arise enabling for grain growth to occur leading to a significantly larger grain size of 112.2 ± 14.8 μm. That is, as the welding heat flowed through conduction from the FZ towards the solid material,

[2] The results discussed in this sub-section are already published in the Materials Science and Engineering: A journal, corresponding to reference [25].

there will be recrystallization phenomena, but eventually grain growth will be predominant. It should be noted, however, that favoring of a grain growth mechanism over recrystallization is not only dependent on the welding parameters but also on the distance to the heat source: regions of the HAZ further away for the heat source, i.e., that experience lower peak temperatures, will be dominated by recrystallization phenomena, while for those closer to the fusion boundary grain growth will be predominant.

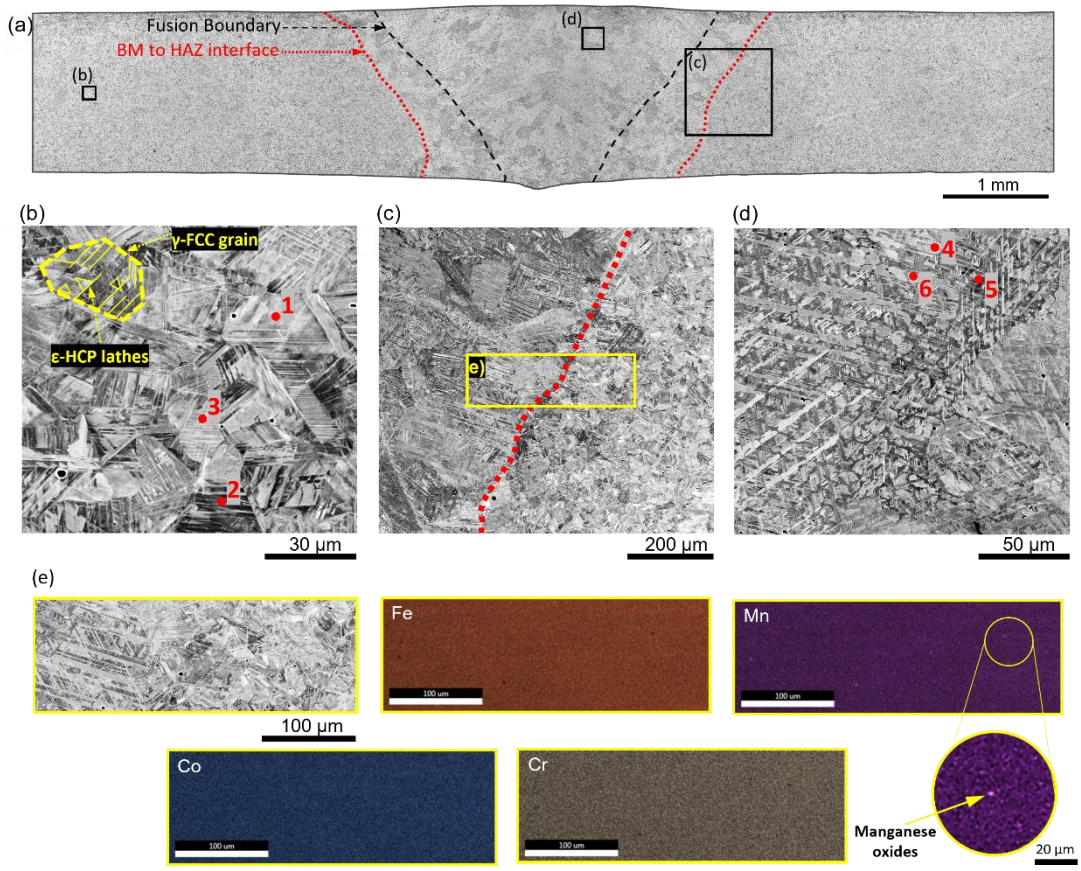


Figure 21 – Microstructure of the $Fe_{50}Mn_{30}Co_{10}Cr_{10}$ HEA welded joint: (a) Macrograph detailing the joint cross section, indicating the BM to HAZ interface and the fusion boundary; (b) BM, where a parent γ-FCC grain is highlighted with a yellow dashed line, while the ε-HCP laths are also shown; (c) BM to HAZ interface; (d) FZ; (e) EDS mapping of the BM to HAZ interface. The red dots in b) and d) detail locations where EDS point analysis was performed. The yellow box c) details the location for EDS mapping.

To assess and compare the potential existence of compositional changes between the BM and FZ, EDS point analysis was performed considering three points in each region. These results are summarized in Table 6, showing that the composition is practically constant along the analyzed points, although slightly different from the nominal composition of the present

DP-HEA: $Fe_{50}Mn_{30}Co_{10}Cr_{10}$. Overall, the EDS point measurements performed are close to the alloy nominal composition, with the minor changes observed being related to the casting of the alloy, as well as to the semi-quantitative nature of SEM/EDS measurements.

Table 6 – Compositional measurements, as obtained by point EDS, in the BM and the FZ.

s		Atomic percentage [%]			
Re-gion	Point	Fe	Mn	Co	Cr
BM	1	50.4	29.2	11.2	9.2
	2	51.4	28.2	11.1	9.3
	3	50.4	29.2	11.4	9.0
FZ	4	53.1	26.8	11.0	9.1
	5	45.9	33.5	11.5	9.2
	6	53.3	23.7	10.9	9.2

EDS mapping in a region comprising both the BM and HAZ was also performed, as shown Figure 21 (e). A homogenous composition distribution is observed. However, sparsely dispersed Mn-rich oxides are observed. These can be assigned to Mn oxides, as previously found in [99].

Delving into the FZ, refer to Figure 21 (a), it is possible to observe large and elongated grains with an average γ-FCC grain size of 124.2 ± 16.4 μm, aligned towards the weld center line. This occurs due to the overall tendency for grains to grow epitaxially from the pre-existing BM in the opposite direction of the heat flow during solidification of the melt pool. On closer analysis, dendrites and martensitic laths, the latter being formed as a stress relieving mechanism or through stacking faults to cope with the internal stresses developed upon cooling [98], can be observed within the grains, as shown in Figure 21 (d).

A large-scale EBSD map was performed to further evaluate changes in both grain size and orientation along the welded joint, as depicted in Figure 22 (a). The corresponding phase map is shown in Figure 22 (b). Considering the inverse pole figure (IPF) data of Figure 22 (a), is possible to observe the previously referred epitaxial growth at the HAZ/FZ interface (delimited by the black dashed lines), while toward the center of the FZ competitive grain growth is

predominant. Upon heat extraction from the melt pool to the colder HAZ and BM, grains start to grow in the opposite direction and those who have the preferred growth direction aligned with the maximum heat extraction direction, typically perpendicular to the HAZ/FZ boundary, will have their growth facilitated at the expense of poorly oriented and newly formed grains. While near the weld centerline grains are approximately equiaxed, despite being coarse, outside of this region the grains are predominantly columnar and grew perpendicularly to the HAZ/FZ boundary. This is also related to changes in the thermal and solidification conditions, namely thermal gradient, G, and growth rate, R, that are known to modify the grain morphology during material solidification.

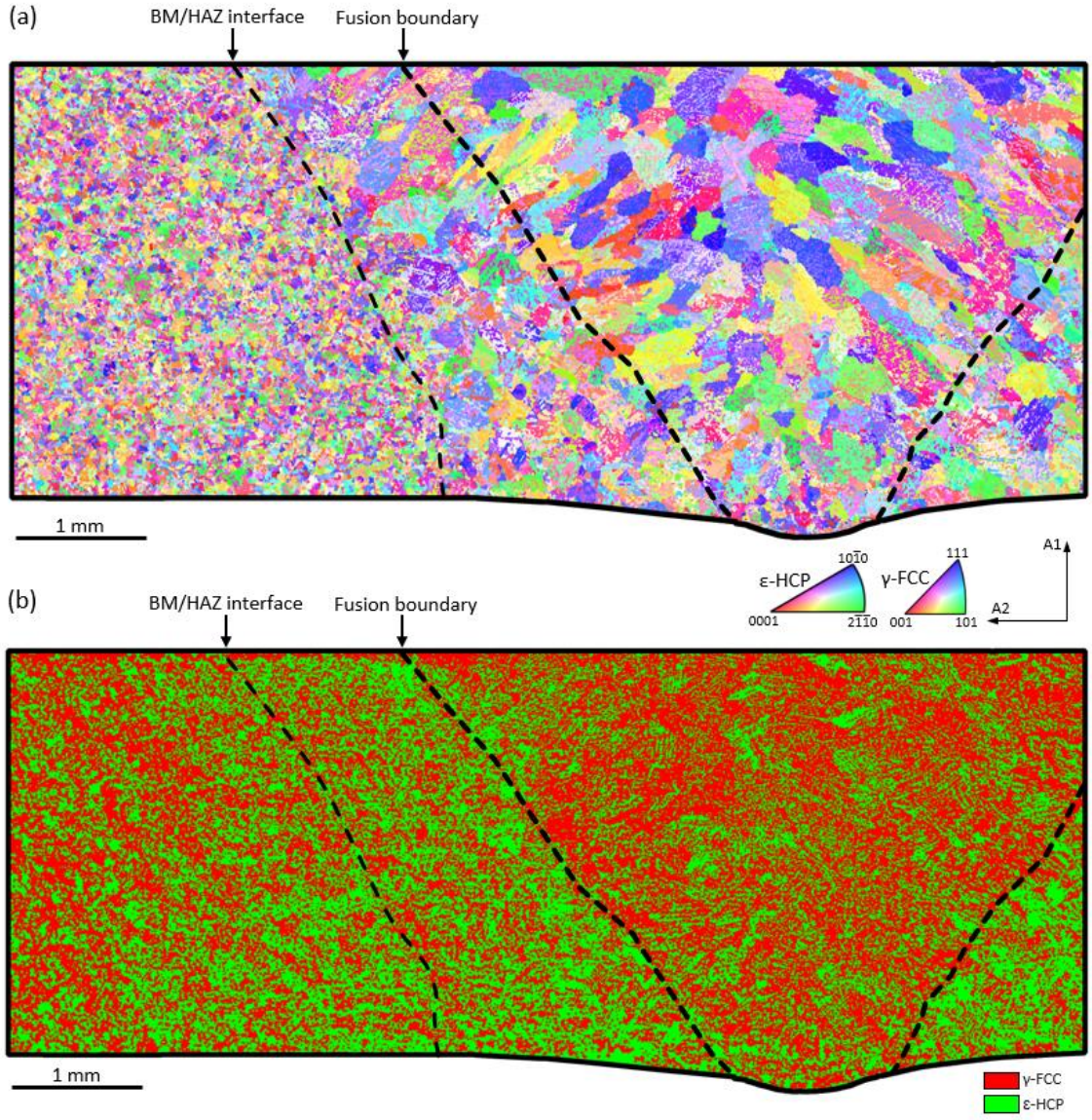


Figure 22 – Weld microstructure analysis: (a) IPF map and (b) Phase map.

In the EBSD phase map of Figure 22 (b) is observed that the microstructure along the joint is composed of both γ-FCC from the ε-HCP phases, in good agreement with that was previously observed by light optical microscopy. Comparing the BM and FZ regions reveals that in the latter the γ-FCC phase is predominant over the ε-HCP phase. In contrast, in the BM, the ratio of both phases' approaches unity. For comparison, the evolution of phase fractions obtained in each region (BM, HAZ and FZ), calculated using ImageJ, is detailed in Table 7 .

Table 7 – Phase fraction distribution along the weld microstructure, calculated using ImageJ on a representative location of each region.

Weld region		**BM**	**HAZ**	**FZ**
Phase fraction	γ-FCC	55.5 %	42.5 %	71.1 %
	ε-HCP	44.5 %	57.5 %	28.9 %

As it is possible to perceive, going from the BM to the HAZ, that the ε-HCP phase fraction increases by 13%, while transitioning from the HAZ to the FZ is clear that the γ-FCC phase fraction is superior to that measured in the other regions, reaching 71.1%. The phase distribution that characterizes this welded joint, depends on the different processing conditions that the BM (in the as-cast condition) and the FZ were subjected during welding, which eventually was responsible for generating the ε-HCP phase. In the HAZ, the higher phase fraction of ε-HCP can be explained by the initial condition of the BM, which already contains ε-HCP laths that act as nucleus for the continuous transformation of γ-FCC into ε-HCP. This transformation occurs as the temperature rapidly decreases due to the heat sink effect of the BM and of the shielding gas, which was directed towards the face and the root of the welded joint.

It is important to keep in mind that one main factor influencing the γ-FCC to ε-HCP martensitic transformation is the temperature reached by the material and its subsequent cooling rate, provided that the latter is directly dependent on the difference between peak temperature and the temperature at which formation occurs. Alongside with is, other factors, such as the accommodation of thermal stresses combined with the residual stresses left on the microstructure after cooling, are also important to consider since the indirectly supplied mechanical work lowers the driving force necessary for ε-HCP to form [91]. As such, the higher amount of ε-HCP on the HAZ is justified by different factors (i.e., peak temperature and

stresses occurring on the HAZ) acting to produce an ε-HCP-richer region at this location of the joint.

The significantly lower phase fraction of ε-HCP in the FZ can be explained by the fact that in this region the material endured total remelting, allowing for new grains to form. The formation of ε-HCP is related to the lattice defects induced during solidification [92]. While transitioning to a solid phase and losing thermal energy, the atoms present in liquid arrange themselves into an ordered arrangement. However, in this process, defects can arise in the crystal lattice, due to a variety of factors, such as variations in cooling rates or impurities, disrupting the regular stacking sequence of atomic planes and leading to the formation of stacking faults. Eventually, these stacking faults coalesce resulting in the formation of thin plates of ε-HCP, by the gliding of Shockley partials of the 1/6 <112> Burgers vector. As such, the presence of this thermally induced ε-HCP is often commonly found in this HEA, and occurs as a means of relaxation of the thermally induced stresses generated during solidification. It is only with the application of an external stress that these structures will act as nuclei for the mechanically induced ε-HCP, via the TRIP effect [36,94,100].

Beyond this, one relevant factor that must be assessed is the influence of the parent γ-FCC grain size in the lower fraction of ε-HCP observed on the FZ . Liu et al. [93] related the γ-FCC grain size with the nucleation of ε-HCP, stating that the larger γ-FCC grain size, the easier it is for the martensitic phase to form, given that ε-HCP tends to nucleate around grain boundaries and grow towards the center of the γ-FCC grains. They also concluded that with grain refinement the formation of ε-HCP can be hindered, which translates into a decrease of grain boundaries, that have previously been assigned as primary nucleating sites for the ε-HCP phase. This fact, indeed, is in line with the larger amount of ε-HCP observed in the HAZ, where the grain size is larger. Nevertheless, the same conclusion cannot be reached in the FZ, where the γ-FCC grain size is at its higher values. As it is noticeable that the ε-HCP phase fraction variation is directly dependent on the ε-HCP grain size present within each region. That is, the higher phase fraction of ε-HCP also corresponds to larger thickness of the ε-HCP laths in the HAZ region (approximately 11.9 ± 1.7 μm), especially when compared to the FZ (5.8 ± 1.6 μm) and the BM (5.1 ± 2.5 μm).

For understanding the lower phase fraction of ε-HCP on the FZ, one must consider the dynamics associated with the solidification process and heat transfer that occurs during the solidification of the molten pool in non-equilibrium processes as in welding. As previously noted, the FZ is comprised of large dendritic grains with a high directionality towards the top-most center of the weld, which occurred due to competitive grain growth. Such process occurs from the HAZ/FZ interface, where the molten pool begins to solidifying and new grains start developing towards the center of the FZ, where the material experiences the higher temperatures and is still at the liquid state. At the same time, stacking faults may develop within the already solidified γ-FCC lattice. Nevertheless, the localized high temperatures surrounding the grains, aided by the liquid material present at that stage during solidification, can ease the movement of atoms allowing them to correct themselves within the lattice, achieving a lower energy phase condition. Such can hinder the progressive accumulation and thickening of stacking faults required for thermally induced ε-HCP to nucleate, as the γ-FCC grains progressively grow.

For further analysis, high-resolution EBDS maps, detailed in Figure 23 , were performed to further characterize the microstructure of the BM and FZ. The difference in shape of the grains in the two regions becomes clearer now, with the BM possessing angular-shaped grains while in the FZ they possess a more elongated morphology, with these differences arising from the different conditions of their formation. Martensitic laths observed on both the IPF (Figure 23 (a) and (d)) and phase maps (Figure 23 (b) and (e)), detail that their thickness is larger in the BM, as it would be expected from the previously explained ε-HCP formation on the FZ.

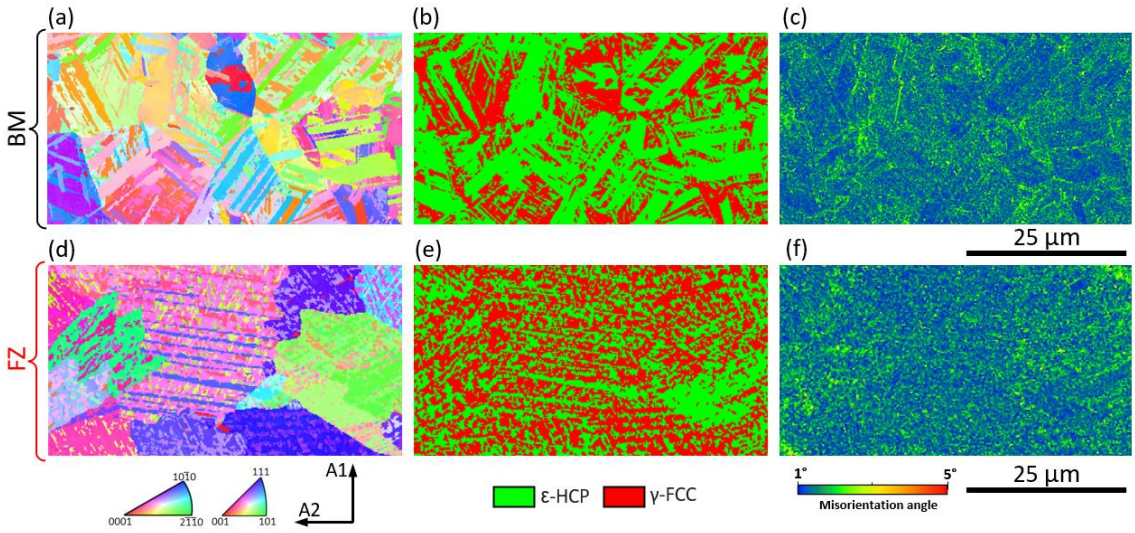


Figure 23 – High-resolution EBSD analysis of the BM and FZ. The IPF maps in (a) and (d), phase maps in (b) and (e), and KAM maps in (c) and (f) provide valuable insights into the crystallographic orientation, phase distribution, and deformation within the samples.

The Kernel Average Misorientation (KAM) maps detailed in Figure 4 (c) and (f), corresponding to the BM and FZ, respectively, can be used to obtain a qualitative evaluation on the existing residual strains before and after welding. During welding there is an non-uniform expansion and contraction along the welded joint which generates thermal strains within the different regions of the joint. Eventual distortions within the crystal lattice can be relieved by the formation of dislocations at the grain interfaces, which results on a type of subgrain boundary being formed, often referred to as geometrically necessary dislocations (GND) [26]. Considering the relationship between the misorientation angle and the GND density, it is possible to interpret the KAM data in the context of the distribution of residual strains within welds.

In both cases, it is possible to perceive that higher KAM values, which are associated with a higher GND density, occur at the γ-FCC/ε-HCP phase boundaries, reflecting the increased local tendency for accumulation of microstrain [101,102]. However, comparing both regions it is possible to perceive that the BM has a more homogenous distribution of the misorientation angle, with a tendency for it to increase at the geometrically shaped grain boundaries. Nevertheless, given the dendritic nature of the FZ aided by the fast solidification rate of the molten pool, a scattered misorientation level is present amongst the larger γ-FCC grains. This occurs especially given the smaller ε-HCP grain size and the consequent necessary

accommodation of the different lattice structures, resulting on a higher accumulation of strain at the subgrain level. Such can contribute to a higher level of residual strain in the FZ.

4.2.3.2 Synchrotron X-ray diffraction

Figure 24 displays representative SXRD patterns taken from both the BM and FZ where the two principal phases, γ-FCC and the ε-HCP, are identified. The presence of Mn oxides in the microstructure can also be observed with a very low phase fraction, as it can be noted by the extremely low intensity of the associated diffraction peaks.

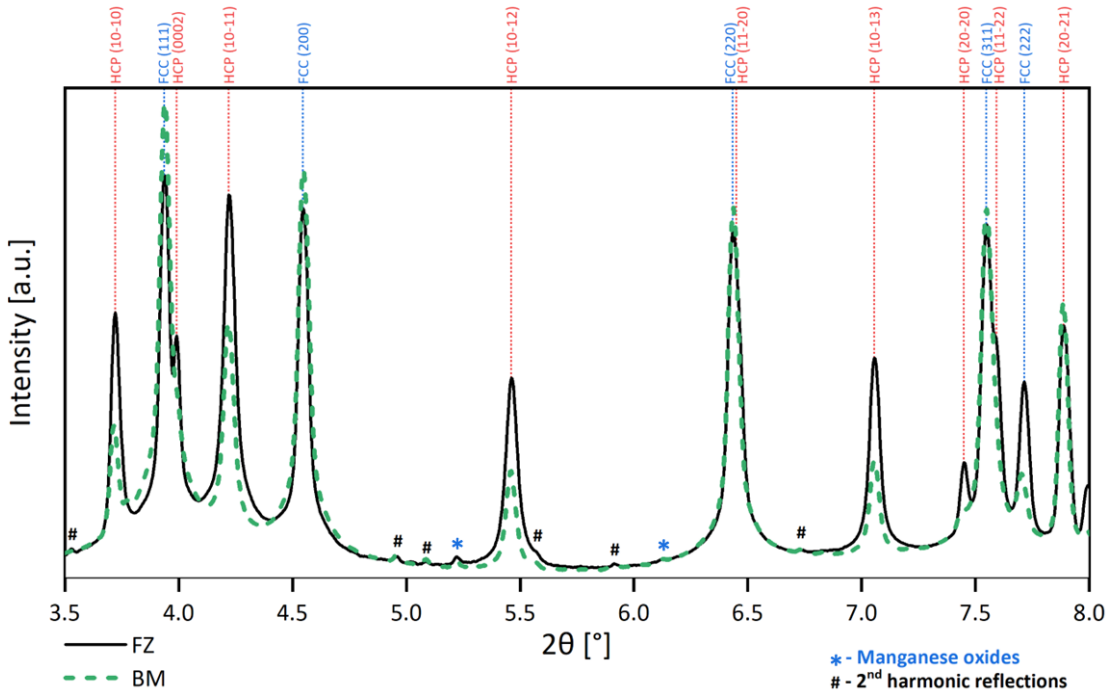


Figure 24 – Representative SXRD patterns from the BM and FZ. The diffraction peaks corresponding to the γ-FCC and the ε-HCP phases are identified on the top. Lower intensity reflections corresponding to manganese oxides (*****) and 2nd harmonic reflections (**#**), the latter resulting from the beamline setup, are also identified.

Although this representation of the existing phases in the BM and FZ can yield an insightful characterization of the sample, further analysis can be made by superimposing the diffraction patterns along the whole joint. Such can yield a good visualization of the differences that locally occur from one side of the BM to the other, due to the spatially varying weld thermal cycle. As such, synchrotron X-ray diffraction measurements were performed along the full extension of the welded joint. Figure 25 (a) details a colormap of the full azimuthal integrated Debye Scherrer rings, which takes into consideration all the data captured by the

2D detector from the analyzed spot. Here, is possible to obtain a qualitative observation on the variation of both peak intensity and width, where changes in the HAZ and FZ, compared to the original BM, can be related to thermal cycle conditions due to the intense heat generated by the electric arc during welding. Furthermore, the intensity and width variations are especially noted for the ε-HCP peaks (refer to Figure 25 (b)).

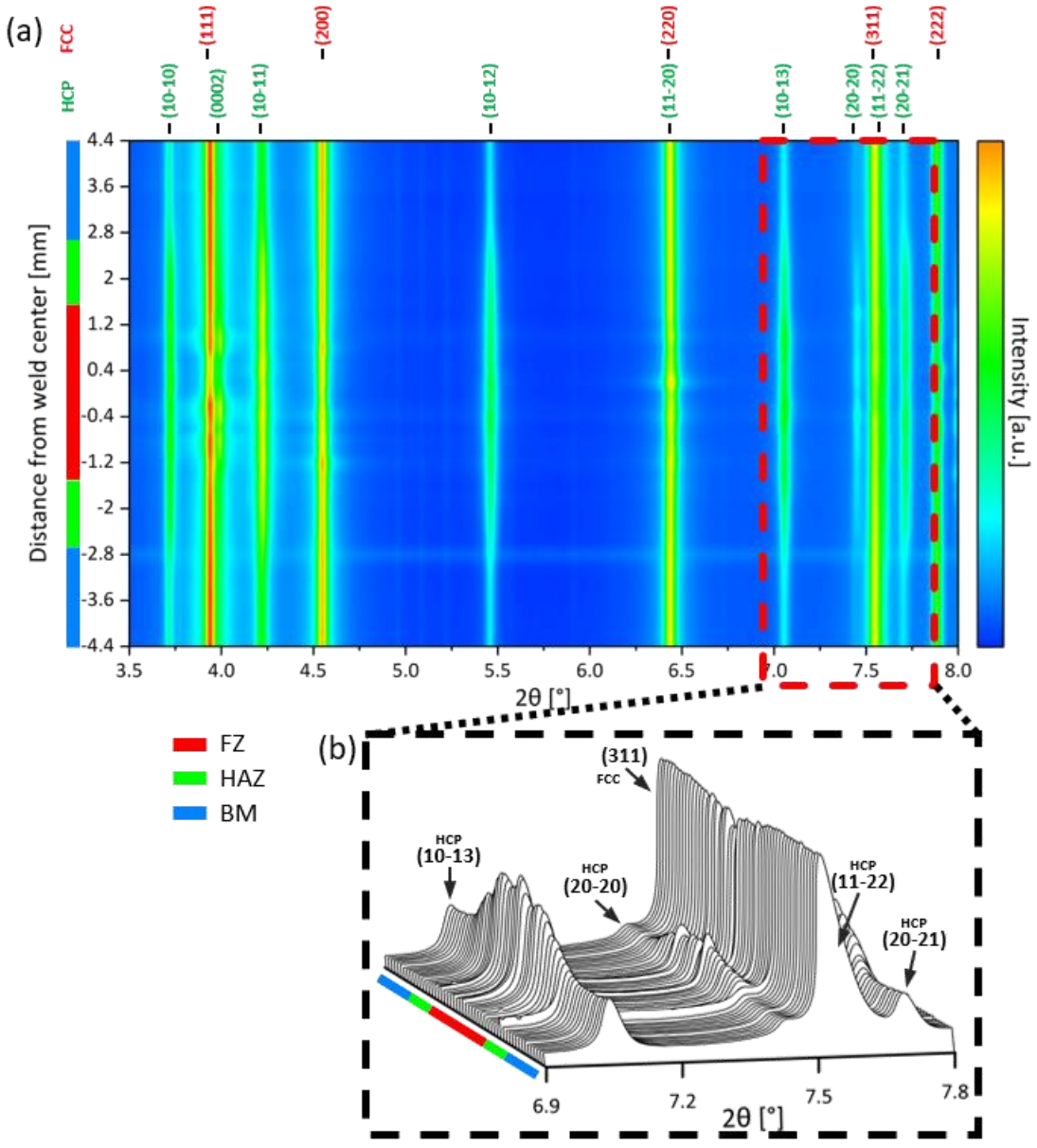


Figure 25 – SXRD mapping: (a) colormap exhibiting the variation of the diffraction peaks after full azimuthal integration; (b) 3D depiction highlighting the diffraction peaks within the 6.9-7.8 2θ range.

Equivalent to this, a 3D depiction of the γ-FCC (311) and ε-HCP (10-13) diffraction peaks can be observed in Figure 25 (b), allowing to obtain a better perspective on the peak shape evolution along the analyzed regions. The reason for the selection of these diffraction reflections is related to their insensitivity to intergranular strains [95]. To further understand the obtained synchrotron X-ray diffraction data, fitting of the γ-FCC (311) of and the ε-HCP (10-13) diffraction was performed to retrieve relevant peak parameters, namely the peak intensity and full width at half maximum (FWHM).

Starting with the peak intensity, this parameter can be related to the phase fraction of each phase, while also being strongly related to texture effects of the analyzed spots [103]. These results are presented in Figure 26 (a) and are discussed next.

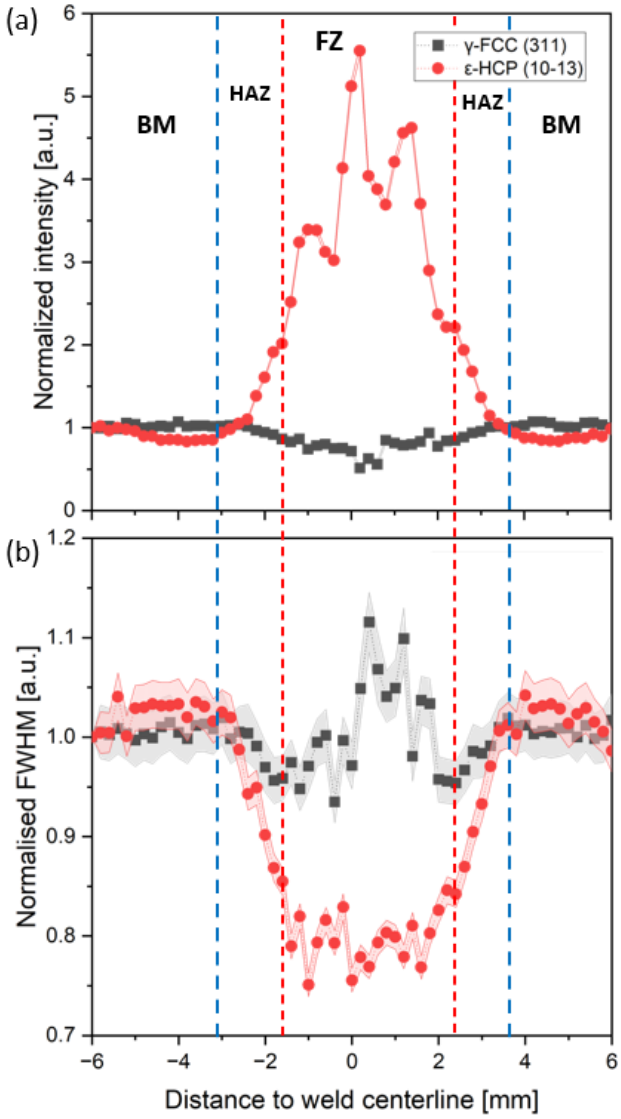


Figure 26 – Evolution of (a) peak intensity and (b) full width at half maximum along the welded joint.

However, it is important to note that these values correspond to the normalized intensity (I/I_0, where I_0 is the peak intensity of the corresponding peak in the BM), thus a quantitative analysis of phase fraction cannot be inferred from this graph. Nevertheless, as the matrix phase in this HEA, the peak intensity variation of the γ-FCC shows a steady variation, while only a slight decrease is visible when reaching its minimum at the weld centerline. However, for the ε-HCP phase, the three weld regions are clear. Here an increase in intensity of about 1.8 times that of the BM can be observed in the HAZ, while an even higher increase is visible in the FZ, reaching about 5 times the intensity of the BM at its maximum, which highlights the variation in phase fraction and grain morphology (texture) along the welded joint. Although this variation in peak intensity cannot directly translate the phase fraction of ε-HCP, the reason for this increase in intensity in the HAZ, in comparison to the BM, can be indeed due to the thickness increase of the already present ε-HCP laths. This affects the texture of the HAZ due to the larger ε-HCP grain size, which results in a lesser number of grains diffracting the X-ray beam, although the present of larger grain size means that the diffracted intensity coming from a single grain will be significantly higher. Such factors influence the statistics of the representative ε-HCP phase diffraction peaks and consequently their intensity, resulting, in the present case, in an increase in peak intensity. However, the massive increase of intensity in the FZ cannot be explained by only that, since the amount of ε-HCP is lower in this region, as observed by electron microscopy. Thus, to understand this feature one must consider the local material texture that arises from the highly directional temperature flow during welding. Nevertheless, as this analysis only encompasses the full azimuthal integration of the Debye-Scherrer rings, another way to infer on this phenomenon is to evaluate the peak intensity vs FWHM plot (see Figure 26), where in the FZ is possible to observe that the ε-HCP diffraction peaks are sharper (higher intensity) with less width (lower FWHM). Such can be translated into the fact that, although the newly formed ε-HCP grains have a lower grain size, these grains are highly oriented resulting in higher peak intensities in this region.

On a different note, the FWHM evolution translates the combined influence of microstrain, coming from structural defects, with the size of the smaller domains within a grain (crystallites) that can coherently diffract the incoming X-rays [103]. Such results are displayed in Figure 26 (b).

Concerning the γ-FCC phase, different trends can be observed throughout the welded joint, allowing to easily separate the three typical regions of a fusion weld (BM, HAZ and FZ). Going from the approximately constant behavior in the BM, the FWHM exhibits a slight increase followed by a sudden decrease marking the position of the HAZ. This decrease is then followed by an accentuated increase, where the FZ can be identified. A mirrored behavior can be observed detailing a symmetry axis along the weld centerline, as expected since autogenous welding was performed in this work. On the other hand, the ε-HCP phase exhibits a different trend. In this case, beyond the nearly constant FWHM on the BM and decrease when reaching the HAZ, the FZ exhibits a fluctuation at the lower level of values. With complementary knowledge coming from the previous optical and electron microscopy microstructural analysis, it is possible to correlate grain features with the synchrotron data, especially concerning the HAZ. As mentioned, this region experienced the effect of recrystallization and grain growth phenomena which is clear on the FWHM evolution throughout the weld. That is, as it is possible observe via optical microscopy (refer to Figure 21) the extension of the HAZ is roughly 1mm. However, in the case of the FWHM the extension of the HAZ reaches approximately, 1.5 mm in each side of the FZ, highlighting the recrystallization phenomena that occurred during the welding process, beyond the visible effect of the grain growth on the microstructure.

Setting the BM as the standard for comparison, where a steady behavior can be observed for both phases, the decrease in FWHM occurring in both phases can come from the residual stress relaxation conditions arising from the high temperatures experienced during welding associated to the relatively low cooling in the HAZ. Here, the higher amount of the martensitic phase ε-HCP, which can be a direct result of the cooling rate, can result on a region with a lesser amount of structural defects by allowing the atoms to readjust on the lattice. Additionally, recovery mechanisms may also take place during the permanence time a high temperature, in which case the relieving the microstrain developed upon welding is attained. These factors result in a region where the FWHM decreases on both phases.

On the FZ, the fraction of γ-FCC and its grain size is visibly higher when compared to the BM (refer to Figure 23). While the probability for more structural defects to occur in the γ-FCC phase is increased in the FZ, due to the massive development of large dendritic grains

in a short time period, the effect of grain size in the FWHM is also worthy of discussion. As such, the dynamic thermal gradient (G) that takes place in welding is relatable to the growth rate (R) in terms of the microstructure that develops upon solidification of the molten pool. The combined action of both G and R, under the previously discussed GTAW welding conditions, results on a microstructure comprising grains that tend to develop rapidly during solidification. Therefore, small differences between the atomic arrangements of the atoms are to be expected amongst the dendrites and the solidifying interdendritic space. Such can result and on small crystallographic deviations between grains of the same crystal structure, which in turn may result in minor differences on the diffracted peak positions. These small-scaled differences, when added together by the coherent diffraction volume of the incoming X-ray beam, can influence the peak shape in a manner that the smaller they are, the larger the value of the FWHM associated to a certain peak. As such the impact of (smaller) sub-grain structure size translates into the higher FWHM of the γ-FCC phase in the FZ, as the refined grains (as part of the solidification substructure) that develop within the γ-FCC grains during the fast cooling of the weld are different, in size, from the grains that develop during the slower cooling of the BM upon casting. Likewise, the same does not occur for the ε-HCP phase, which exhibits only a decrease on it FWHM with a large fluctuation of values in the FZ. In summary, the different FWHM values exhibited throughout the weld regions depend simultaneously on competition between microstrain and grain size developed, with for the latter the sub-grain structure size being of primary importance.

Furthermore, beyond the different grain sizes visible throughout the microstructure in Figure 21, it is possible to quantify the microstrain within the microstructure, via the Williamson-Hall method. This method allows us to separate the influence of the microstrain and the size of the sub-grain structures on the FWHM. Therefore, after removing the instrumental apparatus influence on the FWHM, it is possible to separate the contribution of both factors on this parameter and finally provide a quantification of the microstrain distribution on the sample. The procedure for this calculation is detailed in [104] and the results are exhibited in Figure 27.

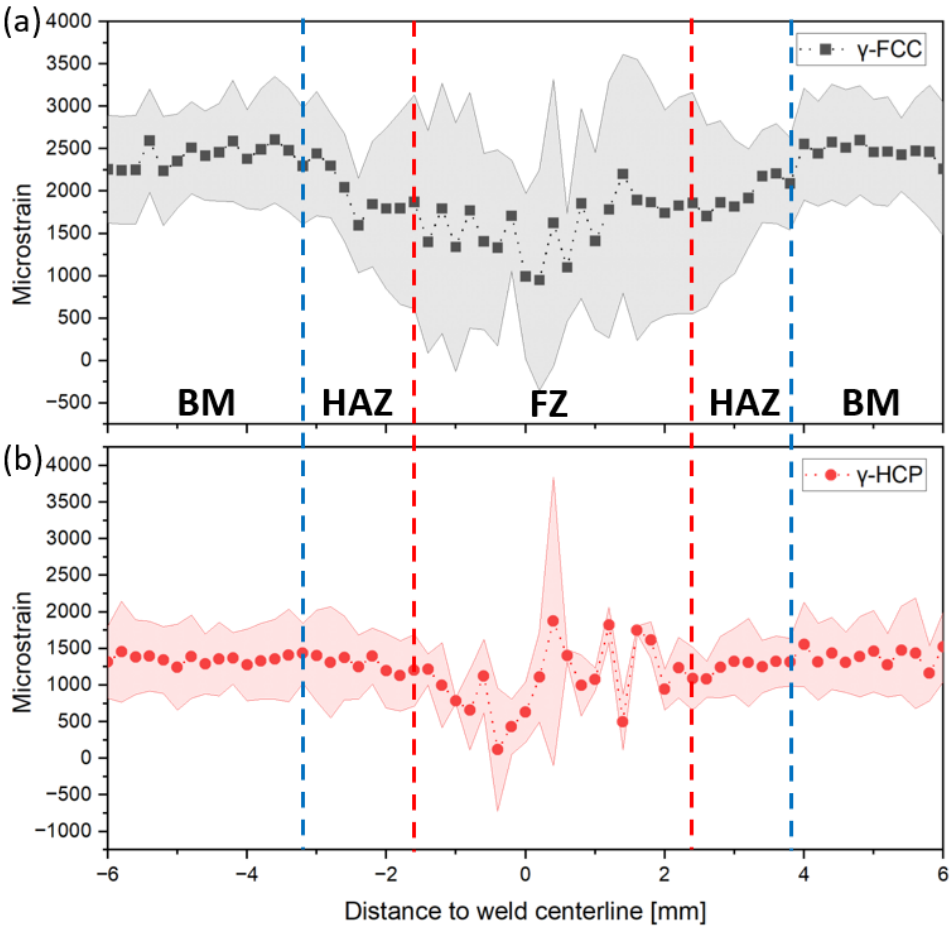


Figure 27 – Distribution of microstrain on the (a) γ-FCC and the (b) ε-HCP phases along the full extension of the weld

As an averaged contribution of the peaks on the diffraction patterns, it is again possible to observe the distribution of microstrain along the full extension of the weld. In both cases the BM exhibits the steadiest behavior, while the remaining regions of the weld showcasing a more scattered distribution of values. Considering the γ-FCC phase, the microstrain exhibited by the BM is characterized by a value of 2457 ± 577 με, reducing in value in the HAZ and reaching its minimum in the FZ, corresponding to 949 ± 741 με. In the ε-HCP phase, however, the BM exhibits a microstrain of 1341 ± 457 με, which also reduces when reaching the HAZ. The microstrain distribution in the FZ behaves differently from the γ-FCC, reaching a maximum of 1872 ± 1966 με and a minimum of 118 ± 841 με. Such distribution is with good agreement previous EBSD microstructural analysis.

However, full azimuthal integration of the Debbye-Scherrer rings is not sufficient to fully evaluate the microstructure evolution of the different regions of a welded joint, as the

orientation-dependent microstructure changes are averaged [7]. To overcome this, partial integration of the Debbye-Scherrer rings enables the identification of such orientation-dependent changes. Figure 28 details the evolution of the diffraction patterns on the 6.9 to 7.8 º 2θ range, after using a 1-degree integration step along the azimuthal angle. The analyzed 2θ range is the same as that shown in Figure 28 (b), allowing to observe the evolution of both the γ-FCC (311) and the ε-HCP (10-13) diffraction peaks in the BM, HAZ and FZ. Furthermore, quantification of the peak center with respect to the azimuthal angle of the (311) and (10-13) planes is also presented to showcase the different microstructural features occurring in the γ-FCC and the ε-HCP grains, respectively.

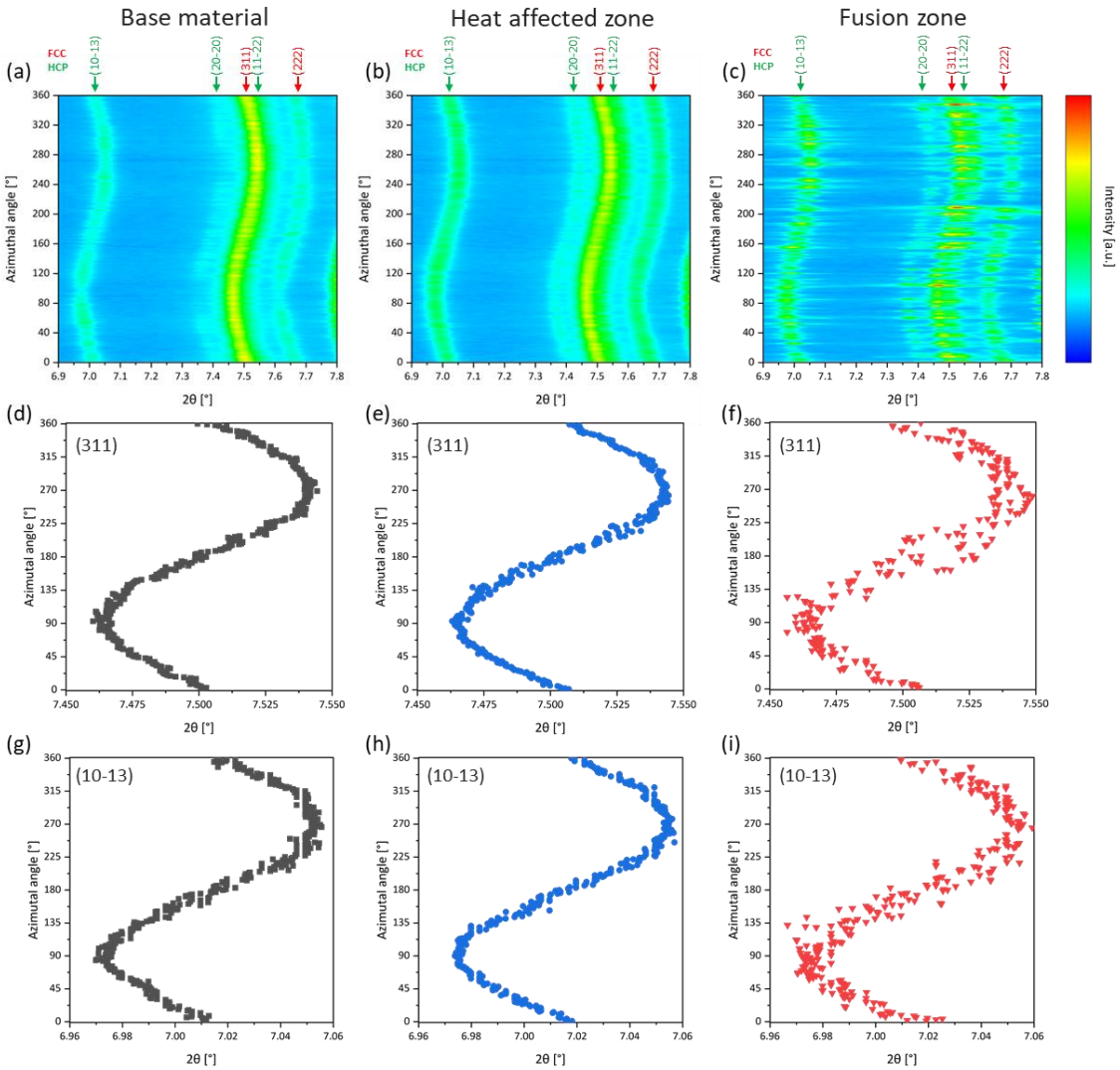


Figure 28 – Evolution of 2θ angle obtained by integrating in 1-degree segments along the azimuthal angle on representative zones of the: (a) BM, (b) HAZ and (c) FZ. On each region, peak fitting was performed on: the (311) peak of the γ-FCC (d), e) and f)) and on the (10-13) peak of the ε-HCP phase (g), h) and i)).

In these azimuthal angle vs diffraction angle plots is possible to see how the peak position changes along the azimuthal angle. In a non-textured and stress-free condition, the peak position would be kept constant all along the azimuthal angle (as it occurs with LaB_6 calibration powder, for example). However, this does not occur in any of the regions of the joint (BM, HAZ and FZ), being an indication of the existence of both texture and stresses across the material. From a texture perspective, it can be observed an overall trend in all cases for the peaks to deviate to lower 2θ values from the averaged value when near the azimuthal angles of 90 and 270°, which is the direction perpendicular to the fusion boundary, where preferential growth occurs during solidification of the molten pool. The opposite behavior, i.e., a shift of the peak position to higher 2θ values, corresponding to a decrease in the interplanar spacing, occurs for the 0 and 180° angles. It should be mentioned that a positive shift in 2θ, corresponds to a decrease in the interplanar spacing and suggests the development of a negative microstrain for the 0 and 180° azimuthal angles. The opposite occurs for the 90 and 270° azimuthal angles. Although, qualitatively, the FZ presents the same behavior as that of the BM and HAZ (refer to Figure 28), the colormap pattern corresponding to this region (refer to Figure 28 c)) evidences a high variation on the diffraction peaks, resulting in areas on the Debbye-Scherrer rings where no peaks are observable. This evidence the effect of large grain size combined with the preferential texture developed on the microstructure upon solidification of the molten pool. Alongside with this, the peak center distribution in Figure 28 (f) and (i) do not follow a steady alignment as in the BM or the HAZ, as expected from the microstructure of the FZ, which can be an indication of non-uniform strain distributions, owing to the non-equilibrium cooling conditions experienced by this region of the joint. However, the peak center variation still showcases the same positive and negative variations in 2θ along the azimuthal angle, translating in microstrain differences, which are azimuthal-dependent.

For reference, here the microstrain, ε, which is calculated from a representative peak of each phase, is defined by Equation 5.

Where d is the interplanar space of the analyzed diffraction plant and d_0, corresponds to the interplanar space in a stress-free condition. Although d_0 is not defined in this case, as its determination is difficult [105] and outside the scope of this work, it is reasonable to assume that d_0 takes the average value in between the minimum and maximum shift for each peak.

For the (311) γ-FCC phase, the higher variation on 2θ was obtained in the FZ, with a variation of 0.092° (corresponding to a microstrain of ≈6400 με), while the lower variation was exhibited by the HAZ with 0.081° (microstrain of ≈5500 με). For the ε-HCP (1013) peak, a similar behavior can be observed where the FZ (with a variation of 0.096° and microstrain of ≈6800 με) attains the higher difference and the HAZ has the lower amount, with a variation of 0.083° (microstrain of ≈6100 με). Such values allow to conclude that concerning the 2θ variation (and consequently the microstrain), the HAZ has the most stable behavior when compared to the other regions of the weld. Such can be related to the higher amount of ε-HCP phase in this region, whose formation contributes to the reduction of internal strains developed by cooling and concurrent solidification of the adjacent molten pool.

Such agrees with the data obtained with the KAM maps.

4.2.3.3 Thermodynamic simulations

Beyond the performed microstructure analysis, understanding the solidification path occurring in terms of the decreasing temperature on the FZ can provide significant knowledge within a simulation/predictive basis. Such can be obtained through CalPhaD (Calculation of Phase Diagrams) calculations that can offer a consistent description of the microstructure to be expected when the liquid material finally reaches the solid state under non-equilibrium conditions. As such, to predict such solidification path, one can use the Scheil-Gulliver methodology [106,107] instead of standard equilibrium phase diagrams. This method can be used for predicting the solidification behavior in non-equilibrium conditions by distinguishing the composition of the newly formed dendrites from that of the interdendritic fluid that surrounds them.

Figure 29 details the solidification path using the Scheil-Gulliver calculations following the CALPHAD-based methodology. Contrary to what would have been expected from the joint microstructure, the results indicate that only the disordered γ-FCC and σ phases are expected to be formed during solidification. Nevertheless, three stages are visible on the solidification path. Upon descending from the liquidus temperature, the first stage comprises a liquid to σ phase transformation. When reaching ≈1353°C, γ-FCC starts to form characterizing the beginning of the second stage of the solidification path, where the solidification curve starts to deviate from that associated with the equilibrium curve (dashed line in Figure 29). The third

stage, however, occurs at ≈1257°C, where σ phase is no longer thermodynamically stable, finally resulting on a microstructure composed only by γ-FCC. The formation of σ however, is debatable since the development of this phase in the microstructure usually occurs after long time exposure at high temperatures [108]. Moreover, no evidence of such phase was observed in the high energy synchrotron data of the present work, which may suggest that the undercooling experienced by the melt pool does not enable the formation of σ phase but rather of a metastable γ-FCC as the primary solidification phase.

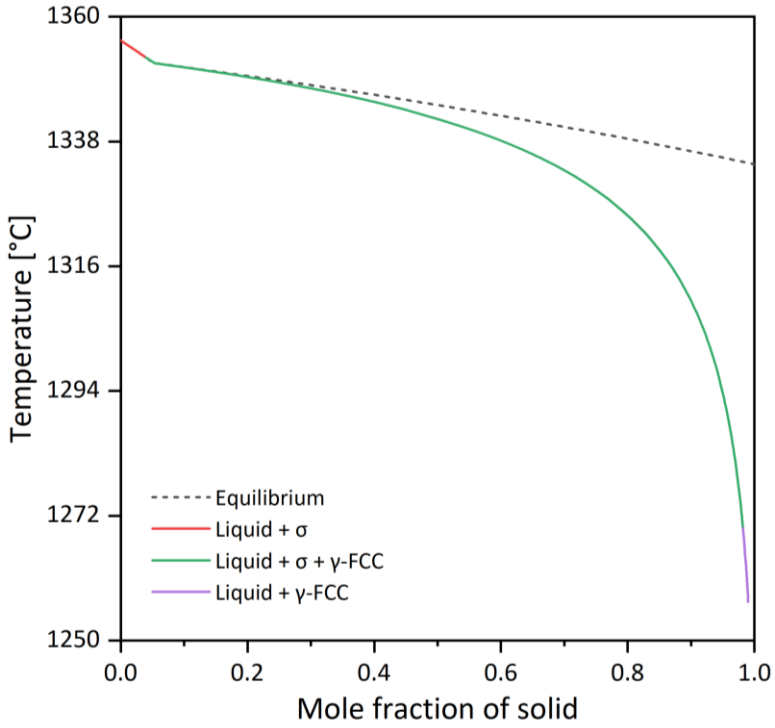


Figure 29 - Scheil calculations performed considering the nominal composition of the HEA base material.

Contrary with what would be expected considering the Scheil-Gulliver calculations, the presence of ε-HCP in the weld joint requires that this thermodynamical analysis must account for other conditions, such as chemical and non-chemical factors that can alter the Gibbs free energy of formation of ε-HCP, rendering it more thermodynamical stable than the γ-FCC. Considering chemical factors, the previously detailed above EDS analysis (refer to Figure 21) detailed that solute redistribution among the dendrites and the interdendritic fluid in the FZ occurred in a somewhat uniform way. However, the HAZ which did not endure any chemical changes capable of altering its microstructure, as demonstrated in the phase map displayed in Figure 22 (b) exhibiting a higher amount of ε-HCP, and the same can be said concerning the

BM. Therefore, to understand the solidification and possible solute segregation from the newly formed dendrites to the interdendritic fluid, the partition coefficients of the γ-FCC phase regarding the composition of the liquid, are displayed in Figure 30. The partition coefficient, k, allows to infer on the variation in composition of the liquid throughout the solidification enabling to understand which elements tend to segregate to the interdendritic fluid and which remain stable within the dendrites. Here it is possible to understand that when the solidification starts Mn, Co and Cr elements all have a $k < 1$, meaning that these elements are prone to be stable in the dendritic core. The same, however, does not occur for Fe, which remains well above 1 during solidification. Such indicates that Fe is being segregated into the interdendritic fluid, not contributing as much as the other elements for dendritic formation.

At the last stages of solidification, it is also noticeable that for Cr k rises above 1, being segregated alongside with Fe. Overall, an increasing trend can be observed in all elements, except for the Co curve, which indicates that the amount this element is less available for the further formation of the γ-FCC matrix phase.

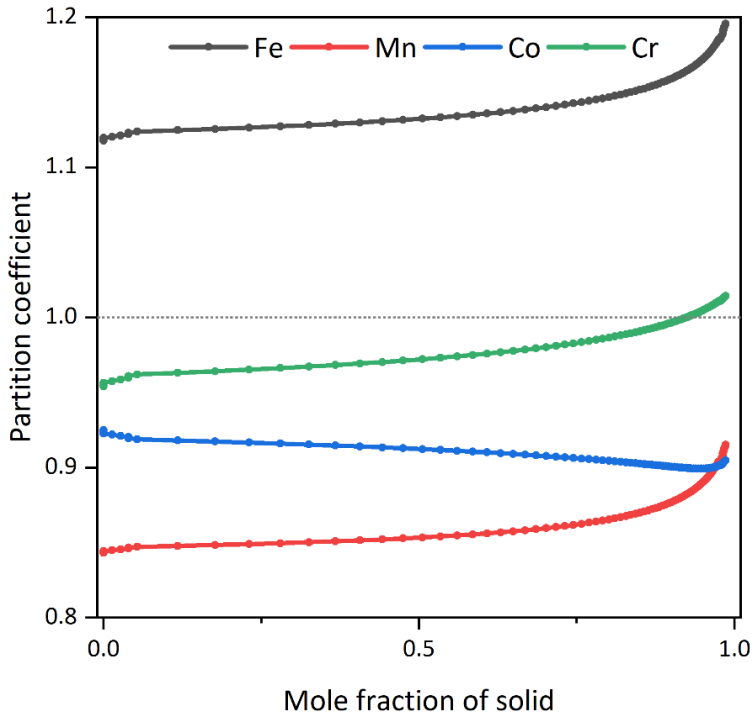


Figure 30 - Partition coefficients of the matrix γ-FCC phase during solidification, calculated from the data obtained from the calculations obtained with the Scheil-Gulliver method.

Nevertheless, non-chemical factors also play a key role in the formation of ε-HCP. Beyond the mechanism of formation thermally induced ε-HCP through stacking faults, where phase transformation can occur to relax stresses induced by thermal strains. Such internal strains are associated to the thermal cycle characteristic of fusion welding that can be left in the weld by the conjoined influence of the peak temperature experienced in the HAZ, combined with the cooling rate, which tends to be high in arc-based welding. Furthermore, another topic that should be accessed it the variation in Gibbs free energy between the ε-HCP and the γ-FCC phases. For this analysis in Figure 31 displays the Gibbs free energy (G) curves of the γ-FCC and ε-HCP phases, on the 300°C to 1100°C temperature range. Here, the G(ε-HCP) curve corresponding to the metastable phase is higher than the G(γ-FCC) which corresponds to the matrix stable phase exhibited by the DP-HEA, such is compliant with the results exhibited in Figure 29. Nevertheless, the probability for the stabilization of the ε-HCP phase in the microstructure can be qualitatively accessed by subtracting the G(γ-FCC) to the G(ε-HCP) curves. The result is displayed in Figure 31 (b). As it is possible to observe the d´ifference the G(ε-HCP) and the G(γ-FCC) decreases as the temperature drops, making it easier for ε-HCP form in the weld microstructure. That is, although the γ-FCC is more prone to occur, comparing the order of magnitude of the G(γ-FCC) curve with the descendent tendency that the G(ε-HCP) - G(γ-FCC) curves show, it is possible to infer that the probability for ε-HCP to form amidst the γ-FCC matrix is relatively high. Nevertheless, it is important to keep in mind that the martensitic transformation, having a thermal or mechanical nature, still requires an additional driving force to overcome the energy barrier that tends to decrease with decreasing temperature for the ε-HCP to develop within the weld microstructure.

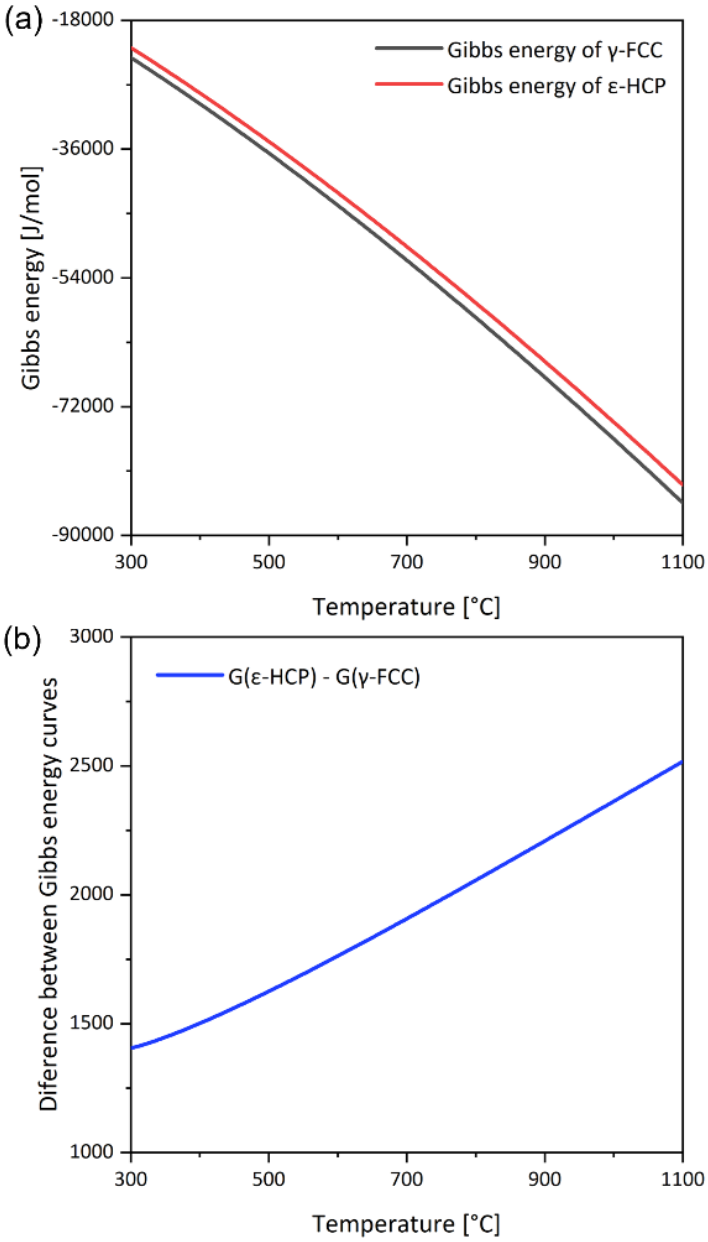


Figure 31 - Analysis of (a) Gibbs energy of the γ-FCC, ε-HCP and Liquid phases and (b) difference between the Gibbs energy curves of the ε-HCP and Liquid phases and the matrix γ-FCC phase.

4.2.3.4 Mechanical performance of the welded joints

From an application standpoint, analyzing the joint's mechanical behavior is of importance since it can provide a reliable way to evaluate the suitability of the material as a structural component.

Figure 32 (a) details the microhardness mapping performed on the welded joint comprising all regions of the weld. Here, it is possible to observe that the BM exhibited the lowest

values of microhardness, around 174 $HV_{0.5}$, while a constant increase culminating in the middle region (FZ) of the analyzed cross section, with approximately 239 $HV_{0.5}$, can be observed. As such, other than what should have been expected from the larger grains of the softer γ-FCC phase, the higher hardness values were obtained in this region, which contradicts what should have been expected according to the phases that comprise this DP-HEA. One factor that can be accounted for such to occur is the subsequent martensitic transformation that occurs upon plastic deformation (imposed by the indenter during hardness measurement), given the TRIP effect characteristic of this HEA, which may render some inaccuracy on this type of measurements.

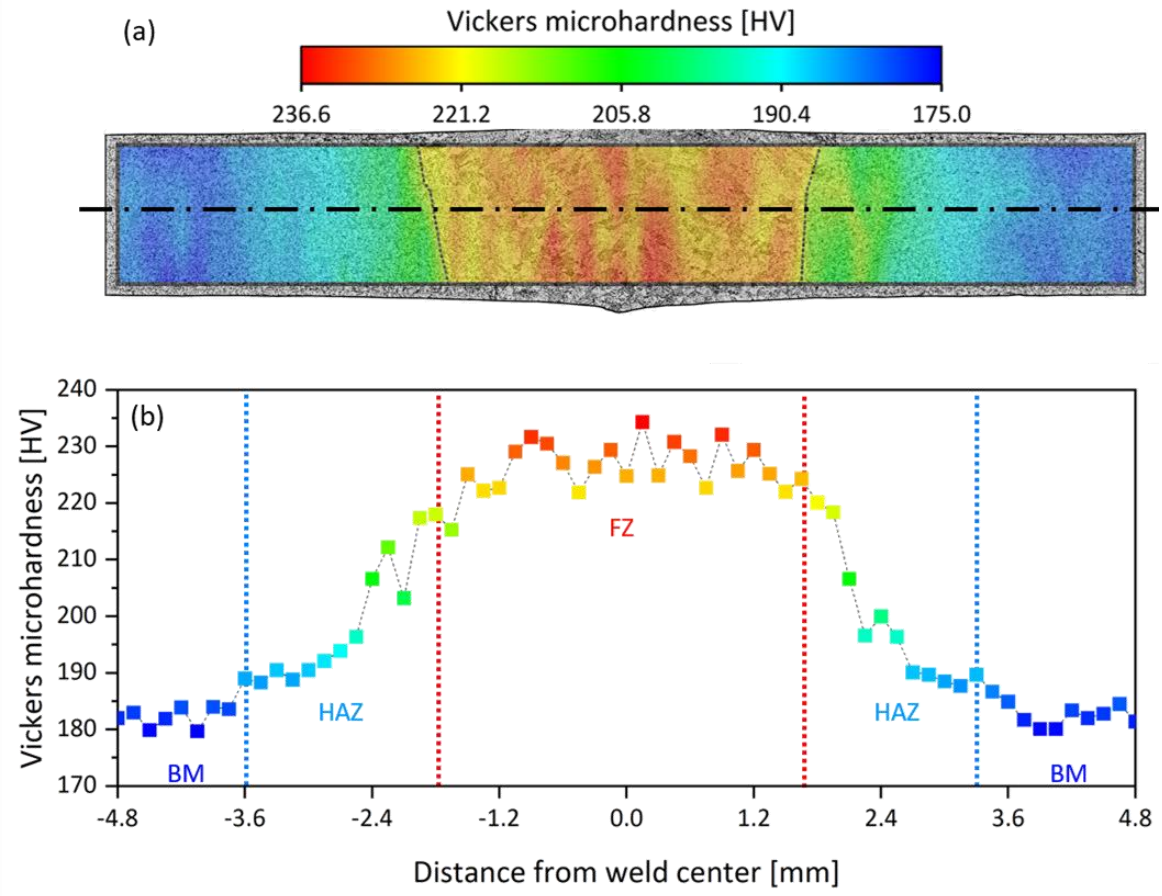


Figure 32 – Microhardness evaluation of the welded joint: a) mapping of the variation of hardness along the full extension of the weld superimposed with optical microscopical results and b) representative hardness evolution taken from the middle line of the map.

Nonetheless, provided that the composition remains approximately constant throughout the weld, this variation on the microhardness can also be explained in terms of grain size, as well

as existing phases and their volumetric fractions. Additionally, as both phases are widely present in all regions of the weld, one possible reason for the results displayed in the microhardness map is especially dependent on the grain morphology of the harder ε-HCP phase and its conjugation with the softer γ-FCC phase. However, the BM possesses the lower values of hardness across the joint, although this region of the material has a smaller γ-FCC grain size. Here, several factors, such as grain morphology and phase fraction, may yield different effects on the mechanical behavior of the material. According to the Hall-Petch equation, smaller grain size translates into increased strength. Nevertheless, as the grain increases in both the HAZ and FZ, and the hardness of these locations is higher than in the BM, one possibility is that the volume phase fraction of ε-HCP compared to γ-FCC plays a significant role on the hardness measurements. Such implies that the increased volume fraction of ε-HCP phase contributes in a more substantial way to increase the hardness at both the HAZ and FZ.

Conversely, opposite results are observed in the FZ, where the phase fraction of the ε-HCP is lower and so is it size. Here, the strengthening effect induced by the reduced grain size of the ε-HCP phase is significantly higher than that of the γ-FCC, thus although there is a decrease in the volume fraction of the ε-HCP phase, its lower grain size significantly aids in increasing the material hardness at the FZ.

Consequently, as readily observable in Figure 32 (b), which correspond to the measurements taken at half the thickness of the joint, the microhardness in the BM is stable starting to increase when entering the HAZ, which has a slightly larger ε-HCP phase fraction in its microstructure. In addition, the larger hardness values appear in the FZ where the ε-HCP exhibits its smaller grain size.

Figure 33 displays representative tensile data of the welded, benchmarking against the BM. Overall, the welds fractured at a final strain of 17.6 ± 1.7%, achieving a maximum tensile stress of 717 ± 36 MPa. In comparison, the BM had a tensile strength of 749 ± 32 MPa and fracture strain of 30.5 ± 7.7 %, all engineering values. Therefore, the welded samples reached 96 % of BM strength, while preserving nearly 58 % of its ductility. The reduced ductility of the welded joints can be ascribed to the microstructural variations present in the weld. As previously discussed, the microstructure (spatially varying grain size and volume fraction variations), as well as the residual stress conditions of the weld have a major influence on the

individual behavior of each analyzed region resulting, in total, on different mechanical response between the weld and the BM.

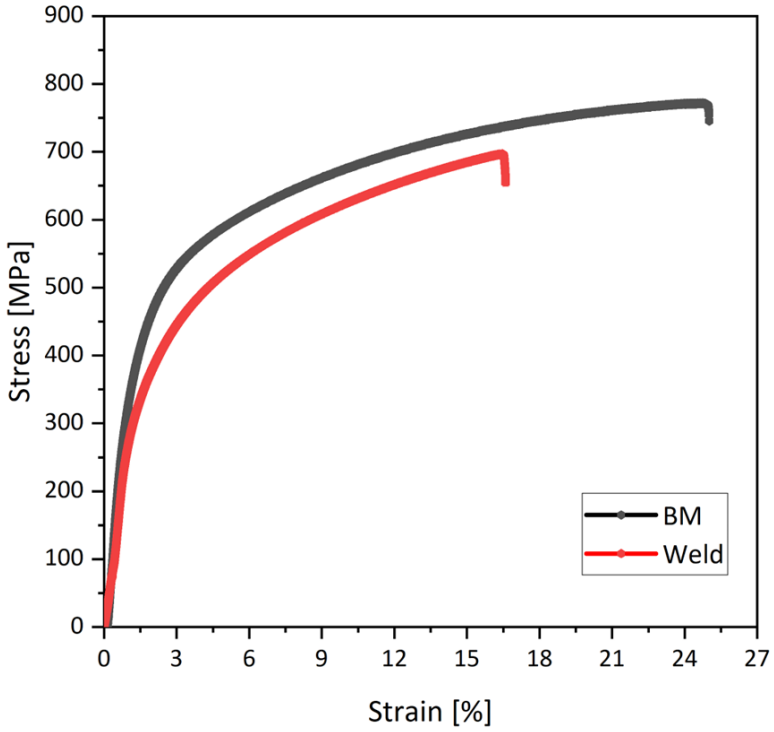


Figure 33 - Tensile test behavior comparison between the BM and the welded joints.

To extrapolate how different is the tensile behavior of each region of the weld during macroscopic tensile solicitation, DIC was performed, and these results are displayed in Figure 34. As can be observed, the BM and the FZ exhibited the lowest elongation of 16.4% and 14.4%, respectively, before fracture occurring in the HAZ. The maximum elongation, however, was observed in the HAZ, reaching 29.0%.

The reason for this behavior can be expected by the combined effect of microstructural differences and the microhardness variation exhibited throughout the weld. While the FZ is the region with the largest grain size, it is also the region that exhibits a higher hardness. Such can be related to the higher amount of γ-FCC, which transforms into ε-HCP via the TRIP with plastic deformation, alongside the ε-HCP smaller grain size, granting it a stiffer behavior than the other regions. On the other hand, the BM exhibits a similar behavior to the FZ, although with showcasing a higher ductility, which was expected from the microhardness measurements combined with the effect granted by the small and equiaxial grain size with multiple

ε-HCP nuclei within, ready to develop into larger ε-HCP lathes. Furthermore, the behavior exhibited by the HAZ can be due to the combined effect of larger grain size that this region exhibits when compared to the BM, and the relatively lower hardness when compared to the FZ, although exhibiting a higher fraction of the martensitic ε-HCP phase. Furthermore, we would like to point out that the γ-FCC to ε-HCP transformation rate in each region, should be a topic of interest to discuss for further analysis in subsequent works.

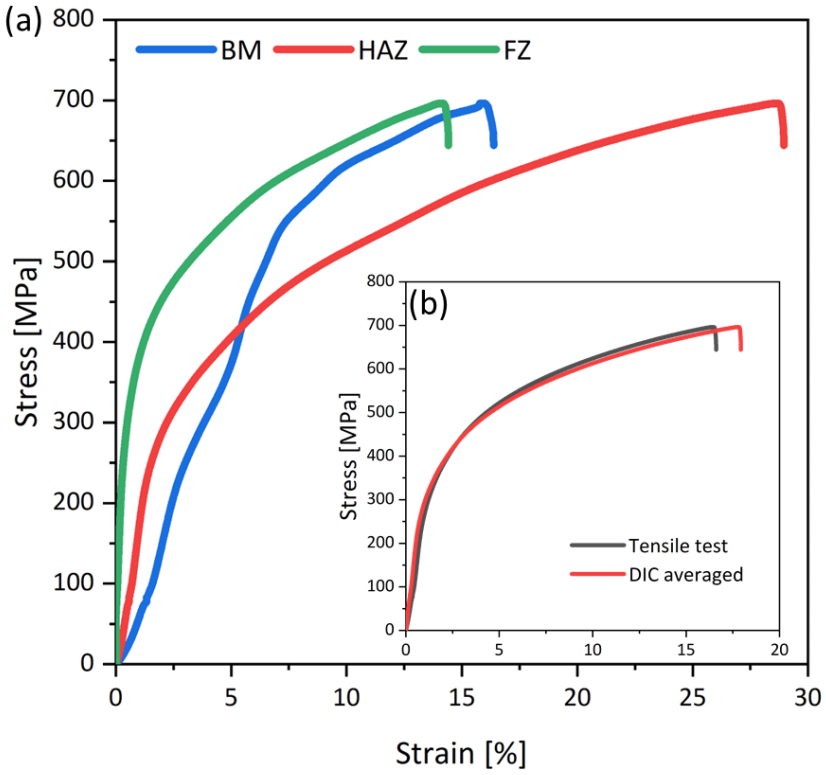


Figure 34 - Stress-strain behavior of: (a) representative points located in the BM, HAZ and FZ obtained with DIC during tensile testing of the welded joints and (b) welded joint and the DIC average response.

Analysis of the joint's fracture surface in detailed Figure 35, where evidence of a ductile-like fracture can be observed, as validated by the large and homogeneously distributed dimples. The presence of small particles can also be observed in the close-up view of Figure 35 (b). These particles were previously reported by A.M. Hossain et al. [109] on the fracture surface of tensile samples as containing high content of Mn. These correspond to the Mn-rich particles scattered within the microstructure pointed out in Figure 21 (e) and were identified via synchrotron x-ray diffraction as Mn-based oxides in the present study. Other features, such as the cleavage markings, highlighted in yellow, can also be observed as they are characteristic

of localized brittle fracture caused by the presence of the ε-HCP phase in the microstructure, alongside with the larger dimples resulting from the more ductile γ-FCC phase.

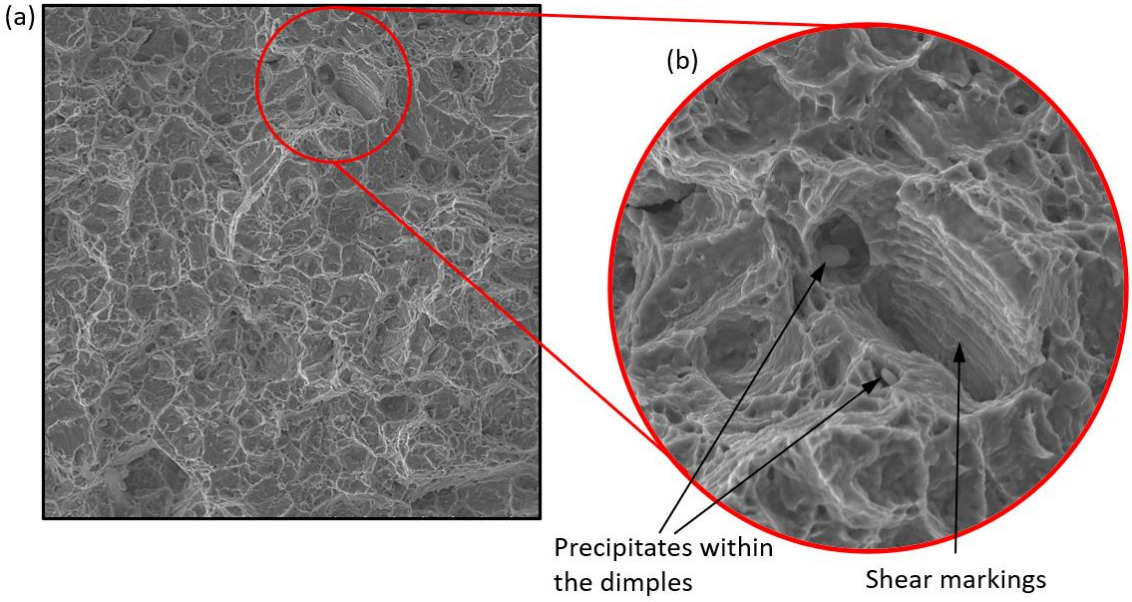


Figure 35 – Fracture surface after tensile testing inspected by SEM: a) Overall Overview and b) detailed view of the fracture surface.

It is, nonetheless, proved that processing this DP-HEA through welding leads to a material with intense microstructural variation throughout the regions that comprise the joint, although macroscopically it was possible to achieve a mechanical performance similar to that of the base material. Further work will assess the role of heat treatments on these welded joints targeting an improvement on their mechanical behavior.

4.2.3.5 Conclusions

The results delve into the investigation of the weldability of an as-cast $Fe_{50}Mn_{30}Co_{10}Cr_{10}$ DP-HEA. This HEA's main characteristic is the TRIP effect, in which the matrix γ-FCC phase transforms into the martensitic ε-HCP upon the application of an external stress. Nevertheless, the presence of ε-HCP on the microstructure can also be of a thermal nature, being formed because of stacking faults coalescence.

Having observed the excellent weldability via GTAW on the present DP-HEA, where defect-free welds were obtained, the current work explored the correlation between

microstructure and mechanical behavior of GTAW welded joints. As such, it was possible to derive the following major conclusions:

- Microstructurally, quantification of grain size and phase fraction fluctuations of the γ-FCC and ε-HCP phases, using multiple characterization methods, allowed to observe the differences between the weld regions which is attributed to the spatially varying thermal cycle. No evident chemical differences were found within the weld, beyond the presence of Mn-oxides at a lower fraction.
- Beyond grain size variations, EBSD data revealed distinct phase distribution along the joints between the two major phases that compose this alloy. While the BM exhibited the higher amount ε-HCP, the FZ proved to be richer in the γ-FCC phase.
- Synchrotron x-ray diffraction allowed to identify the γ-FCC and the ε-HCP phases, permitting also to confirm the presence of Mn-oxides. Further analysis was performed to investigate the stress conditions of the regions that comprise the weld by means of peak analysis of the synchrotron data. Lower values for microstrain were observed on the FZ, while the HAZ showcased a more uniform lattice strain distribution.
- Thermodynamic calculations, using the Scheil Gulliver model, evidenced the formation of γ-FCC from the Liquid. The formation of σ was also predicted, although no trace of it was found in the welded joints, likely due to the undercooling that occurs within the FZ. No indication of σ phase was found in the synchrotron x-ray diffraction patterns.
- No evidence of the TRIP effect was observed, being the ε-HCP present in the welded joint a result of the thermal cycles induced by the GTAW process.
- Considering the mechanical behavior, the FZ exhibited higher hardness values while the BM exhibited the lowest. Overall, the tensile tests indicated that the welds could endure stresses up to 717 ± 35.7 MPa at a 17.6 ± 1.65% strain, which corresponds to 96% and 58 % of the BM, respectively.

The use of post-weld heat treatments will be evaluated in the future to assess how the microstructure and properties can be controlled, and eventually improved, after welding.

4.2.4 Analyzing the weldability of a Fe-based shape memory alloy[3]

Fe–Mn–Si–Cr–Ni shape memory alloys are unique alloys that can be used in both functional and structural applications. These properties grant these Fe-based SMAs to be capable of playing a key role in construction sector for the creation of new components and/or the reinforcement of damaged ones. In this section, GTAW was performed on a Fe–17Mn–5Si–10Cr–4Ni–1(V, C) wt%, with the objective to investigate the microstructure and mechanical performance changes occurring after welding and further investigate its compatibility with the $Fe_{50}Mn_{30}Co_{10}Cr_{10}$ HEA.

4.2.4.1 Optical and scanning electron microscopy

To fully assess the effect of GTAW on the Fe-Mn-Si-Cr-Ni SMA, it is important to characterize the resulting welded joint considering both microstructural and mechanical aspects. This paves the way to establish connections between each other, and consequently generating a more precise understanding on the processing-microstructure-properties relationships for this material/welding process pair combination. In this section standard and advanced characterization techniques are employed to investigate the microstructure encountered on the cross-section of the weld with the purpose of correlating it with the mechanical behavior exhibited by the welded joint.

Commencing by the microstructure assessment, Figure 36 (a) displays a representative cross-section of the welded sample. Here, clear microstructural differences between the BM and the FZ are evidenced. That is, while the BM is composed mainly of small equiaxed grains, with a grain size of 11.4 ± 3.0 µm, the FZ presents itself as a plethora of grain morphologies that formed upon the non-equilibrium cooling conditions experienced by the molten pool. Nevertheless, before a detailed analysis of FZ is provided, understanding the microstructural changes that occurred throughout all the regions that comprise the weld must be done.

For this we refer to Figure 36 (b), where a SEM image taken using a backscattered electrons detector reveals the microstructural variations that occurred near the FB. The FB

[3] The results discussed in this sub-section are already published in the Journal of Materials Science, corresponding to reference [135].

encompasses both the HAZ, where the material did not experience full melting, and the FZ, where complete melting occurred. The HAZ is characterized by the potential occurrence of solid state transformations that alter the original BM microstructure. Here, recovery, recrystallization and grain growth can occur, although the extent of these transformations will be dependent on both the distance to the heat source, which impacts the local thermal cycle, and the previous thermomechanical processing of the BM, which will influence the magnitude of the eventual solid state transformations that can occur. Evidence of grain growth in the HAZ is clearly observed in Figure 36 (b), where the average grain size is 42.2 ± 8.7 µm, while in the BM this value was solely of 11.4 ± 3.0 µm.

When crossing the FB, the FZ is reached, a variety of grain structures of different sizes and morphologies are observed. Here, the optical micrographs of Figure 36 (c) and (d) clearly display regions that are commonly identified from solidification theory: the chill, columnar and equiaxed zones. In welding-related literature, however, evidence of small equiaxed grains at the FZ boundary is often referred to as fine equiaxed zone (FQZ), being commonly found in Al alloys, for example, and can be a weak point in the joint [110,111]. Nevertheless, in this study we refer to it as the chill zone to maintain the consistency with the classical metallurgical theory of solidifying ingots, allowing us to make the parallel between the fundamental knowledge of solidification and the microstructures possible to obtain during GTAW. Thus, the chill zone presents itself as a region comprising small and tightly packed equiaxed grains with an average size of 9.9 ± 2.1 µm. Further into the FZ, the columnar zone is formed, and this region is composed of highly directional columnar dendrites that grow epitaxially from the grains formed in the chill zone. Measured along their growth direction these grains reach 107.9 ± 20.0 µm. Their high directionality is due to the competitive growth that occurs, as grains tend to follow the path for maximum heat extraction, growing as the cooling rate decreases due to their proximity to the center of the FZ, where the process peak temperature is attained. Lastly, in the core of the FZ, an equiaxed zone can be observed with an averaged grain size of 27 ± 6.8 µm. This region is comprised by relatively larger equiaxed dendritic grains that form during dendritic growth, where under the appropriate conditions the dendritic arms can break providing, in the process, new nucleation sites for new and equiaxed dendrites to form, as depicted in Figure 36 (d).

Amidst the grain boundaries of the solidified dendrites, which is especially evident in Figure 36 (d), the presence of vermicular ferrite (δ-BCC) is also shown. Over the past years, the formation of δ-BCC has been related to the relationship between the Cr_{eq}/Ni_{eq}, material solidification modes [112,113] and cooling rate [114,115]. Given this, Peng et al. [113], developed Equation 16 to help predict the solidification modes of cast Fe-Mn-Si-Cr-Ni SMAs, as follows:

$$\frac{Cr_{eq}}{Ni_{eq}} = \frac{Cr + 1.5 \cdot Si}{Ni + 0.164 \cdot Mn + 22 \cdot C} \quad (16)$$

Using the nominal composition of the SMA, the Cr_{eq}/Ni_{eq} ratio was calculated to be 0.98, which is below the 1.35 threshold, indicating that the solidification mode of the alloy should follow the sequence: L (Liquid) → L + γ-FCC → γ-FCC. Thus, in the final stages of solidification the material should be fully austenitic. Such is indeed the case of the BM and the HAZ, which did not undertake fully remelting during welding. Nevertheless, the displayed results indicate that the microstructure is not only composed of γ-FCC. To understand how other phases appear on the microstructure, the constitutional supercooling theory allows us to interpret the continuous compositional change that the molten pool undergoes. As the molten metal starts to solidify, small dendritic arms start growing from the already present solid material, which acts as primary solidification sites. With the decrease in temperature, while some atoms arrange themselves in the matrix γ-FCC phase crystal structure, the dendritic boundaries become richer with the remaining elements present in the molten pool, with the continuous decrease in temperature and the consequent solute-rich interdendritic fluid [32]. The remaining atoms will solidify in the crystal structure that has the lowest Gibbs free energy for such interdendritic fluid composition. In the present case the formation of δ-BCC can be explained by the enrichment of Cr and/or Si via segregation into the molten pool, as these present themselves as factors that can dictate the Cr_{eq} value used to determine the solidification mode of the alloy [113]. Other phases are nonetheless possible to appear in the microstructure, depending on the overall Gibbs free energy of the system at specific sites with determined compositions, as well as cooling and mixing conditions experienced by the material, which are known to vary within the welded joint. Nevertheless, predicting the solidification path that the molten material undergoes during welding is not trivial, as several other factors come into play during the process. Beyond the composition and phase structures enveloped

in the microstructure, grain morphology and orientation are also a product of material solidification.

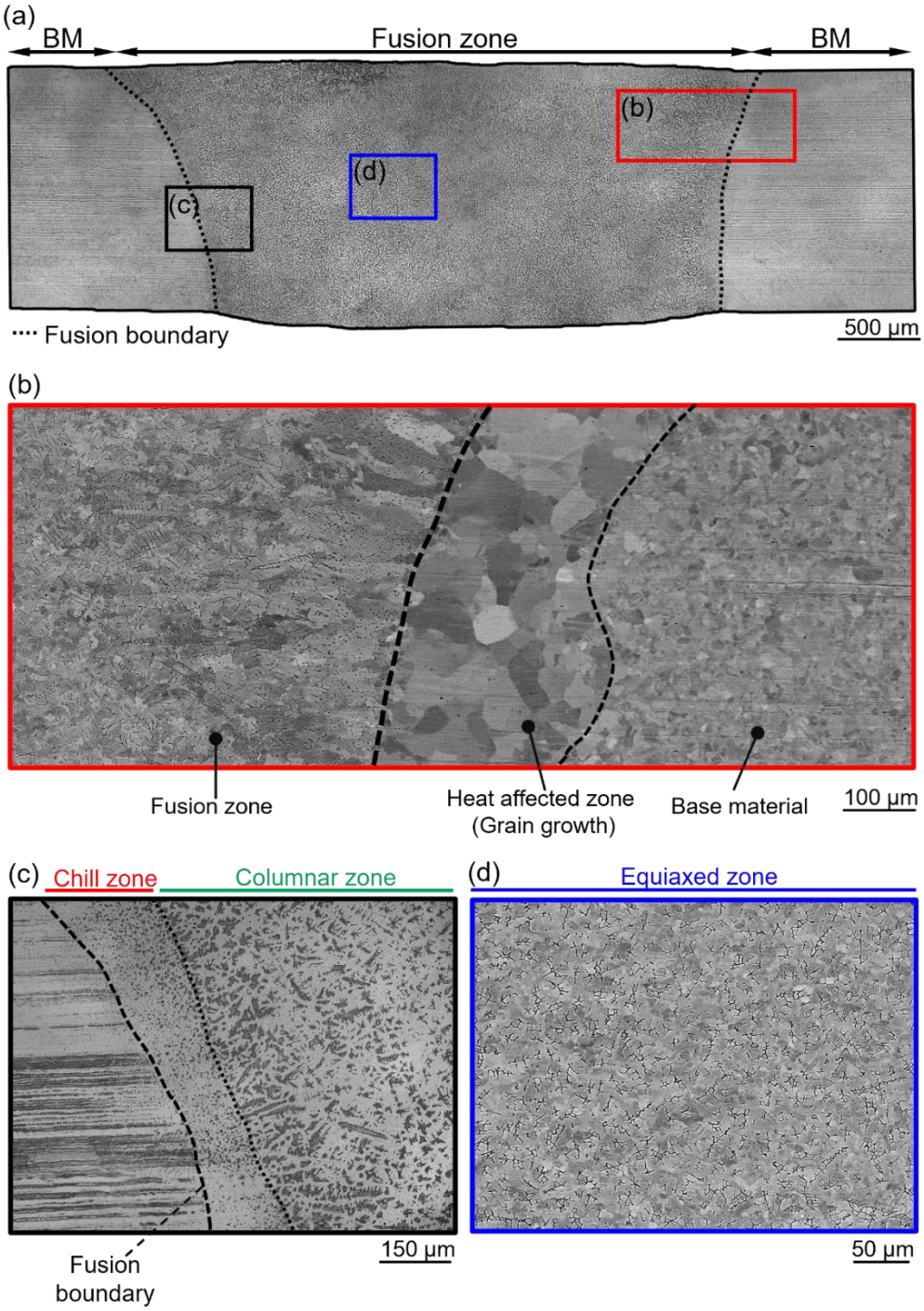


Figure 36 – Microstructural analysis of the welded joint: (a) Overview of the joint as obtained by optical microcopy; (b) Scanning electron microscopy of the transition from the BM to the FZ highlighting the several regions generated during welding; (c) Close-up view of the transition from the BM to the FZ by optical microscopy; (d) Close-up view of the FZ by SEM.

Figure 37 displays the IPF orientation map of the welded joint. Here, the same microstructural features observed via optical microscopy along the weld are also put in evidence alongside a clearer perspective on the grain orientations. Considering Figure 37 (b), it is observed that the BM is randomly oriented, then in the HAZ there is evidence of massive grain growth. Crossing the FB, entails the FZ regions which is composed by: i) the chill zone, containing the small sized grains; ii) the columnar region, where grain growth is preferential along the easy growth direction for cubic alloys, i.e., the <100> direction; and iii) the equiaxed grain regions, where the formed grains are randomly oriented.

Returning to the topic of grain morphologies, which has already been mentioned briefly, Figure 37 (a) shows a clearer distribution of the grain structures located throughout the several regions of the molten pool. The presence of this microstructural variation in the molten pool, as shown in Figure 37, arises from the process thermal cycle experienced by the material, which is essentially controlled by the process heat input and material thermophysical properties. The heat input ultimately impacts the overall shape of the weld and, more importantly, has a major impact on the microstructural features of the weld by dictating how the G and the R parameters vary along the solidifying molten metal. In this study, the presence of these different grain shapes highlights the varying conditions that reign over the thermal gradient and growth rate that eventually results on the formation of the several regions present in the FZ [32].

The small equiaxed grains that composed the chill zone occur as the combination of an elevated growth rate and a low thermal gradient, compounded by the high cooling rates enabled by the cold BM that then transforms to HAZ due to heat dissipation from the FZ. This will be the first region to solidify, and grains formed here will act as substrates for columnar grains to start growing towards the center of the FZ. The small dimension exhibited by this region, when compared to the remaining regions of the FZ, indicates that the influence of the BM in the temperature distribution is the key factor that reins over the solidification microstructure of the molten pool developed here.

Next, there exists the columnar zone, where dendritic structures grow collectively aligned with the maximum thermal gradient. In this region, the thermal gradient factor increases over the growth rate, thus allowing for the competitive growth showcased by the large

dendrites exhibited in this region. Finally, at the center of the FZ, where the equiaxed zone developed, the temperature reaches its maximum values during welding, while the cooling effect induced by the cold BM is reduced due to it being further away, therefore also decreasing the effect of G. In this region other factors such as the fragmentation of dendritic arms, due to their rapid and directional growth combined with the molten pool turbulence, can ease the formation of new dendrites providing new nucleation sites for the liquid to solidify from, increasing R in the process. Additionally, being so near to the torch, the cooling rate is also slower in this region, thus larger equiaxed grains structures can be observed, when compared to those formed in the chill zone.

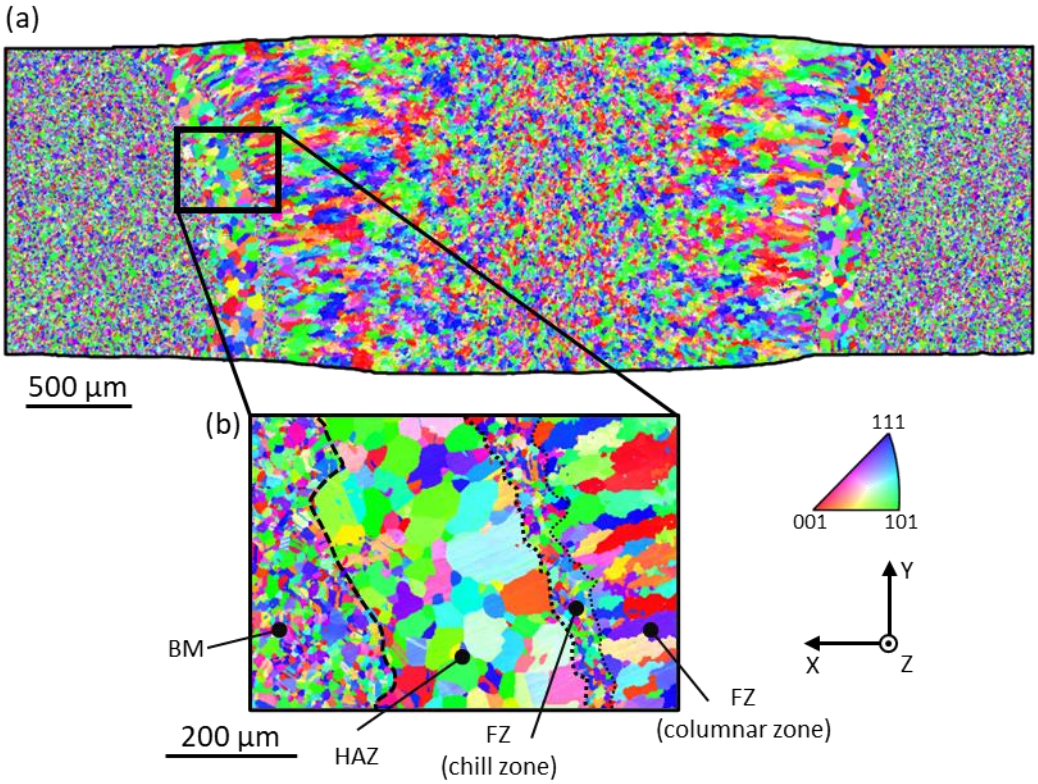


Figure 37 – Electron Backscatter Diffraction Inverse Pole Figure map parallel to the Z axis: (a) cross section of the welded joint; (b) Detailed view of the fusion boundary.

4.2.4.2 Transmission electron microscopy

Beyond the optical and SEM observations made until now, a deeper analysis of the microstructure of the BM and the FZ at the nanoscale was performed using S/TEM. Nanoscale characterization of the BM using TEM is detailed in Figure 38, where the features present at the sub-grain level are exhibited.

In Figure 38 (a) it is possible to observe the multiple sets of stacking faults (SFs) within all the grain structures, for example, as marked by the yellow dashed lines. These are characteristics of the previous thermomechanical processing endured by the BM during its manufacturing processing, acting as a method to release energy alongside the possible formation of deformation twins. Additionally, a representative selected area electron diffraction (SAED) pattern is depicted in Figure 38 (b), showcasing the γ-FCC matrix phase as the only identifiable phase in the microstructure, as no other obvious diffraction spots were noticeable within the analyzed region of the BM.

Emphasis is now given to an annealing twin with a thickness of ≈250 nm shown in Figure 38 (d). This feature is associated with the thermal influence associated with the hot-rolling endured by the BM, resulting from the recrystallization mechanisms undertaken during the process. The corresponding SAED pattern is displayed in Figure 38 (c), where two sets of diffraction pattern spots are evidenced, indicating the misorientation between the annealing twin and the matrix. Interestingly within these twins, the presence of fine SFs can be observed, which are compliant with the extensive streaking along the <111>γ direction, which extends through the γ-FCC matrix reflections and is associated with fine SFs.

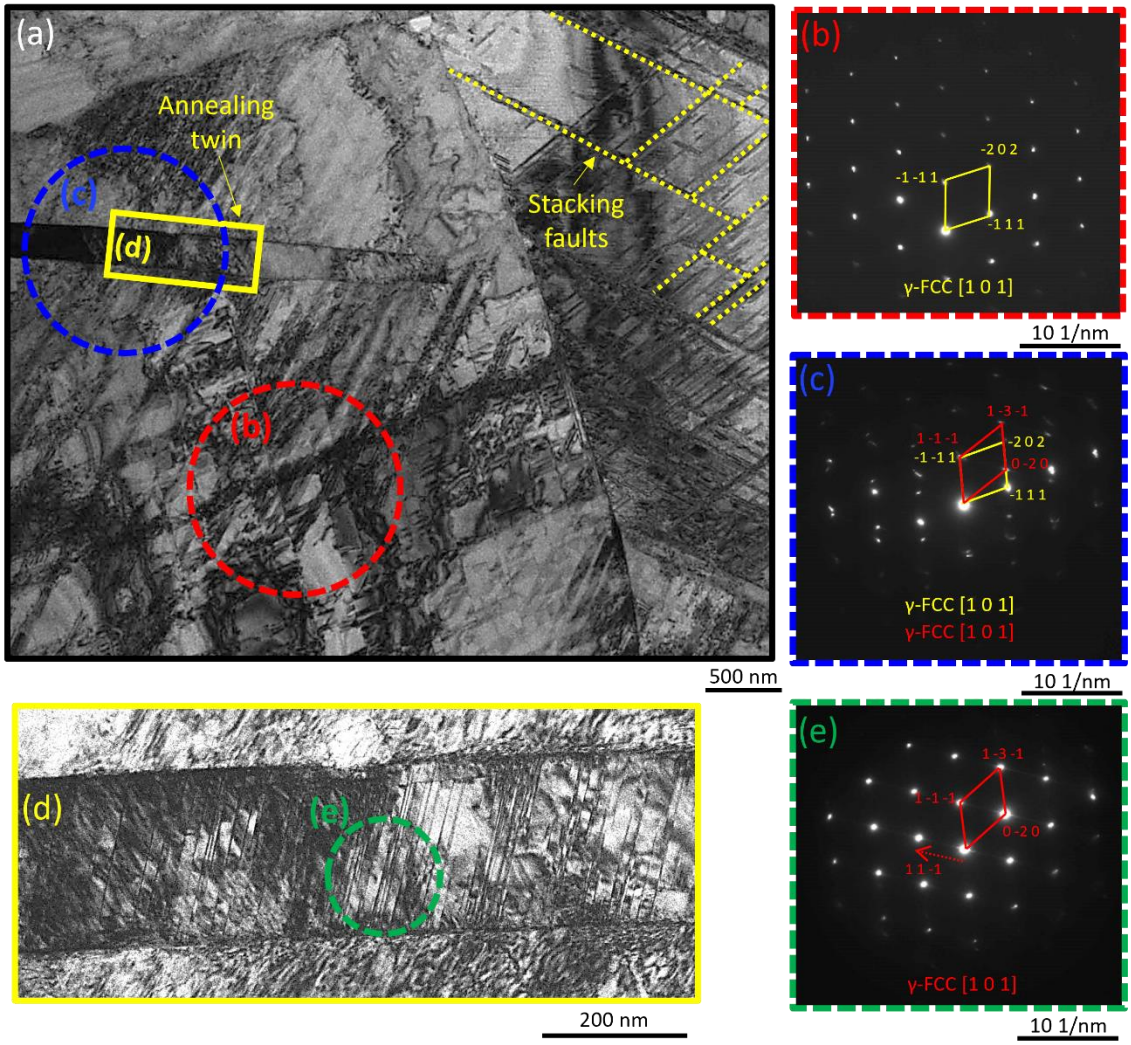


Figure 38 – (a) representative bright field TEM image of the BM; (b) SAED pattern highlighting the γ-FCC matrix; (c) SAED pattern indicating the presence of an annealing twin alongside the γ-FCC matrix; (d) TEM image detailing the presence of stacking faults within the annealing twin, and (e) SAED pattern of the annealing twin showcasing streaking due to the presence of stacking faults.

Figure 39 depicts a TEM image obtained from the FZ region. Here, larger γ-FCC matrix grains are composed of smaller polygonal sub-grain structures exhibiting a lower density of defects within the γ-FCC matrix, when compared to the BM (see Figure 38). Additionally, two different types of precipitates are also visible. Firstly, as noticeable in Figure 39 (b) and (c), small particles corresponding to vanadium carbides were distributed near the sub grain boundaries. This was expected to occur in the microstructure given the nominal composition of the alloy. On a second instance it was also possible to identify Fe-rich nanoparticles (refer to Figure 39 (d) and (e)) scattered within the grains. An EDS line scan was acquired to further

highlight their presence, as shown in Figure 39 (f)). Phase identification using SAED was not possible to conduct in these particles, given their small size and/or their random orientation on the γ-FCC matrix. The identification of these nanoparticles will be detailed when presenting the high energy synchrotron X-ray diffraction data.

SAED analysis was conducted in the transition between two different sub-grains and their boundary, depicted in Figure 39 (g), (h) and (i), the diffraction patterns corresponded to that of the γ-FCC matrix phase. Interestingly, a small disorientation angle, indicating a low angle boundary between these structures.

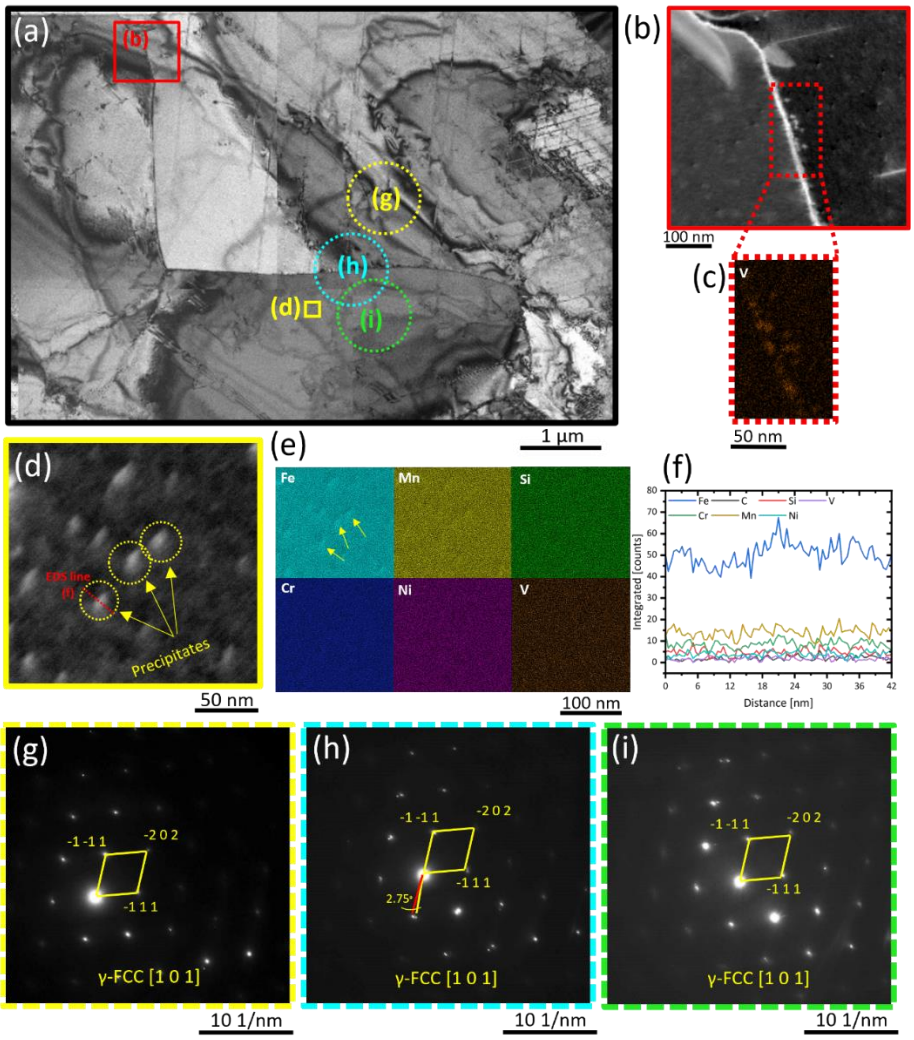


Figure 39 - (a) representative bright field TEM image of the FZ; (b) detail of VC precipitates near the sub-grain boundaries, and (c) corresponding EDS map of Vanadium; (d) detail of Fe-rich precipitates scattered withing the sub-grains and corresponding EDS maps in (e) alongside the (f) EDS line results marked in (d). The transition from one sub-grain to another was inspected using SAED as in (g) upper sub-grain; (h) boundary between sub-grains and (i) lower sub-grain.

4.2.4.3 High-energy synchrotron X-ray diffraction analysis

To further investigate the microstructure throughout the welded joint, high energy SXRD was performed. For this, a series of diffraction patterns were retrieved from a linear path that encompasses the full extension of the welded joint. The 3D superimposition of the obtained diffraction patterns is presented in Figure 40 (a). Here, distinguishing these regions is easily achieved by observing the variation on diffracted intensity of the (111) peak of the γ-FCC phase, as marked.

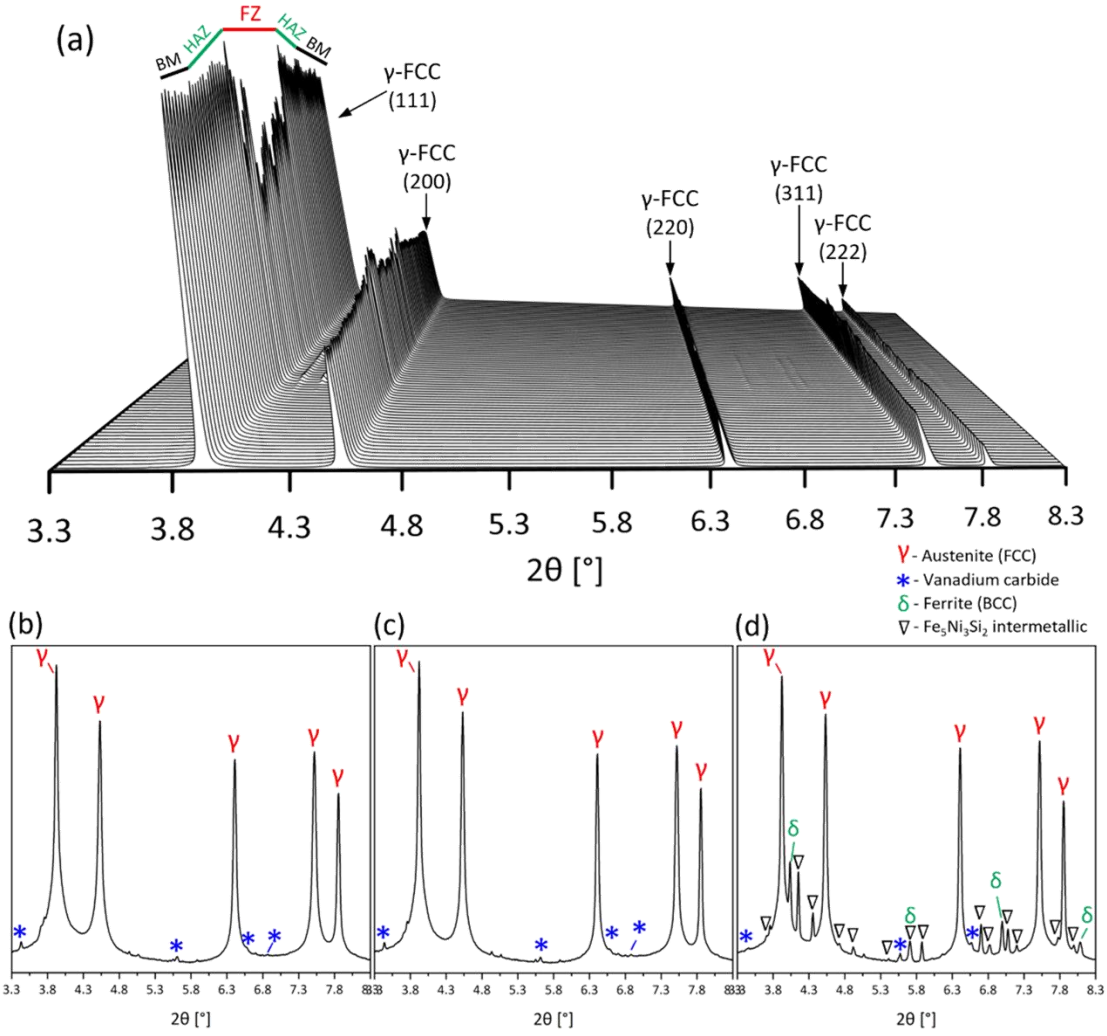


Figure 40 – Synchrotron X-ray diffraction patterns taken form (a) the full extension of the weld, highlighting the matrix γ-FCC phase; representative diffraction patterns of: (b) BM, (c) HAZ, (d) FZ, with corresponding phase identification. Low intensity 2nd harmonic diffraction peaks were left unidentified because they do not correspond to any structure present on the alloy.

Figure 40 (b), (c), and (d) exhibit site specific patterns of the BM, HAZ and FZ, respectively, using a logarithmic scale for intensity, which allows us to observe the low intensity reflections. In all regions the γ-FCC matrix phase is dominant. The BM lattice parameters calculated by fitting each peak and using the intensities as averaging weighting factors was a_γ = 3.6012 Å (rounded to the fourth decimal). Such value is coherent with that obtained from Rietveld refinement in the same region (a_γ = 3.6018 Å) and with the lattice parameters found in the literature for similar Fe-based SMA [114,116–120]. Additionally, Vanadium carbide (VC) peaks, a_{VC} = 4.1599 Å, space group: Fm-3m, are noticeable throughout the BM and HAZ, corresponding to a total phase volume fraction of 0.11%. This phase volume fraction reduces to 0.06% in the FZ, potentially due to the non-equilibrium and faster cooling conditions experienced in this region of the joint. Interestingly, the BM and the HAZ have the same phase structures present within them. Conversely, throughout the FZ (either in the FQZ, columnar or the equiaxed region), the presence of a δ-BCC phase (a_δ = 2.8580 Å, space group: Im-3m) corresponding to ferrite is also evident, with a phase volume fraction of 1.04%, as well an intermetallic precipitate which occupies a volume fraction of 0.75% on the bulk of the FZ and corresponds to a $P2_13$ cubic crystal structure (a_∇ = 6.2130 Å). This allows us to identify the Fe-rich particle scattered within the sub-grains in the FZ TEM samples. As identified in [114], this precipitate is common to find in Fe-Mn-Si-Cr-Ni shape memory alloys, being a $Fe_5Ni_3Si_2$-type intermetallic isostructural to the π-phase in steels. Such precipitate has also been observed in similar alloys [114,116,118,119,121]. Nevertheless, the presence of these additional minor intensity phases is only noticeable within the FZ because of the complete localized melting of the material and subsequent non-equilibrium cooling conditions. Concerning the lattice parameters calculated in this region, Rietveld refinement yields an a_γ = 3.6012 Å, while the peak intensity averaged data results on an a_γ = 3.6014 Å. Additionally, no indication of the reversible ε-HCP and non-reversible α' phases was found on the joint, as often mentioned in the literature [122–126].

Beyond phase identification and Rietveld refinement for phase quantification, single peak fitting was conducted using an in-house developed python scripts to perform least-squares fitting with a Voight profile, on all the first order reflections of the matrix γ-FCC phase. This procedure aims to gather data and reveal trends from the intrinsic microstructural

phenomena contained within the weld. Here, a qualitative analysis of both the normalized FWHM and intensity can be done conjointly, as displayed in Figure 41 (a) and (b). These values were normalized with respect to the BM.

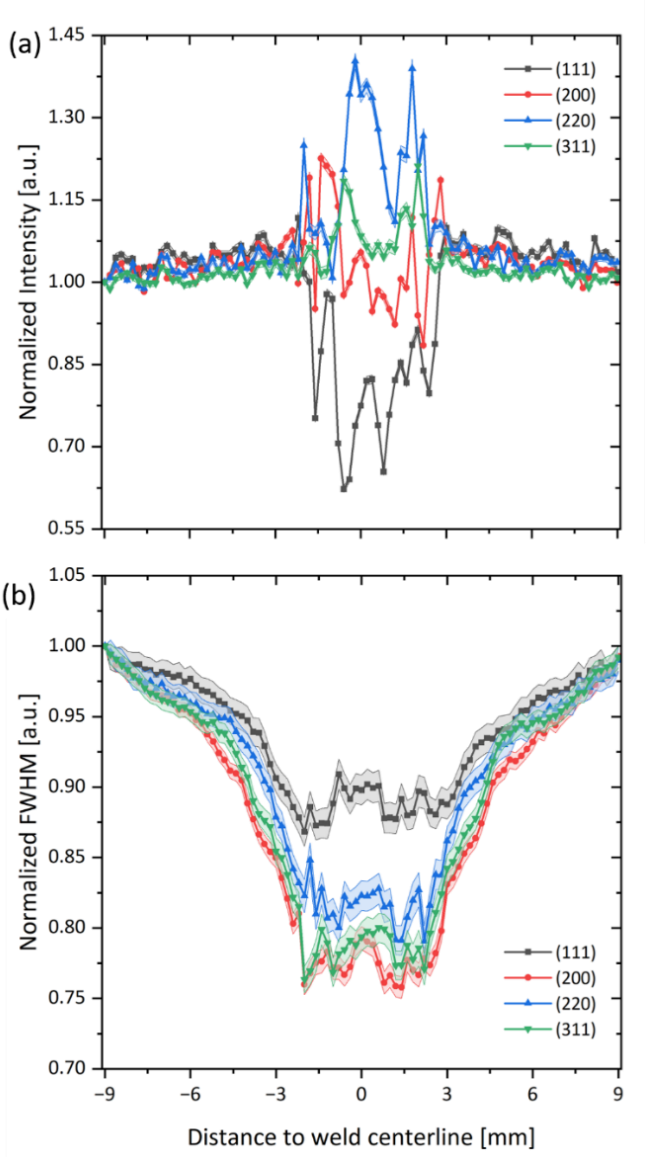


Figure 41 – Distribution of (a) peak intensity, and (b) FWHM per diffraction peak along the welded joint.

The FWHM is affected by the microstrain caused by defects within the lattice, and the size of intragranular structures that can diffract light in a coherent manner, as well as by the beamline optics (although this component was removed using LaB_6 calibration powder). The intensity, however, is influenced by texture and volume fraction of each phase within the weld. Nevertheless, both parameters (microstrain and size of the intragranular structures) have a significant impact on the overall shape of the peaks, the only difficulty associated with

it being knowing how to interpret them. As such from these two parameters, one conclusion that can be taken right away is the fact that going towards the FZ, all peaks tend to decrease in FWHM, while increasing in intensity, with exception to the (111) peak. In this case, while the FWHM decreases, the intensity decreases. As mentioned before, this is coherent with the fact the BM is in the as-rolled condition, given that this corresponds to the preferential orientation taken by the grains during deformation. As such, due to high temperatures that cause the material to melt, the texture obtained during the rolling process is annulled, resulting in an overall tendency for its intensity to decrease. Furthermore, the peak that shows the highest FWHM decrease is the (200) peak, whereas its intensity tends to fluctuate between approx. 0.85 and 1.15 of the value exhibited by the BM, indicating that these diffraction reflections become sharper with proximity to the FZ, which is coherent with the easy growth direction of FCC alloys. Next, we have the (220) reflection, whose intensity increases more than 30% of its intensity on the BM. Such does not quantify the number of grains oriented along the (220) plane, when compared with the (200) oriented grains, but it allows to infer that sharper (220) peaks are present in the FZ, which is related to the crystallographic plane associated with the easy growth direction of the FCC materials [25]. Additionally, of special note is the (311) peak, whose characteristic insensitivity to intergranular strains allows us to highlight the behavior of matrix γ-FCC phase along the welded joint [29]. This is especially, observable in Figure 41 (a), where the intensity exhibits an increase near the fusion boundary, corresponding to the FQZ and columnar regions, and finally exhibiting a slight decrease indicating the boundaries of the epitaxial region present in the bulk of the FZ.

Furthermore, quantification of the lattice strain (ε) can be done using Equation 17 [127].

$$\varepsilon = \frac{a - a_0}{a_0} \tag{17}$$

Where a corresponds to the intensity weighted averaged lattice parameter obtained from all the γ-FCC peaks available on the diffraction patterns. Due to the lack of knowledge of a_0, which corresponds to the strain-free lattice parameter characteristic of this alloy, in this work we set a_0 as the lattice parameter obtained at 0 MPa on the BM. This allows for a still meaningful qualitative assessment of the microstrain evolution, rather than a quantitative evaluation.

Given this, for an understanding of the strain field associated with each zone of interest with sufficient dimensions for a complete acquisition of data given the utilized beam spot size, measurements from the HAZ and columnar and equiaxed regions of the FZ are compared to those obtained from the BM in Figure 42 (c), with relation to the azimuthal angle. For such, representative diffraction patterns of each region were integrated into 1-degree segments, allowing to obtain the 2θ center parameter of each peak at any given azimuthal angle segment, where the intensity is sufficient to acquire reliable results.

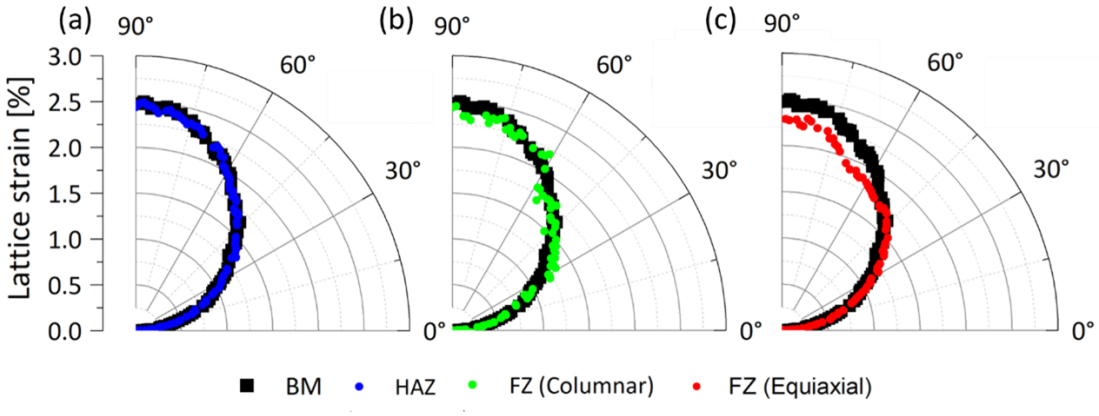


Figure 42 – Comparison between the microstrain of the BM and the: (a) HAZ, (b) columnar region of the FZ and (c) equiaxed region of the FZ.

By comparison, all the analyzed regions evidence a similar distribution of microstrain, which is symmetrical on the horizontal and vertical axis. Here the higher macrostrain values are present in the 90° azimuthal angle and the lowest are oriented in the 0° angle. This is coherent with the expected strain conditions considering the as-rolled condition of the BM, where the 90° angle corresponds to the rolling direction and the 0° angle corresponds to the direction normal to it. Interestingly in all regions, including the FZ, where the material underwent total remelting, the microstrain distribution is also higher at the 90° angle when compared to the 0° direction. This allows us to conclude that upon solidification the newly formed grains tend to adjust to the already present microstructure due to epitaxial growth. Thus, causing the lattice parameter evolution to mimic that of the BM, thus granting an approximately isotropic microstrain response throughout the weld.

Additionally, it is also possible to conclude that with increasing distance from the FB the microstrain tends to decrease. Comparing the values obtained in the BM distribution with

those expected from the calculated average lattice parameter, the microstrain increases approx. 2.48% in the rolling direction and decreases 0.02% in the 0° direction. On the other extreme, when considering the equiaxed region in the FZ, however, the microstrain is 2.35% higher in the 90° angle and 0.01% lower in the 0° direction.

Up to now a thorough microstructural analysis of the welded joint has been performed. To complement this characterization, an electrochemical comparison of the BM and FZ was performed and these results are presented in the next section. Such was conducted to investigate the corrosion properties of these two regions, allowing us to establish a starting point, from a corrosion-focused electrochemical behavior standpoint, for the design of applications that may rely on welding of this Fe-based SMA.

4.2.4.4 Electrochemical characterization of the weld

Setting the BM as the benchmark, the corrosion behavior of the weld, namely the FZ (which is region mostly affected by GTAW), was analyzed to attain an understanding of what to expect when exposing such welded material to different environments. These two regions (BM and FZ) correspond to the two microstructural "extremes" on the joint. It is also relevant to mention that for this analysis the FZ was considered in bulk.

For this matter, Figure 43 displays the anodic polarization curves alongside the corresponding open circuit potential data obtained from the BM and the FZ. Using the Tafel model [128,129], the corrosion current, I_{corr}, was estimated to be 0.96 mA for the BM and 0.97 mA for the FZ. Although, these values are quite close to each other it is possible to conclude that the corrosion rates of the BM and FZ under the testing conditions were similar, with the FZ exhibiting a slightly lower corrosion resistance that the BM. Nevertheless, interpreting electrochemical results solely based on one parameter may does not capture the entire complexity of the corrosion process.

As such, the EIS measurements performed the BM and the FZ are presented in Figure 43, in terms Bode and Nyquist diagrams. It can be noted that the impedance modulus, |Z|, of the BM is greater than that of the FZ, corresponding to values up to ≈307 Ω and ≈285 Ω, respectively, at the lowest values of frequency. Regarding the phase angle, for the BM the lower values corresponded to ≈-18.8° at a frequency of ≈20 Hz, while the FZ attained its minimum of ≈-19.7° at a frequency of 12.4 HZ. On the other hand, the maximum phase angle for the BM

was ≈-1.7° (at a frequency of ≈50.3 KHz), while for the FZ the maximum was ≈-1.4°, recorded at a frequency of ≈15.7 KHz.

While exhibiting a similar corrosion behavior, it can be noted that the BM has a higher corrosion resistance when compared to the FZ, such can be associated to the different microstructural condition of both regions, where the FZ is characterized by varying array of different microstructures.

With this matter established, next we analyze the mechanical properties, correlating them with processing conditions and local microstructure features in order to establish a parallel between the mechanical properties and the obtained microstructure. This highlights the fact that the microstructure not only affects the corrosion behavior of the joint, but also has an important role in its mechanical performance.

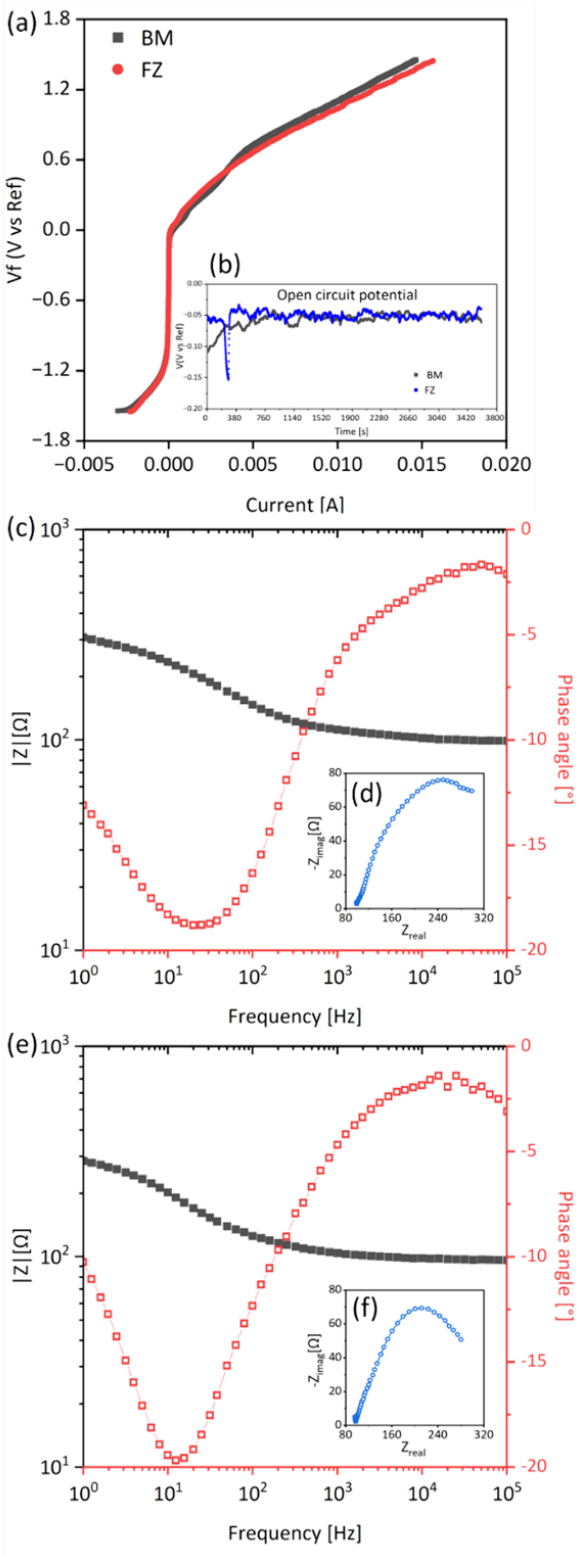


Figure 43 – Electrochemical characterization of the welded joint in terms of: (a) polarization curves alongside with the (b) corresponding open circuit potential; (c) Bode plot and corresponding (d) Nyquist plot, obtained on the BM; (e) Bode plot and corresponding (f) Nyquist plot, obtained in the FZ.

4.2.4.5 Mechanical behavior of the welded joint

Understanding the intricate relationship between microstructure and mechanical properties is paramount when selecting a material for a determined purpose, especially when there is a gradient of microstructures (and therefore of mechanical behavior) in thermomechanically processed material. Having discussed the microstructural aspects that developed within the welded joint, generated by the intense heat imposed during GTAW, in this section we explore the mechanical and functional properties of the joints. Firstly, we start by observing the anisotropic distribution of the microhardness on the weld, followed by the analysis of the tensile and cyclic properties exhibited by it.

4.2.4.6 Microhardness distribution along the joint

Microhardness maps performed on the full extension of the joint are displayed in Figure 44. Here, a clear distinction of the regions previously identified in the microstructural section is possible. Interestingly the three regions that comprise the FZ microstructural gradient are again easily identifiable by observing the FZ microhardness variation. Furthermore, the microhardness line data obtained at half height of the cross section of the weld are plotted in Figure 44 b). This also permits us to highlight the microhardness variation between the regions that comprise the welded joint and ease the interpretation of the microhardness map. Here the softening behavior of the chill zone is evident as it marks the region where the weld achieves its lowest microhardness values.

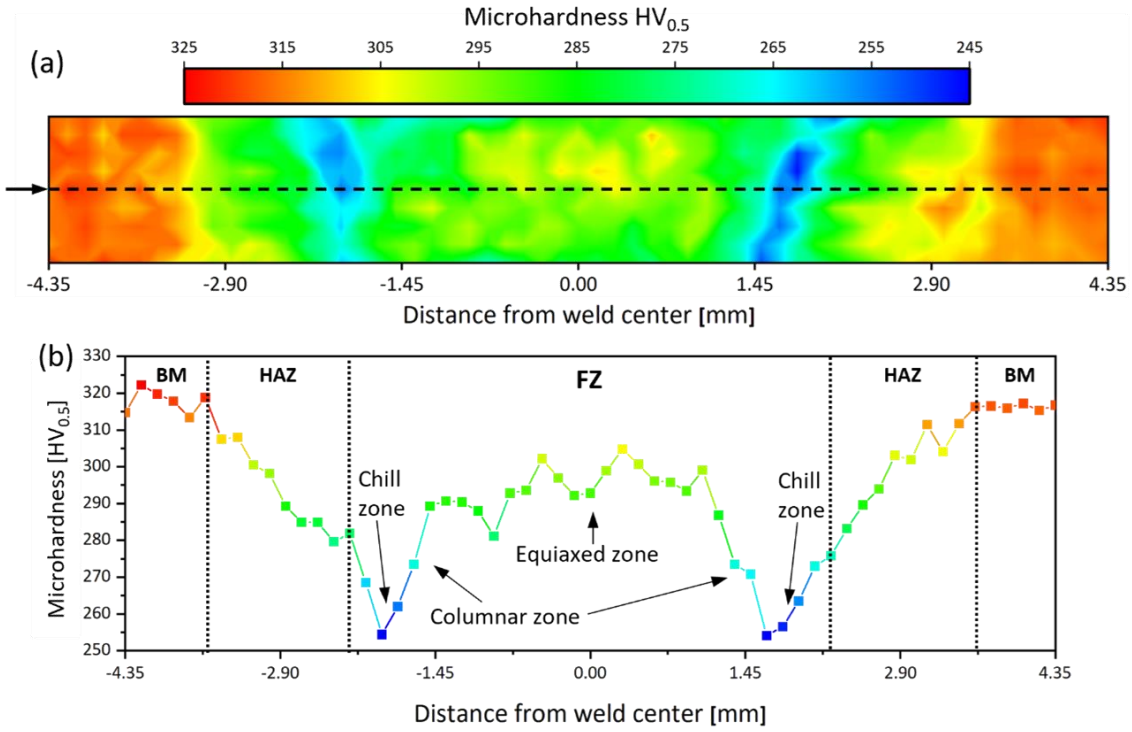


Figure 44 –Microhardness distribution of the Fe-SMA welded joint: (a) colormap and (b) evolution at mid height of the weld (marked by the black arrow and dashed line).

Quantification of the results regarding the microhardness distribution along the joint are displayed in Table 8, where the percentual variation of the results of the regions affected by the welding process are compared to the measured BM values. While the BM achieved an averaged microhardness corresponding to 316.7 ± 2.9 $HV_{0.5}$, the lowest hardness on the weld was observed in the FQZ of the FZ, reaching 254.5 ± 6.0 $HV_{0.5}$. Concerning the HAZ, the microhardness achieved an average of 286.3 ± 3.8 $HV_{0.5}$. Also, the columnar dendritic and the equiaxed region of the FZ attained the values of 281.5 ± 3.6 $HV_{0.5}$ and 299.0 ± 7.3 $HV_{0.5}$, respectively. This microhardness gradient allows to put in evidence the varying mechanical behavior that the different microstructures induced throughout the weld.

Table 8 – Quantification of the microhardness distribution throughout the welded joint microstructure.

	BM	HAZ	FZ (Chill zone)	FZ (Columnar zone)	FZ (Equiaxed zone)
Microhardness [$HV_{0.5}$]	316.7 ± 2.9	286.3 ± 3.8	254.5 ± 6.0	281.5 ± 3.6	299.0 ± 7.3
Percentual deviation from the BM	---	-9.6%	-19.6%	-11.1%	-5.6%

4.2.4.7 Tensile properties of the welds coupled with Digital Image Correlation (DIC)

With the microhardness distribution determined, an obvious anisotropic distribution of the microstructure and its impact on the local mechanical response is clear. Given this, the next step is to analyze the tensile behavior of the welded joint, to highlight the mechanical performance differences that arise from the microstructural changes developed in the HAZ and FZ. The representative stress-strain curves of the BM and welded joint are plotted in Figure 45.

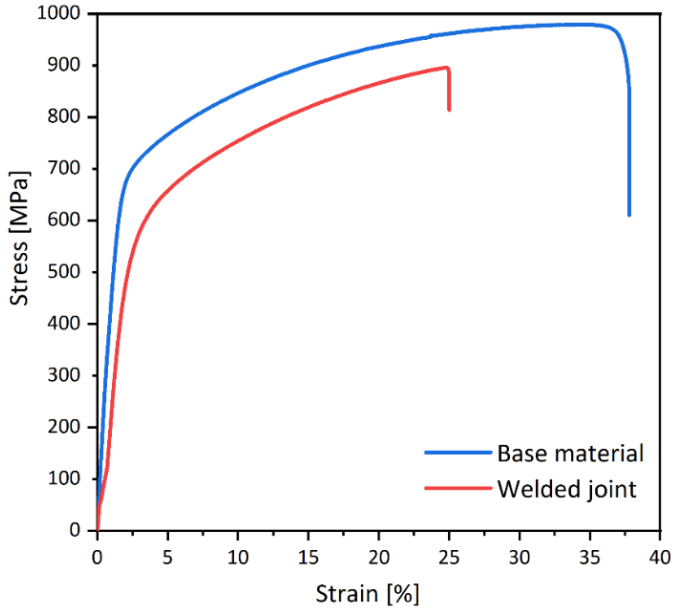


Figure 45 – Representative stress-strain curves of the (a) base material and (b) welded joint, taken from the multiple tensile tests performed on the samples (three in each condition).

Overall, the obtained tensile test data indicates that regarding the ultimate tensile strength (UTS), the BM samples achieved 1032.9 ± 76.3 MPa, while the welds reached an averaged UTS of 883 ± 18.4 MPa, corresponding to fracture strains of 36.8 ± 1.5 % and 23.6 ± 2.1% (all engineering values), respectively. This indicates that the welds retained 85.5% of the UTS exhibited by the BM, reaching 64.1% of the strain-to-fracture exhibited by it. The UTS values show a good agreement with those found in the literature [130–133], while the elongation to fracture tends to vary accordingly with the thermomechanical treatment they are subjected to.

It can be concluded that the tensile strength evidences a small decrease when comparing the welds with the BM, while the ductility deteriorated more severely after the GTAW

process. This, as seen through the microhardness measurements, can be related to the varying microstructural features arising from the solidification of the molten pool and consequent inhibition of the overall strength of the BM imposed by rolling process. Furthermore, the presence of δ-BCC ferrite and the ∇-precipitate phases can also explain the different tensile behavior exhibited by the welded samples. Nonetheless, the overall macroscopic mechanical behavior of these Fe-based SMAs make them suitable candidates for structural engineering application scenarios.

Under the effect of a constant tensile force imposed on the joints, the data regarding the mechanical behavior of the welds corresponds to the combined behavior of all regions of the weld. For this reason, to further evaluate the microscopic tensile behavior exhibited by each welded region, DIC data was recorded during tensile testing and specific locations were monitored to evaluate their site-specific behavior. The strain distribution results during tensile testing are displayed in Figure 46. Here the evolution of the strain distribution along the welded joint is shown, clearly indicating that more deformation occurred in the GTAW affected area than in the BM itself.

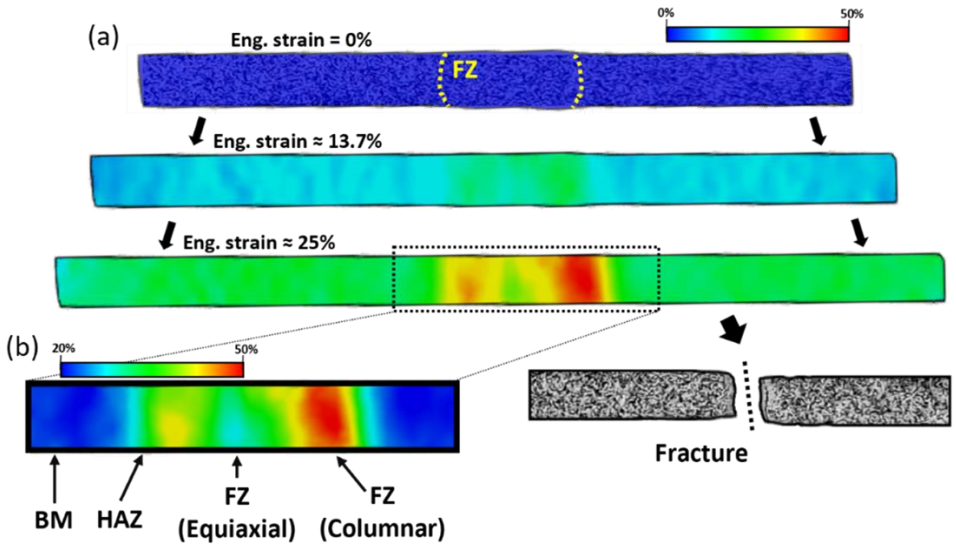


Figure 46 – Depiction of the strain distribution during tensile testing in the as-welded condition, using digital image correlation: (a) corresponds to the evolution until fracture, while in (b) the last stage before fracture is depicted on a different scale. The regions marked in (b) are utilized to plot the local tensile behavior in Figure 47.

As expected, from the start of the tensile test until sample fracture, an increase in strain is observed as can be seen through the color distribution at the displayed engineering strain values. By inspecting the last moments of the tensile test (see Figure 46 (b)), it is possible to observe that the variating microstructure present within the samples indeed has an important effect on the overall strain that is accommodated by each region of the weld. By direct observation, it is possible to observe that while the BM was the region where less strain was accumulated, the columnar zone of the FZ presents itself with the most amount of strain. Interestingly the equiaxed zone located at the middle of the FZ (refer to Figure 36) exhibits a higher resistance to the imposed stress. This was expected considering the refined morphology of the grains in this region and the associated higher microhardness. Thus, this equiaxed microstructure present in the equiaxed zone is preferred over the other microstructures existing in the FZ of the weld. For further analysis Figure 47 displays the stress-strain curves calculated considering specific regions of the weld, as mentioned, and a clear distinction and quantification of the strain experienced by each region is presented.

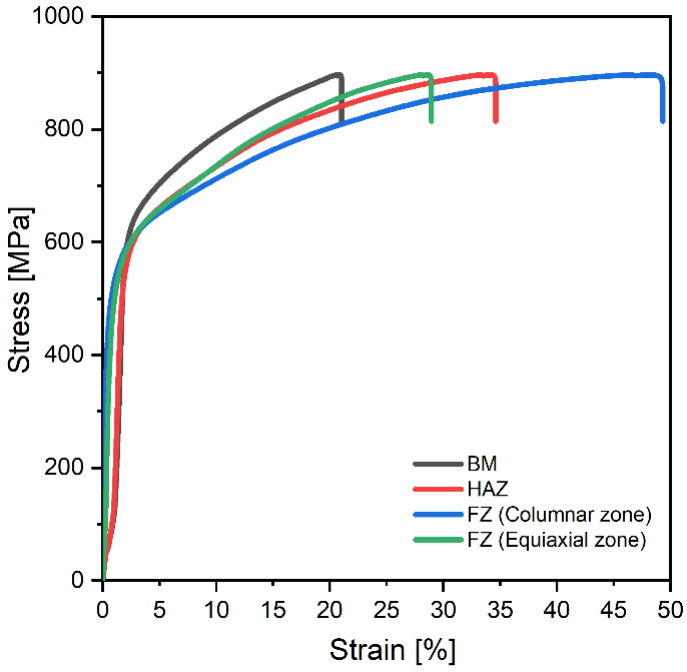


Figure 47 - DIC results for the BM, HAZ and two region (columnar and equiaxed) zones of the FZ.

Qualitatively, it can be observed that the BM and the equiaxed zone in FZ, exhibited a lower amount of deformation upon loading. While both are characterized by their small grain size and higher microhardness which grants them strength, another factor influencing their

behavior is the deformed state of the BM (which hinder dislocation movement) and the occurrence of precipitates in the FZ.

These regions are followed by the HAZ which experienced grain growth during the welding process and is composed of large equiaxed grains. Finally, the region with the most amount of deformation experienced is the columnar region of the FZ, which reaches similar microhardness values to the HAZ but has larger and highly oriented grains. Nevertheless, as necking started to occur on the sample it was clearly observed that the samples fractured on the interface between the FZ and the HAZ, presumably in the chill zone given its lower values of microhardness.

To better understand the fracture mechanisms that occurred during tensile testing, a SEM image of the post-fracture surface is exhibited in Figure 48. There, it is possible to observe several dimples which are characteristic of a ductile-like fracture upon tensile solicitation. That is, as the material is exposed to a plastic deformation, small voids and cavities tend to form inside the material. These eventually grow larger and coalesce into each other, forming fissures that propagate perpendicularly to the stress direction, especially in the peripheral zone of the region that experiences necking.

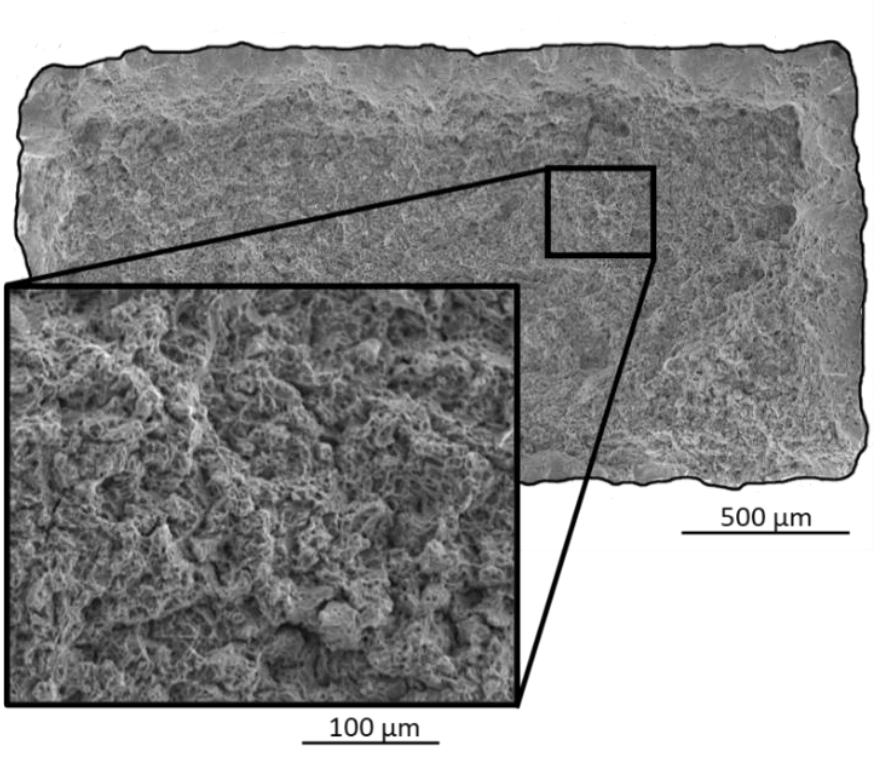


Figure 48 – Representative fracture surface of the welded samples.

4.2.4.8 Weld performance under cycling tests

To further understand the mechanical/functional response of this Fe-Mn-Si-Cr-Ni SMA in the as-welded condition, samples were subjected to a routine of load/unload cycles to investigate parameters such as absorbed energy and accumulated irrecoverable strain. Figure 49 presents the stress-strain curves corresponding to the 1st, 2nd, 10th, 25th, 50th, 75th and 100th loading cycles on both the welded and non-welded (BM) conditions. By comparison, it is evident that in both cases the curves display a small pseudoplastic behavior, showcasing slightly lower stress and strain values on the as-welded condition. In both cases, the first cycle possesses a large hysteresis loop, however, as more cycles are completed, the presence of cycle hardening becomes evident due to the occurrence of plastic deformation that degrades the reversibility of the phase transformation..

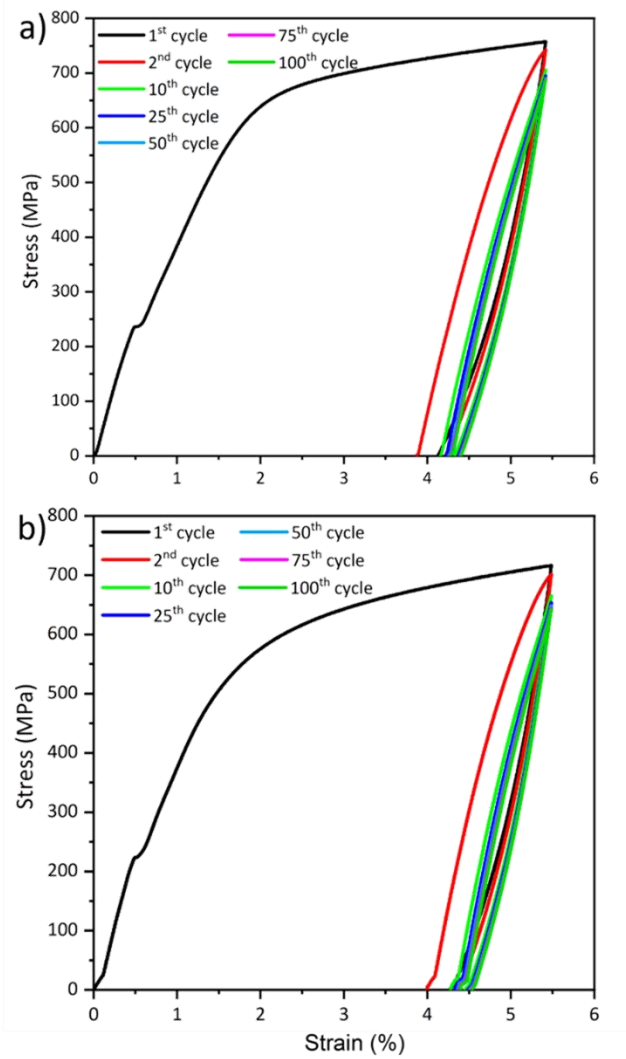


Figure 49 – Load/unload cycling tests performed on: (a) BM and (b) welded samples.

Figure 50 details the evolution of irrecoverable strain, maximum strain and absorbed energy during the 100 load/unload cyclic tests performed. By comparison, it can be observed that in the as-welded condition the percentage of unrecoverable strain exhibits a slight increasing slope after the 20th cycle, while the BM samples appears to become constant, indicating the start of a functional fatigue in the welded condition. This can be explained by the fact that by the end of each cycle, dislocations and defects start to accumulate throughout the various regions that compose a weld. This behavior is further compounded by the non-uniform microstructure of the joint which renders a preferential plastic deformation to occur, rather than a homogenous distribution as it occurs in the BM. Furthermore, the behavior highlighted by the irrecoverable strain curves indicate the development of a ratcheting behavior, which is typical in stress-controlled cycling and was also observed in [133,134]. As explained by Koster et al. [133], the superelastic behavior that this alloy exhibits, occurs due to the low stacking fault energy of the Fe-based SMAs, which provides the means for Shockley partial dislocations to occur and shift easily throughout the austenitic microstructure upon loading. Such process generates stacking faults and induces the martensitic transformation on the alloy. In this particular composition, the VC precipitates alongside the grain boundaries act as barriers to the movement of dislocations, promoting localized stresses in the newly formed martensitic phase. Conversely, during the unloading cycles this accumulated stress is released, pushing the Shockley partial dislocations in a reverse movement, resulting in the reverse transformation of the martensite back to austenite, and consequently causing the partial recovery of strain.

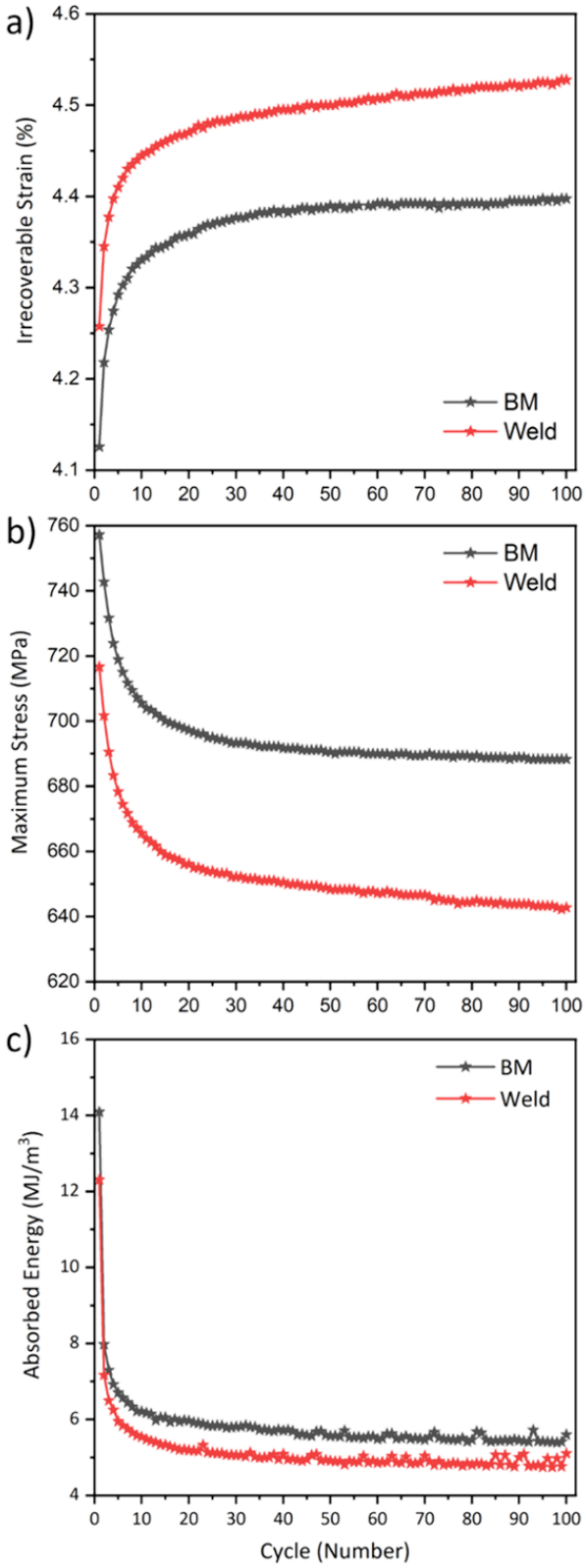


Figure 50 - Results from cycling tests: (a) Irrecoverable strain; (b) maximum stress at 6% strain and (c) absorbed energy.

Figure 50 b) displays the maximum stress for an imposed strain of 6%, obtained from the BM and welded joints at each cycle. As it is possible to observe in both curves, there is a sharp decrease in slope up to the 20th cycle, after which the curves exhibit a steadier decrease in value, with the BM case showcasing a minor tendency for further decrease, stabilizing at approximately 690 MPa. Considering the difference from the beginning of the cycling test to the 100th cycle, the BM exhibits a decrease of 69 MPa, while the weld exhibits a decrease of a total of 74 MPa. In comparison to the BM, this behavior indicates that in the as-welded case a slightly higher functional fatigue can be noted, possibly due to the varying microstructural features that were previously highlighted and are presented along the welded joint. This factor may ease the conditions for the continuous formation of microstructural defects, developed on the larger grains on the HAZ or on the varying dendritic structures in the FZ, easing stress accommodation at each loading step. Similar conclusions on the maximum stress analysis were also reported in [130,133], although using different testing parameters and with prior thermal activation of the SMA.

Furthermore, the amount of absorbed energy upon each cycle is also a relevant property for any engineering applications operating under dynamical loading. The results exhibited by the welded SMA and BM counterpart for this property are shown in Figure 50 c). As it is possible to observe, the first cycles are characterized by the stabilization of the superelastic hysteresis, where a sudden decline on the absorbed energy can be seen in the behavior of both samples. Here the difference between the first two cycles was approximately 6.12 MJ/m^3 in the BM and 5.14 MJ/m^3 in the weld. Further on, with the increasing number of cycles, the behavior exhibited by both samples presents several similarities, with the welded joint absorbing a slightly lower amount of energy throughout the tests. This can be attributed to the inhomogeneous microstructure of the welded joint. Nevertheless, a decrease of approximately 2.38 MJ/m^3 and 2.06 MJ/m^3 from the 2nd cycle to the 100th can be observed in the BM and welded joints, respectively. This indicates a low functional fatigue in both cases, given the relatively constant energy absorption after the 2nd cycle.

4.2.4.9 Conclusions

The weldability of an Fe-Mn-Si-Cr-Ni SMA was assessed by means of advanced microstructural techniques and mechanical characterization. This thorough analysis allows for the following conclusions to be drawn:

- Defect-free welds were obtained on the studied Fe-Mn-Si-Cr-Ni SMA, indicating that it can be a viable solution for structural applications;
- Optical and electron microscopy revealed the formation of a FQZ, a columnar and an equiaxed zone in the fusion zone, which was correlated to the microstructural condition of the welded joints;
- TEM data analysis of the BM and the FZ was conducted, enabling to observe the differences between both regions and to identify a $Fe_5Ni_3Si_2$-type intermetallic with a $P2_13$ cubic crystal structure, within the bulk of the FZ;
- Synchrotron X-ray diffraction permitted the identification of the main phases present in the welded joint. While the BM exhibited mainly the matrix austenitic phase combined with vanadium carbides, the FZ also comprised ferrite and the $P2_13$ intermetallic;
- Electrochemical characterizations were performed revealing that the BM is less prone to corrosion than the FZ. The obtained impedance modulus was ≈307 Ω for the BM and ≈285 Ω for the FZ;
- The microhardness testing data allowed to identify the BM as the region where the maximum values occurred, corresponding to 316.7 ± 2.9 $HV_{0.5}$. The lowest microhardness values in the weld, corresponding to 254 ± 6 $HV_{0.5}$, were observed in the chill zone of the FZ;
- Tensile testing revealed that a maximum strength of 883 ± 18.4 MPa, at strain of 23.6 ± 2.1%, was achieved on the welded joints, corresponding to 85.5 and 64.1% of the BM, respectively. The fracture surfaces indicated that ductile failure occurred.
- DIC analysis performed during tensile testing revealed the different tensile behavior exhibited by the different microstructural features present within the welded joint.
- Cyclic degradation was slightly exacerbated in the welded joint due to the inhomogeneous microstructure that developed across the thermally affected regions.

Overall, good mechanical properties were achieved, showcasing the potential use of this material and GTAW in different industrial settings. Future works envisage studying the dissimilar weldability of this SMA.

4.2.5 Dissimilar gas tungsten arc welding between the dual-phase $Fe_{50}Mn_{30}Co_{10}Cr_{10}$ HEA and a Fe-based SMA

In this sub-section the results concerning dissimilar gas tungsten arc welding between the dual-phase $Fe_{50}Mn_{30}Co_{10}Cr_{10}$ HEA and a Fe-based SMA are presented.

4.2.5.1 Microstructural analysis and microhardness distribution

An overview of the microstructural features and their influence on microhardness distribution of the joint is shown in Figure 51. Starting from an overall perspective of the joint, (see Figure 51 (c)) and considering the center of the joint at the FZ, it is possible to observe the very different microstructure condition in each side, either one closer to each BM. While the SMA BM comprises an average microhardness of 297 ± 11 HV_{300g} the HEA BM is characterized by microhardness values ranging 202 ± 6 HV_{300g}. Such occurs as a direct result of composition, processing methodology carried to obtain each of the BMs and resulting microstructure characteristics, which resulted on the materials already discussed in [25,135,136]. The SMA being characterized by single-phase (γ-FCC) equiaxed austenitic grains (with an average grain size of 11.4 ± 3.0 μm) comprising annealing twins, while the HEA is composed of equiaxed austenitic grains (γ-FCC), with dimensions ranging 40.2 ± 10.7 μm, with martensitic (ε-HCP) lathes in their midst.

Furthermore, moving from the BM with increasing proximity to the FZ, the HAZ becomes apparent in each side of the joint. The microstructural complexity of this region increases due to its proximity to the molten pool during the welding process, thus being characterized by solid state transformations granted the high temperatures experienced in the area. The high temperatures (not being sufficient to melt the material) result on the recrystallization and grain growth mechanisms which can be especially noted in Figure 51 (c) to (g).

Starting from recrystallization, this region of the HAZ goes is developed near the BM, due to the relatively lower (albeit still high) temperatures attained further away from the FZ. Such phenomenon leads to the formation of comparatively strain free grains within a solid-state matrix. Within the present case, such a region cannot be easily perceived in the microstructure when compared to both BMs. Nevertheless, an evident distinction within the HAZ in the microhardness map of Figure 51 makes its clearly visible in the SMA side, while the microstructural differences of the HEA side are highlighted in Figure 51 (e).

Closer to the FZ, it is also possible to observe the grain growth phenomenon which occurs at higher temperatures (omitting the variable of time, which is sensibly the same for

the whole extension of the HAZ during the welding). As such, it is possible to observe that both sides experienced this phenomenon, which translates in an average microhardness of 233 ± 14 HV_{300g} in the SMA side (with an extension ranging from approximately ≈1.2 mm) and 232 ± 9 HV_{300g} in the HEA (over an extent of ≈1.5 mm). Interestingly, in the SMA side of the joint, a partially melted zone (PMZ) can be observed at the frontier of the HAZ and the FZ, where grains were partially molten at their boundaries, leaving striations of solid metal amidst the grains of this area, such can be seen in Figure 51 (f).

Finally, we reach the FZ, at center of the welded joint. This region underwent complete fusion and, in the present case, can be divided in two areas, as perceived in Figure 51 (a), (b) and (c). That is, on the SMA side of the joint the grains tend to be equiaxial dendritic, with an average size of ≈90.5 μm, while large and elongated grains can be found on the HEA side of the joint, exhibiting approximately ≈1.8 mm, measured longitudinally using the line intercept method. Such variation in the microstructure arises from the different growth rate and thermal gradient parameters experience with the proximity to each side of the joint [32].

With the analysis of the EBSD inverse pole figure (IPF) of Figure 51 (b), it is also possible to observe two major phenomenon which occurred during solidification, these being epitaxial and competitive growth. The first can be clearly observed at the fusion boundary of the SMA side of the FZ. There, all grains, upon the start of solidification grew from those already present in the BM. The second, however, can be clearly noticed at the HEA side of the joint on the EBSD IPF map, where the grains that grew aligned with the easy growth direction of the crystal structure in question (in the present case FCC, whose easy growth direction is <001> [35]) tend to achieve lager dimensions, at the expense of grains align in other directions.

Additional compositional analysis revealed that the FZ is homogenous throughout its whole extension. However, microhardness measurements on the joint reveal that an average of 206 ± 7 HV_{300g} can be found within the FZ region.

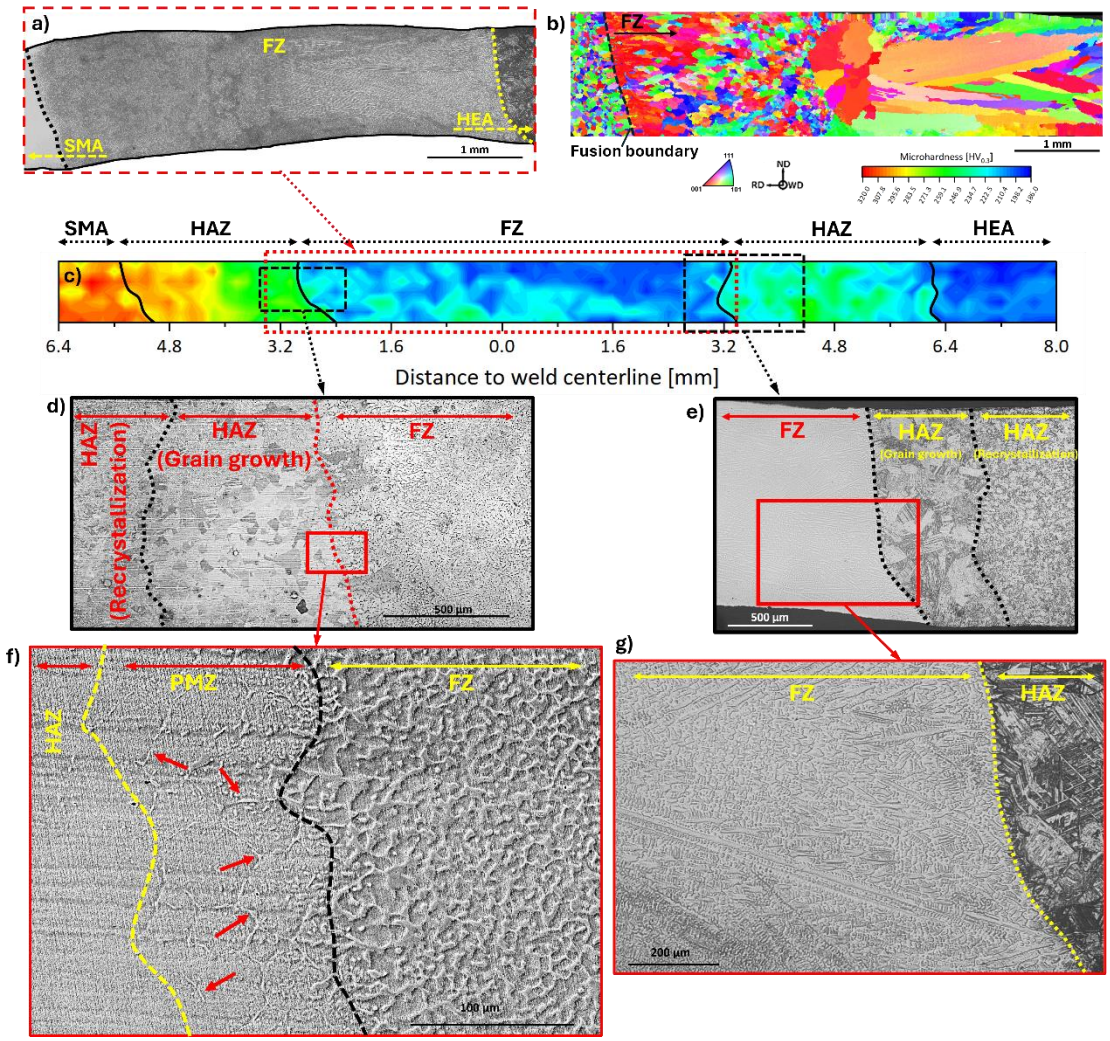


Figure 51 – Microstructural features and their influence on microhardness on the joint: (a) Optical microscopy of the welded joint and (b) EBSD IPF of the FZ highlighting grain orientation; (c) microhardness distribution across the full extension of the joint and detailed view of the HAZ close to the (d) SMA and (e) the HEA BMs. Closer visualization of the transition from the HAZ to the FZ can be seen in (f) highlighting a PMZ and in the (g) highlighting the transition from the HEA side of the joint.

Further analysis was executed in three regions of the FZ, with two being chosen with attention to the proximity to each BM and the third being located at the center of the joint. Such regions were inspected via TEM and APT, with the most significant results being depicted in Figure 52. There, a clear indication of the presence of two crystal structures (γ-FCC and ε-HCP) in the FZ can be seen in Figure 52 (a), where the atomic arrangements highlight two martensitic lathes (with an HCP structure) being separated by the matrix, which is composed by a FCC crystal structure. APT tips gathered from the same analyzed regions, reveled that a homogeneous distribution of the elements that compose the matrix of the joint was achieved

during welding (see Figure 52 (c)), which is coherent with the solid solution effect characteristic of HEAs [3].

Furthermore, provided that the SMA BM has VC inclusions, that are effective in improving its mechanical performance, it also possible to observe that the high temperatures achieved in the molten pool were not sufficient for their fusion (whose melting point is ≈2650°C [137,138]), although partial melting is possible to occur. Such precipitates can be seen in Figure 52 (b), thus showcasing their existence within the FZ.

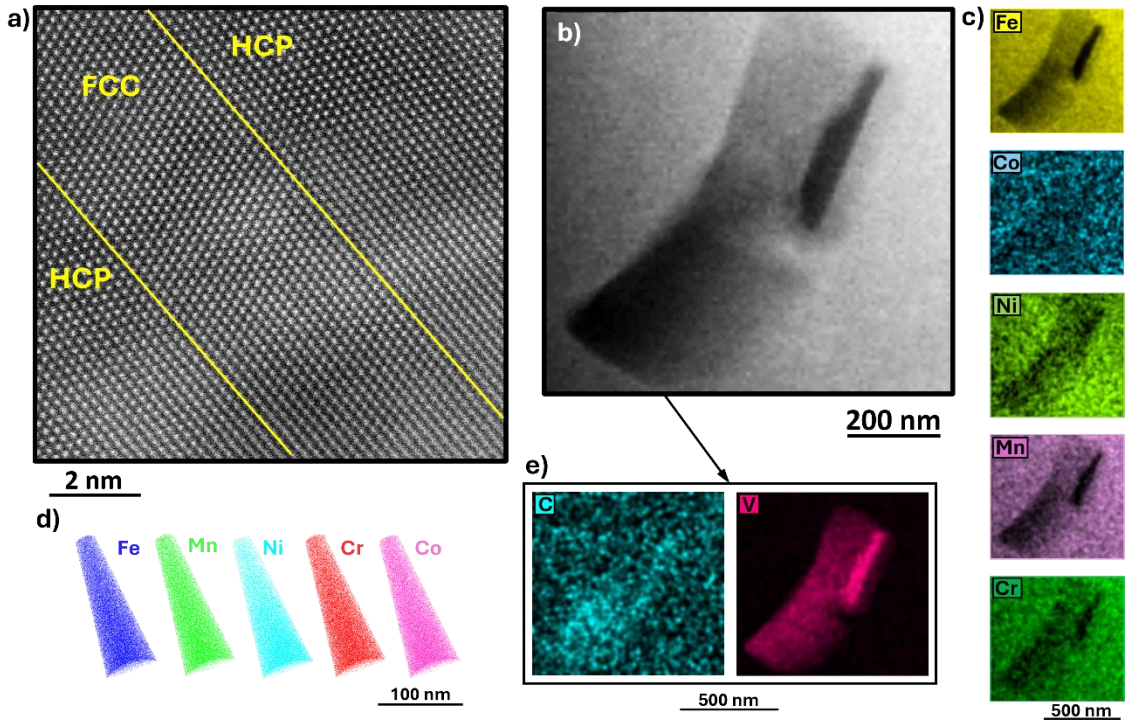


Figure 52 – Advanced characterization of the FZ using TEM and APT: (a) atomic arrangements corresponding to γ-FCC and ε-HCP phases; (b) VC precipitate and corresponding composition maps in (c) and (e); APT tips revealing compositional homogeneity within the FZ.

4.2.5.2 Synchrotron x-ray diffraction

Although previously detailed advanced analysis techniques can grant extensive knowledge on the condition of the FZ, a more holistic approach through synchrotron X-ray diffraction was carried to inspect the crystal structures over a wider area, over the full thickness of the joint (thus, not relying only on surface features). The obtained X-ray diffraction data can be observed in Figure 53. There, a complete map of the joint, produced by iterating throughout the full extension of the joint, is displayed in terms of intensity and interplanar spacing (calculated using Bragg's law of diffraction [73]) showcased by the diffraction peak

(2 0 0) of the γ-FCC phase. Such peak was selected since it is the crystallographic equivalent of the <0 0 1> direction and is distanced from the influence of other diffraction peaks.

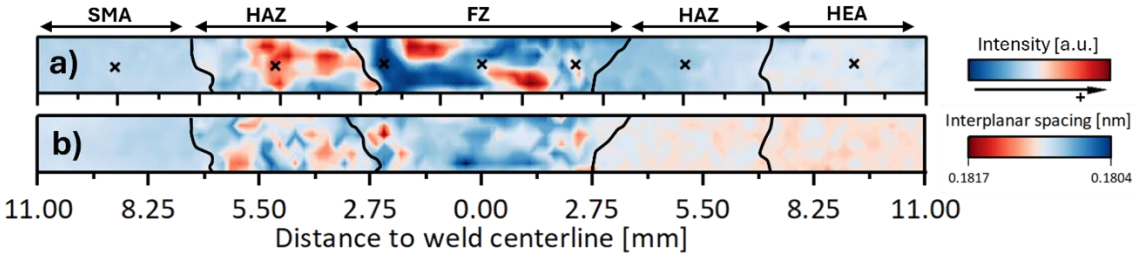


Figure 53 – Synchrotron x-ray diffraction throughout the welded joint: (a) Intensity distribution map of the (2 0 0) peak and (b) Interplanar spacing map. The diffraction patterns taken from the regions marked in (a) correspond to those presented in Figure 54 and Figure 55.

Overall, analyzing the intensity distribution reveals the different regions of the welded joint, which are also highlighted through the interplanar spacing map along the joint. There, the higher values were achieved on the HAZ of the SMA side and the lower on the FZ (with exception to individual points). Such differences are related to the different texture achieved on each particular region due to their specific processing/formation conditions and consequent exposure to high temperatures. However, due to the different compositions that compose the welded joint such a comparison can only be done qualitatively.

Furthermore, a closer inspection on specific diffraction patterns of each BM and corresponding HAZs is displayed in Figure 54 (a), (b), (c) and (e), alongside with the FZ which is shown in Figure 55. There, smaller intensity peaks corresponding to second harmonic reflections were disregarded and marked in Figure 55. As such, it is possible to observe that the SMA BM is composed of a γ-FCC matrix and VC precipitates, as expected. Furthermore, the presence of the γ-FCC and ε-HCP phases are also evidenced in the HEA BM, where MnO can be also detected.

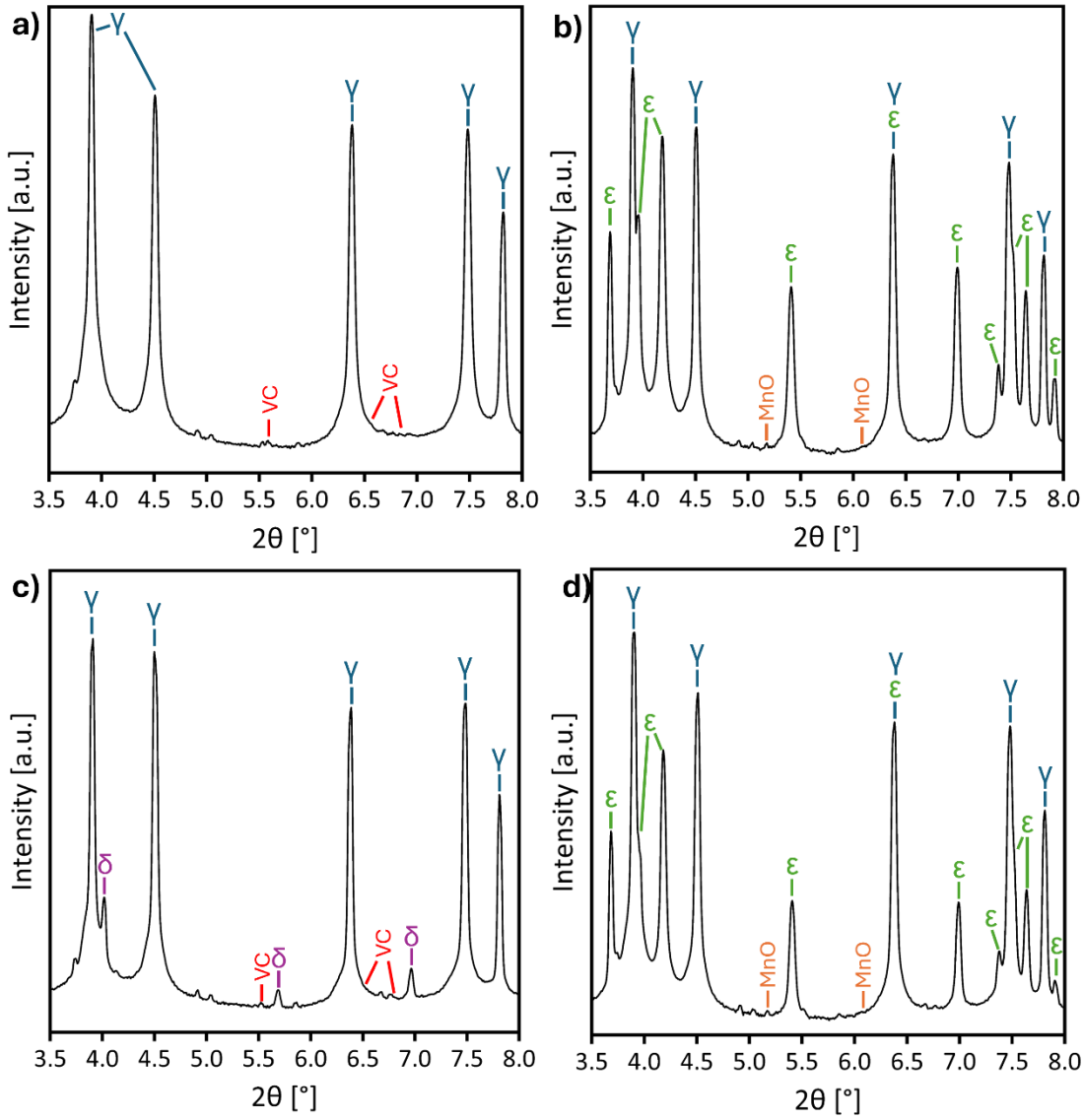


Figure 54 – Representative diffraction patterns from the (a) the SMA BM, (b) the HEA BM, (c) the HAZ from the SMA side and (d) the HAZ from the HEA side of the joint.

Observing each HAZ it can be seen that different phases arose due to the high temperatures that developing during welding. For instances, the SMA HAZ beyond being composed of γ-FCC matrix and VC particles, showcases the formation of ferrite (δ), indicating that recrystallization and grain growth are not the only phenomena occurring within this region. Nevertheless, on the other side of the joint, the HAZ exhibits the same phases as those seen in the HEA BM, as expected from [25].

Furthermore, observing three representative diffraction patterns within the FZ (considering its distance to each BM: near the SMA, in the bulk of the FZ and near the HEA), it can be seen that over its full extent it is composed by an amalgamation of all the phases present

in each of the original BMs, with exception to δ and MnO. Interestingly, small intensity peaks corresponding to sigma phase (σ) were also encountered, hinting for the fact that such phase may have nucleated due to elemental segregation and constitutional undercooling conditions during solidification within the FZ.

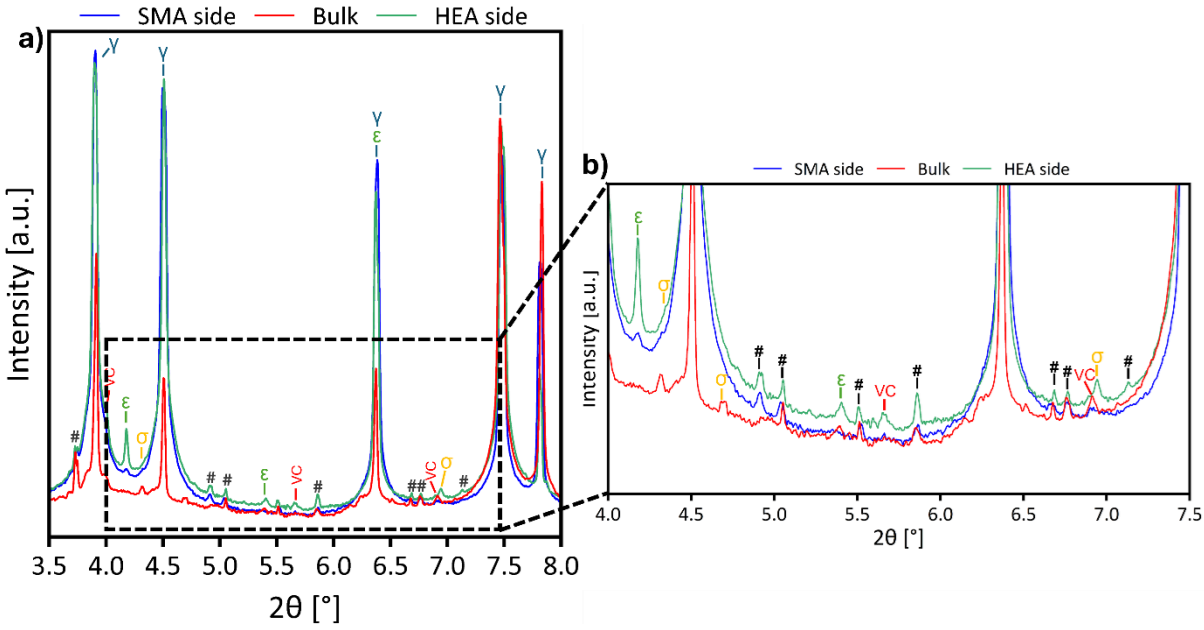


Figure 55 – (a) Superimposition of the diffraction pattern taken from the FZ, namely closer to each of the BMs and at its bulk. (b) Detailed view of the low intensity diffraction peaks corresponding to phases with lower fraction within the FZ.

4.2.5.3 Tensile testing

Given that a thorough analysis of the microstructure was conducted, the next logical step is to analyze the resultant mechanical performance of the dissimilar joint via tensile testing, which yields some of the most important results for structural engineering (refer to Figure 56). Overall, the SMA yielded a maximum tensile stress of approximately 980 MPa, with eventual fracture occurring at a strain of ≈37.8%. Conversely, the HEA attained a maximum tensile stress of ≈725 MPa, finally fracturing at ≈38.9%. The welded joint, however, managed to reach ≈671 MPa, at a strain of ≈15.5 %, upon which it fractured along the interface between the HAZ and the FZ in the HEA side of the weld. DIC analysis of the mechanical behavior of the joint, indicated that FZ was the region where most of the strain was accommodated, being followed by each HAZs and BMs, where the SMA BM exhibited the least amount of strain in the joint during testing. Such mechanical behavior can be related to the different microstructural features along the joint, where according to the Hall-Petch effect a larger grain size induced a lower material strenght, thus causing the regions with a larger grain size to deform more

easily. Alongside with this, there are the TWIP and TRIP phenomena associated to the HEA, that with increasing plastic deformation become more prominent, thus causing the harder, albeit more brittle, ε-HCP phase to increase in the microstructure. Such can increase the microstructural discontinuity on the joint, by inducing phase transformation, twinning barriers and, consequently, the presence of defects, leading to the eventual fracture on the weaker regions on the weld. Besides this, another factor that comes into play is the presence of VC precipitates within the SMA and the FZ, which can hinder dislocation movement, and thus assisting in improving the localized mechanical properties of the joint.

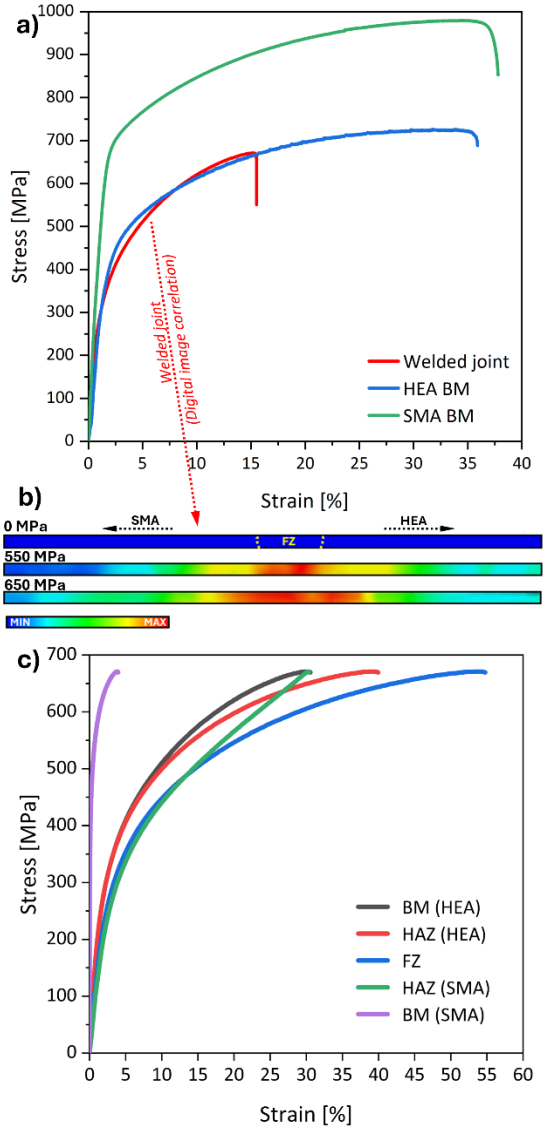


Figure 56 – (a) Representative mechanical response to tensile stress of the welded joints, the SMA and the HEA BMs; (b) DIC results showcasing local strain distribution before fracture;(c) DIC point analysis obtained during tensile testing.

Upon eventual fracture at the boundary between the FZ and the HAZ of the HEA side, failure analysis aided by electron microscopy was performed, as displayed in Figure 57. In line with this, the presence of the precipitates on the joint, although granting superior mechanical performance to the joint, can also act as stress concentrators leading to the initiation of micro-voids during tensile testing.

Observing closely, evidence of ductile-like fracture can be found through the round-shaped dimples present in the fracture surface, where Mn-rich precipitate [85] of a spherical shape can be observed in their midst. These, granted from their geometry, tend to have a uniform stress distribution, showcasing a lower tendency for void initiation. However, the same cannot be mentioned for the VC precipitates, whose plate-like shape can increase stress concentration along their edges, resulting the cleavage voids, which tend to coalesce and cause premature failure of the joint. Nevertheless, the main mechanism of failure on the joint is ductile fracture.

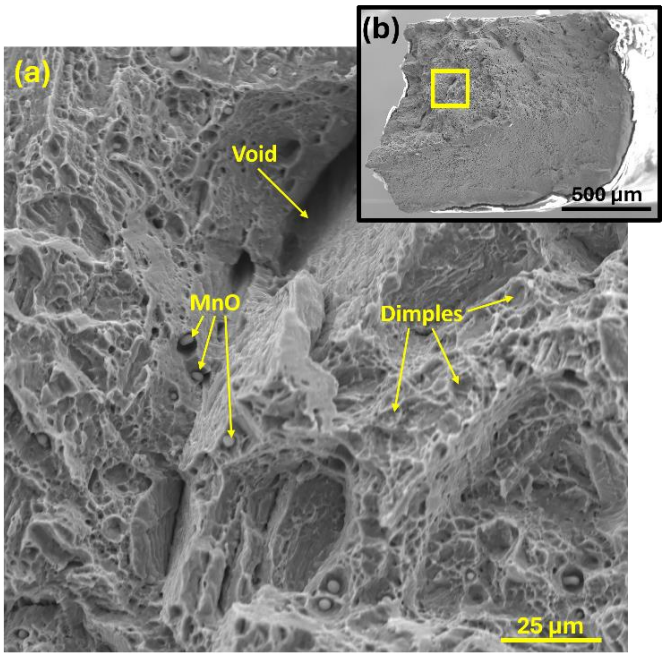


Figure 57 – (a) Fracture surface of the gas tungsten arc welded dissimilar joint. (b) Depiction of the fractured tensile specimen marking the analyzed region.

4.2.5.4 Conclusions

Dissimilar welding via GTAW, between a metastable FeMnCoCr HEA and a Fe-based SMA was successfully performed. The following conclusions can be drawn.

- No welding defects were encountered in the joints, proving a good weldability between the two materials.
- Advanced characterization techniques, including TEM, APT and SXRD enabled to observe the phases present throughout the full extension of the FZ. o special emphasis was the formation of the δ phase in the HAZ of the SMA side and the formation of sigma phase within the FZ.
- Mechanical testing revealed that the joint could achieve a maximum stress of 671 MPa while fracturing at a strain of ≈15.5 %, due to the microstructural features associated to each region of the weld. These are excellent mechanical properties for a dissimilar joint, albeit lower than the mechanical performance of each BM.

Overall, the presented work give emphasis to the possibility of matching HEAs and other advanced engineering alloys for modern day engineering applications.

4.2.6 Section summary

A complete assessment of the weldability and mechanical performance of the $Fe_{50}Mn_{30}Co_{10}Cr_{10}$ HEA was accomplished. In addition to this, contribution to the knowledge regarding the weldability of an Fe-based SMA was also performed, thus paving the way to further developed research on the dissimilar weldability between these two advanced materials.

Overall, with all the analyses performed, it can be stated that the FeMnCoCr HEA stands as a good candidate for structural applications, considering both similar and dissimilar welding.

4.3 Microstructure evolution and mechanical performance of a gas tungsten arc welded AlCoCrFeNi HEA

4.3.1 Section highlights

In this section investigation of the weldability of the $AlCoCrFeNi_{2.1}$ HEA was performed. On a first instance, the introduction of TiB_2 inoculants into the molten pool is accessed and compared to a similar joint performed in the same HEA. Such envisages unveiling the microstructure evolution and its correlation with the joint thermal cycle and/or with the addition of the TiB_2 particles. Additionally, dissimilar welding joints obtained between this HEA and 316 L stainless steel are also investigated.

4.3.2 Role of TiB_2 inoculation particles during welding of a AlCoCrFeNi high entropy alloy[4]

In this work, GTAW was performed with and without the addition of TiB_2 particles on the AlCoCrFeNi HEA system. In this section we delve into the microstructural characterization on both types of samples, highlighting the differences between the inoculated and non-inoculated conditions, and establish a proper understanding of the microstructure of both joints, making it possible to correlate these with their corresponding mechanical performance.

This initial section is divided into four subsections. The first starts to introduce the welded joints at the macroscopic level, highlighting their differences and in the following sections we particularize the discussion to the regions of interest characteristic of these joints, namely the BM (used as benchmark), HAZ and FZ. This will make it possible to unveil the microstructure evolution and correlate it with the joint thermal cycle and/or with the addition of the TiB_2 particles.

[4] The results discussed in this sub-section are already published in the Journal of Alloys and compounds, corresponding to reference [155].

4.3.2.1 Macroscopic overview of the welded joints

Figure 58 displays the macrostructure of the welded joints in the non-inoculated (a) and TiB_2-inoculated conditions (c), allowing to detail the microstructural changes induced by the presence TiB_2 on the molten pool during welding. Additionally, electron backscattered diffraction (EBSD) images quality index (QI) maps overlayed with inverse pole figure (IPF) maps are also displayed for each type of sample (Figure 58 b and d, respectively).

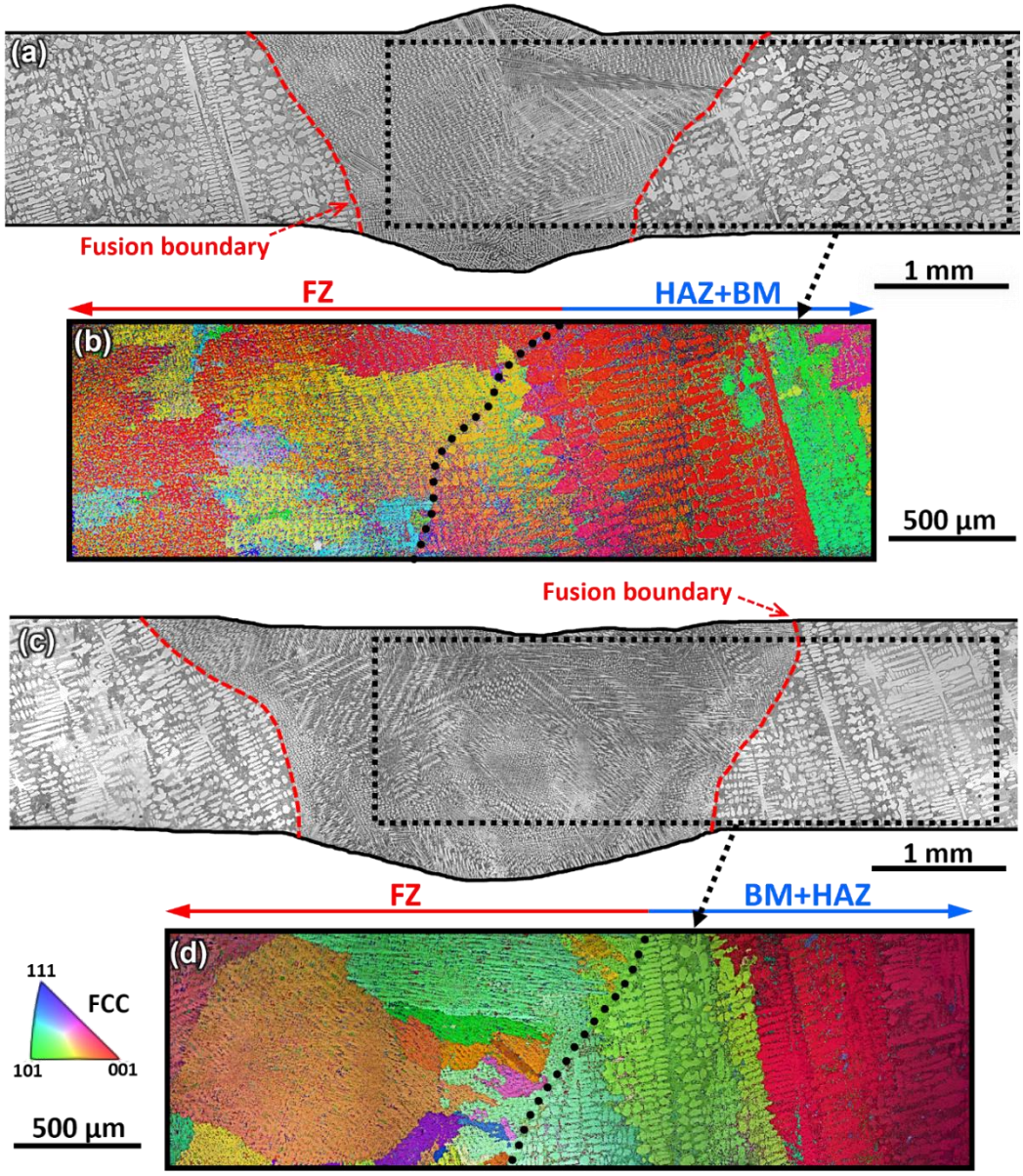


Figure 58 - Macrostructure of the GTAW AlCoCrFeNi HEA joints: (a) and (c) correspond to the optical micrographs of the non-inoculated and inoculated joints, respectively, while (b) and (d) comprise the superposition of the EBSD IQ map of the IPF map and the non-inoculated and inoculated materials, respectively.

It is possible to observe that there is a distinct morphology of the FZ in both samples although the welding parameters used for both conditions were kept the same. These differences in weld shape resulted from the alteration of the electric arc conditions due to the introduction of the TiB_2 particles on the material top surface. That is, due to its good electrical and thermal conductivity [139,140], the TiB_2 layer aided in the conduction of the electric current to the material, allowing the same amount of heat input to be supplied to the joint in a more restricted area, thus increasing the energy density associated to the process. Since the inoculant particles have a higher thermal conductivity, there will be a more pronounced energy transfer to the BM, which aids in increasing the dimension of the FZ. These combined effects alter the weld thermal cycle and extend the length and geometry of the FZ. In fact, the shape of the FZ changed from ≈4.7 mm in the face and ≈3.1 mm in the root of the weld, in the non-inoculated case, to a joint with a face width of ≈3.7 mm and a root width of ≈2 mm for the inoculated samples.

Microstructure differences that arise from the distinct weld thermal cycle in the heat affected zone (HAZ) are not easily identifiable due to the dendritic nature of the BM microstructure. This is related to the previous processing of the original BM where the relatively slow cooling upon casting will delay eventual solid-state transformation to occur in the HAZ of the present joints during welding.

For improved visualization of the joint macrostructure, Figure 58 b) and c) displays low magnification EBSD maps. It can be observed that for the non-inoculated samples there is an increased tendency for the FZ grains to exhibit a red coloration indicating a preferred texture along the <001> direction, this being the easy growth direction of FCC materials. In the inoculated joint, the developed texture is not so strong. This can be ascertained to the heterogeneous nucleation promoted by the TiB_2 particles. It can be observed that, although the microstructural differences are evident, the FZ grains also indicate that growth in other directions also occurred, resulting from the effect of the introduction of inoculants in the molten pool.

With the overall perspective on the welded joints established, the following sections will discuss the microstructural differences present in both welds. Firstly, attention will be given to the initial condition of the BM followed by the analysis of fusion boundary (FB), finally

the discussion of the microstructural features comprising the FZ will be analyzed. Further advanced characterization methods of the welded joints will also be provided alongside their mechanical characterization.

4.3.2.2 Description of the AlCoCrFeNi HEA base material

To ensure the structural integrity of the obtained joints, it is crucial to evaluate their microstructure at a higher resolution scale. Figure 59 illustrates the initial condition of the AlCoCrFeNi HEA BM used in this study. As can be observed from Figure 59 (a), although the present base material came from the same ingot as in [141], where a fully eutectic FCC (white regions) + B2 BCC (black regions) microstructure was observed, here, a primary FCC phase followed by the eutectic FCC + B2 BCC constituent is observed, highlighting a phase structure offset regarding the nominal eutectic composition of the BM.

Such offset can be explained by the cooling conditions experienced by different regions of the ingot, which were left to cool slowly until reaching room temperature. These conditions can provide the means for the formation of a higher amount of primary FCC phase. That is, the cooling rate at which the liquid and subsequently the solid material experiences, affects the time available for diffusion between the solid and liquid phases. Depending on the region of the ingot, different locations experience distinct cooling conditions, potentially giving rise to a heterogenous structure along the ingot. Moreover, faster cooling rates can yield a more uniform eutectic microstructure, while slower cooling can result in the formation of larger grains, compounded by the possible deviation of the liquid composition a solute rich/poor state (depending on the elemental availability and phases developed).

The clear depiction of the microstructural features of the BM was obtained by SEM (refer to Figure 59). Here the distinction between the primary FCC phase and eutectic FCC + BCC constituents are compared in terms of their elemental distribution using energy-dispersive X-ray spectroscopy (EDS). From these EDS measurements (refer to Figure 59 (b), it can be qualitatively observed that the FCC phase has a higher amount of Cr, Co and Fe, while the B2 BCC phase is richer in both Al and Ni.

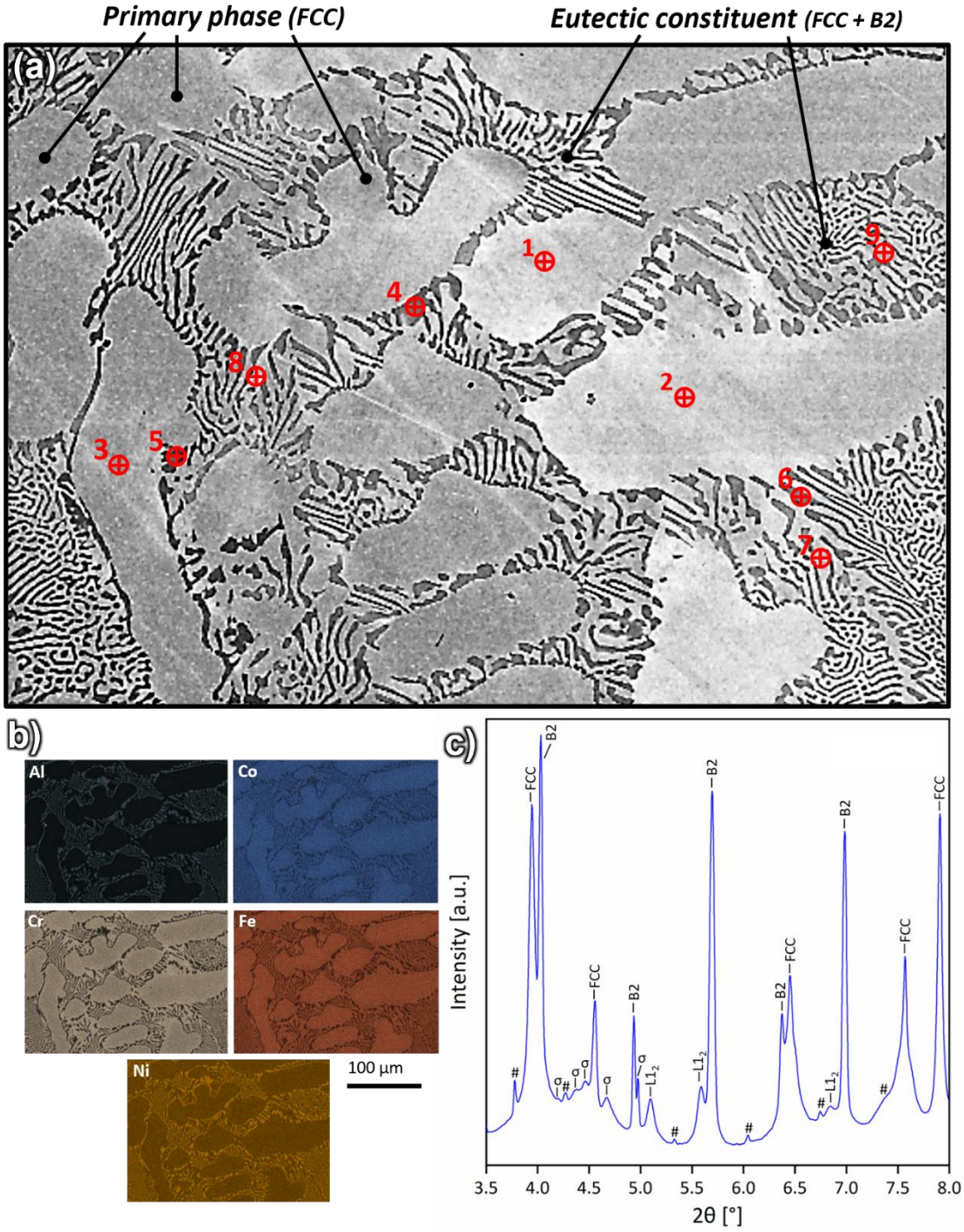


Figure 59 – (a) Initial condition of the AlCoCrFeNi HEA BM showcasing large primary FCC grains and the eutectic (FCC + B2 BCC) constituents observed by SEM and (b) corresponding EDS maps. The points marked in (a) correspond to the EDS point analysis results exhibited in Table 10. In (c) a representative synchrotron X-ray diffraction pattern indicates the presence of more (nanometric) phases in the BM.

Quantification of the composition of the BM is displayed in Table 9. Here it is possible to observe that deviation of the nominal composition occurred, highlighting the non-uniform condition of the ingot from where the plates prior to welding were obtained. For comparison, the composition obtained in the BM in [141], which came from the same ingot, is also presented.

Table 9 – Compositional comparison of the AlCoCrFeNi HEA base material.

	Composition (at. %)				
	Al	**Co**	**Cr**	**Fe**	**Ni**
Nominal composition	16.4	16.4	16.4	16.4	34.4
BM (from [141]**)**	11.2	13.0	15.7	18.2	41.9
BM [present study]	16.0	16.1	18.0	17.1	32.8

Comparing the BM (from this study) with the nominal composition of the eutectic condition of the alloy, it can be perceived that the Al, Co and Ni content is reduced in 0.4, 0.3 and 1.6 at. %, respectively. Conversely, the amount of Cr and Fe is increased, with Cr presenting the highest variation from the nominal composition of the HEA (nearly 1.6 at. %). Such allows us to infer upon the microstructure that formed during solidification of this region of the ingot. The elemental deviation from the nominal composition indicates that the FCC phase has higher propensity to form at higher temperatures, while the B2 BCC phase requires the appropriate conditions to form as part of the eutectic structure. Such can be expected from the preferential elemental enrichment of each phase. This can occur due to the large availability of the components that tend to ease the nucleation of the Co, Cr, and Fe-rich FCC phase, while the scarcer Al and Ni combination required for the nucleation of the B2 BCC phase is only attained when the necessary temperatures and elemental proportions for the B2 BCC phase formation are reached [141,142].

Further quantification of the site-specific phases on the BM marked on Figure 59 (a) can be found in Table 10. There, we can observe that the composition of the large FCC grains (which formed first during solidification) is different from the composition of the FCC phase within the eutectic constituent. This attests to the high entropy effect characteristic of these

novel metals that are capable of forming a crystal structure from a wide variety of atoms. The same can be said for the B2 BCC phase.

Table 10 – EDS single point analysis results. The scanned regions are marked in Figure 59 (a).

Location	Phase	Point	Composition (at. %)				
			Al	Co	Cr	Fe	Ni
Large grains	FCC	1	13.1	16.9	22.8	19.0	28.2
		2	11.6	18.4	23.9	20.8	25.2
		3	11.7	20.8	18.5	20.2	28.8
Eutectic constituent	B2	4	12.9	18.2	19.5	18.6	30.7
		5	10.7	15.7	21.1	21.7	30.8
		6	15.6	18.4	21.1	26.4	27.5
Eutectic constituent	FCC	7	29.9	9.5	11.0	13.3	36.3
		8	23.8	13.4	13.0	17.3	32.4
		9	25.0	13.0	15.2	19.4	27.5

Microscopy techniques only yield information at the surface level of the material. To unveil the bulk microstructural condition, it is necessary to resort to other advanced characterization techniques. Synchrotron X-ray diffraction was performed on the BM of the AlCoCrFeNi, with the associated diffraction pattern being shown in Figure 59 (c). The diffraction data reveals the presence of more phases on the microstructure other than the FCC and B2 BCC phases previously identified by optical and electron microscopy. In fact, it is possible to identify diffraction peaks corresponding to sigma (σ) and L12 FCC phases as well. Such results are compliant with what is expected from the literature regarding this HEA [143–146] and may result from elemental segregation under the solidification conditions taken by this portion of the ingot during its manufacturing, as well as minor material contamination of the raw material used to cast the BM.

Considering the abovementioned compositional differences and the phases encountered via X-ray diffraction, thermodynamic calculations were used to generate an equilibrium phase diagram of composition (nominal and real) as function of Cr (the element with the most deviation from the nominal composition). These results are depicted in Figure 60.

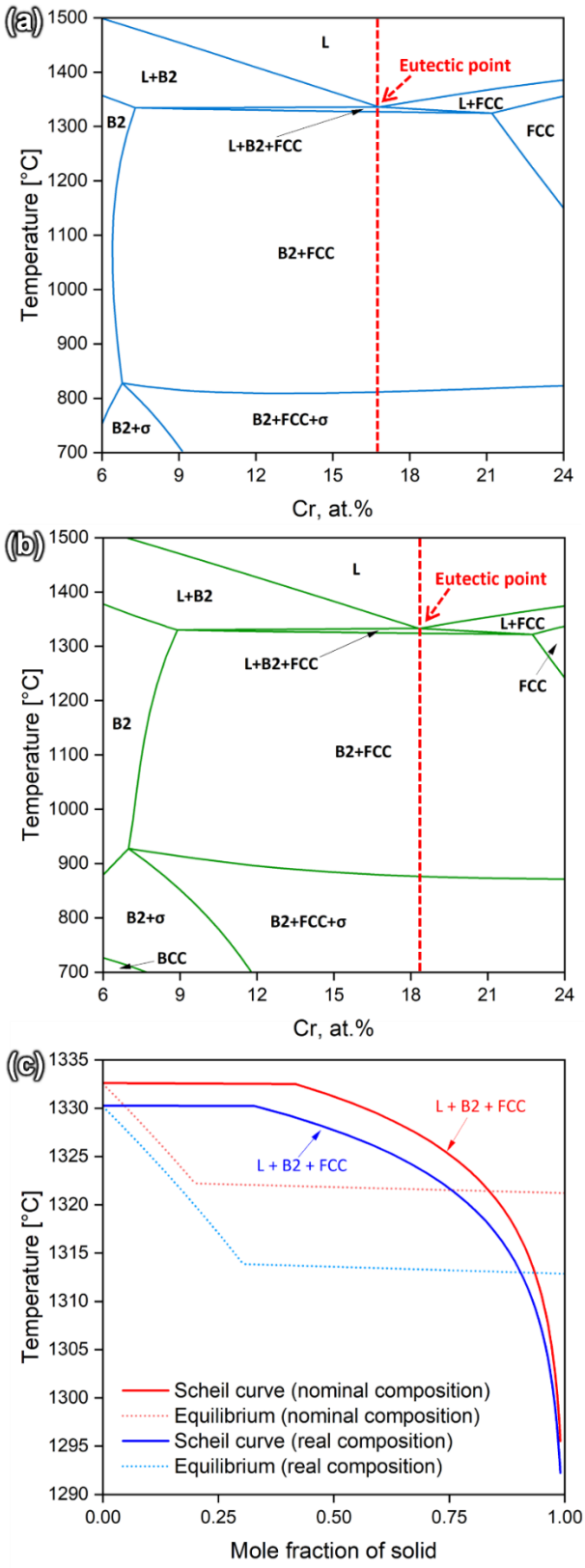


Figure 60 – Phase diagrams calculated considering: a) nominal composition and b) real composition (L stands for Liquid phase). The Scheil solidification curves of both compositions are shown in c).

Clearly, the different compositions result in distinct conditions for phase nucleation during solidification. A shift on the eutectic point can also be observed going from 16.8 to 18.4 at. % of Cr. Equilibrium conditions are based in ideal cooling conditions, which are very difficult to occur in actual thermomechanical processes, such as casting and welding. Nevertheless, according to the equilibrium and Scheil solidification curves of Figure 60 it is possible to expect the formation of B2 BCC and FCC phases, thus in good agreement with the previously shown characterization data (microscopy and X-ray diffraction). The only variation between the Scheil calculation data resides in the temperature at which the liquid starts to solidify, where a minor difference of ≈3°C is noticeable between them.

As such, considering the nominal composition of the HEA, it is possible to infer that the FCC phase starts to solidify in a first stage until reaching the point where the FCC and the B2 BCC phases appear simultaneously within the Liquid phase as a eutectic reaction. At this point, both the B2 BCC and FCC phases start to nucleate from the interdendritic fluid that remained in the liquid state [35]. Such explains why it is possible to observe large FCC grains in the BM ranging from smaller to larger dendrites (52 ± 20 µm vs 649 ± 195 µm, respectively), while in the eutectic domain their size is considerably smaller, with the interdendritic distance between them being 2.7 ± 0.5 µm.

4.3.2.3 Clarifying microstructural differences at the FB of both welded joints

To further evaluate the impact of the welding process on the material microstructure, attention is now devoted to the FB. This region comprises both the microstructural condition of the HAZ and its frontier with the FZ. Again, due to the dendritic microstructure that developed during casting of the HEA BM, distinguishing the HAZ from the BM proves to be difficult using solely microscopy techniques. Since the heat input for both types of joints, i.e., inoculated and non-inoculated conditions, is similar, changes between both the HAZ are expected to be minimal. With this into account, Figure 61 displays a representative synchrotron X-ray diffraction pattern taken from the HAZ, allowing to identify the phase structure at this location. The HAZ displays a different microstructural condition than that of the BM, as the presence of low intensity peaks corresponding to σ and L12 FCC phases are almost non-existent, suggesting a decrease in the phase volume fraction of both phases. This can be explained

based on imposition of a localized heat treatment owing to the weld thermal cycle, which will promote phase dissolution (partial or full, depending on the distance to the heat source). Regarding this, considering the compositions between the nominal and effective composition (refer to Figure 60), it is expected that regions of the joint reaching ≈1300°C develop FCC and B2 BCC phases within its microstructure upon solidification. At the same time, regions of the welded joint attaining temperatures within the 800 to 900°C range are expected to become enriched with σ phase. As such, diffraction peaks corresponding to the FCC, B2 BCC and σ phases can be observed in the HAZ (refer to Figure 61), which is in line with the optical and electron microscopy observations previously shown in Figure 58 and Figure 59.

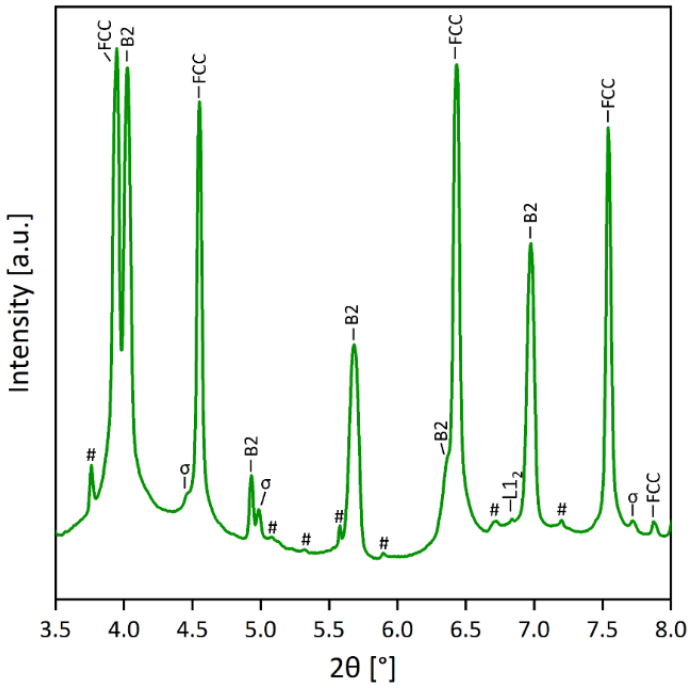


Figure 61 – Representative synchrotron X-ray diffraction pattern from the HAZ. (# stands for the low intensity 2nd harmonic diffraction peaks that do not correspond to any structure present on the alloy)

In opposition to the HAZ, the FZ on both samples exhibits evident microstructural differences. To evaluate the changes induced in the FZ by the introduction of TiB_2 particles, and compare them with the non-inoculated condition, high magnification optical images of the FB of both welded joints are depicted in Figure 62.

Starting with the non-inoculated sample, shown in Figure 62 (a), the transition from the HAZ to the BM evidences a steep variation between the large dendrites comprising the

primary FCC and the FCC + B2 BCC eutectic microstructure in their midst (similarly to the BM) and smaller equiaxial dendritic structures that are formed within the FZ boundaries. Without the addition of TiB2, the microstructure of the FZ, tends to exhibit equiaxed FCC dendrites surrounded by the FCC + B2 BCC eutectic constituents within the interdendritic space. Here, as observed, major changes in microstructure of the FZ occur on the grain size and morphology, where there is a refinement compounded by a change in morphology from large columnar grains in the BM to equiaxial dendritic ones in the FZ, indicating the impact of the cooling rate on the solidification structure. In fact, the cooling rate of the FZ is higher than that experienced by the material during casting, thus justifying the morphological differences observed.

A different microstructural condition at the FB is found when the TiB2 inoculants are added during GTAW (refer to Figure 62 b)). In this case, beyond the solidification parameters, namely temperature gradient (G) and the growth rate (R), that reign over the size and morphology of the microstructural features developed in the non-inoculated welded joints, the introduction of TiB2 on the FZ allows for the intensification of heterogeneous nucleation [32], as these high temperature solid particles aided in the generation of more nuclei which can then evolve to grains. This adds another factor, beyond the cooling rate, that significantly influences the developed solidification structures in the inoculated FZ microstructure.

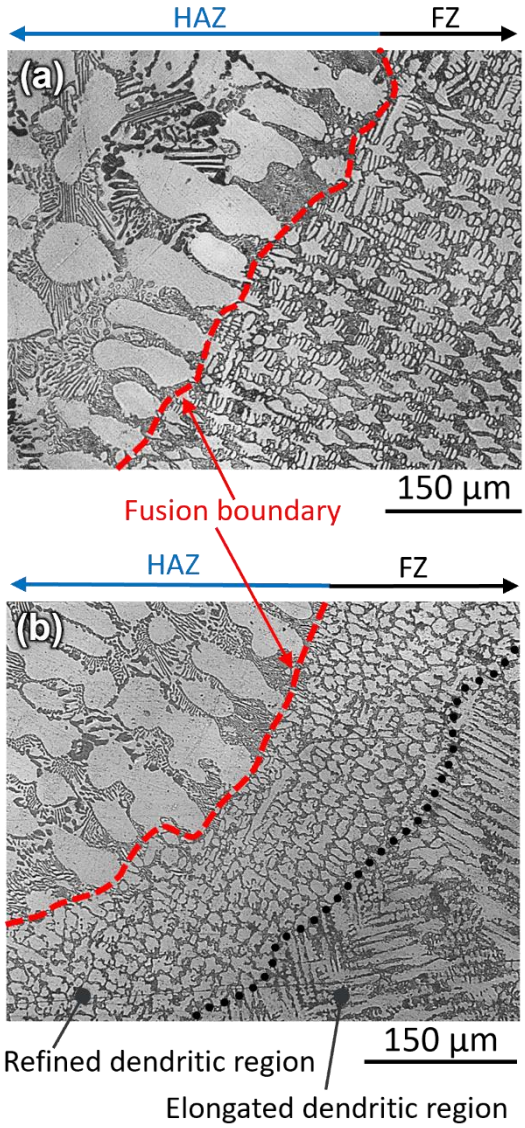


Figure 62 – Detailed optical micrograph view of the microstructure features at the HAZ/FZ boundary: (a) fusion boundary of the non-inoculated joints and (b) fusion boundary of the TiB_2 inoculated samples.

Here, the FZ of the inoculated material exhibits refined equiaxed dendritic grains closer to the fusion boundary, whereas when going towards the bulk of the FZ, small columnar dendrites (reaching ≈ 80 µm of length) grow perpendicularly to the FB towards the bulk of the FZ. This shows that the molten pool's solidification conditions changed to the extent that the structures formed upon cooling deviated from the expected microstructural characteristics of the non-inoculated samples, namely the equiaxed FCC dendrites surrounded by FCC + B2 BCC constituents. The refined dendritic region evident at the FB, is often referred to as a fine equiaxed zone (FQZ) in the literature [111,147,148]. Beyond the fast cooling due to the heat sink

effect caused by the proximity to the BM, its formation can be associated with heterogeneous nucleation, which in the present case can be induced by the TiB_2 particles. Nonetheless, other factors such as welding parameters and fluid flow conditions along the torch path also contribute to its formation and extension. However, since the major difference between the two conditions is the presence of the TiB_2 particles, it can be stated that these particles are the fundamental factor promoting this heterogeneous nucleation phenomena. It should be mentioned that the presence of the FQZ in the microstructure can be detrimental to the mechanical properties by contributing to appearance of a complex stress state of the joint, being this location a region where weld defects, such as microcracks, are prone to occur, since this region is often characterized by its poor intergranular strength, leading to a weak resistance to cracking during mechanical solicitation [147].

From the analysis of the FB, it can be concluded that a different microstructural condition is clearly identifiable near the transition between the HAZ to the FZ. Nevertheless, most changes due to the introduction of the TiB_2 in the molten pool are visible in the bulk of the FZ, which is discussed in the next section.

4.3.2.4 Bulk fusion zone evolution in inoculated and non-inoculated samples

The microstructure features present at the bulk of the FZ on both inoculated and non-inoculated conditions are presented in Figure 63, alongside with the corresponding IPF EBSD maps. As mentioned previously, the microstructure of the non-inoculated sample is comprised mostly of large equiaxial dendritic FCC grains surrounded by the eutectic constituents, FCC + B2 BCC phases. The same, however, does not occur on the TiB_2-inoculated sample where an inexistent uniformity of grain structures is present, ranging from small refined equiaxial grains to columnar dendritic structures distributed amidst the microstructure. To understand these differences, it is important to comprehend how the addition of TiB_2 can affect the solidification conditions of the molten pool, namely what occurs during the welding process that can modify the G and R values to the point of achieving such differences in the FZ.

Given the high melting point of TiB_2 (2790 °C, from [149]), heterogeneous nucleation is intensified in the presence of these solid particles in the melt pool, effectively reducing the

energy barrier for grain nucleation to occur. This allows for new grains to start developing at the TiB_2 particles interfaces, as these inoculants may not dissolve completely due to their size (5-8 μm) and the temperature distribution attained on the molten pool. Such phenomenon differs from epitaxial growth, where grains nucleate from the solid material present at the fusion boundary, where the temperature of the FZ is at its lowest. The introduction of inoculants can, therefore, promote the development of a finer grain structure, as evidenced by the direct comparison of both FZ.

However, GTAW is known for being able to reach temperatures as high as 20000 °C in the electric arc [32,150]. Due to the extremely high temperature that can develop in the FZ of GTAW joints, there is the possibility for (partial) dissolution of the high temperature TiB_2 particles. This will promote changes in the chemical composition of the FZ and can alter the melting point of the liquid material, and thus also modify the conditions for which heterogenous nucleation may occur within the FZ [32,35].

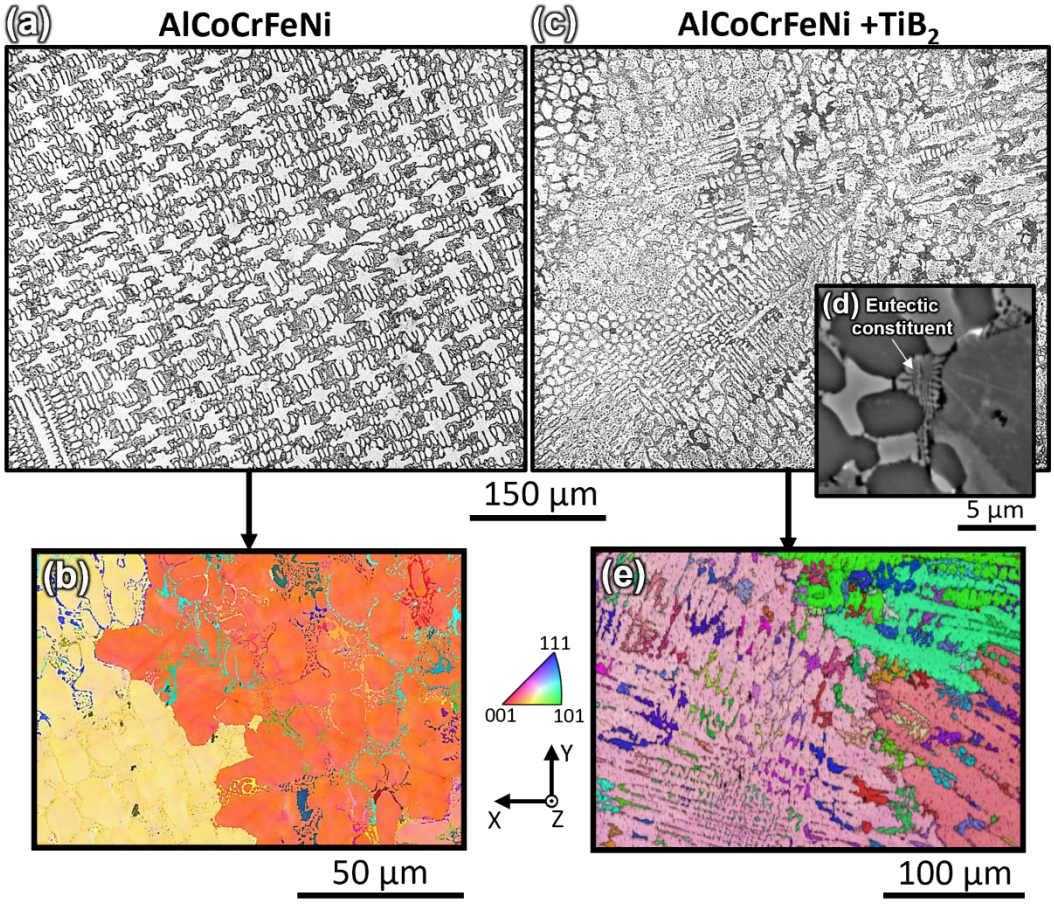


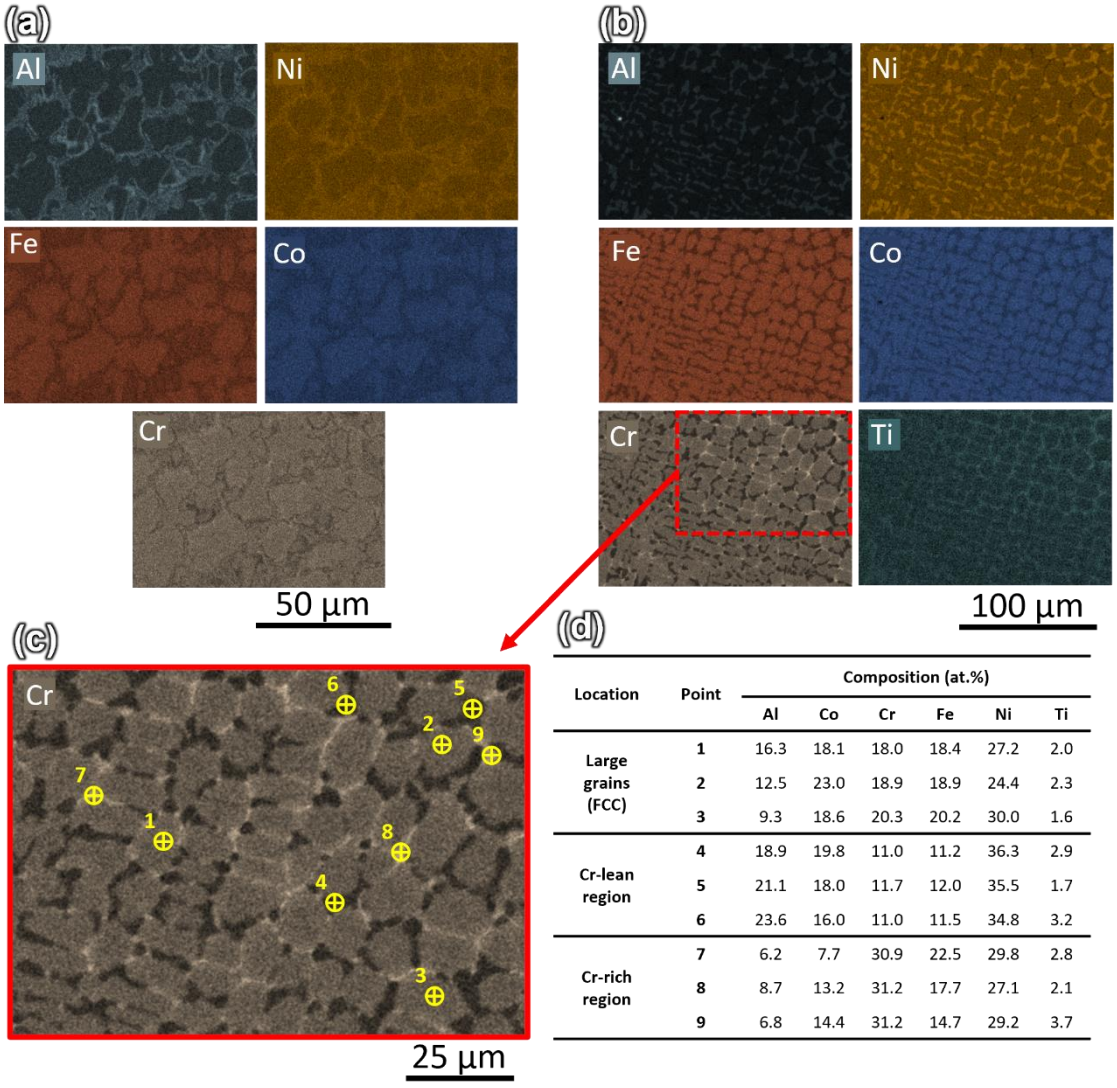
Figure 63 – Microstructural differences between both types of samples: (a) optical microscopy and (b) EBSD of the non-inoculated samples; (c) optical microscopy, detailed view of the eutectic constituent (d) and (e) EBSD of the TiB_2 inoculated samples.

Another difference that can be observed within the FZ is the presence of larger FCC equiaxial dendrites in the non-inoculated joint. In the inoculated sample the equiaxial FCC dendrites exhibit an average size of 38.1 ± 23.1 µm, with the FCC interdendritic spacing achieving maximum values of 4.6 ± 1.8 µm, which contrasts with the 31.1 ± 17.9 µm and 10.9 ± 5.5 µm respectively measured on the larger FCC grains, for the non-inoculated condition. In the case of the TiB_2-inoculated samples, however, we can observe the presence of larger grains amidst smaller sized ones. This phenomenon can be attributed to the uneven distribution and dissolution of the TiB_2 particles during melting, which can effectively alter their dispersion along the FZ, although the thickness of the samples is relatively small (1.5 mm). Furthermore, evidence of eutectic-like morphologies within the microstructure can also be observed

although being scarcer (see Figure 63 (d)). These are a product of the uneven elemental distribution occurring during solidification in the inoculated samples.

Figure 64 details EDS data revealing the elemental distribution on the FZ of both the inoculated and non-inoculated samples. Considering the non-inoculated FZ, using elemental maps and following the corresponding phase diagram, the first phase being formed is the FCC phase. Such is compliant with the obtained microstructure. As expected from the data retrieved from the BM, this phase is mainly composed of Cr, Co and Fe. Additionally, as the FCC phase forms and the temperature decreases the B2 BCC phase becomes stable, being richer in Al and Ni and forming the eutectic constituent within the larger FCC grains.

However, on the TiB_2-inoculated sample the EDS maps revealed that the FZ had an averaged composition of 14.9% of Al, 16.2% of Co, 18.1% of Cr, 17.3% of Fe, 32.8% of Ni and 0.7% of Ti (contrasting to the approximately 10% of Al, 17% of Co, 24% of Cr, 19% of Fe, 29% of Ni measured in the non-inoculated condition). No evidence of Boron was observed due to its low atomic weight and fraction. Interestingly, another difference occurring between both cases is in the Al, Ni and Cr content. While the presence of the FCC and B2 BCC phases is still clear, some regions hint for the formation of a different phase within the microstructure which possesses a high amount of Cr and being practically depleted of Al and Ni.



(d)

Location	Point	Composition (at.%)					
		Al	Co	Cr	Fe	Ni	Ti
Large grains (FCC)	1	16.3	18.1	18.0	18.4	27.2	2.0
	2	12.5	23.0	18.9	18.9	24.4	2.3
	3	9.3	18.6	20.3	20.2	30.0	1.6
Cr-lean region	4	18.9	19.8	11.0	11.2	36.3	2.9
	5	21.1	18.0	11.7	12.0	35.5	1.7
	6	23.6	16.0	11.0	11.5	34.8	3.2
Cr-rich region	7	6.2	7.7	30.9	22.5	29.8	2.8
	8	8.7	13.2	31.2	17.7	27.1	2.1
	9	6.8	14.4	31.2	14.7	29.2	3.7

Figure 64 – EDS maps of non-inoculated (a) and inoculated (b) joints. For b) a Ti map was added to track the changes induced in the FZ composition due to partial dissolution of the TiB_2 particles. A detailed view of the Cr map of the inoculated FZ is displayed in (c) marking the points where EDS scans were performed. The EDS point results are shown in (d).

EDS point quantification of the inoculated FZ composition can be observed in Figure 64 (c) and (d). Interestingly, the presence of BCC Cr-rich precipitates amidst the B2 BCC phase was evidenced by Miao et al. [151], indicating that the conditions for the formation of this phase can be fulfilled as segregation of Al, Ti, Cr and Ni occurs. However, these regions also evidence the presence of Co and Fe, beyond the high amount of Cr, indicating the possibility for σ phase formation [152,153].

Given this, the elemental distribution observed in the EDS maps of Figure 64, it is possible to further infer upon solute redistribution during solidification and subsequent phase nucleation using a CalPhaD-based analysis. As such, considering the non-equilibrium solidification conditions generated during cooling of the molten pool due to the GTAW process, Scheil calculations were performed as shown in Figure 65 (a).

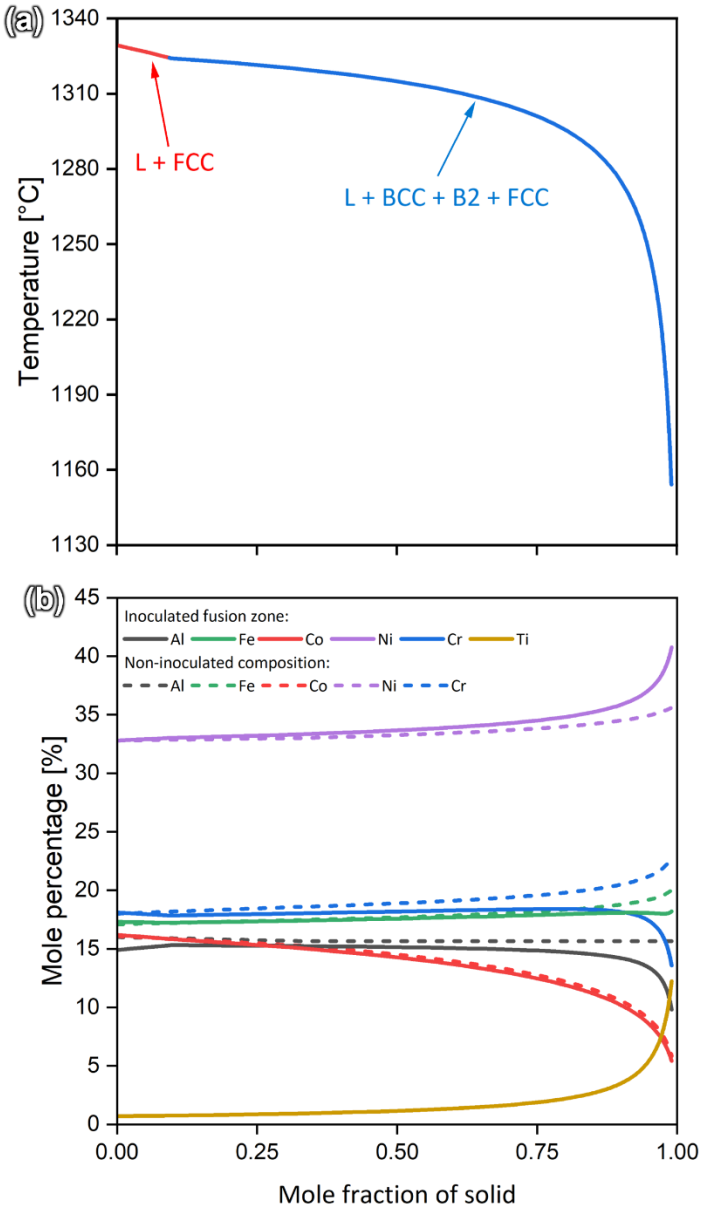


Figure 65 – CalPhaD-based analysis of the phases formed during solidification using the Scheil-Gulliver method. The curve in (a) highlights the solidification path of the inoculated sample. Additionally, (b) shows the evolution of o the composition in the liquid phase is shown for the non-inoculated and the TiB_2-inoculated compositions.

As expected, the Scheil-Gulliver curves of both conditions display several differences between them (refer to Figure 60 (c)). While the non-inoculated sample only shows a direct nucleation of B2 BCC and FCC from the Liquid phase, the inoculated sample exhibits two solidification steps. Taking this into consideration, the first step consists of the formation of FCC phase from the Liquid. Subsequently, it experiences the nucleation of a BCC and a B2 BCC phases amidst the FCC grains, from the remaining Liquid. Nonetheless, it is important to refer that the possibility for nucleation of each of these phases on the weld's microstructure is highly dependent, not only on the composition, but also on the temperature gradient and cooling rate. Furthermore, another major difference on the calculation results is the temperature solidification range of each one: while for the BM, the Scheil model predicts a temperature range from 1333 to 1296 °C, in the non-inoculated and inoculated FZs vary between 1330°C and 1292°C and 1329°C and 1154°C, respectively. While minor composition changes induced by preferential evaporation led to minor changes in the solidification temperature range of the FZ (compared to the as-cast BM), the dissolution of Ti due to partial decomposition of TiB_2 promotes a significant change, which can lead to poorer weldability. However, despite the increasing solidification temperature range, which is often associated to higher probability for solidification cracking during welding, no such defects were found in the present joints.

From the Scheil-Gulliver calculations it is also possible to infer on the composition of the liquid phase during solidification of the molten pool. The variation of elemental distribution is displayed in Figure 65 (b). In the non-inoculated case, the Al content remains practically constant, while the Cr, Fe and Ni amounts tend to increase within the interdendritic fluid. Additionally, it is possible to observe that the amount of Co in the liquid in decreases significantly. Therefore, such would allow us to infer that the interdendritic fluid would become richer in Cr, Fe and Ni, while being depleted in both Co and Al. However, such is not the case of the FZ nor the BM (refer to Figure 64 (a) and Figure 59 (b), respectively), provided that the FCC phase, which solidifies first, is richer in Co, Cr and Fe, with the remaining Al and Ni elements being segregated to the remaining Liquid. Furthermore, in the inoculated case, Fe has the most stable evolution, while the content of Ni and Ti increases in the Liquid throughout solidification with the amount of Cr and Al decreasing in the final stages of solidification. The

behavior of Co is similar to that observed in the non-inoculated case, which agrees well with the EDS map of Figure 65 (b), where the FCC (the first phase to form) showcases a higher content of Co.

Taking into consideration these CalPhaD-simulated microstructures both with and without TiB_2 added, further microstructure characterization using high energy synchrotron X-ray diffraction was performed. Representative diffraction patterns of the FZs of both conditions are detailed in Figure 66.

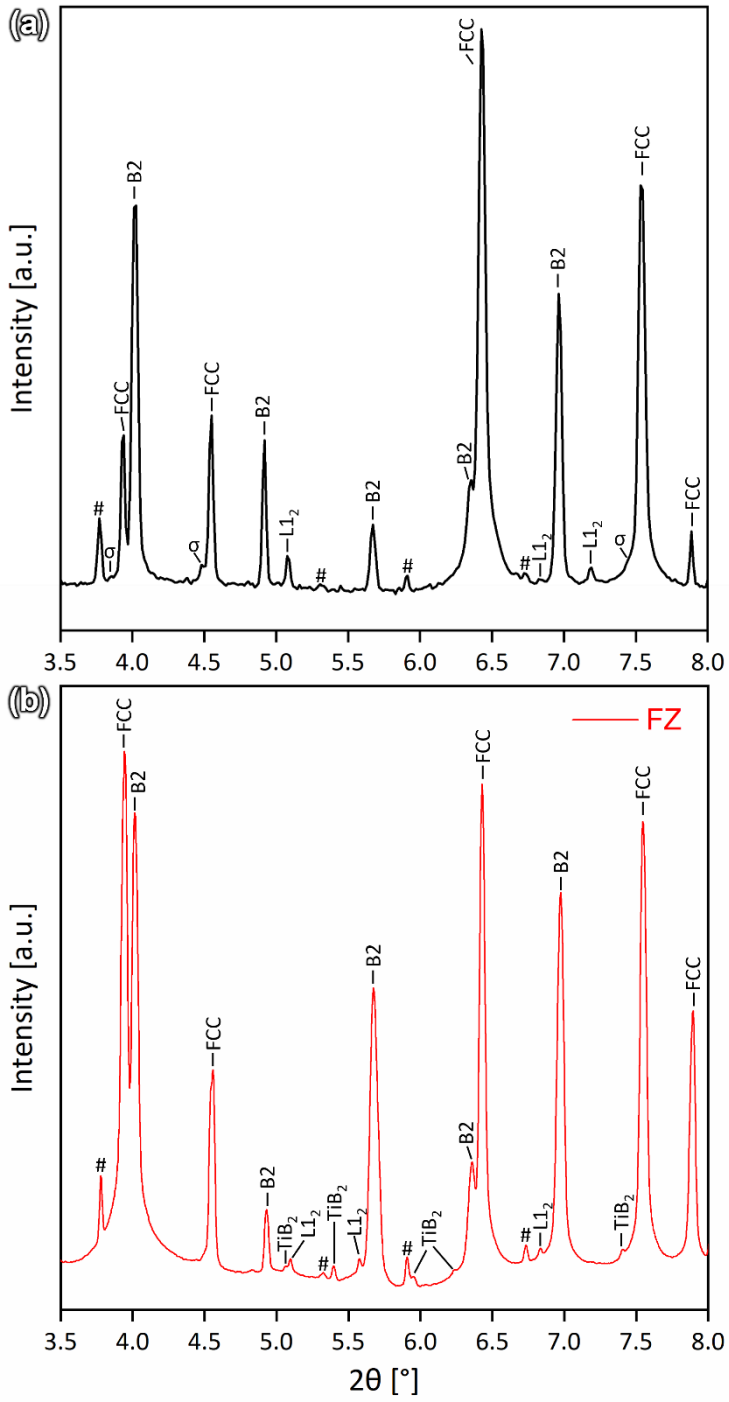


Figure 66 – Representative synchrotron x-ray diffraction patterns in: a) non-inoculated sample and b) in the TiB_2-inoculated case. (# stands for the low intensity 2nd harmonic diffraction peaks that do not correspond to any structure present on the alloy)

Here it is possible to identify FCC and B2 BCC phases, including small intensity peaks corresponding to TiB_2, and in some cases, we have overlapped phases, such as $L1_2$ and BCC with the FCC and B2 BCC phases, respectively. Interestingly, the identified phases are more

compliant with equilibrium calculations than with the non-equilibrium Scheil calculations. The presence of TiB_2 diffraction peaks also confirms that full dissolution of the micron scale inoculant particles did not occur, which can then further improve the mechanical strength of the FZ.

The present section detailed the microstructure evolution along both joints, clarifying also the role of the TiB_2 particles on the as-solidified microstructure of the FZ. Given the distinct microstructure characteristic observed, it is conceivable that the local and macroscopic mechanical performance will be impacted. The next section assesses the mechanical behavior of the joints, correlating it with the observed microstructures.

4.3.2.5 Mechanical performance of the welded joints: Microhardness distribution

Beyond the discussed microstructural condition samples, the analysis of the mechanical behavior of the welds under mechanical solicitation is a measure that must also be considered for the evaluation of the microstructural influence on the behavior of the samples, whether imposed by the inoculation of the molten pool or not. As such, Figure 67 exhibits the microhardness maps performed on both types of welded samples.

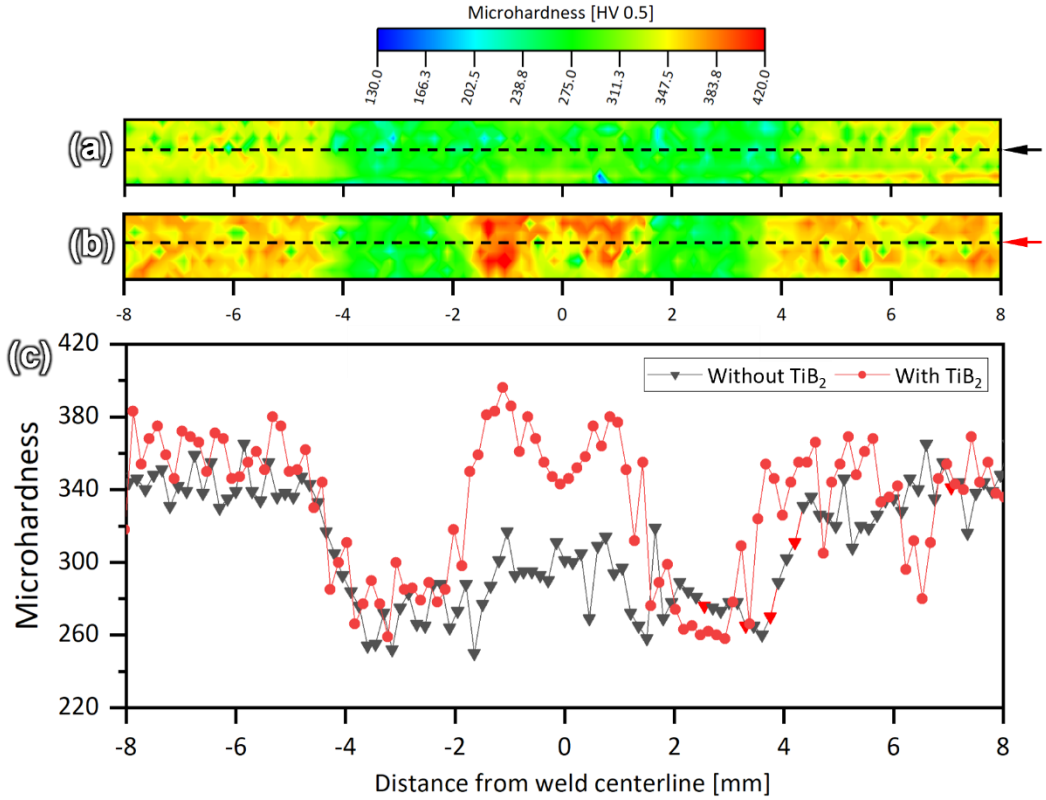


Figure 67 – Microhardness distribution along the welded joint: a) microhardness map of the non-inoculated samples; b) microhardness map of the inoculated sample and c) microhardness distribution comparison at half height as indicated by the red and black arrow.

Comparing the microhardness maps from both samples it is possible to perceive that the in the non-inoculated sample the BM exhibit the higher values reaching 344 $HV_{0.5}$. Additionally, in both cases the HAZ exhibits similar values of microhardness, attaining a maximum of 283 $HV_{0.5}$, while the FZ is the region where most discrepancies exist, as expected due to the changes in microstructure observed. Regarding the non-inoculated sample, the FZ reached approximately 280 $HV_{0.5}$ at its peak, whereas in the TiB_2-inoculated sample the same region reaches values up to 358 $HV_{0.5}$, as clearly indicated in Figure 67 (b) and (c).

In this sense, it is possible to conclude that the introduction of TiB_2 affected the final condition of the samples resulting in a ≈28% increase in hardness of the non-inoculated FZ values and ≈4% increase when compared to the BM. This can be ascertained not only to the presence of the TiB_2 particles, acting as secondary phase strengthening, as well as due the refined grain structure originated by the higher number of nucleation points associated to the presence of high temperature particles in the molten pool during welding.

4.3.2.6 Mechanical performance of the welded joints: Tensile behavior

To further inspect the weld mechanical behavior, stress-strains curves obtained on both types of welded samples are compared to the original BM as obtained by uniaxial tensile testing. These results are displayed in Figure 68.

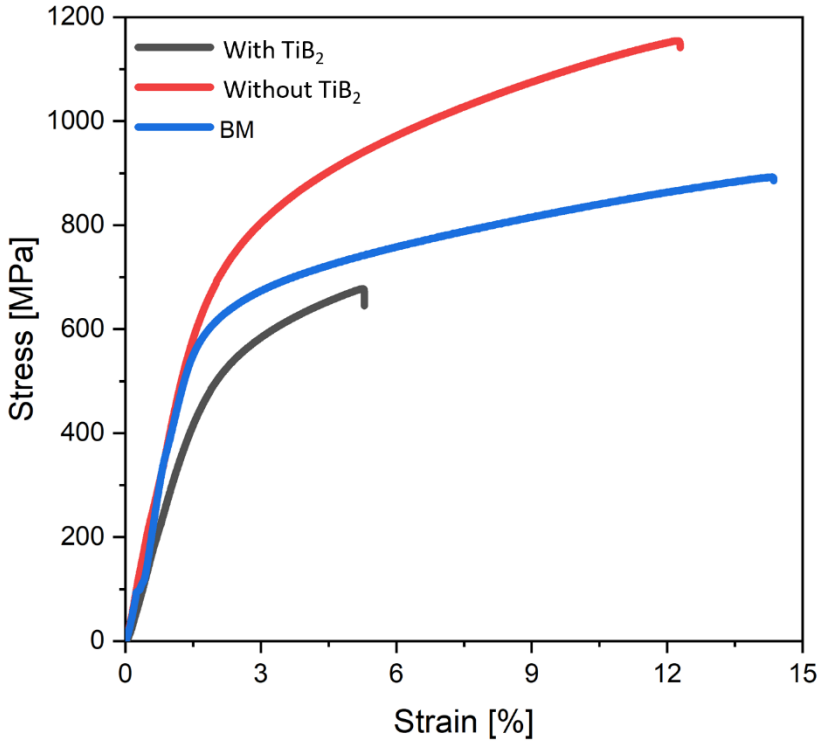


Figure 68 – Representative tensile test results, showcasing the macroscopic mechanical properties of BM and welded joints.

Starting by the tensile behavior of the non-inoculated joints, we can observe that the microstructural changes caused by the welding process, managed to improve the ultimate tensile stress (UTS) up to 1140 ± 21 MPa contrasting to those of the BM (877 ± 23 MPa). Nevertheless, the strain to fracture is reduced from 12.1 ± 0.3 % in the BM to 12.4 ± 2 % in the non-inoculated material. Overall, the conventional welding procedure, i.e., without the use of TiB_2 in the FZ, promoted a ≈30% increase in UTS and a decrease of ≈3% in the strain to fracture. Nevertheless, one must consider that the highly dendritic nature of the BM is a key factor influencing its mechanical performance, as the smaller dendritic size attained on the FZ can help in improving the HEA's mechanical resistance. These results are in accordance with those observed in [141]. Nevertheless, the tensile test results on the inoculated sample indicate that despite the positive microstructural changes that occurred with the introduction of TiB_2 on

the molten pool, the associated mechanical performance was diminished. Comparing the results with the BM the UTS of the inoculated samples (667 ± 15 MPa) showed a 63% decrease and the strain to fracture (corresponding to 4.6 ± 0.9%) a 24% reduction. Eventually, both types of samples fractured in the HAZ/FZ interface.

Given the exhibited mechanical behavior, it is also of interest to understand the load partitioning between each region of the weld to evaluate how the strain is distributed during tensile testing as function of the different microstructure characteristics. For this, Figure 69 a) and d) displays the DIC data corresponding to the regions corresponding to the BM, HAZ and FZ, in the moment right before fracture. Additionally, in Figure 69 b) and e) it is possible to observe the time-resolved strain along the welded joints (where the stars mark the positions of interest analyzed).

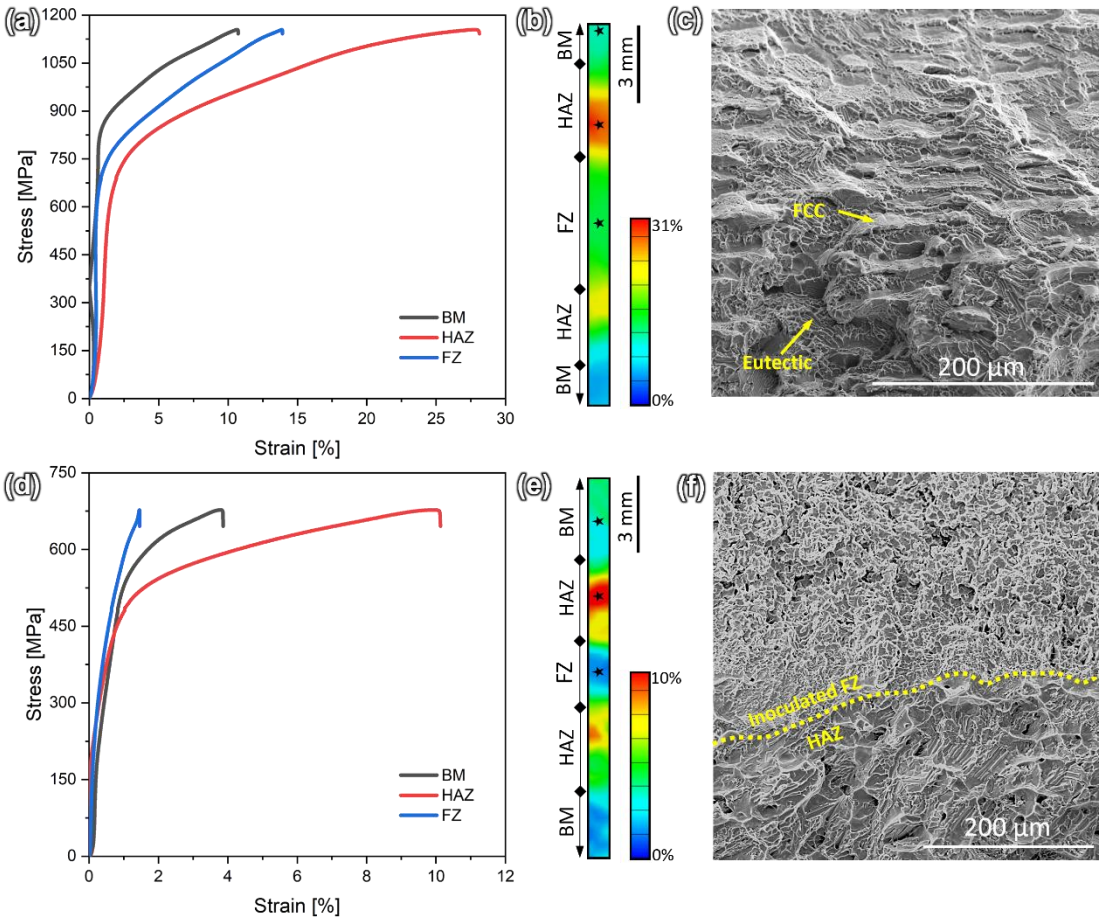


Figure 69 – DIC point analysis obtained during tensile testing of: a) non-inoculated and d) TiB_2-inoculated samples. Additionally, b) and e) exhibit the local strain distribution right before fracture of each sample. The fracture surfaces of the non-inoculated and inoculated samples are displayed in c) and f), accordingly.

From the DIC point analysis it is possible to observe the very different mechanical performance undertaken by each of the analyzed regions. Firstly, in the non-inoculated welds we can observe a combined effort from the BM, HAZ, and FZ to accommodate the strain that is being applied upon the sample, with the BM displaying the most rigid behavior and the HAZ having the largest deformation. Such is expected from the microhardness exhibited by each region of the weld and can be correlated to the aforementioned effects of the weld thermal cycle on the observed microstructure.

In the TiB_2-inoculated case, however, it is possible to observe that most of the strain is accommodated by the softer HAZ, while the FZ and the BM play a minor role in the deformation of the alloy. This phenomenon can be associated with the higher microhardness exhibited in these two regions, translating the higher strength performance of the FZ and the BM in comparison to the HAZ. Additionally, it must also be noted that compositional dissimilarity between the inoculated FZ and the non-inoculated HAZ can cause the generation of stress concertation areas to develop leading to premature failure of the weld. Moreover, the presence of the TiB_2 particles in the FZ can also act as stress concentrators further accelerating the material fracture. This suggests that the amount of TiB_2 added must be regulated to avoid excessive stress concentration effects, while grain refinement is still enabled by the particles.

Furthermore, one relevant information that is possible to take, is the fact the inoculated FZ is capable to sustain stresses up to ≈ 670 MPa without any visible deformation, which in turn can sustain the premise for the development a new HEA composition with the possibility for high mechanical performance. Such, however, would require further analysis, which goes beyond the purpose of the present study.

In both cases, the HAZ is the region that exhibits the largest deformation, as it would be expected from microhardness mapping in Figure 67, given the softening behavior of the HAZ which occurred during welding.

Given the eventual fracture of the samples during tensile testing, Figure 69 c) and f) display the fractures surface of the inoculated and non-inoculated samples. It is possible to observe that in the non-inoculated case fracture occurred at the dendritic boundaries leaving traces of a composite-like FCC + Eutectic (FCC + B2 BCC) structures present on the surface. Such resulted from the combination of ductile and brittle fracture mechanisms arising from

the presence of both phases on the microstructure. On the inoculated case however, it is possible to trace the discontinuity between the fracture surface resulting from the refined grain size of the FZ and the fracture surface arising from the HAZ microstructure. Such indicates that the interface between these two regions is critical to the inoculated weld performance.

4.3.2.7 Conclusions

This work delved on the investigation of the influence that TiB_2 particles have on the molten pool of GTAW welded plates of a AlCoCrFeNi HEA system. While defect-free welded joints were obtained, microstructural differences arising from the introduction of TiB_2 particles were evident. A distinct mechanical behavior of the inoculated and non-inoculated samples was observed, highlighting that the inoculation of the samples did not result in an improved mechanical condition of the HEA system, likely due to preferential stress concentration effects. Nevertheless, the results proved that tailoring the mechanical properties of GTAW welds on this HEA system is a possible procedure to be considered for potential engineering applications, as long as a correct selection of inoculant particles and their fraction is accomplished.

Overall, from this work the following topics can be assertively concluded:

- Excellent weldability via GTAW was observed on the AlCoCrFeNi HEA, where defect-free welds were obtained, both in the inoculated and non-inoculated condition.
- Grain size and phase fraction fluctuations allowed to observe the microstructural differences across the weld regions, where EBSD and conventional microscopy
  revealed a distinct phase distribution along the joints. The presence of a BCC phase in the TiB_2-inoculated samples was unveiled by the Cr-rich regions on the corresponding FZ.
- Synchrotron X-ray diffraction was used to identify the phases present in the BM, HAZ and FZ of both types of samples. These being mainly composed of large FCC grains together with an eutectic constituent comprising a FCC and B2 BCC phases. Such phases were predicted via thermodynamic calculations, which allowed for a deeper analysis of the solidification path undertaken by both FZ during solidification.
- Considering the microhardness evolution, the BM exhibited the higher values in the non-inoculated samples. However, the higher microhardness values occurred in the inoculated sample's FZ, reaching up to 358 $HV_{0.5}$. Such values contrasted with the significantly softer FZ

on the non-inoculated case (280 $HV_{0.5}$). In both cases the HAZ was the softer region of the joints.

- In terms of tensile behavior, in the as-welded condition, the best results occurred in the non-inoculated sample, which reached an UTS of ≈1140 MPa at a strain of ≈12 %. The inoculated sample reached a UTS of ≈667 MPa (corresponding to ≈5% of strain) indicating that the TiB_2 particles were not successful in improving the macroscopic mechanical properties of the BM. Both samples fractured in the HAZ.

Future works will envisage the application of different inoculants and fractions, as well as the use of different thermal treatments to optimize the mechanical properties of welded joints obtained from the AlCoCrFeNi HEA system.

4.3.3 Dissimilar gas tungsten arc welding between the AlCoCrFeNi HEA and 316L stainless steel

A representative optical micrograph of the cross-section of the dissimilar joints is shown in Figure 70 (a). There, the evident distinction of the AlCoCrFeNi BM, the FZ and the 316L SS BM (from left to right), can easily be identified. Furthermore, as it is known from the well-established microstructure developed during GTAW, a HAZ is expected to develop on both sides of the FZ due to high temperatures attained close to it [32,154]. Such indeed is the case of the 316L SS side, where an increasing gradient grain size can be observed when going from the BM towards the FZ. Nevertheless, due to the large dendritic nature of the AlCoCrFeNi BM, the HAZ on this side of the joint is not easily noticeable via microscopy techniques.

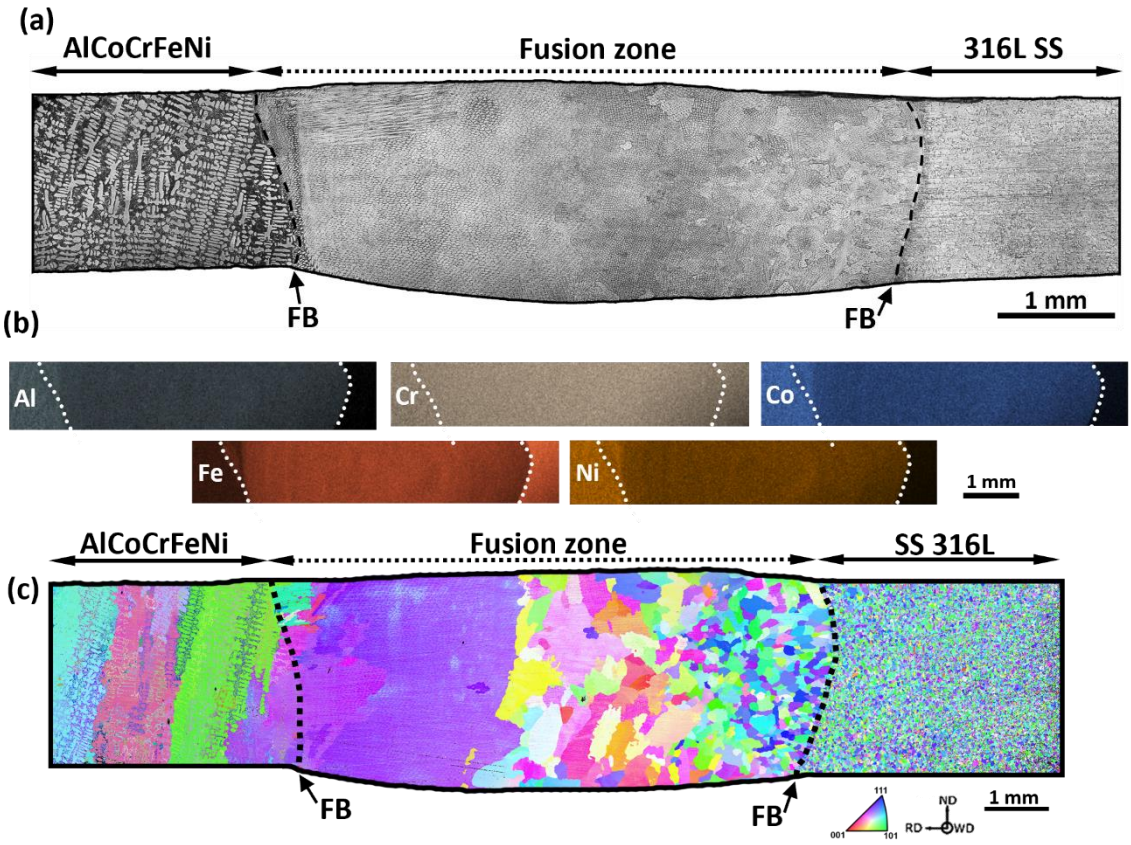


Figure 70 – Optical microscopy of the cross-section of the dissimilar weld: (a) Macrograph highlighting the FZ and the two BMs; and (b) EDS maps displaying an overall perspective of the elemental distribution throughout the joint (c) Collage of IPF EBSD maps of the dissimilar welded joint, highlighting the variation in grain orientation and morphology throughout the joint. (FB corresponds to the fusion boundary).

At this macro level, the compositional differences between both BMs are further highlighted in the EDS maps in Figure 70 (b), where a clear distinction between the distribution of

all the analyzed elements can be observed. As expected, while Al, Co and Ni are more prevalent in the AlCoCrFeNi side of the weld, the amount of Fe is higher in the 316L SS BM, with Cr practically evenly dispersed throughout the weld.

Furthermore, the microstructure of the weld is highlighted in Figure 70 (c), where a collage of consecutive EBSD inverse pole figure (IPF) maps can be observed, representing the whole extension of the welded joint, while allowing to observe the variation in grain orientation along the joint.

With particular emphasis on the FZ, which originated from the solidification of the molten pool, this region showcases an intricate distribution of grain size and morphology that changes with the proximity to each BM. Such is the result of the temperature gradient and growth rate parameters that are imposed on the molten pool during solidification. These factors have a significant impact on the developing grains by being strongly associated to the cooling rate, and, in turn, occur simultaneously with epitaxial and competitive growth phenomena to produce the final microstructural features of the FZ.

As evidence of epitaxial growth, which refers to the tendency of the grains to grow with the same crystallographic direction as those already present in the BM, the region of the FZ closer to the AlCoCrFeNi BM showcases grains with a similar color tone, i.e., possessing similar grain orientation, as the ones that can be found in the HEA near the fusion boundary (FB). The same can be said for the FZ grains closer to the 316L SSl BM, where a tendency to lean towards a bluish color tone, i.e., <111> orientation, can be seen.

On the other hand, competitive growth is noticeable at the central region of the FZ, where the grains that are oriented more favorably in their easy growth direction (which is <001> for cubic structures), which are now far from the influence of each BM, tend to increase in size at the expense of smaller, poorly oriented ones. However, before the microstructural changes occurring during GTAW can be closely inspected, it is necessary to infer the microstructural condition of each BM. For this, representative EBSD maps taken from both BMs are displayed in Figure 71.

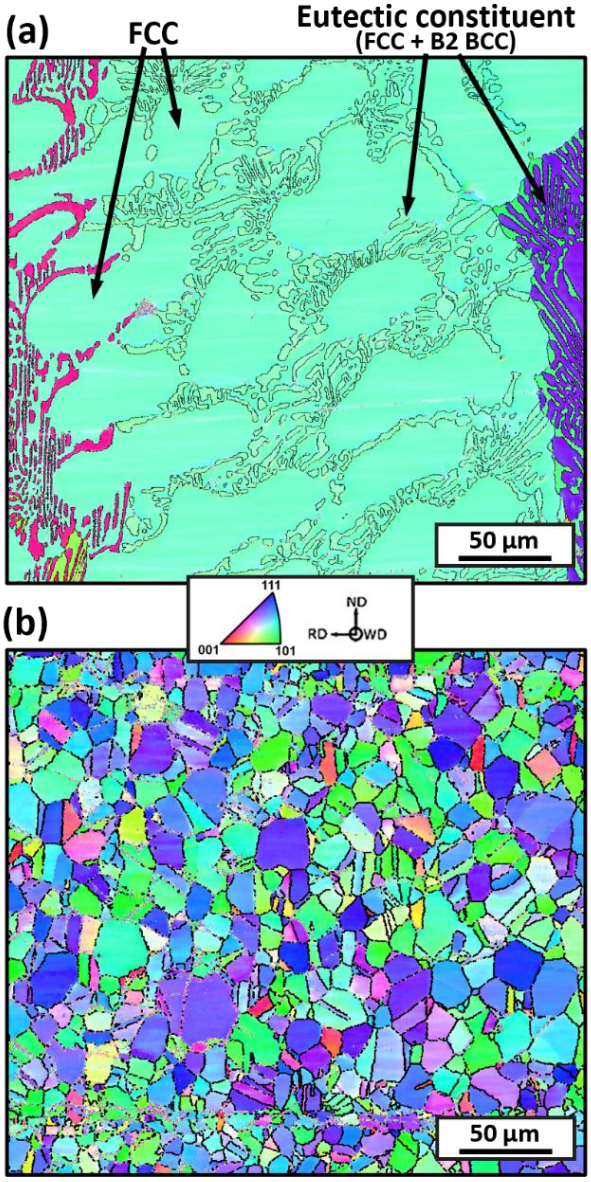


Figure 71 – Representative EBSD maps of the BMs: (a) AlCoCrFeNi HEA and (b) 316L SS.

Starting with the AlCoCrFeNi HEA BM (refer to Figure 2 (a)), the microstructure is mainly composed of large FCC grains, averaging 83.6 ± 23.5 µm in size, which are surrounded by a eutectic constituent composed of both FCC and B2 BCC phases. Further analysis via EDS allowed us to quantify the composition of the present HEA yielding 14.9% of Al, 16.5% of Co, 18.1% of Cr, 17.4% of Al and 33.4% of Ni (all values in at. %).

Furthermore, while a comprehensive discussion on a similar HEA's microstructure was conducted in [155], it can be inferred that such large dendritic features are a product of the cooling conditions and elemental segregation that took place during solidification of the original casting block used to obtain this BM. Such is to be expected from the time and

temperature factors imposed on the ingot, which was left to cool down slowly during its production [156].

Similar conclusions can be drawn from the analysis of Figure 72, where we can see that while the FCC phase is mainly composed of Co, Cr, and Fe, the B2 BCC phase is richer in the Al and Ni, further highlighting the effects of elemental segregation during solidification.



Figure 72 - EDS maps of the AlCoCrFeNi HEA.

On the opposite side of the welded joint is the 316L SS BM. A representative EBSD map of this region is depicted in Figure 2 (b). There we can see that the 316L SS BM is composed of small equiaxed grains with an approximate size of 19.8 ± 2.3 µm. Within the grains, it is also possible to observe several annealing twins, which have their inception associated with growth accidents in the stacking sequence within the grain structure during recrystallization and grain growth phenomena arising from the high temperatures achieved during the hot rolling process [30].

With a fundamental basis established regarding the initial state of each BM, it is now possible to evaluate the microstructural evolution that is visible when progressing toward the bulk of the FZ and is a direct product of the GTAW process. As such, Figure 73 delves into the analysis of the two FBs which are located at the interface of the FZ with each HAZ side. There, once again, the HAZ in the AlCoCrFeNi HEA side cannot easily be distinguished. Nevertheless, beyond this fact, a sharp microstructural transition between each FB can be observed directly through the different grain sizes and morphology that developed with the proximity to each BM, as it going to be discussed next.

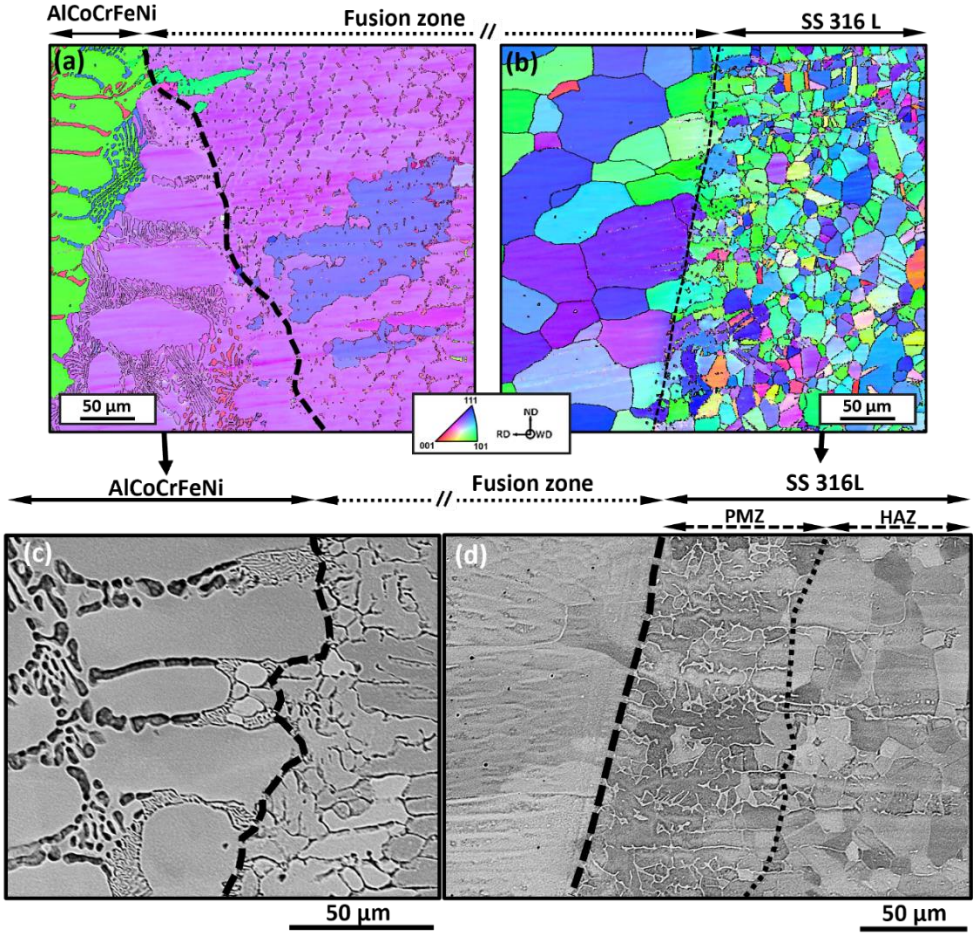


Figure 73 – Microstructural features at the fusion boundary: a) EBSD maps obtained on the AlCoCrFeNi side and b) 316L SS side. SEM micrographs highlighting the sharp microstructural differences, i.e., grain size and morphology variations, can be observed in c) for the AlCoCrFeNi side and d) for the 316L SS side of the weld.

A close-up view of each FB reveals large grains composed of smaller dendritic structures within the FZ can be seen in Figure 73 (c) and (d), contrasting with the structures present in each HAZ. Such differences are caused by the different temperature conditions experienced by each region of the weld, where the HAZ tends to experience recrystallization and grain growth phenomena, while the FZ undertakes complete remelting and subsequent solidification.

Furthermore, it is also possible to locate a partially melted zone (PMZ) between the HAZ and the FZ on the 316L SS side of the joint (see Figure 73 d)). This region is formed due to the segregation-induced liquation at the FCC matrix grain boundaries of the FCC matrix of the 316L SS. In such cases, alloying elements/impurities in the grains that decrease the melting temperature of the BM, segregate towards the grain boundaries during its manufacturing. Upon reaching the high temperatures during welding, these lower melting temperature grain

boundaries tend to melt, leaving the remaining portion of the grains in the solid state [32]. This allows the material in this region to undergo to solid + liquid domain state instead of reaching a full liquid condition.

Aside from that, another interesting fact that can be observed is the discrepancy in grain size on the FZ, at both FBs. In this sense, the grains near the AlCoCrFeNi HEA side are larger than the grains closer to the 316L SS HAZ. This can be associated with the grain size on each side of the joint, where larger size leads to less nucleation events occurring at the solid/liquid interface. Furthermore, EDS maps taken from the two FBs can be observed in Figure 74, qualitatively revealing a similar elemental distribution of the FZ to the HEA side of the weld and a sharp compositional change near the FB at the 316L SS side, especially regarding Al, Co and Ni.

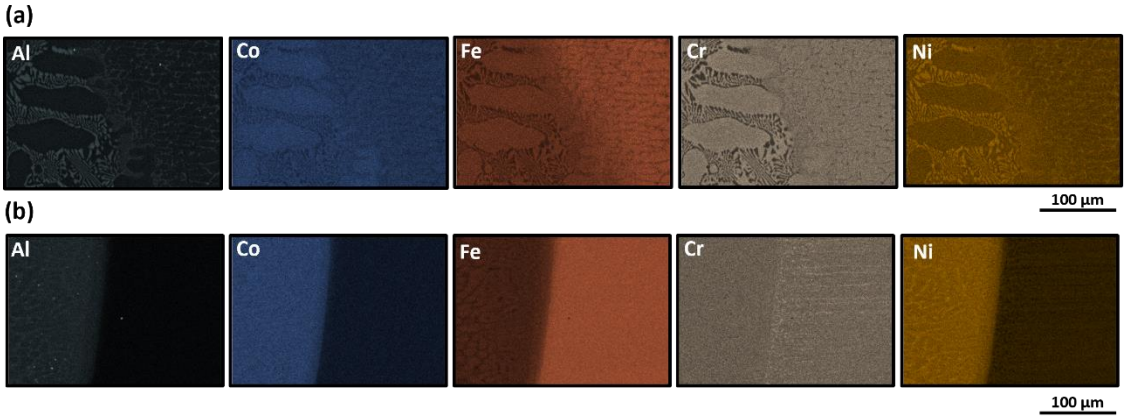


Figure 74 – EDS mapping at the fusion boundary near the: a) AlCoCrFeNi HEA and b) 316L SS BMs.

Further into the FZ and evoking the microstructural gradient evolution visible in Figure 70 a) and c), we delve deeper into the characteristics mainly in its bulk and at its two extremes (near the AlCoCrFeNi HEA and the 316L SS sides). These regions of the FZ are exhibited on the EBSD IPF maps of Figure 75 a), b) and c). There we can observe that both the grain size and the size of the cross-section of the dendrites that compose them are drastically different. That is, by comparison of the two extremes, while the FZ near the AlCoCrFeNi HEA does not have a sufficient amount of visible grains due to their massive size (near 1 mm), the grains closer to the 316L SS BM have an approximate size of 69.6 ± 20.0 µm. In the middle of the FZ, grains tend to have a size of 210.2 ± 85.9 µm. As mentioned, this showcases the impact that proximity to each BM had during solidification, in terms of, composition and thermal conductivity, affecting the cooling rate and the thermal gradient responsible for final grain size and morphology [32].

From these two peripheral regions, APT tips were produced to investigate small compositional fluctuations that occur due to the elemental segregation or due to the presence of nano-sized precipitates within the FZ. The observations are depicted in Figure 75 d), e) and f). While not representing in full the inspected regions, the APT data reveals that all elements are homogenously distributed, at a nano level. Nevertheless, as it is possible to observe in Figure 75 g), near the 316L SS BM, the segregation of Si occurred at the sub-grain boundaries (sub-GB), that is at the dendritic level.

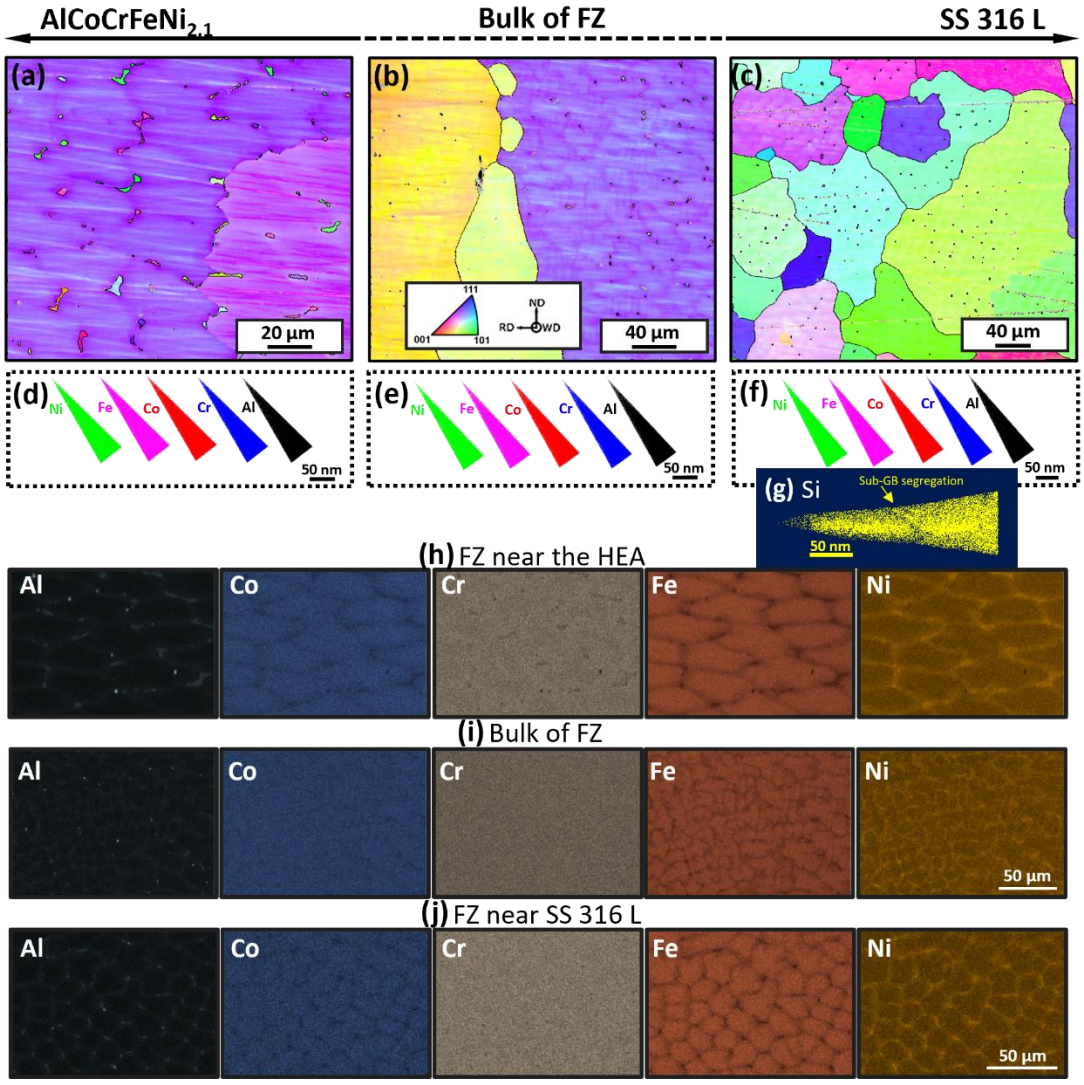


Figure 75 – EBSD maps obtained (a) near the AlCoCrFeNi HEA, (b) at the bulk and (c) near the 316L SS side of the FZ, alongside (d), (e) and (f) and (g) representing the composition at obtained at each of these regions utilizing APT, respectively. The EDS maps in (h), (i) and (j) highlight the composition of each examined regions.

Apart from that, considering a broader compositional analysis, Figure 75 displays EDS maps corresponding to the three investigated regions of the FZ. For these, aside from the

evident disparity in grain size, it is also possible to observe that, in terms of location within the grains, the elemental distribution is identical. This means that, in both cases, Al and Ni tend to segregate towards the grain boundaries during solidification of the molten pool, while Co, Cr and Fe are present in more quantity within the dendritic cores. A similar elemental distribution can be observed in the AlCoCrFeNi HEA, which presents a dendritic microstructure in its BM (see Figure 72). The quantitative results obtained from Figure 75 are shown in Table 11.

Table 11 – Compositional measurements in FZ obtained by EDS.

FZ region	Al	Co	Cr	Fe	Ni
Bulk	8.0	9.6	19.3	40.8	22.3
Near AlCoCrFeNi HEA	8.7	10.1	19.2	38.6	23.4
Near 316L SS	8.6	10.0	19.2	39.2	23.0

To further assess the welded joint microstructure beyond the features that can be noticed through surface inspection methods (optical and electron microscopy) high energy synchrotron X-ray diffraction scans were taken from the joint. These scans were obtained on both base materials and from two different regions of the FZ, each near both BMs. These results are displayed in Figure 76.

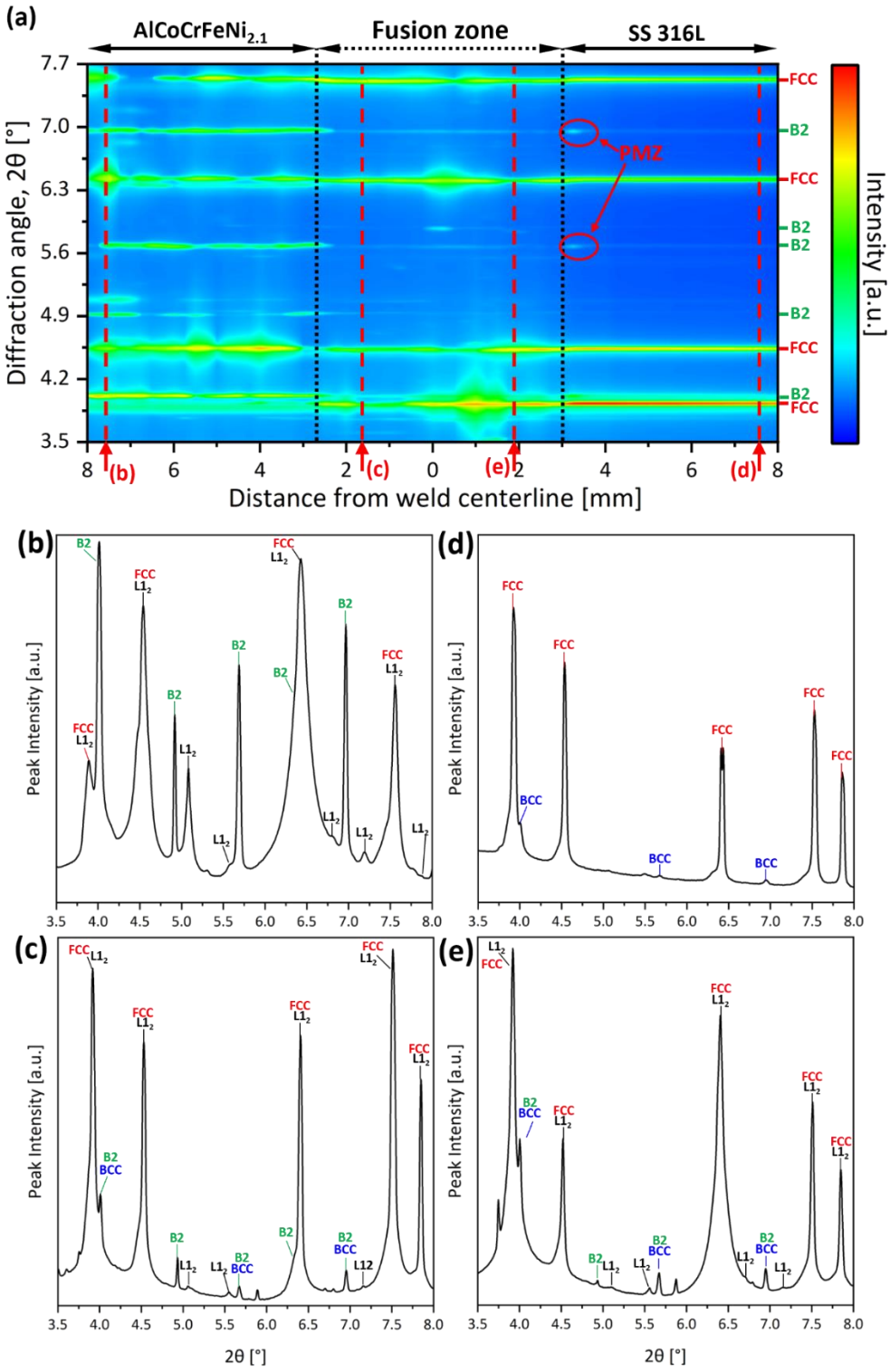


Figure 76 – Synchrotron X-ray diffraction analysis of the welded joint: (a) superimposition of full azimuthal integrated diffraction over the full extent of the joint (major peaks from the FCC and BCC B2 phases are marked on the left side of the map). Representative synchrotron X-ray diffraction scans were obtained from: (b) AlCoCrFeNi HEA BM; (c) 316L SS BM; (d) FZ near the AlCoCrFeNi HEA and (e) FZ near the 316L SS BM. Peaks coming from 2nd harmonic reflections, due to P07b/PETRA III beamline conditions, were left unidentified.

Concerning both base materials, the results indicate that the 316L SS comprises both an austenitic FCC phase alongside a ferritic BCC phase, as indexed (refer to Figure 76 (a)). This is in good agreement with the previous analysis performed in [157], where the lower intensity ferrite peaks corresponded to a low phase fraction on the microstructure. On the other side of the weld, regarding the AlCoCrFeNi HEA, the respective diffraction patterns show that this BM is composed mainly of two main phases: a disordered FCC and a B2 (ordered) BCC phase, accompanied by peaks corresponding to nanosized $L1_2$ (ordered FCC) phase particles present within the microstructure, as previously highlighted in [158].

Regarding the HAZ, it still is not possible to easily observe and distinguish this region in the AlCoCrFeNi HEA, while on the 316L SS side, we can see an increase in the ferrite (BCC) peak intensity, as marked by the red circles in Figure 76, close to the interface between the BM and the FZ. This indicates the presence of the PMZ in between the HAZ and the FZ on the 316L SS BM side of the weld.

Considering the FZ, it is possible to observe that the diffraction patterns coming from each analyzed region are distinct from each other, although having in common the presence of a predominant FCC phase, whose composition varies concerning its distance from each BM, as seen previously.

Despite this, both sides of the FZ exhibit peaks corresponding to the FCC, B2 BCC, BCC and the $L1_2$ FCC phases, similar to those found within both BMs and thus suggesting the mixing of both materials during welding. In addition to this, however, the difference between each FZ mainly resides in peak intensity.

Investigating the thermodynamic compatibility between both types of BMs aids in identifying the possible phases that may form during their mixing and subsequent solidification, thus potentially enabling the avoidance of potential detrimental effects caused by undesired precipitates. Following this route, non-equilibrium solidification calculations based on the Scheil-Gulliver method were performed considering the partial mixture of the 316L SS BM into the AlCoCrFeNi HEA, as shown in Figure 70 (a). The compositions utilized for this analysis are detailed in Table 12.

Table 12 – Compositions utilized for Scheil-Gulliver calculations (all values in at. %).

Fraction of 316L SS	Fe	Cr	Co	Ni	Al	Fraction of HEA
100%	73.0	17.4	0.0	9.6	0.0	**0%**
90%	67.4	17.5	1.7	12.0	1.5	**10%**
80%	61.9	17.5	3.3	14.3	3.0	**20%**
70%	56.3	17.6	5.0	16.7	4.5	**30%**
60%	50.8	17.7	6.6	19.0	6.0	**40%**
50%	45.2	17.8	8.3	21.4	7.5	**50%**
40%	39.6	17.8	9.9	23.7	8.9	**60%**
30%	34.1	17.9	11.6	26.1	10.4	**70%**
20%	28.5	18.0	13.2	28.4	11.9	**80%**
10%	23.0	18.0	14.9	30.8	13.4	**90%**
0%	17.4	18.1	16.5	33.1	14.9	**100%**

There it is possible to observe the temperature at which the material starts to solidify ($T_{liquidus}$), the temperature at which the solidification process terminates ($T_{solidus}$) and the temperature for the formation of a eutectic constituent ($T_{eutectic}$) in terms of the ratios between each BM. In addition to this, the phases that are prone to nucleate within the microstructure are also highlighted. Within the range of 0 to 20% of 316L SS, where the composition is closer to the HEA system, the microstructure is predicted to be composed of an FCC phase and ordered B2 BCC. In the other extreme, where the compositions are closer to the 316L SS BM, the microstructure is composed of the disordered FCC and BCC phases. In between, these two extremes, the thermodynamic calculations reveal the nucleation of these three phases, where the ordered B2 BCC phase only nucleates at the final solidification stages (being practically isothermal, as shown in Figure 77 (b)).

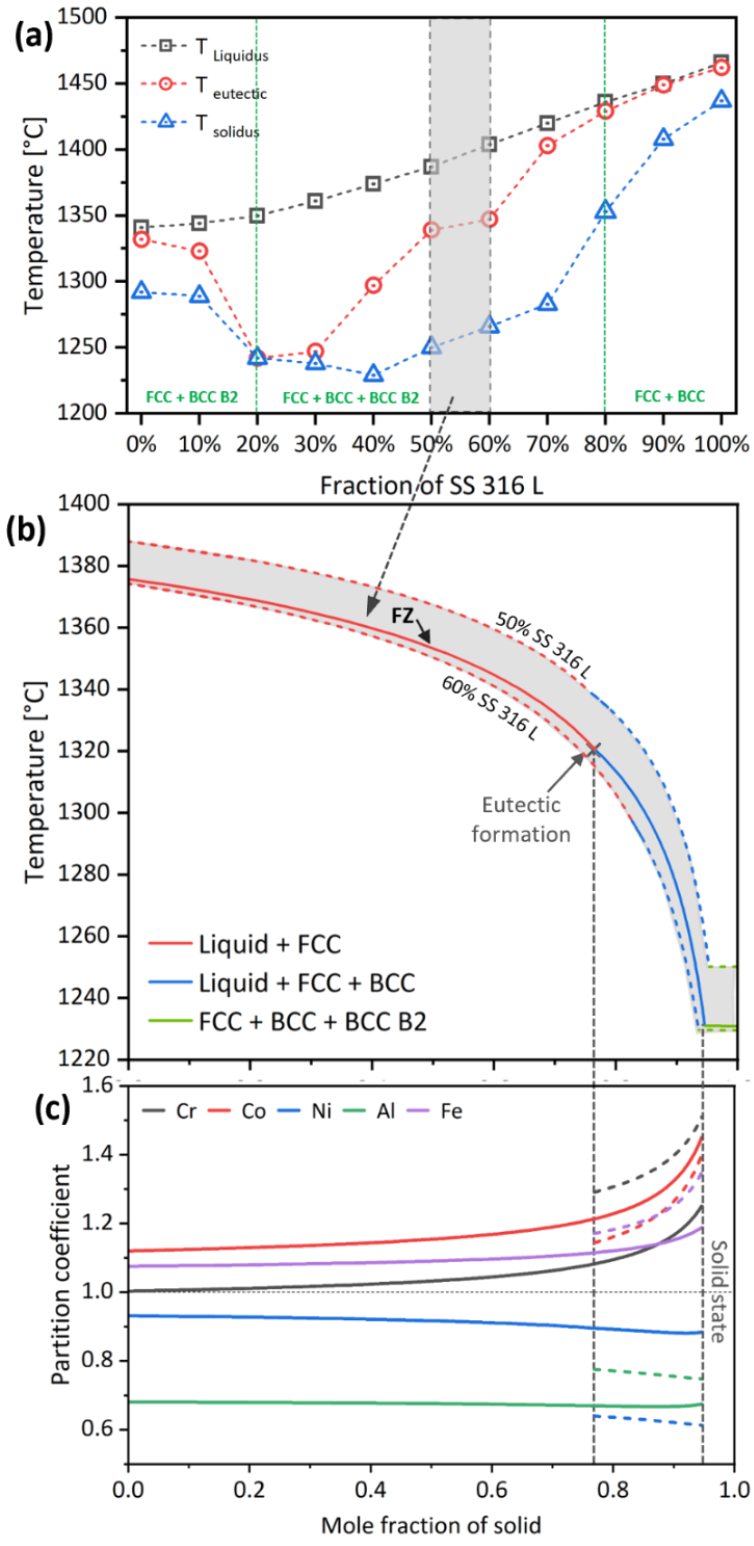


Figure 77- CalPHaD-based simulation of the phases that may develop during solidification: (a) variation of Liquidus, solidus and eutectic temperatures with an increasing amount of 316L SS; (b) Scheil-Gulliver solidification curves corresponding to the FZ and the compositions of 50% and 60% of the mixture of 316L SS; and (c) partition coefficient evolution of the FZ.

Likewise, it must be mentioned that within the compositional extremes corresponding to each BM, the variation in solidification temperature (Tliquidus - Tsolidus) is smaller, while the value of Tliquidus is closer to Teutectic. Such results on a composition capable of forming the eutectic constituent, albeit highlighting the difference in solidification temperature, which is lower in the HEA case, where the molten material stays liquid for longer (provided the same starting temperature). Beyond this, an overall, increasing trend for $T_{liquidus}$ to increase with the growing percentage of 316L SS, can also be observed.

Further inspection of the Scheil curve obtained for the FZ (calculated based on the averaged compositions presented in Table 11), allows us to situate the obtained curve between the 50-60% of 316L SS composition, which is displayed in Figure 77. There it is possible to observe that the solidification path is composed of two stages, where, in the first instance, the FCC phase starts forming (at 1376°C) until reaching 1320°C, corresponding to the eutectic point, at which the conditions for the disordered BCC phase to nucleate are attained. Eventually, in the final solidification stage, the conditions for the formation of the BCC B2 phase are reached, at 1250°C, where the solidification process finalizes. This agrees with the obtained microstructure where large FCC grains are visible within the FZ.

With the elemental distribution data retrieved from the FZ Scheil-Gulliver curve, the partition coefficient for each of the elements present within the FZ was calculated by dividing the amount of each component of each solid phase by the corresponding amount in the liquid phase. The results are shown in Figure 77 (c). As such, during solidification, should the partition coefficient decrease, it means that its concentration in the liquid is being segregated from the forming microstructure towards the remaining liquid, and vice-versa. Given this, both phases in the two stages of solidification showcase a similar evolution in terms of the partition coefficient. Furthermore, apart from Ni and Al, all elements tend to increase above the value 1, which corresponds to the point where the concentration of a component within the liquid equals the concentration within the solid. As such, these elements, namely Co, Cr and Fe, contribute to the formation of the FCC matrix, while Ni and Al are segregated towards the interdendritic fluid up to the point where the conditions for the nucleation of the B2 BCC phase are met, thus producing the eutectic constituent. Such results are coherent with the elemental maps displayed in Figure 75. N Nevertheless, it is also important to mention that evidence of a eutectic structure was not found by the applied microscopy techniques. Such can be due to the mentioned solidification conditions imposed in the molten pool by the welding process, thus slightly deviating the solidification path from the predicted microstructure.

Corroborating this fact is the non-prediction of the L12 nanoprecipitates, which are possible to be observed via SXRD.

Figure 71 displays a microhardness map taken from the cross section of the weld, where it is possible to observe the impact of the varying microstructure on the local mechanical behavior per region of the joint.

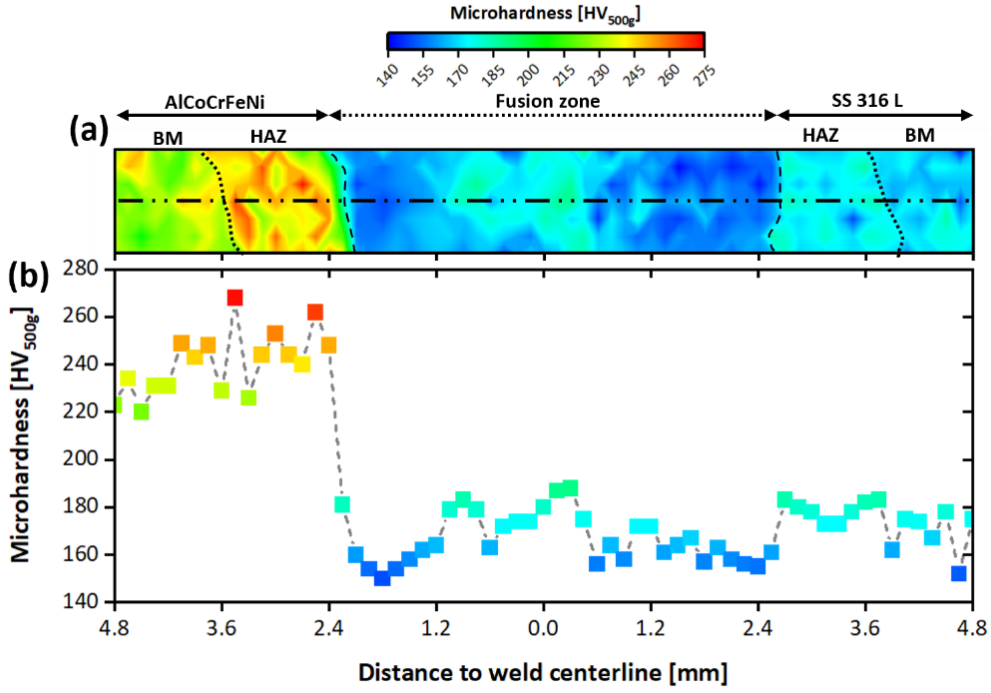


Figure 78 – Microhardness map of the dissimilar welding joint, highlighting the differences arising from the varying microstructure.

Starting from the BMs, the AlCoCrFeNi HEA has an average hardness of 221 ± 3 HV_{500g} while the 316L SS showcases an average of 169 ± 5 HV_{500g}. However, in the HAZ, an increase in hardness can be observed in both cases, with the HAZ on the HEA side reaching 247 ± 10 HV_{500g} and in the 316L SS side attaining values of 162 ± 12 HV_{500g}. In the HEA side the hardness increase can be explained by the precipitation strengthening effect of nanosized $L1_2$ and BCC phases on this region as explained by Xiong et al. [159] for the same HEA system. On the other hand, the increase in BCC peak intensity on the 316L SS side can be associated with the increase in hardness in its HAZ. Such is due to the fact that peak intensity is highly related to phase fraction, as well as texture, and the BCC phase in stainless steels corresponds to ferrite, thus causing the localized increase in hardness in this HAZ.

Furthermore, observing the FZ we can observe an inconstant variation in hardness, which can be related to the gradient microstructure and composition throughout the joint.

On the HEA side, the joint hardness is 155 ± 4 HV_{500g}, however, when going towards the center of the FZ it increases, reaching 173 ± 9 HV_{500g}. Closer to the 316L SS side, however the hardness is 153 ± 6 HV_{500g}. Such complies with the results obtained from the discussed microstructure details, as the 316L SS BM is mainly composed by an FCC matrix, while the AlCoCrFeNi HEA exhibits a composite microstructure between the softer FCC and the harder BCC B2 phase, alongside with the $L1_2$ nanoprecipitates. Therefore, resulting in a varying microhardness distribution throughout the welded joint.

Figure 72 depicts the results obtained by tensile testing the welds in comparison to both base materials, considering only engineering values. The representative stress/strain curves of the welded joint show that the fracture occurred at a strain of ≈12.7 %. The maximum tensile stress was achieved at ≈568 MPa, corresponding to a strain of ≈11.4%. The 316L SS base material, achieved a maximum of 432 MPa (corresponding to a strain of ≈54.6%) eventually fracturing at a strain of ≈56.6. The AlCoCrFeNi HEA, however, achieved the higher value for maximum tensile stress, ≈892 MPa, at a strain of ≈14.4 %. From this is possible to conclude that the weld reached a similar mechanical response concerning the maximum tensile stress of the 316L SS BM while maintaining the strain at which it fractured similar to the AlCoCrFeNi HEA BM.

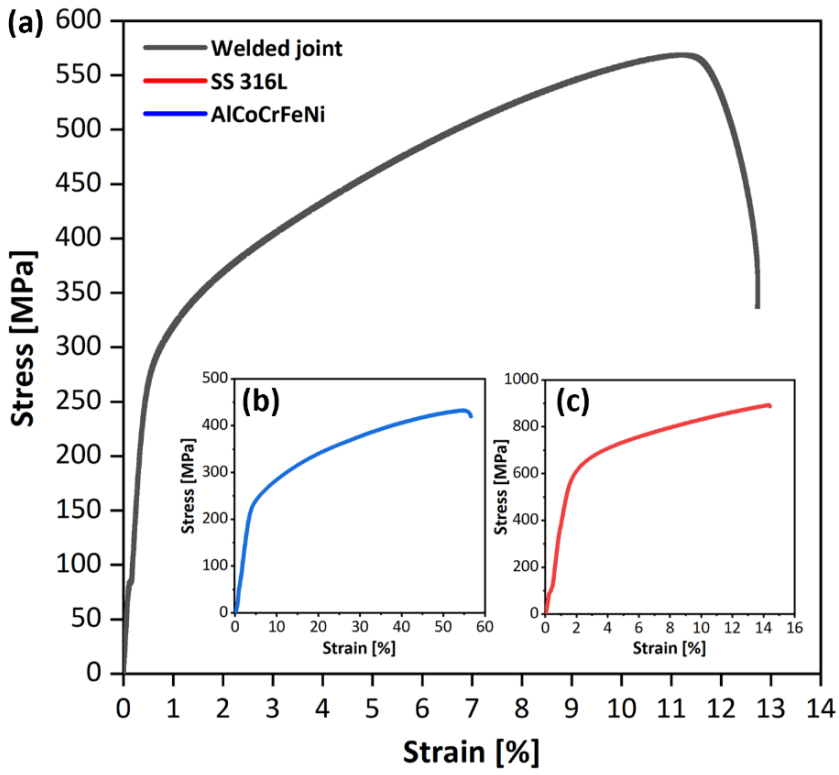


Figure 79 – Representative mechanical response to tensile stress of: (a) the welded joints; (b) 316L SS base material and (c) AlCoCrFeNi HEA base material.

The DIC data, as shown in Figure 80 (a), exhibits the different mechanical behavior highlighted by each of the different regions of the welded joint, which when spatially averaged considering the full extension of the joint yields the macroscopic mechanical response of weld shown in Figure 79.

Of special interest, we can observe that the side of the joint that sustained most of the plastic deformation corresponded to the FZ reaching 53% of strain. This behavior is followed by the 316L SS side, whereas the HEA side of the joint remained practically unaffected, thus highlighting the superior mechanical strength of the HEA. Such can be especially noted in Figure 80 (b), where further analysis of the behavior of region-specific points allows further elucidation on the local mechanical behavior on the joint. There, beyond the fact that was already noted in terms of BMs, we can see that the HAZ on both sides presents itself with a similar mechanical behavior, with that of the HEA showcasing a 20% higher strain than the 316L SS side. Such behavior on the HAZ near the HEA, albeit exhibiting higher hardness values, is expected to occur due to the effect of the larger grain size visible in Figure 70 and Figure 74.

Furthermore, observing closely the shape of the FZ (marked in purple) in Figure 11, it is possible to observe a change in slope after a of strain 13% is reached. Such phenomenon occurring upon deformation of the FZ may be linked to elemental dilution that occurs during the formation of the molten pool, thus making it more favorable for the activation of strain accommodation mechanisms other than dislocation slip, such as twining.

Upon eventual failure of the joint, which in the present case occurred in FZ, the fractured surface (refer to Figure 80 (c)) reveals several dimples characteristic of a ductile-like fracture, which is in line with that expected from the analyzed mechanical performance of the joint.

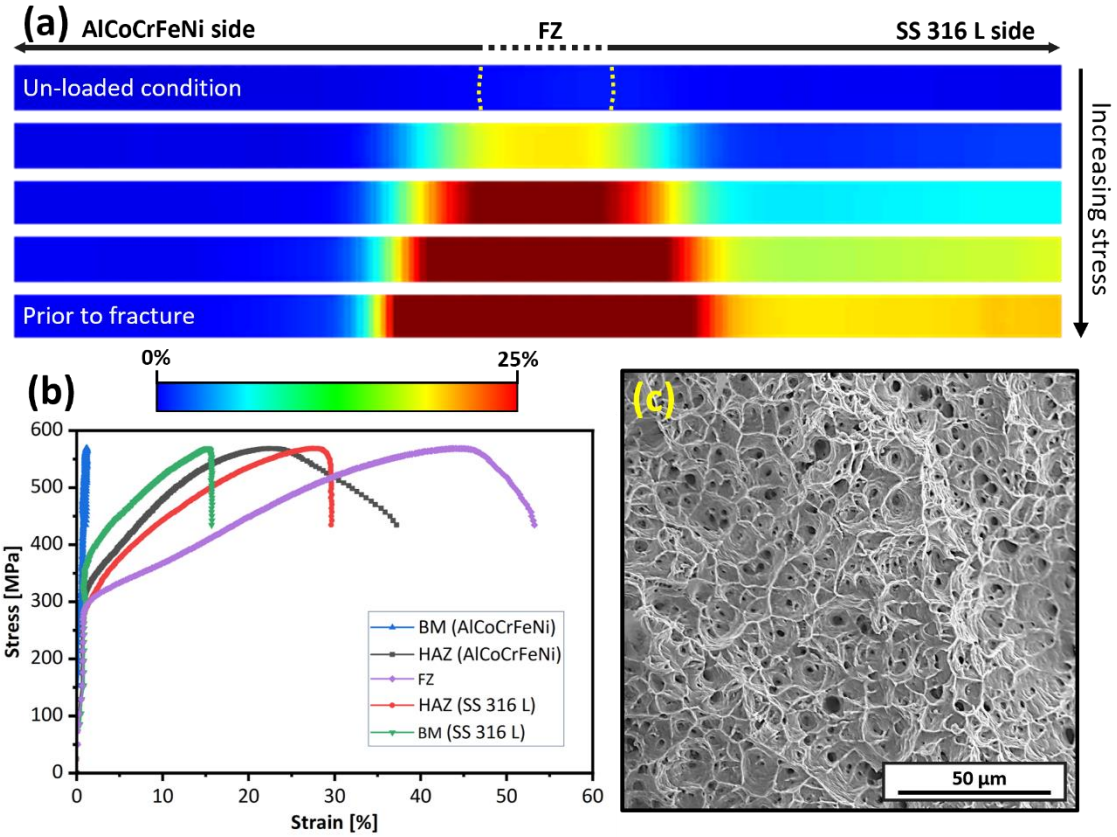


Figure 80 - Digital image correlation results exhibiting: (a) the local strain distribution before fracture and (b) point analysis obtained during tensile testing; and fracture surface after failure of the sample.

4.3.3.1 Conclusions

Dissimilar welding between a dual-phase AlCoCrFeNi HEA and commercially available 316L SS was successfully conducted via GTAW. While the grain size within the FZ showcases a clear transition from one BM to another, it can be observed that a larger size is prominent close to the HEA side of the joint.

Concerning the BMs, the 316L SS is characterized by an homogenous distribution of the constituent elements, and equiaxial microstructure throughout its full extent. The same is not applicable to the HEA, where a fully dendritic microstructure is composed of large FCC grains with a eutectic constituent in their midst, with the latter being rich in Al and Ni. A closer look at the FZ, however, reveals a similar compositional distribution throughout its full extent, with FCC as its matrix. Further analysis of the FZ via APT, reveals no significant changes within key areas of the FZ, except for the segregation of Si when near the 316L SS side of the joint.

With special emphasis on the FZ, further analysis with synchrotron X-ray diffraction was conducted, revealing the presence of an ordered $L1_2$ FCC phase and a disordered BCC phase,

beyond those already identified via microscopy, namely FCC and BCC B2. Such results were coherent with the thermodynamic-based calculations, which hinted at the formation of a disordered BCC phase during solidification.

On the topic of mechanical performance analysis, a clear distinction of the regions that comprise the weld can be found within the microhardness maps, with the FZ reaching values close to the 316L SS BM. This was also verified via tensile testing with the aid of DIC data, where most of the imposed strain is imparted by the 316L SS BM. Overall the welds attained an excellent strength and ductility balance, with a maximum tensile stress of ≈568 MPa and eventual fracture occurring in the FZ, at a strain of ≈11.7%.

Such data highlights the excellent weldability between the AlCoCrFeNi HEA system and 316L SS, hinting at the possibility of introducing HEAs in modern day engineering applications.

4.3.4 Section summary

With this section complete, the assessment of the weldability of the welded AlCoCrFeNi HEA was accomplished. Such was possible by researching the feasibility of introducing TiB_2 particles during the process, while comparing with a non-inoculated case, and via dissimilar welding with the conventional SS 316L, which is a key engineering material in the modern-day world.

Overall, the results indicate that tailoring the mechanical properties of this HEA can be accomplished, while further investigation on the matter is research topic that should be pursued from optimization of the HEA microstructure and its mechanical properties. Moreover, this section also reveals that the AlCoCrFeNi system is a good candidate for engineering applications comprising dissimilar joining with other Fe-based materials, such as stainless steels.

4.4 Microstructure and mechanical performance comparison between gas tungsten arc welded $CoCu_{20}FeMnNi$ and the $CoCu_{30}FeMnNi$ HEAs

4.4.1 Section highlights

In this chapter, a comparative analysis is introduced regarding the use of GTAW on two distinct multiphase high entropy alloys, the $CoCu_{20}FeMnNi$ and the $CoCu_{30}FeMnNi$.

Here, microstructural observations are coupled with CalPhaD-based calculations and synchrotron X-ray diffraction analysis. Overall, it was possible to observe the dual phase nature of the alloys alongside the nucleation of a B2 BCC phase in the HAZ of both welds. The mechanical behavior of the welded materials was observed to be poor yet still exhibiting an acceptable mechanical performance. Such was attributed to the residual stress conditions and large grain size that developed owing to the process thermal cycle, which contrasted deeply with the microstructure of each BM.

4.4.2 Microstructural characterization of the joints and CalPhaD analysis

After GTAW, welded joints with full penetration without any visible defects were obtained. As such, standard metallographic preparation techniques were employed on the $CoCu_xFeMnNi$ (x = 20 or 30 at. %) welded samples. Figure 81 depicts representative EBSD IPF images of the resulting joints.

At a first glance it is possible to observe that in both cases large and highly aligned columnar grains grew from the BM towards the center of the FZ, differing massively from the highly deformed microstructure that composes the BM. In fact, the microstructure of the BM corresponds to the black (non-indexed) regions of the EBSD IPF maps, where the highly distorted microstructure prevents proper indexation of the Kikuchi patterns. Nevertheless, the impact of the heat input on the HAZ, formed between the non-affected BM and the FZ, is clear due to the existence of a refined grain structure with an average grain size of 4.56 ± 0.61 µm and 4.54 ± 1.26 µm, for the $CoCu_xFeMnNi$ alloys with x = 20 or 30, respectively. It should also be noted that at the fusion boundary there is the development of a refined grain structure, due to the high cooling rates imposed by the cold (previously BM now HAZ) supporting

material. This refined grain structure will then be used as support for the development of the large columnar grains observed in the FZ.

The highly oriented and columnar grains that developed during GTAW will introduce anisotropy on the mechanical properties in the FZ. This fact, combined with the existence of a highly deformed microstructure in the BM and of a small equiaxed grain structure in the HAZ, compounded by the columnar grains in the FZ, render the expectation of an inhomogeneous mechanical behavior across the joint.

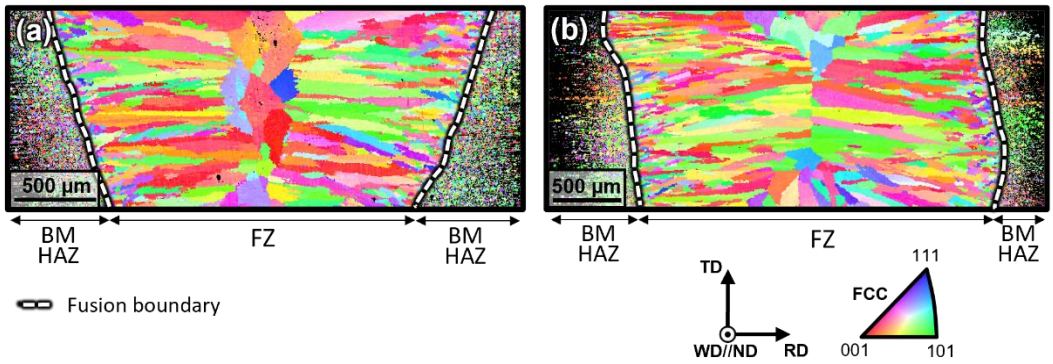


Figure 81 - Representative electron backscatter IPF macroscopic images of the welded joints of: (a) CoCu20FeMnNi; (b) CoCu30FeMnNi.

Figure 82 showcases the initial condition of the two BM prior to welding. It can be observed that in both cases the microstructure is comprised by interlayered elongated stripes corresponding to two different FCC phases (as seen by in EBSD phase maps in Figure 82 a) and b)). Further characterization using EDS allows to characterize the phase's composition, as detailed in Figure 82 c) to d). The elemental mapping data reveals that one of the FCC phases in both materials is rich in both Co and Fe, while the other FCC is primarily Cu- and Mn-rich. For this reason, from this point we address these two FCC phases as the Co, Fe-rich phase and the Cu-rich phase. It is also possible to observe that the $CoCu_{30}FeMnNi$ has a higher amount of the Cu-rich phase within it, which is related to its higher nominal content of Cu.

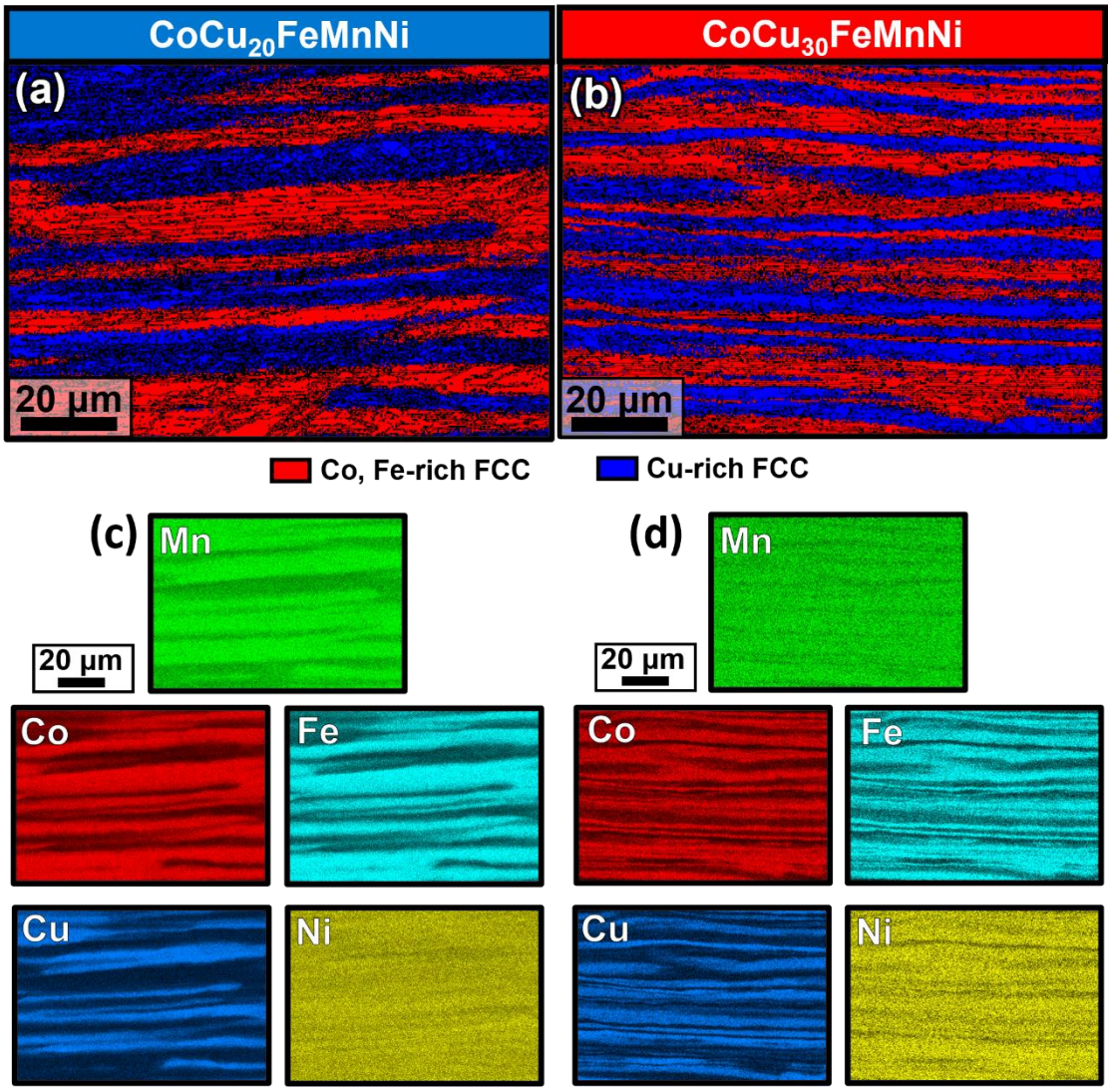


Figure 82 – EBSD phase maps highlighting the initial condition of the (a) CoCu20FeMnNi and (b) CoCu30FeMnNi HEAs, alongside with the corresponding elemental distribution in (c) for the CoCu20FeMnNi and (d) for the CoCu30FeMnNi BMs.

As the phase distribution on both BMs is highly dependent on the processing conditions prior to welding, the associated phase diagrams depicted in Figure 83 allow to infer on the possible phases passible to occur in the alloys during their thermomechanical processing. In both cases, at high temperatures liquid first solidifies into a FCC phase (FCC #1). Eventually, at ≈930 °C a different FCC phase (FCC #2) starts to form as part of a solid state transformation, as Cu and Mn diffuse into the FCC #1 grain boundaries, thus giving origin to the two mentioned major phases that were previously shown in Figure 82 a) and b). Beyond these two phases, of relevant notice is also the formation of a B2 BCC phase, which is formed at ≈560 °C, for both

alloy compositions. This cooling path is compliant with that found in the literature [48,160,161]. As such, it is important to highlight that the formation of the different FCC phases occurs in the solid state through solute diffusion.

Nevertheless, although phase diagrams can yield a basic understanding of the solidification of an alloy, these only consider equilibrium conditions with infinitively fast diffusion in both the liquid and the solid phases. Such is seldom achieved in real life processing conditions, especially during any fusion-based welding process, providing in this way sufficient conditions for other (metastable) phases to occur in the weld microstructure. However, at a first instance it allows us to infer upon the possible phases that may form upon the solidification of these HEAs. Further analysis is made through Scheil-Gulliver calculations, detailed further ahead in this paper, when analyzing the FZ microstructure evolution (in Figure 85).

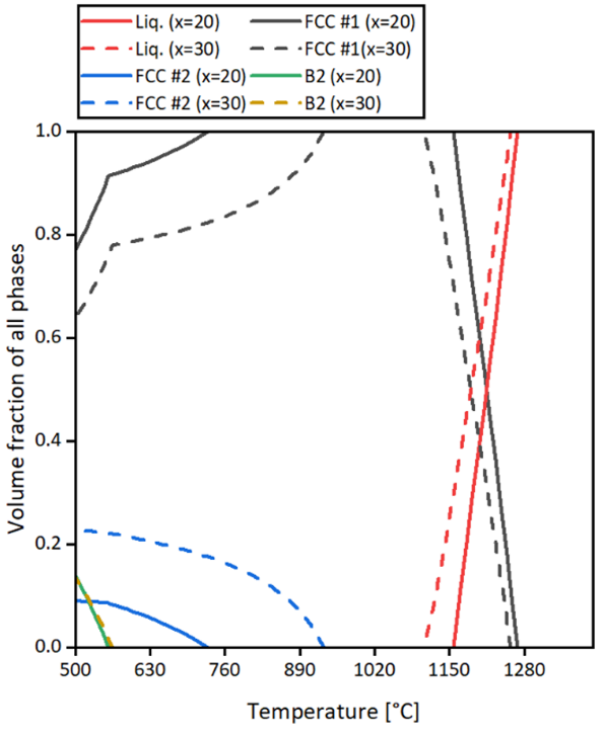


Figure 83 – One axis equilibrium performed to evaluate the phase formation in equilibrium conditions. The calculations were computed using TCHEA5 databases.

Attention is now devoted to the fusion boundary (FB), and the regions surrounding it: the HAZ and FZ. From the HAZ we can observe that the microstructure is characterized by near equiaxed grains within elongated packs of the domains that contain the two FCC phases. From

this, we can also observe grain growth phenomena that caused larger grains to develop with increasing size, when approaching the FZ. Such is particularly visible in Figure 84 (c) and (d).

The columnar dendritic nature of the FZ contrasting with the grains beyond the FB towards the BM can also be identified here, comprising also both FCC phases. We can qualitatively observe in the EBSD phase maps (refer to Figure 84 e) and f)) that the $CoCu_{30}FeMnNi$ alloy comprises more of the Cu-rich FCC phase than the $CoCu_{20}FeMnNi$ in the corresponding FZ. Additionally, by complementing the IPF maps of Figure 81 and Figure 84 we can see that the grain size exhibited by this region is larger than any of the other regions of the weld, given the competitive growth phenomena that occurs during welding. This occurs as the grains present in the region that will comprise the HAZ, acts as a platform for new grains to grow in the maximum temperature gradient, which is aligned perpendicularly to the FZ centerline. As these new grains form, competitive growth takes place, where those which have their growth direction aligned with the easy growth direction (<001> for FCC materials) tend to grow faster and larger than those that are aligned in other directions. Such tendency can be seen in the IPF maps of Figure 81, where the most grains in the FZ have a red color tone, corresponding to a predominant <001> orientation.

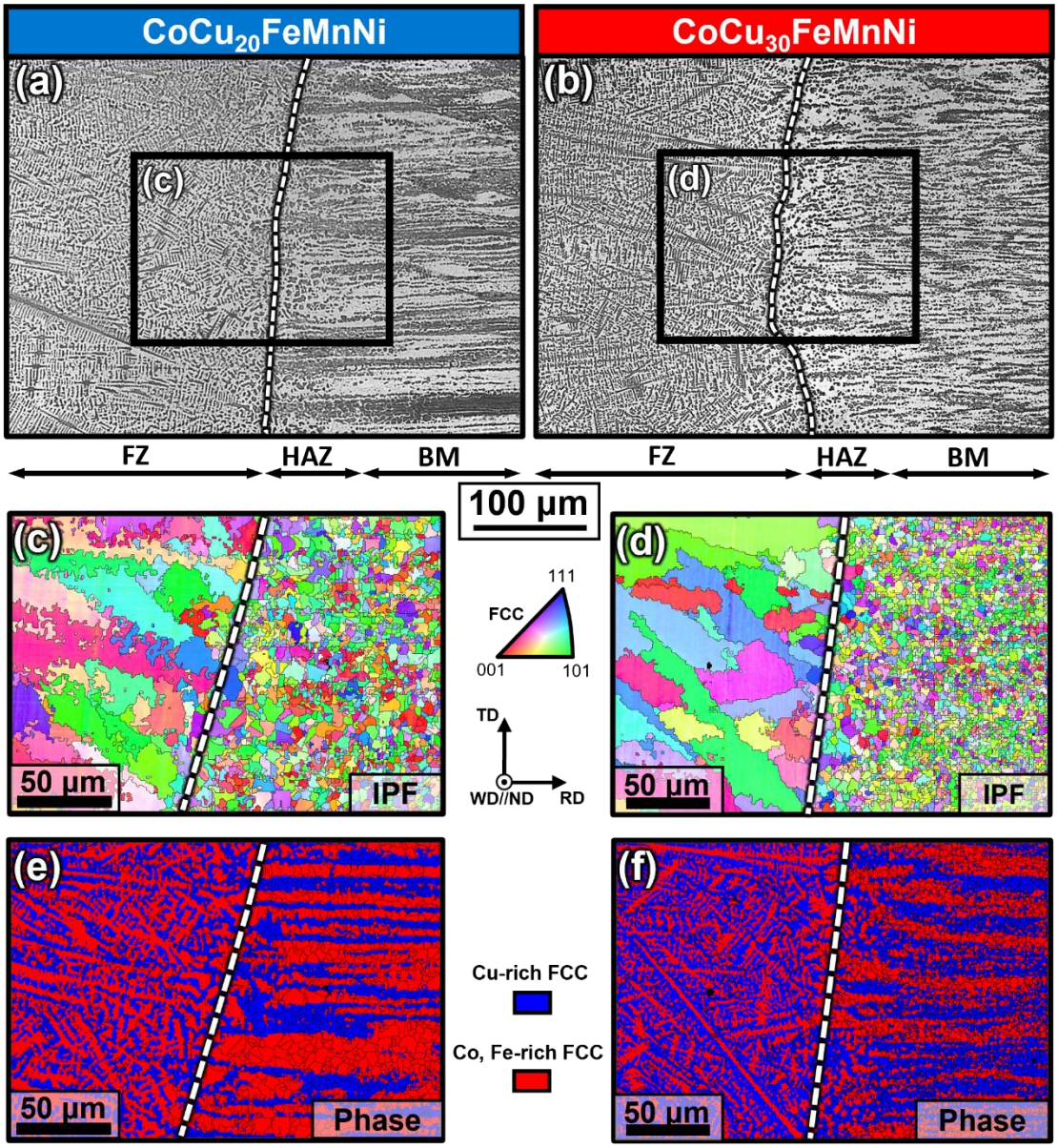


Figure 84 – Microstructural analysis at the fusion boundary, highlighting the optical microscopy image of the (a) CoCu20FeMnNi HEA and (b) CoCu30FeMnNi HEA and corresponding EBSD IPF and phase maps in (c) and (e) for the CoCu20FeMnNi, and phase maps in (d) and (f) for the CoCu30FeMnNi HEA.

Furthermore, given the already mentioned non-equilibrium solidification conditions to which the molten pool is exposed to during welding (on both types of materials), the solidification paths can deviate from those calculated considering only equilibrium conditions. As such, to evaluate the microstructure under non-equilibrium conditions Figure 85 a) displays the solidification curves of both alloys using the Scheil-Gulliver methodology available.

The solidification path details that for the $CoCu_{20}FeMnNi$ alloy, the liquid phase starts to solidify at ≈1270 °C, with a solidification range of ≈310 °C. Additionally, for the $CoCu_{20}FeMnNi$ case solidification starts at ≈1250 °C, ending at ≈910 °C, corresponding to a solidification range of ≈340 °C. Thus, it can be inferred that the addition of Cu in the material is beneficial to lower the solidification temperature range, which is often associated to hot cracking during welding. In both cases, the solidification curves only indicate the formation of a Co, Fe-rich FCC phase. A possible reason for the non-existence of the Cu-rich phase can be due to the fact that the Scheil model only assumes infinitively fast diffusion in the liquid, while neglecting the diffusion phenomena occurring in the solid phases. Nevertheless, according to the phase diagram, the Cu-rich FCC phase only forms at lower temperatures, after the liquid was fully consumed. This would be expected as the Scheil-Gulliver simulation does not consider diffusion on the solid state, which is the cause for the formation of a second FCC phase. To further detail the evolution upon solidification, we now turn to identify how elemental segregation occurs along the predicted solidification paths, considering the partition coefficient of all elements in the Co, Fe-rich phase during solidification, not considering solid-state transformations. These results are displayed in Figure 85 b).

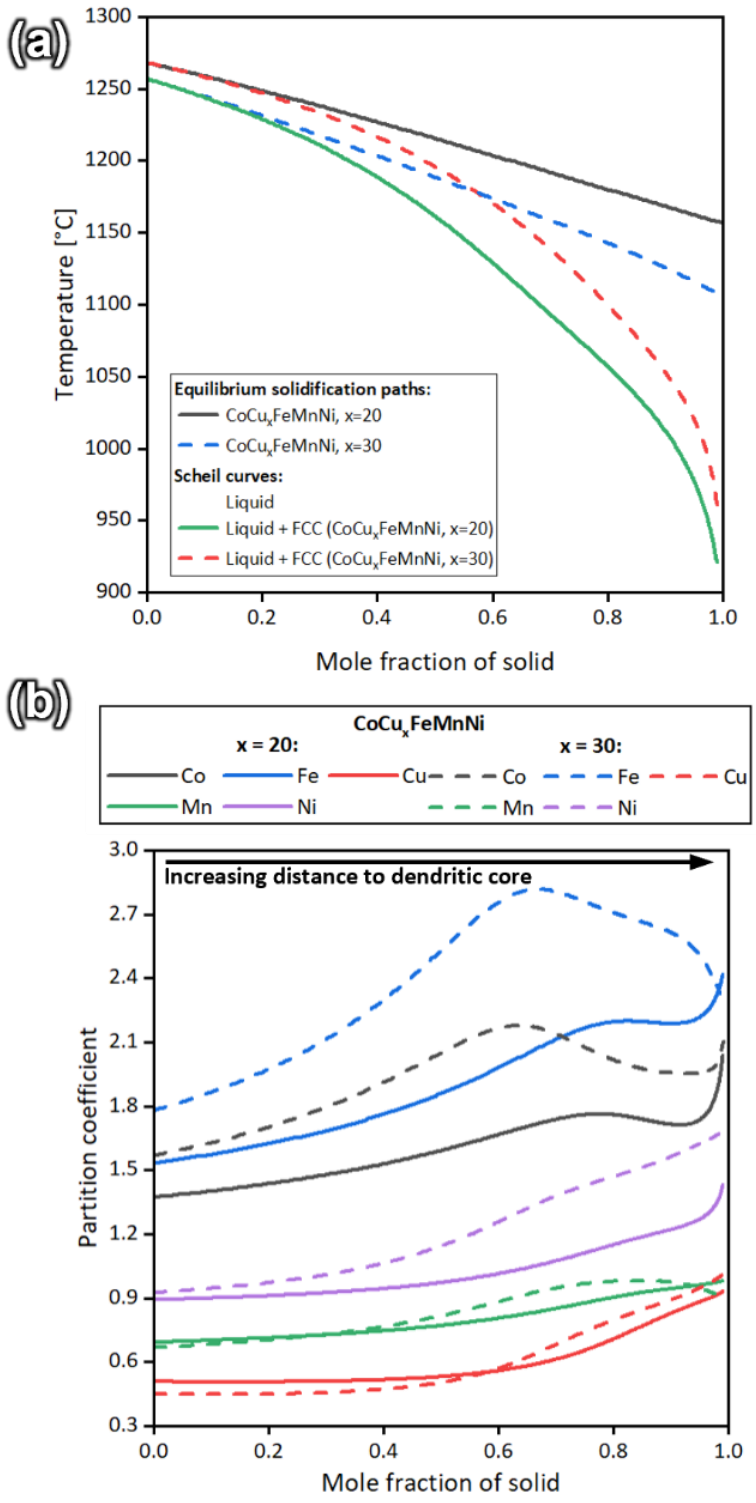


Figure 85 – (a) Simulation of the non-equilibrium solidification using Scheil-Gulliver method, and (b) partition coefficient of the elements throughout solidification.

The partition coefficient can be calculated by dividing the concentration of an element on a solid phase and the concentration on the liquid. In this sense, if the partition coefficient

attains values superior to 1, this means that such solid-state phase is being enriched by these elements. Should the partition coefficient reach values lower than 1, this indicates that such element is being segregated into the interdendritic liquid. Given this, the partition coefficient can help us to understand how the elements tend to be distributed within a forming dendrite. That is, the mole fraction of solid values that are closer to zero, correspond to when the liquid is starting to solidify, having a wide amount of all elements available for the formation of any solid phases. Such corresponds to the dendritic cores, which are the first regions to solidify. Contrarily, when the mole fraction of solid reaches values closer to 1, it means that the elements that are still available within the liquid eventually solidify at the interdendritic regions.

Considering the $CoCu_{20}FeMnNi$ case, it is possible to observe that the Fe and Co elements partition coefficient curves have a similar behavior, where it is possible to see that up to an approximately 0.80 mole fraction of solid, these tend to increase, meaning that the initially formed phase is being enriched by these elements. From that point on, their partition coefficient tends to decrease, indicating that the regions further away from the dendritic cores are getting depleted of these elements. However, when the mole fraction of solid is above 95 %, a sharp increase in the partition coefficient of Co, Fe and Ni can be observed. Particularly, in the case of Ni, the partition coefficient starts below 1 and exhibits an increasing tendency throughout all solidification path, meaning that the newly formed dendrites are getting enriched with this element. Finally, the partition coefficient of Co and Mn is also consistently increasing. This indicates that we can expect a Cu and Mn concentration peak at the dendritic interfaces, as these elements are consistently being segregated into the liquid.

A similar behavior can be seen in the $CoCu_{30}FeMnNi$ case. However, here the Fe and Co peak occurs at an earlier stage, when the mole fraction of solid reaches a value of nearly 0.65. In this case elemental segregation is even more obvious, as the dendritic regions away from the core become depleted of these elements.

With this information it can be concluded that the dendritic cores are richer in Fe, Co and Ni, while the dendritic boundaries tend to be richer in Cu and Mn upon solidification. As such, it is possible to conclude that with further cooling, the formation of the Cu-rich FCC phase at the dendritic grain boundaries is eminent and very likely to occur, but as a solid state transformation. These thermodynamic-derived results agree with the EDS data obtained in

the FZ of both welds displayed in Figure 86. In fact, the element distribution results show coherence with the predicted compositional distribution obtained considering the partition coefficient, especially in the Co, Fe-rich phase and the Cu-rich phase, which also has Mn in a lower percentage in its constitution. However, it would have been expected a higher amount of Ni in the interdendritic region, which is not the case for both alloys´ welded joints, as the EDS indicates that the Co, Fe-rich phase has more Ni than the Cu-rich phase. Such can be explained by the fact that no diffusion in the solid phase was considered for these non-equilibrium thermodynamic calculations. Additionally, the assimilation of Ni in the Co, Fe-rich dendrites can also occur in later stages of temperature decrease, as the Cu-rich phase starts to form.

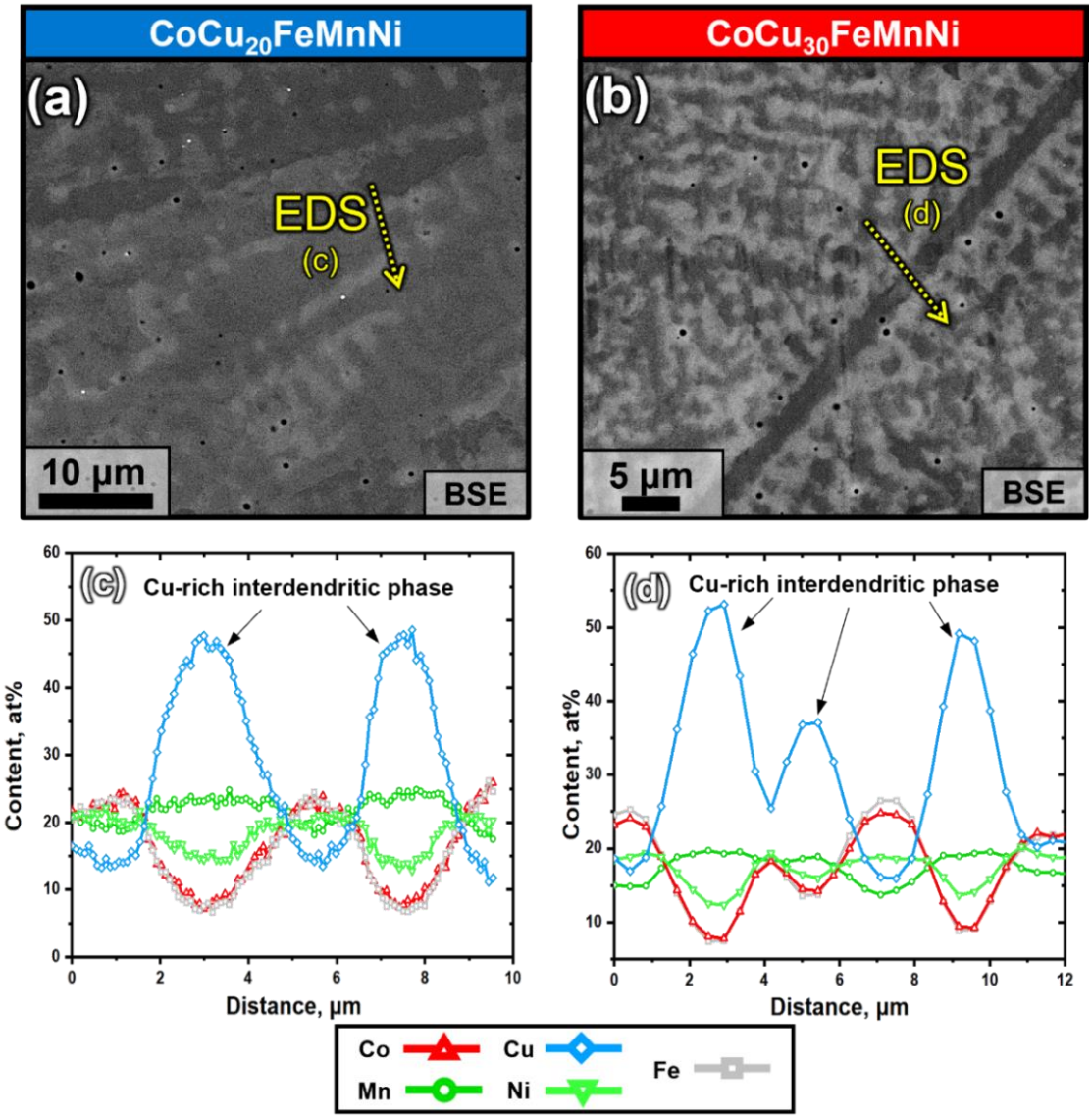


Figure 86 - Microstructural analysis of the fusion zone on the (a) $CoCu_{20}FeMnNi$ and (b) $CoCu_{30}FeMnNi$ HEAs in the as-welded condition, and corresponding EDS line scans (c) and (d).

4.4.3 Synchrotron X-ray diffraction of the welded joints

The phases present in the welded joints are further unveiled by the SXRD patterns displayed in Figure 87 a), b), and c) corresponding to the BM, HAZ, and FZ, respectively. Such allows us to inspect on the potential formation of other phases in the material, that otherwise cannot be identified by either conventional or advanced microscopy (due to limited surfaces areas for analysis available, whereas high energy synchrotron radiation allows to work in transmission mode over wider regions, yielding improved statistics).

Starting from the BM, as expected it is possible to identify the two phases sharing the same FCC crystal structure and similar lattice parameters. Furthermore, analysis of the patterns corresponding to the HAZ reveals significant changes. Phase identification in this region allows to observe precipitation of a B2 BCC phase (at a lower intensity level) in the region of the joint for both alloys. Such a phase is predicted by one axis equilibrium diagrams (refer to Figure 83) to nucleate at relative lower temperatures than the Cu-rich FCC (B2 BCC nucleates at ≈560 °C), which highlights the different thermal processing conditions that arose from the exposure of the solid-state material to the high temperatures impending from the molten pool. Nevertheless, in the FZ no indication of the formation of this B2 BCC was encountered in the patterns, only the two main FCC phases were encountered. This is coherent with the results obtained from the EBSD data and CalPhaD simulations.

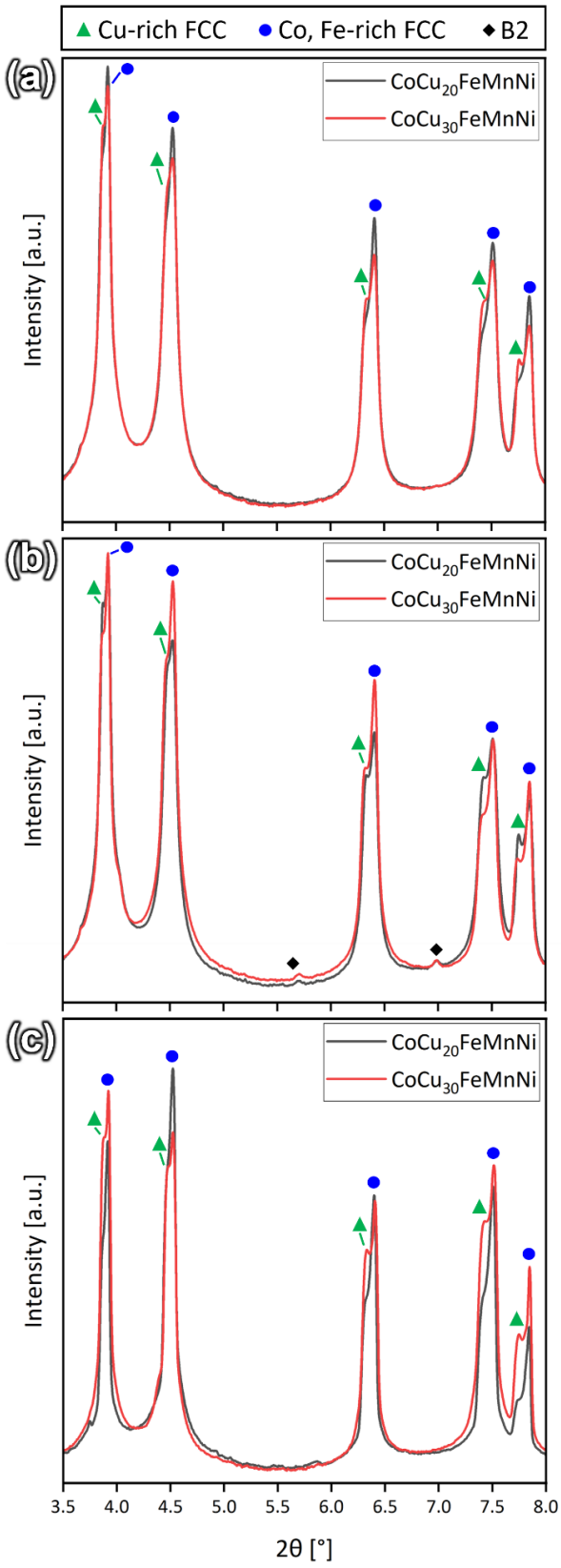


Figure 87 – Representative synchrotron X-ray diffraction patterns, from both HEAs welded joints on the: (a) BM, (b) HAZ, and (c) FZ.

The lattice parameters of these phases were determined from the diffraction patterns using Rietveld refinement (via GSAS II), and are depicted in Table 13. Here, the BM results show proximity to the HAZ and FZ, although with slight deviations which is to be expected given the different microstructure exhibited in each of these regions.

Table 13 - Lattice parameter in the HAZ and FZ (rounded to the fourth decimal case)

	Phase	Crystal structure (space group)	$CoCu_{20}FeMnNi$ [Å]	$CoCu_{30}FeMnNi$ [Å]
BM	**Co, Fe-rich FCC**	FCC (F m -3 m)	3.6008	3.6025
	Cu-rich FCC	FCC (F m -3 m)	3.6430	3.6442
HAZ	**Co, Fe-rich FCC**	FCC (F m -3 m)	3.6007	3.6013
	Cu-rich FCC	FCC (F m -3 m)	3.6403	3.6478
	B2 BCC	B2 BCC (P m 3 m)	2.8658	2.8599
FZ	**Co, Fe-rich FCC**	FCC (F m -3 m)	3.6031	3.6099
	Cu-rich FCC	FCC (F m -3 m)	3.6461	3.6466

Further analysis of the synchrotron diffraction data reveals the phase volume fraction present in the base material of each alloy: the $CoCu_{20}FeMnNi$ BM is composed of 68.3% of the Co, Fe-rich phase, while the remaining is Cu-rich FCC; for the $CoCu_{30}FeMnNi$ the fractions change to 62.8% for the Co, Fe-rich phase, and 37.2% of the Cu-rich phase. The phase fraction data obtained for the diffraction experiments is in good agreement with the EBSD phase maps, as previously shown in Figure 82.

Given the microstructure alterations occurring in the HAZ and FZ on both alloys, the phase volume fraction of each phase is also bound to differ from the BM. As such, starting on the HAZ of the $CoCu_{20}FeMnNi$ HEA, the results indicate that the phase volume fractions of each of the phases is 61.2, 34.1 and 4.7% for the Co, Fe-rich, Cu-rich and B2 BCC phases, respectively. For the $CoCu_{30}FeMnNi$ HEA, however, the phase volume fraction distribution is 58.2, 39.5 and 2.3% corresponding to the Co, Fe-rich FCC, Cu-rich FCC and B2 BCC.

Furthermore, the FZ is the region, where there is a more notorious modification in the phase fractions between both alloys. Here, the $CoCu_{20}FeMnNi$ HEA exhibits an overall amount of 78.9% of the Co, Fe-rich phase (with the remaining 21.1% corresponding to the Cu-rich phase), while the $CoCu_{30}FeMnNi$ HEA has a 51.1 and 48.9% percentage of the Co, Fe-rich phase

and Cu-rich phase, respectively. Such phase volume fraction distribution may have a considerable influence on the final mechanical behavior of the resulting joints.

Nevertheless, before we delve into the mechanical properties of the welded joints, another important topic of discussion concerns the microstrain variation. The microstrain changes along the welds can be derived from the change in lattice parameters exhibited by each phase as obtained by SXRD. Such allows us to infer on the residual stress condition of the welds and role of the weld thermal cycle along the different regions of the joint. However, calculation of the microstrain requires knowledge of the unstrained interplanar spacing (d_0) of each of the phases in both materials. Using single-peak fitting, analysis was performed in the (311) diffraction peak of each of the FCC phases, and the (211) for the B2 BCC phase was also to retrieve the values for interplanar spacing (d) along the joints. The choice of these peaks for this analysis is based on their insensibility to intergranular strains in the FCC and BCC crystal structures, respectively [104]. The variation is depicted in Figure 88.

In both cases, it is evidenced that the d values are constant in the BM, which was expected. Eventually, the presence of the B2 BCC phase marks the beginning of the HAZ, where the d-spacing for this phase tends to decrease. As the B2 BCC diffraction peaks disappear, the HAZ in both welds continues until reaching the fusion boundary, where an increase on the d-spacing can be observed in the Co, Fe-rich FCC phase. The disappearance of the B2 BCC phase is related to the temperature and time to which a given region of the weld was subject to. Being located in the region of the HAZ further away from the FZ (where the maximum temperatures are attained), the conditions for the nucleation of the B2 BCC phase are granted, given that this phase is characterized by its nucleation at relatively lower temperatures, as indicated in Figure 83.

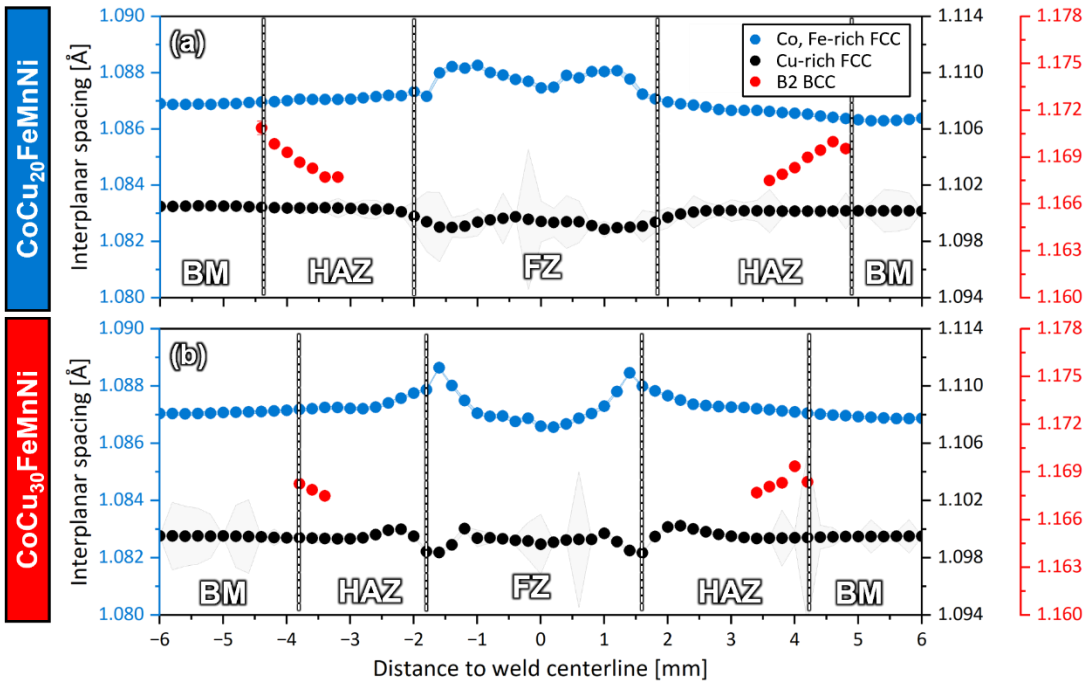


Figure 88 - Interplanar spacing distribution corresponding to the different phases identified throughout the microstructure of $CoCu_{20}FeMnNi$ (a) and $CoCu_{30}FeMnNi$ (b) welded HEAs.

Furthermore, in the FZ a consequent decrease on the d-spacing of the Cu-rich phase can also be observed, such is related to the marked impact in the microstructure caused by the GTAW. This disparity in d-spacing values is especially visible in the $CoCu_{30}FeMnNi$ welded joint, where a not so smooth evolution translates the complex microstrain state of the joint at the fusion boundary. Nevertheless, eventually in the bulk of the FZ the d-spacing values evidence a decrease, achieving values closer to those exhibited by the BM.

4.4.4 Electrochemical characterization of the joints

To assess the corrosion behavior of the welded joints, the two extreme microstructural conditions of the joints, that is BM and FZ, were analyzed. As such, representative anodic polarization curves comparing the BM and FZ of both types of samples are displayed in Figure 89. Using the Tafel model [129,162], the corresponding corrosion currents, I_{corr}, were extrapolated to be 24.8 µA/cm^2 for the $CoCu_{20}FeMnNi$ BM and 28.2 µA /cm^2 for the $CoCu_{30}FeMnNi$ BM. Considering the corresponding FZs, the extrapolated I_{corr} for the $CoCu_{20}FeMnNi$ case was 94.9 µA/cm^2, while for the $CoCu_{30}FeMnNi$ joint the value was 153.3 µA/cm^2. Such allows us to

verify that deterioration of the corrosion behavior can be seen in both cases when comparing the BMs to their corresponding FZs, being more prominent in the $CoCu_{30}FeMnNi$ HEA case.

On the other hand, comparison of the corrosion potential, E_{corr}, for each condition, revels that for the $CoCu_{20}FeMnNi$ case, the BM and the FZ showcase values of -0.891 V and -0.894V, respectively. These however, contrast with those extrapolated in from the $CoCu_{30}FeMnNi$ joint, where the BM, corresponding to -0.667 V, exhibits a significantly higher value than its corresponding FZ (-0.806 V). This indicates that the $CoCu_{30}FeMnNi$ HEA has a lower tendency to corrode than the other analyzed regions.

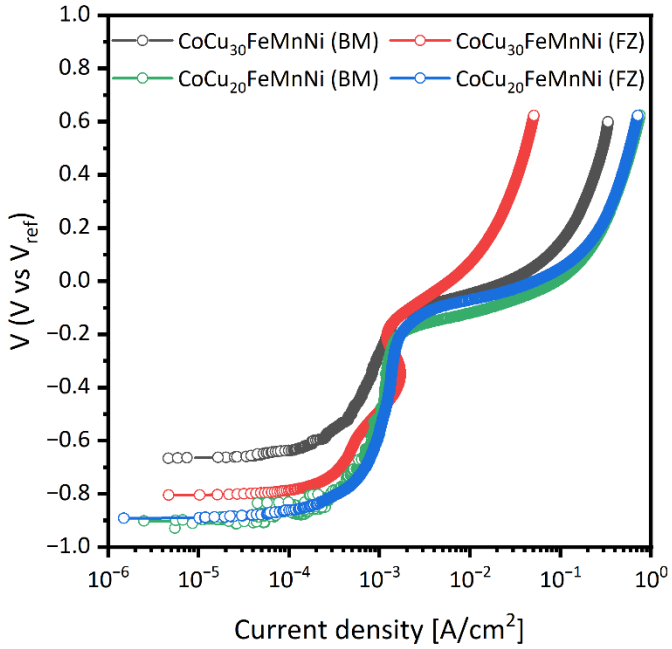


Figure 89 – Comparison between the polarization curves of the $CoCu_xFeMnNi$ (x=20,30) BMs alongside with the corresponding FZs.

Likewise, the EIS measurements, performed the BM and the FZ of both samples are presented in Figure 90, in terms Bode and Nyquist diagrams. There it is possible to observe that, at low frequencies, the impedance modulus, |Z|, of the BMs reach values up to 50.3 Ω for the $CoCu_{20}FeMnNi$ HEA and 528.4 Ω for the $CoCu_{30}FeMnNi$ HEA. Conversely, for each analyzed FZ the maximum measured values were 63 Ω and 141 Ω, respectively. Additionally, the maximum values attained for the phase angle was ≈-0.27° for the $CoCu_{20}FeMnNi$ BM and ≈-0.7° in the $CoCu_{30}FeMnNi$ BM case. Similar values were noted for the $CoCu_{20}FeMnNi$ FZ, corresponding to ≈-0.35°, while in the $CoCu_{30}FeMnNi$ FZ a distinct behavior from its corresponding BM was verified, these measured to be ≈-0.66°.

Overall, these values agree with those expected from the polarization curves, where the corrosion behavior of the $CoCu_{30}FeMnNi$ FZ is significantly more different than its corresponding BM, which in the $CoCu_{20}FeMnNi$ joint is not as obvious.

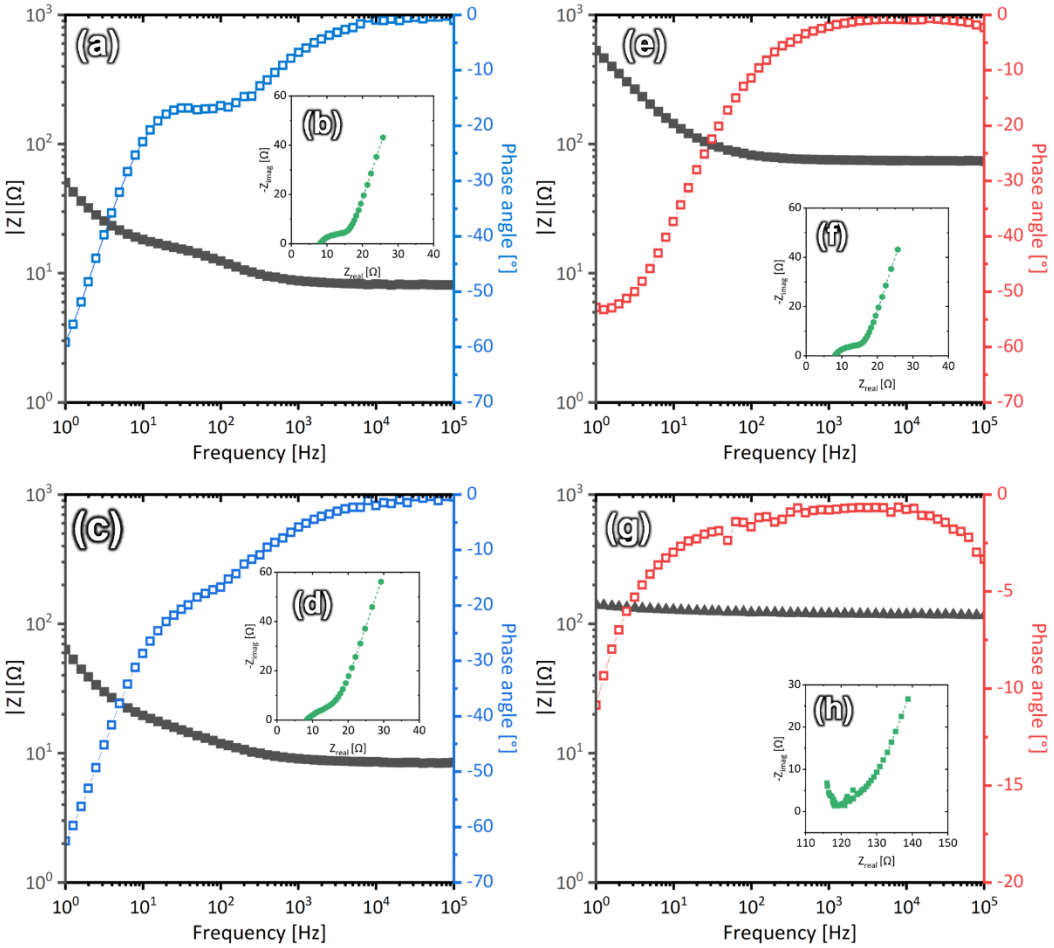


Figure 90 – EIS measurements of the welded joints: (a) and (b) are the Bode and Nyquist diagrams of the CoCu20FeMnNi BM, respectively, while (c) and (d) are the Bode and Nyquist diagrams of its corresponding FZ; (e) and (f) correspond to the Bode and Nyquist diagrams of the CoCu30FeMnNi BM and (g) and (h) are the Bode and Nyquist diagrams of the CoCu30FeMnNi FZ.

4.4.5 Mechanical properties assessment via microhardness mapping and tensile testing

Considering the evolution of microstructure and the microstrain distribution previously unveiled, it is important to evaluate the mechanical performance of the welded joints to assess their potential use as part of structural components. This is the premise on which the inspection of such novel metals using welding technologies is based on. Figure 91 displays

the microhardness distribution along each welded joint. A major difference between samples is the extension of each weld, where the FZ of the $CoCu_{20}FeMnNi$ is larger than that of the $CoCu_{30}FeMnNi$ HEA (≈2.7 mm vs ≈2.55 mm). This can be explained by the different thermal dissipation conditions granted by each phase upon their nucleation on the welded joints, clearly suggesting that the thermal field experienced by this portion of the welded joints is different.

As such, thermal conductivity calculations per phase were performed based on the nominal compositions of both alloys. The results evidence that upon its nucleation and subsequent phase transformations, the Co, Fe-rich FCC phase holds an approximately constant thermal conductivity value of 23 W/mK. The same, however, is not the case of the Cu-rich FCC, where the thermal conductivity increases from ≈ 54 W/mK (upon its nucleation) to ≈ 100 W/mK (at 500°C), in the $CoCu_{20}FeMnNi$ case. For the $CoCu_{30}FeMnNi$ HEA, as the Cu-rich FCC begins to nucleate at a an earlier stage (refer to Figure 83), its thermal conductivity goes from ≈ 27 W/mK reaching ≈ 100 W/mK at 500°C). This allows us to infer that heat dissipation conditions were different between welded samples, although the same welding parameters were utilized, thus resulting in different dimensions for the HAZ and FZ. This is also coherent with the larger extent of the region containing the B2 BCC phase on the $CoCu_{20}FeMnNi$ material, highlighting that heat transfer was more efficient in the $CoCu_{30}FeMnNi$ case, by not providing sufficient time for more B2 BCC to form (as it would be expected from the one-axis equilibrium diagram in Figure 83).

Overall, the microhardness distribution in both types of samples is similar. The results reached a maximum of ≈361 HV_{50} in the BM and a minimum of ≈137 HV_{50} in the FZ. Such decrement in the microhardness of the FZ can be related with the large grain size characteristic of this region visible in Figure 81.

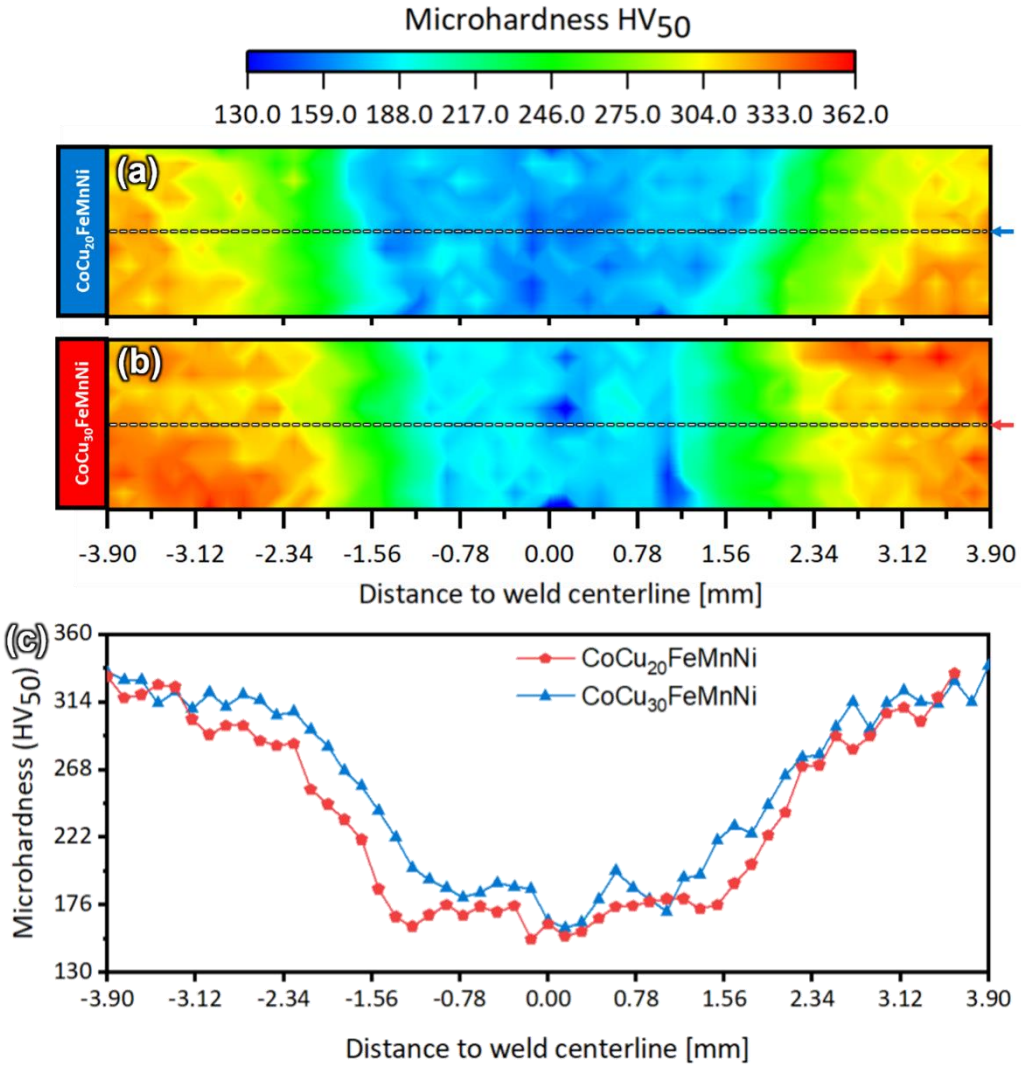


Figure 91 – Microhardness distribution along the (a) $CoCu_{20}FeMnNi$ and (b) $CoCu_{30}FeMnNi$ welded HEAs. Comparison of the hardness variation taken from the middle line of the map is displayed in (c).

Further analysis of the mechanical properties was done by performing tensile tests. Representative stress-strain curves of both BMs and corresponding welded joints are displayed in Figure 92 a). As it is possible to observe from the tensile behavior of both BMs, the $CoCu_{30}FeMnNi$ HEA reached a higher elongation than the $CoCu_{20}FeMnNi$ HEA, with corresponding values of 9.1 and 4.2 %, respectively. Considering the ultimate tensile strength (UTS), the $CoCu_{20}FeMnNi$ BM possesses a slightly lower strength than the $CoCu_{30}FeMnNi$ HEA: 902 vs 942 MPa, respectively. These results indicate that the Cu enrichment on the composition positively contributes to its mechanical performance. This occurs as the increase of Cu as alloying element on the composition of the $CoCu_{30}FeMnNi$ HEA, contributes to an enhancement

in its ductility, allowing it to become more ductile as the fraction of Cu-rich phase also increases. The higher amount of this ductile phase, combined with the remaining Cu confined in the Fe, Co-rich FCC, then translates into the increase in ductility on the HEA.

Considering the resulting welded joints, however, it can be observed that the tensile properties of both materials deteriorated considerably, with the Cu-lean HEA possessing a strength of 437 MPa, while the Cu-rich reached 368 MPa. As for the elongation, the welded joints performed poorly compared to their BMs counterparts. However, the drop in elongation was more significant for the Cu-rich material (8.6 vs 2.5 %), rather than the Cu-lean alloy (3.8 vs 3.3 %). This decrement in both strength and elongation primarily stems from the microstructure changes induced by the weld thermal cycle. In fact, the gradient of microstructures that are found in both joints (deformed grains in the BM, small equiaxed grains in the HAZ and predominantly large columnar grains in the FZ), will render not only an heterogenous deformation behavior. In fact, strain will tend to be concentrated in the low hardness FZ, which is further compounded by the anisotropic behavior arising from the columnar grain structure present at this region of the joint.

Such factors are further intensified by the microstrain distribution in the $CoCu_{30}FeMnNi$ welded joint (refer to Figure 88). Here it is possible to infer that the local strain concentration is higher near the fusion boundary than in the bulk of the FZ. The same does not occur in the Cu-lean weld, where a smooth microstrain transition from the BM to the FZ can be observed. Additionally, the phase fraction ratio between the major FCC phases can also be detrimental to the mechanical performance of the welds, as the higher content of the Cu-rich FCC can be detrimental to the maximum strength achieved by the alloy, although granting it more ductility, when a homogenous microstructure distribution can be found (as in the case of the BMs).

Nevertheless, evidence of the relatively poor mechanical performance of the welded joints can be found in Figure 92 b) and c), taken prior to fracture during tensile testing. Here it is possible to observe that the fusion zone, being the softest region in both materials, is also the location, where most of the strain is sustained, leading to fracture in this region in both cases. These results are coherent with the impact that the microstrain levels encountered in the welds (refer to Figure 88) on the local strain distribution, which is observed via DIC. Given

this, it is possible to observe that the mentioned sharper increase of d-spacing at the fusion boundary on the $CoCu_{30}FeMnNi$ weld results on the fracture on this region, instead of the center of the FZ, which is the case of the Cu-lean welded joint.

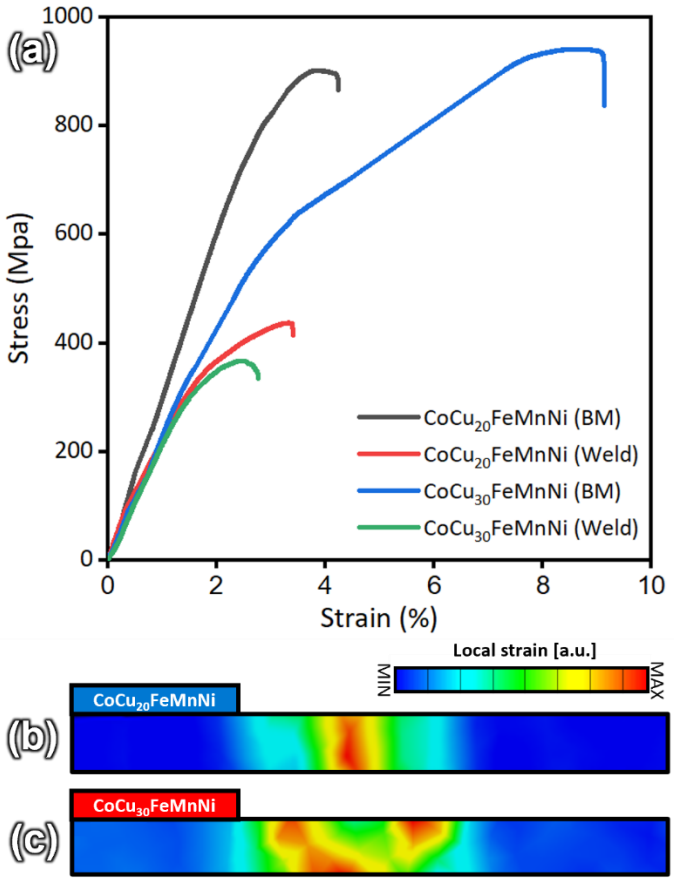


Figure 92 – (a) Representative stress-strain curves obtained from both HEAs in the as-welded and base material conditions. Digital image correlation images taken prior to fracture of the (b) $CoCu_{20}FeMnNi$ and (c) $CoCu_{30}FeMnNi$ welded HEAs, highlighting the FZ as the softest and weakest point of the joint.

The fracture surfaces of the joints are shown in Figure 93. In both cases there is evidence of interdendritic cracking, occurring as brittle type of failure. Such is caused by the inhomogeneous phase distribution on the FZ, alongside their compositional differences. This results in the previously mentioned anisotropy of mechanical properties on the different regions within the material, which can then generate stress concentration in between the interdendritic boundaries, making them susceptible to cracking. With progression of the tensile test, small sized fractures are formed amongst the large dendritic grains. As these fractures

coalesce, the inevitable failure of the joints occurs, leaving behind dendritic markings on the surface.

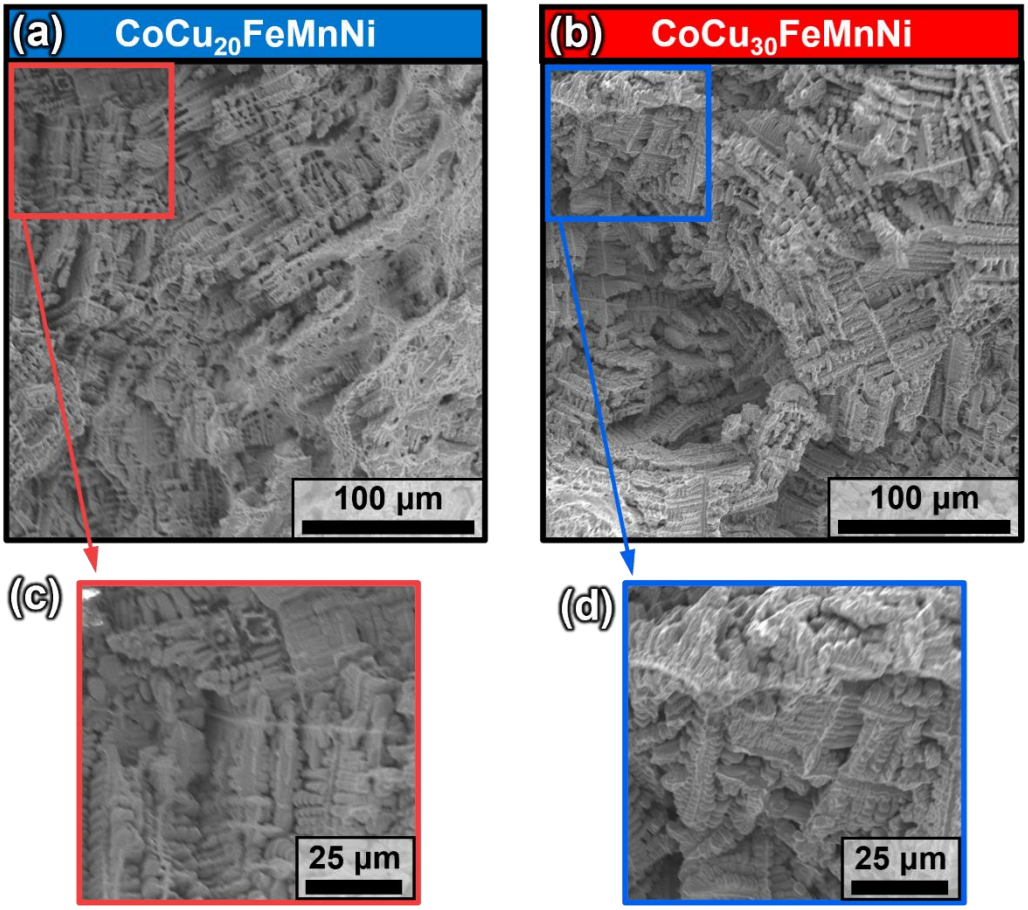


Figure 93 - Fracture surfaces of welded specimens: (a) $CoCu_{20}FeMnNi$ and (b) $CoCu_{30}FeMnNi$ welded joints and corresponding detailed views in (c) and (d), respectively.

4.4.6 Section summary and conclusions

The present study highlighted the differences in microstructure and mechanical performance arising from the gas tungsten arc welding on a $CoCu_xFeMnNi$ (x=20,30) HEAs. The results showed that although defect-free joints could be achieved, the mechanical performance was diminished. The main reason being the inhomogeneous microstructure achieved throughout the weld.

Furthermore, in terms of microstructure, multiple characterization methods allowed to observe the phase distribution of both welded HEAs, comprised by two different major FCC phases. Of special notion, high energy synchrotron X-ray diffraction permitted to observe that the major differences between the welded samples resided on the phase fraction distribution

developed upon welding. Through this technique, it was possible to identify a B2 BCC phase in the HAZ, which is predicted by thermodynamic calculations.

Additionally, the welded joints mechanical performance is significantly lower than those of the original BM, with the $CoCu_{30}FeMnNi$ case being the one that exhibited a higher contrast in the maximum strength and ductility achieved during tensile testing. Such is a product of the different microstructures across the joint combined with the microstrain developed throughout the welds upon the non-equilibrium solidification of the molten pool. These can facilitate crack initiation upon mechanical solicitation, especially when large grains of two dissimilar phases, with very different compositions, are present in the microstructure.

As such, future work should envisage the use of post-weld heat treatment to modify and improve the microstructure and mechanical properties of these welded joints. The grain size disparity between the BM and the FZ is also of major concern, as achieving a FZ comprising refined grains can play an important role in improving the mechanical performance of the welded HEAs. Taking this into consideration, research on how the phases present within the microstructure interact with each other during loading is also a relevant topic, as it can supply the grounds to further improve these HEAs concerning their weldability and consequent mechanical performance.

4.5 Microstructure and mechanical performance analysis on a gas tungsten arc welded CoCrNiAlTi HEA[5]

4.5.1 Section highlights

In this chapter, GTAW is used for similar welding of a recently developed precipitation hardened $Cr_{29.7}Co_{29.7}Ni_{35.4}Al_4Ti_{1.2}$ MPEA. The microstructural evolution and characterized combining optical and electron microscopy techniques, coupled with SXRD and CalPhaD based analysis. Additionally, the resulting mechanical properties are shown in terms of microhardness mapping and tensile testing.

4.5.2 Microstructural analysis

To determine the suitability of a welded joint for any given application, the first step should be to correlate their microstructural features to its mechanical performance. However, this task can only be properly performed if no welding defects exist within the welded joint. If present, these defects can significantly compromise the mechanical performance of the material and prevent its use in structural-oriented applications. Figure 2 (a) details a light optical microscopy overview of the GTAW joint without any indication of welding-related defects. Moreover, a full penetration joint was obtained.

The effect of the weld thermal cycle across the microstructural features of the joint is detailed next considering Figure 94, where it is possible to observe the different regions that compose any fusion weld: BM, HAZ and FZ.

[5] The results discussed in this subsection are published in the Advanced Engineering Materials journal, corresponding to reference [180].

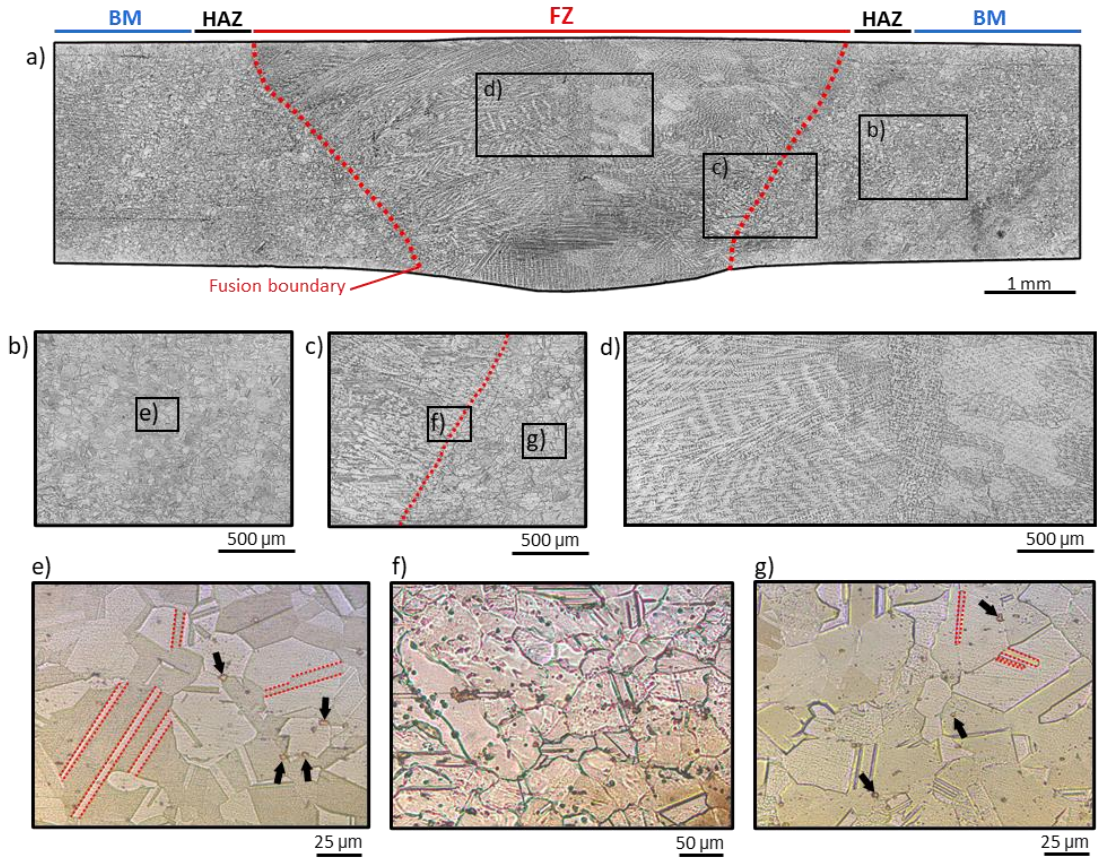


Figure 94 - Microstructural features of the GTAW Cr29.7Co29.7Ni35.4Al4Ti1.2 MPEA joint: a) Overall perspective indicating the BM, HAZ and FZ regions; b) BM; c) Transition from the HAZ to the FZ; d) FZ; e) Detailed view of the BM, highlighting the presence of TiN inclusions, as indicated by black arrows, and annealing twins marked with red dashed lines; f) Detailed view of the PMZ (Partially Melted Zone); (g) Detailed view of the HAZ, indicating similar features to those identified in e).

The $Cr_{29.7}Co_{29.7}Ni_{35.4}Al_4Ti_{1.2}$ MPEA BM microstructure, detailed in Figure 2 (b), is characterized by equiaxed grains with annealing twins that can be observed upon further magnification in Figure 2 (e). These twins occur naturally associated with recrystallization and grain growth mechanisms imposed by the thermal treatment after mechanical deformation (in this case rolling imposed prior to welding) of the BM. Such features are associated with growth accidents in the staking sequence within the grain structure, which result from an overall tendency for the material to reduce its surface grain boundary energy [163,164]. Titanium nitride (TiN) particles, exhibiting a polygonal shape and an orange coloration in optical microscopy images, are observed scattered throughout the BM and HAZ regions, as indicated by the black arrows on Figure 2 (e) and (g). Although N was not intentionally added during alloy fabrication,

previous analysis of the elemental materials used for casting revealed that both Cr and Co had trace amounts of N. The observed TiN particles are identical to those observed in [57,165], and they nucleate spontaneously due to the high concentration of Ti in the alloy during its solidification at the initial manufacturing stages. As the liquid phase tends to solidify, the concentration of Ti becomes higher and thus provides the means for TiN formation. Additionally, the presence (and possible formation during the solidification) of other precipitates/oxides may also promote the formation of such particles [165,166].

Upon entering the HAZ, the weld thermal cycle provided sufficient temperature and/or time for solid-state transformations to occur. The grains that comprise this region undertook several microstructural changes that play an important role in the mechanical performance of the alloy. In fact, from Figure 94 (a), it is possible to observe the grain size variation starting from the BM to the fusion boundary. Nevertheless, as evidenced by the phase transformations and grain growth features observed at different locations of the welded joint, which is further discussed next. Such occurs due to the spatially varying thermal conditions along the weld. The latter occurs mainly during the welding procedure, where the peak temperature and permanence time for solid-state transformations to occur, are a function of the distance to the heat source. Additionally, it should be mentioned that TiN particles were also observed in the HAZ suggesting that the weld thermal cycle is not enough to promote the dissolution of these precipitates into the material matrix. This is in good agreement with the extremely high melting point of this particles (≈ 2930 ºC) and their well-known high stability in Ni-based alloys [167].

Transitioning from the HAZ to the FZ, is the Partially Melted Zone (PMZ), that corresponds to the region in close proximity to the fusion boundary. The PMZ consists of partially melted and resolidified material along the grain boundaries where the temperature required for incipient melting was reached. Upon cooling, the existing liquid will solidify exhibiting the light-colored striations on the grain boundaries visible in Figure 94 (f).

The red dashed lines in Figure 94 (a) comprise the Fusion Zone (FZ), which correspond to the region where the BM completely melted and then solidified. Looking further into this region's microstructure, large dendritic grains can be observed growing from the solid HAZ/FZ interface towards the center of the FZ, indicating the alignment of these grains in the direction

perpendicular to the FZ boundary. These large grains grow parallel to the heat flow, i.e., from the colder HAZ/FZ interface towards the weld centerline. Due to the relatively fast solidification during welding, diffusion in the solid is reduced, promoting the formation of a solute-rich boundary at the frontier of both phase states, i.e., liquid and solid. According to the constitutional supercooling theory, the high solute concentration at this boundary, causes the material to reach a state in between the liquidus and solidus line, where the liquid phase interface becomes unstable allowing the coexistence of both solid and liquid. This way, small dendritic structures start growing from any existing protuberances in the semi-molten grain boundaries of the solid-state material surrounding the FZ. Upon their formation and depending on the temperature gradient and growth rate, these dendrites keep growing within the liquid at the expense of smaller ones, minimizing their overall surface energy, which can then generate large dendritic arms [156]. This phenomenon results in a highly directional columnar grain structure, where grains comprising dendrites whose preferential growth direction is aligned with the heat flow extraction are favored (through a process called competitive growth, which will be discussed alongside the EBSD analysis next) granting the FZ the larger grain size of all regions of the joint, with that being 164.6 ± 62.7 μm (measured perpendicularly to the fusion boundary).

To understand the microstructure evolution of the welded joint, a thorough characterization of the HAZ and FZ is needed, and a comparison to the BM, allows understanding the effects induced by the introduction of heat during welding. To compare the different microstructural features within the three regions of the joint (BM, HAZ and FZ), SEM imaging coupled with EBSD was performed. Figure 95 presents an SEM image of the joint separating the HAZ from the FZ and the BM, complemented with EBSD mapping where the grain morphology and preferential orientations are exhibited more clearly. Nevertheless, the PMZ region is not easily observable, due to its relatively small dimensions.

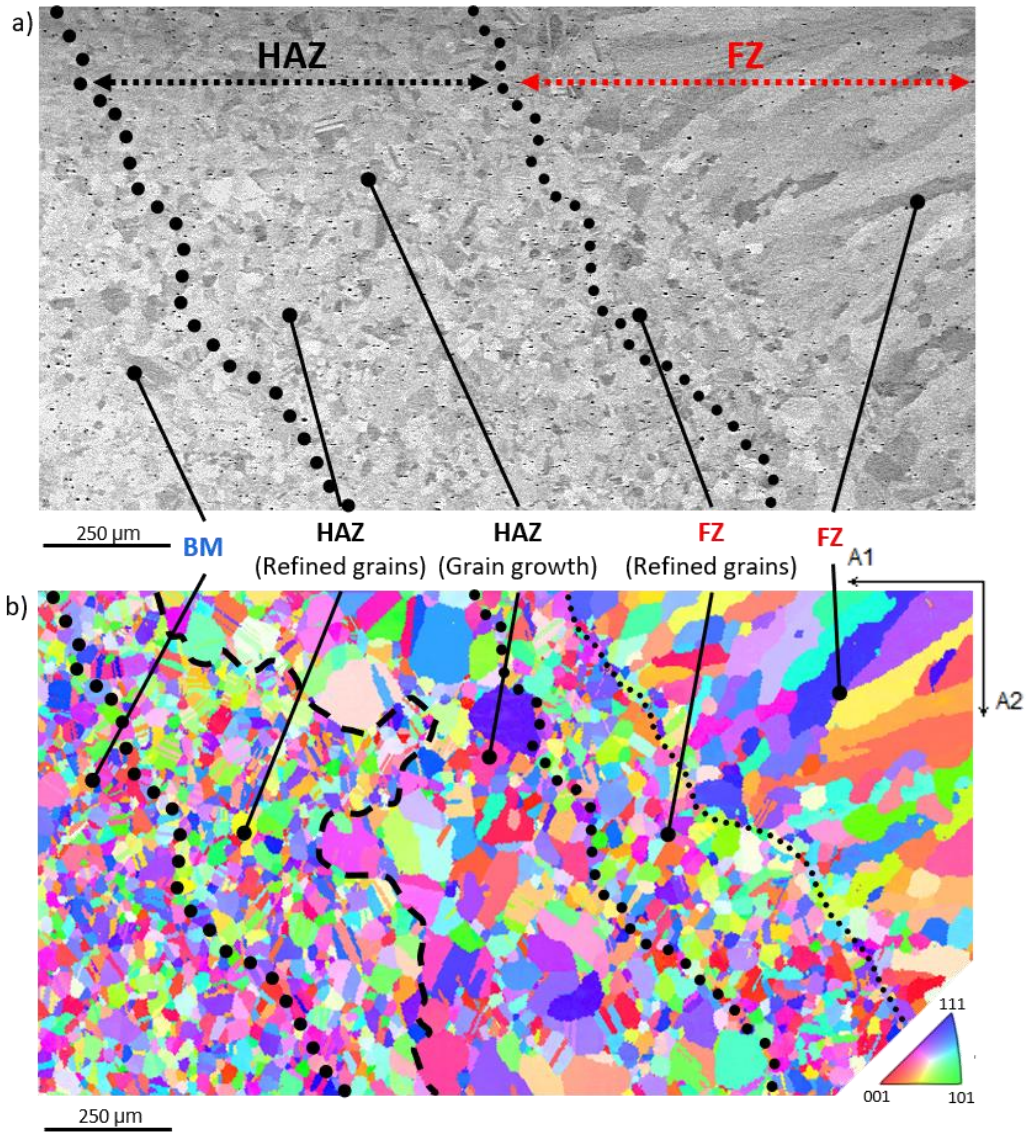


Figure 95 – Analysis of a region comprising the BM, HAZ and FZ: (a) SEM micrograph and (b) EBSD map.

Starting from the BM, the fine equiaxed grains with annealing twins resulting from the cold rolling and annealing processing can be observed, similarly to Figure 94 (b) and (e). In this region the measured grain size was 21.1 ± 3.5 µm.

Going to the HAZ it is possible to observe that the grain size variation does continuously increase from the BM towards the FZ (refer to Figure 95 (b)), as it would be expected since there is an increase in temperature along this direction during welding. In fact, when entering the HAZ, there is evidence of a region with minor grain size followed by a region where grain growth is predominant (refer to Table 14 for the average grain size on the HAZ).

To understand the variation in grain size occurring in the HAZ, one must consider the influence of the permanence at high temperatures on the solid-state phenomena that modify the microstructure, that is, the mechanisms that regulate the grain refining and grain growth. These mechanisms can, however, be succinctly explained from a thermodynamic perspective, where the most stable condition of a system is the one that minimizes its global energy. The stable phases are a function of the temperature of the alloy, as will be further discussed in the next section, since the nature of the welding process generates a temperature gradient on the sample, leading to different microstructures being obtained in each position.

Going further on this point, the initial BM has a low internal strain energy stored within its microstructure resulting from the initial processing of the plates, that is rolling followed by solution annealing. Likewise, the practically inexistent internal strain energy in the MPEA prevents the material from undergoing a recrystallization process, as the material is already in a low state of internal residual stresses. During welding, however, the high temperatures experienced by the material or due to longer permanence times, cause some grains to start to assimilate other grains in their vicinity, minimizing the surface energy between them and increasing in size during the process. This is the process of grain growth, being favored by higher temperatures and/or longer permanence times at critical temperatures.

However, when reaching the FZ, it is possible to observe that near its interface with the HAZ, at the fusion boundary, there is a decay in the grain size compared to the grain growth region of the HAZ detailed in Figure 95 b). For easier assessment, Table 14 details the average grain size evolution with proximity to the FZ, measured from the EBSD maps at each region of interest on the welded joint.

Table 14 – Average grain size measurements ordered taking the proximity to the FZ in consideration.

Region	BM	HAZ (refined grains)	HAZ (grain growth)	FZ near fusion boundary	FZ
Average grain size ($\mu \pm \sigma$ µm)	21.1 ± 3.5 µm	23.1 ± 2.1 µm	40.2 ± 9.7 µm	25.8 ± 3.8 µm	164.6 ± 62.7 µm

Here, contrary to what was discussed in the optical microscopy where the FZ is mainly composed by large dendritic grains, the EBSD data allows us to highlight small-sized grains on

the FZ side near fusion boundary, with an average size of 25.8 ± 3.8 μm. This microstructural phenomenon is called the fine equiaxed zone (FQZ) and, depending on the alloy system, can cause hot cracking during welding procedure. Its formation mechanisms, however, are a topic that has been under discussion in the literature, where the alloy composition, heterogeneous nucleation and welding parameters are found to play major role on the FQZ formation [147]. Its formation is common to occur in on other system such as Ni-superalloys [148,168] and in Al-alloys [169]. In the current work, no evidence of hot cracking was observed.

Given the processing conditions, the cooling imposed by the Argon shielding gas while being projected into the molten pool both in the face and the root of the weld, to prevent oxidation, can also be sufficient to prevent massive dendritic grain growth. Moreover, the contact with the stainless-steel fixture also acted as a heat sink with this region being also cooled by the root shielding gas, thus minimizing the temperature and time at which the region close to the HAZ/FZ boundary could experience extensive grain growth. The lower thermal conductivity of the present MPEA (within the 14 – 17 W/m K range, from [170]) compared to the stainless-steel substrate can also have influence on this phenomenon.

Furthermore, the crystallographic texture that arose from the phenomena associated with the welding process is exhibited in Figure 96. Comparatively, it is possible to perceive that going from the BM to the FZ, the previously discussed microstructural features have an evident impact on the texture of the welded joint. Observing the condition of the BM, a weak texture is observable. Such is relatable to the recrystallized and solubilized condition of the MPEA and its small equiaxed grain structure. Going further towards the FZ, at the interface of the HAZ/FZ the influence of the increasing temperature on the weld starts to become more evident on the texture of the joint. Nevertheless, the distribution of grains in the various directions is still practically imperceptible. However, in the FZ it is possible to observe that the <101> and <111> directions exhibit an obvious gradient on the crystallographic orientation, especially aligned with the A1 axis which is parallel to the longitudinal direction of the weld. The same trend can be related to the microstructure exhibited in Figure 97 (a) and (b), which detail a more localized analysis of the FZ. Here large columnar grains are visible growing from the fusion boundary towards the center of the FZ. As such, it is possible to observe that closer to the fusion boundary the grains tend to be preferentially oriented along the <101> and

<111> directions, while in the middle of FZ a preference for the <001> direction can be observed.

The reason for the grains to be preferentially oriented close to the <101> and <111> directions at the HAZ/FZ interface can be explained based on the dominant mechanism occurring in this region, which is epitaxial growth. Here, as previously discussed, as the temperature starts to decrease, the grains of the BM act as nucleation sites for new grains to form. In the case of autogenous welding, nucleation occurs by rearranging atoms from the molten metal upon the solid grains without (significantly) altering their crystallographic orientation.

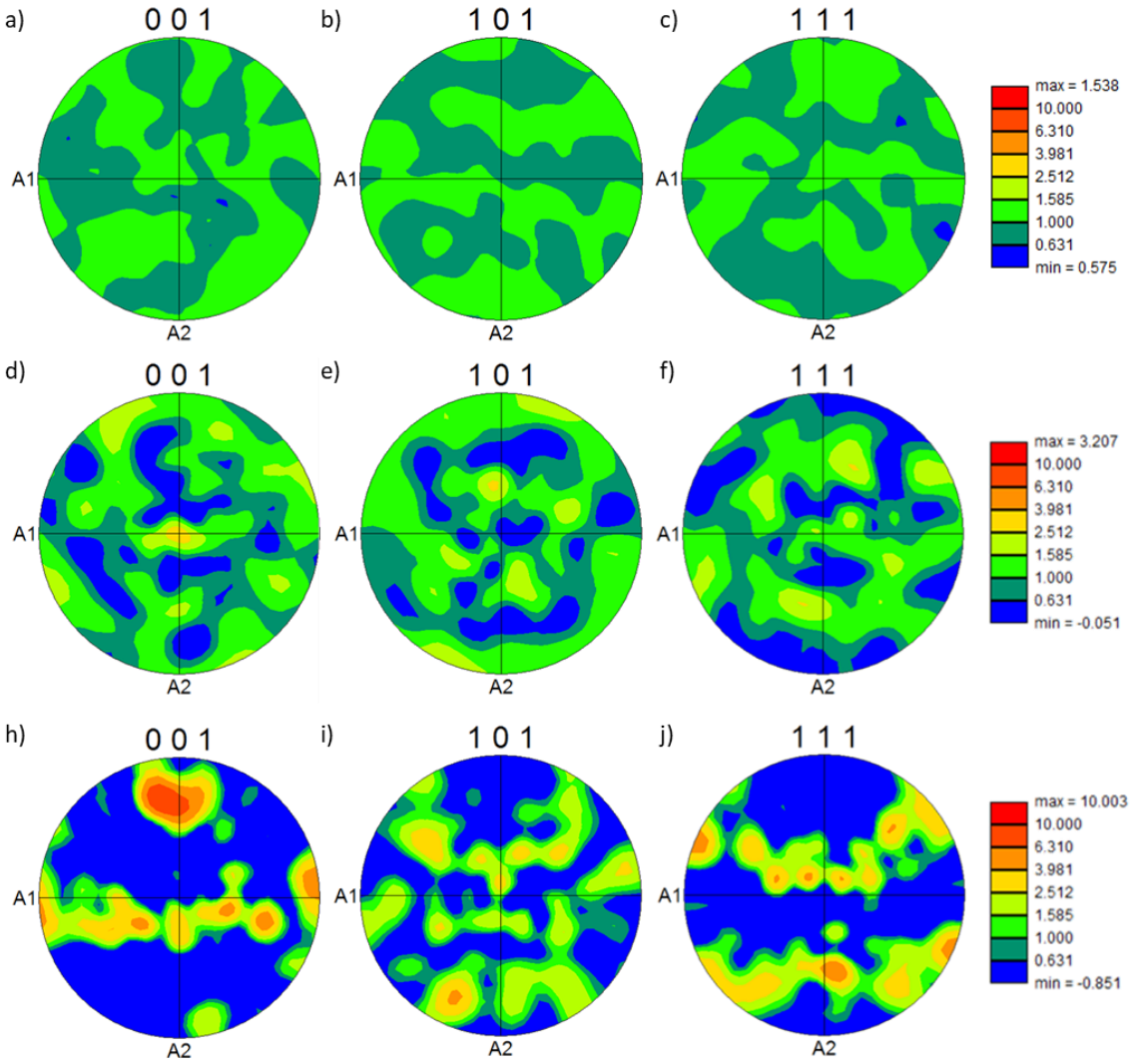


Figure 96 – Pole figures displaying the crystallographic texture on the (a) [001], (b) [101] and (c) [111] directions of the base material; (d) [001], (e) [101] and (f) [111] directions of the grain refined region near the interface of the Heat affected zone with the fusion zone and (g) [001], (h) [101] and (i) [111] directions of the fusion zone. All pole figures are presented on the same scale for a direct comparison.

Furthermore, in the bulk of the FZ, competitive growth between the grains occurs. Here, the grains keep growing in the most effective way to maximize the temperature gradient, that is perpendicular to the FZ. So, the dendrites that comprise them tend to grow along the easy growth direction, which for FCC alloys corresponds to the <001> direction. Thus, all grains that align themselves with the easy growth direction of the dendrites tend to enlarge in comparison with the grains that have dendrites growing in a distinct orientation. This solidification mechanism coupled with the fact that the weld center is the region where the peak temperature is achieved, is the main reason for a preferential orientation of the grains close to the <001> direction.

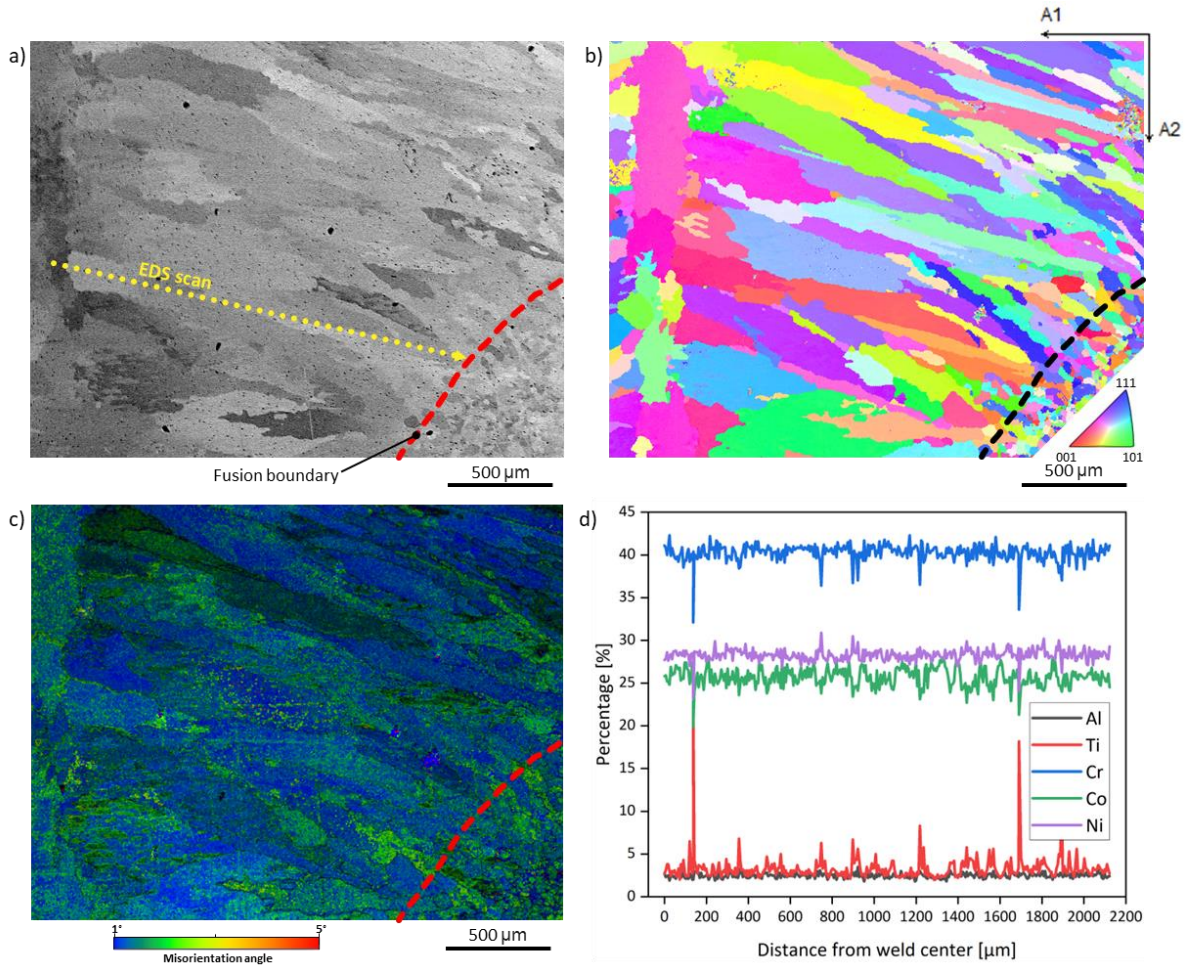


Figure 97 - Analysis of the region comprising the FZ: (a) SEM micrograph and (b) corresponding EBSD and (c) KAM maps; (d) EDS line scan results performed across the joint to evaluate the possibility for macrosegregation.

Figure 97 (c) details a Kernel Average Misorientation (KAM) map of the FZ region. KAM maps reveal the mean misorientation of a point with respect to its nearby points on the microstructure. Regarding this, it is possible to observe that a gradient on the misorientation angle can be found within the grains of the FZ. Interestingly, it can be noted that the degree of misorientation increases near the grain boundaries. This suggests that during cooling of the molten pool, the competitive growth and solidification of the interdendritic liquid material generate sufficient stresses to trigger the accommodation of strain at the grain interfaces, progressing on its way from the grain boundaries towards the dendritic cores. This can be ascertained to the relatively slow cooling rate of high heat input welding processes, as GTAW, which allow for the material to self-accommodate some of the thermal strains that develop during the non-equilibrium heating and cooling."

Furthermore, an EDS line scan was performed across the FZ (refer to the analyzed region detailed in Figure 97(a) with these results being detailed in Figure 97(d)). Here the analyzed line evidence some points with a higher concentration of Ti, which can be attributed to the presence of TiN in the FZ. Nevertheless, no apparent macrosegregation can be observed in the weld, thus an evaluation of the possibility for microsegregation and the elemental distribution among the microstructural features was performed using a localized EDS map detailing the elemental variations of Al, Ti, Cr, Co, and Ni as depicted in Figure 98.

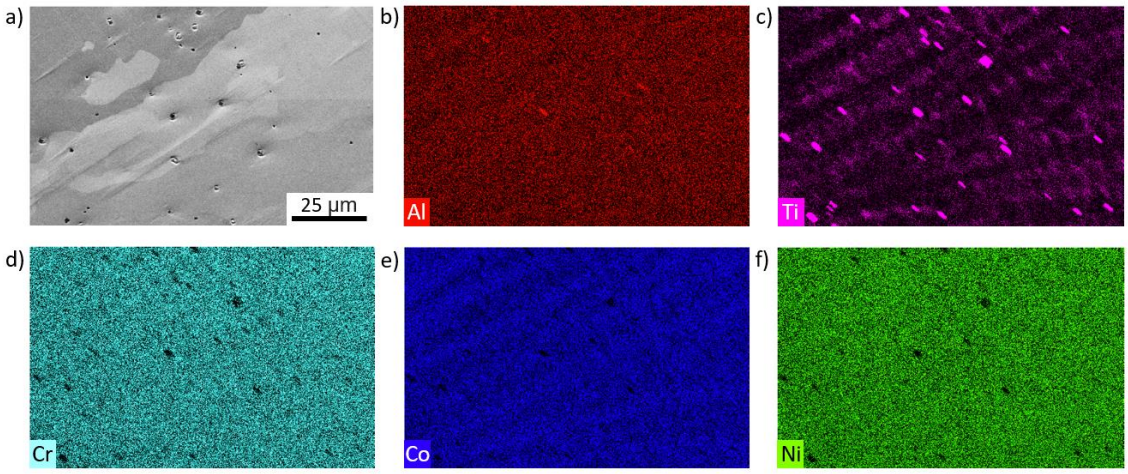


Figure 98 - EDS mapping of the FZ: (a) Inspected region and elemental distribution of (b) Al, (c) Ti, (d) Cr, (e) Co and (f) Ni.

At a first glance, the TiN inclusions can be immediately observed through the presence of Ti-rich spots (refer to Figure 98 (c)). Additionally, some other Al-rich spots can also be observed although sparsely distributed in FZ (see Figure 98 (b)). Nevertheless, the EDS map of Figure 98 reveal microsegregation of both Ti and Co, while the other elements present a relatively even distribution throughout this region. Microsegregation occurs due to solute redistribution when going from the liquid to the solid phase which have different compositions. Thus, the excess solute is rejected into the interdendritic space, which can be translated into a compositional variation that occurs during solidification leaving a composition pattern in between dendrites. This phenomenon may also be aggravated due to the partial fusion and dissolution of the TiN particles in the molten pool, which enriches the weld composition with both Ti and N. Elemental diffusion also plays a key role in here, as small composition gradients are left during solidification. Thus, the development of different phases other than the high entropy matrix phase (in this case FCC) is often inevitable, possibly leading to harmful welding defects, such as hot cracking. Nonetheless, it is important to mention that no such defects were observed in these welded joints.

Other than the matrix and TiN particles found in the FZ, Figure 99 (a) evidences the presence of a distinct phase with small volume fractions being present at some grain boundaries. Confirmation of the presence of this phase is also observed through the elemental distribution variation near and at the particle phase, as shown in Figure 99 (b) and (c). Interestingly, it evidences that the composition of this new phase is different from the surrounding grains. This intermetallic phase is Cr-rich, although being depleted in Cr compared to the surrounding matrix, also being composed by Ni, Co and Ti in similar quantity. The content of Al is the lowest, with nearly 10 % (at. %) of this element. Different possibilities for structural identification of this phase present in the FZ, was enabled by the synchrotron X-ray diffraction, as it will be shown later.

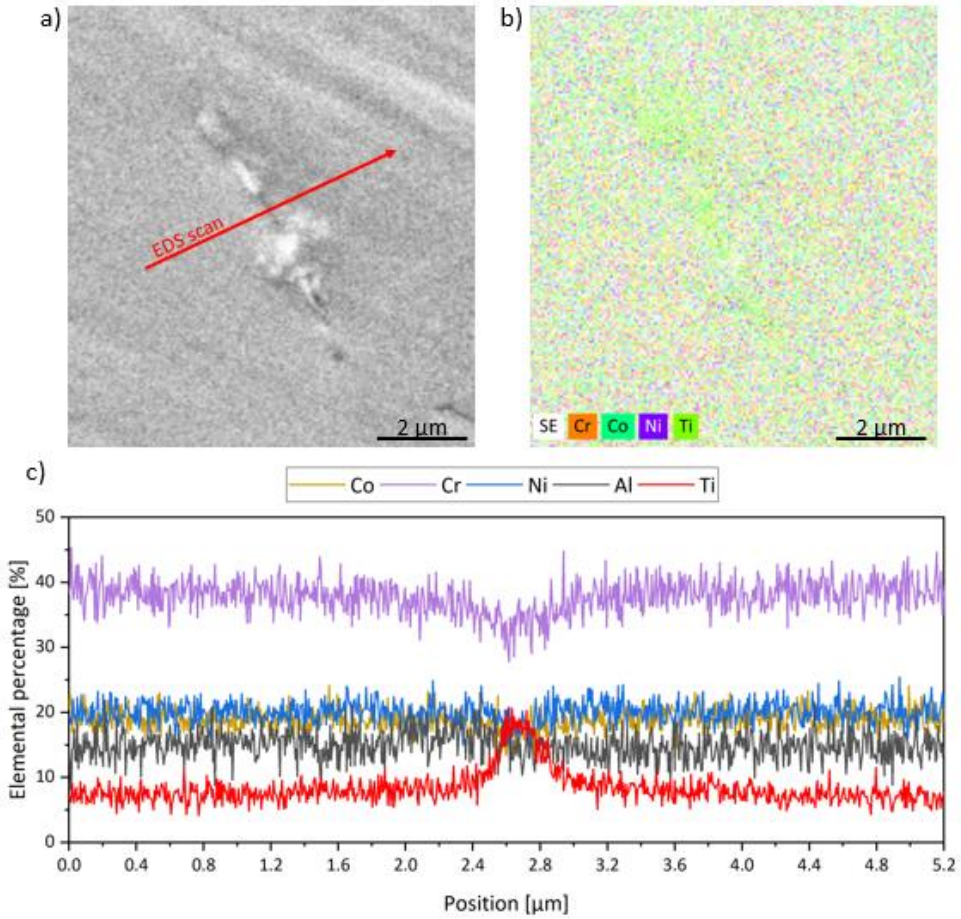


Figure 99 – Intermetallic phase present within grain boundaries: (a) Morphology at the grain boundary; (b) Elemental map and (c) Line scan taken in the region indicated by the red line in (a).

4.5.3 Thermodynamic Calculations

Given the elemental redistribution and non-equilibrium conditions that occur during fusion-based welding, thermodynamic calculations were executed using the thermodynamical CalPhaD-based Scheil simulation module available in Thermo-Calc (TCHEA5 database) and Pandat (PanHEA2022 database) software, to predict the solidification path of the FZ.

Differing from equilibrium calculations, the Scheil-Gulliver model provides a way to infer on the possible phases developed during non-equilibrium solidification conditions. Some assumptions for this model are described considering the rapid cooling rate that the molten pool undergoes, practically resulting in insufficient time for compositional homogeneity to be attained through diffusion. As such, solid-state diffusion is assumed negligible, while in the liquid diffusion is considered infinite. These assumptions rely on the basis that equilibrium only occurs at the transition between the liquid to solid states and that the liquid phase is

uniform in composition while the solid-state material is not. Therefore, since the solute cannot back diffuse into the solid material, all excess solute goes to the liquid phase, which becomes more concentrated, allowing the possibility for the development of different phases from those that would be expected from an equilibrium simulation [171,172].

For these calculations, the nominal alloy composition ($Cr_{29.7}Co_{29.7}Ni_{35.4}Al_4Ti_{1.2}$) was used, and the results obtained are depicted in Figure 100. Comparing the non-equilibrium Scheil-Gulliver curves obtained via both software it is possible to observe that the predicted solidification path is different from each other, namely on the temperature at which the material achieves full solid state, although maintaining some phases in common. These being the γ, γ' and the hexagonal $D0_{24}$ (η) phases.

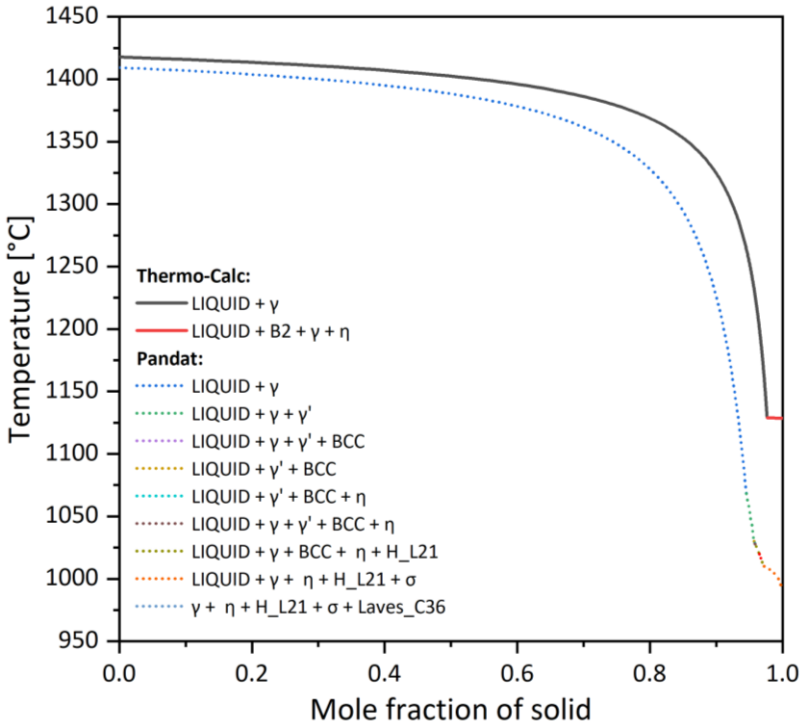


Figure 100 – Comparison between the non-equilibrium Scheil-Gulliver thermodynamical calculations performed using Thermo-Calc (TCHEA5 database) and Pandat (PanHEA2022 database), to interpret the molten pool solidification.

Considering the results obtained using the TCHEA5 database, the Scheil solidification curve shown in Figure 100 predicts the formation of three phases once the liquid has completely solidified: a disordered FCC phase, corresponding to the γ phase; an ordered body centered cubic (B2) phase and the η phase. As such, while the γ phase has the higher phase

fraction in the MPEA, the remaining phases, if present, would correspond to minor phases within the microstructure, which can present a challenge in their identification especially in a large FZ region, as typical of arc-based welding processes, known for highly dynamic and variable conditions [173]. These conditions result on the inhomogeneous distribution of elements within the liquid phase, that once solidified may or may not result on the formation of the phases observed according to the Scheil calculations.

Additionally, it is possible to observe that the solidification of the alloy comprises two stages, the first comprising only the matrix γ phase and the later, corresponding to final steps of solidification, where the ordered B2 and the η phases nucleate from the remaining liquid.

On further analysis, observing the thermodynamic calculation results obtained using the PanHEA2022 database, the solidification path provides a somewhat different insight on the nucleation of the different phases that can expected to form upon cooling of the molten pool. In fact, nine different solidification stages occur and the phase array that can be observed from this calculation comprises beyond the matrix γ phase, the γ', η, BCC, Heusler ($L2_1$), σ and Laves (C36) phases. It is common for different databases to yield different predictions for phase equilibria since the free energy curves and assessed thermodynamic systems are typically different.

Next, the partition coefficients of all the elements present in the alloy were calculated to observe the elemental segregation that occurs solidification, considering the results obtained from the Scheil simulations. The partition coefficients can be calculated through the ratio between the concentration of an element in a solid phase and the concentration of such element within the liquid phase. These results are displayed in Figure 101.

Furthermore, the partition coefficient can be used to understand elemental segregation. Meaning, that when the liquid is richer in a particular element than the solid phase, the partition coefficient acquires a value below 1, that is the excess solute is not being used in the dendritic formation, eventually segregating into the interdendritic fluid. The opposite is true for the enrichment of the newly created dendrites with such an element.

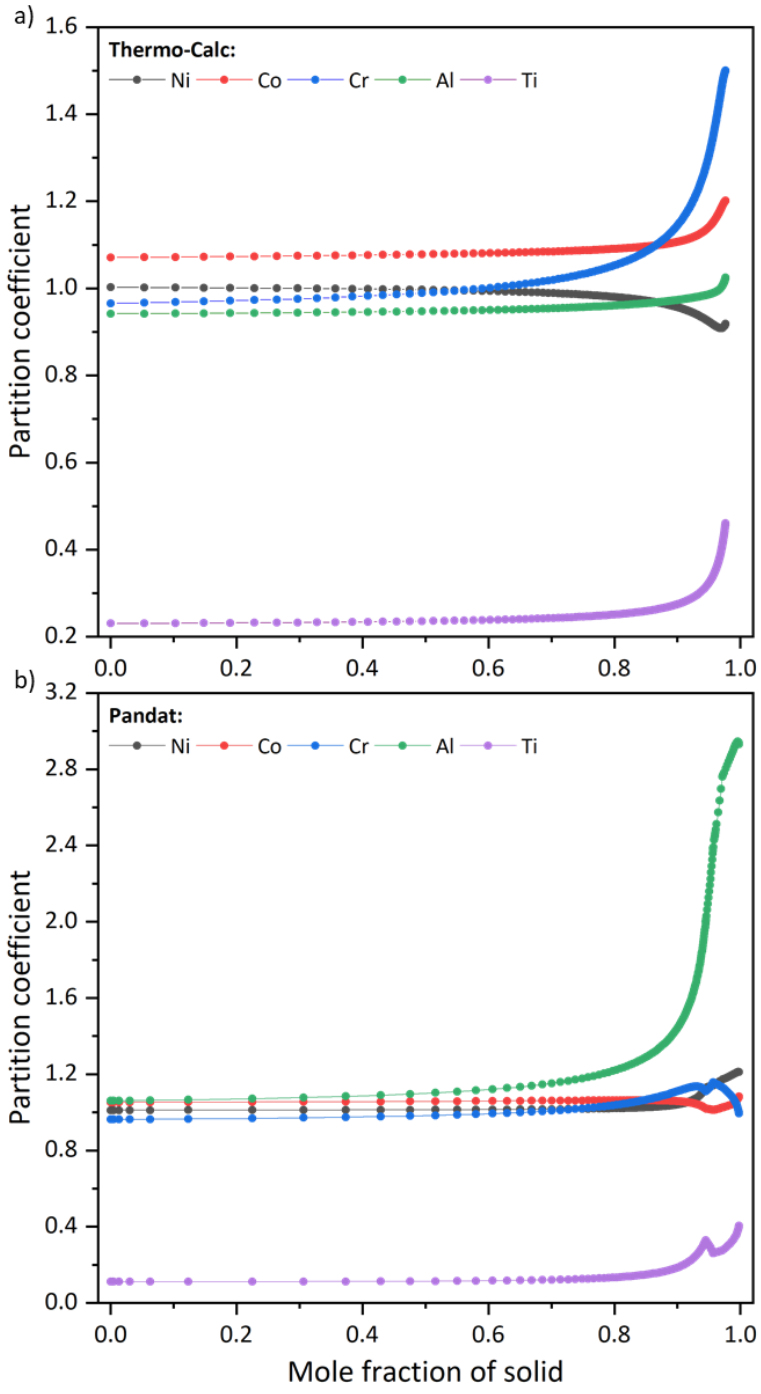


Figure 101 – Comparison between the elemental partition on the matrix γ phase throughout solidification, calculated with (a) Thermo-Calc, using the TCHEA5 database and (b) Panda, using the PanHEA2022 database.

Considering the dada obtained with TCHEA5, it is possible to perceive that all elements excluding Ni, tend to exhibit a positive slope with increasing fraction of solid, thus it is possible to conclude that the interdendritic regions of the γ phase would be predicted to be more concentrated with these elements. Moreover, analyzing the evolution of the partition

coefficients, it is also possible to perceive that Co, Cr, and Al all being above 1, are the elements that are mainly employed in the dendritic formation. This occurs as the Ti and Ni are segregated into the interdendritic fluid and can possibly aid on the nucleation of other intermetallic phases in the microstructure.

Furthermore, the same analysis calculated using the PanHEA2022 database, predicts a major segregation of Al to the interdendritic fluid, while the other elements aside Cr also tend to have their partition coefficient increased with the increasing amount of solid. These results offer a very different perspective on the solidification path of the MPEA since that the Cr and the Al elemental partition between the dendrites and the interdendritic fluid, is not coherent between both databases.

Another aspect that can be assessed is the differences between the EDS maps and the CalPhaD calculations. The EDS results evidence the microsegregation occurred especially among the Ti and Co elements. In this regard, both databases/software's indicate that the interdendritic fluid is enriched with such elements with further solidification. Although these CalPhaD simulations may not completely represent the observed experimental behavior, both software's are still able to provide an important insight on the possible phases present on the FZ. Nevertheless, it is important to note that a good database is imperative for a reliable prediction of the microstructure of any engineering alloy, but especially for complex materials as MPEAs.

Furthermore, although an asset when predicting the microstructure, the Scheil simulations may not be the most reliable way to infer on the microstructure that develops upon cooling o of the molten pool. Such solidification path may differ from the Scheil-Gulliver curve due to the already mentioned fast cooling conditions imposed on the FZ of the welded MPEA. In fact, due to the cooling being relatively fast, there is no complete homogenization of the liquid phase as predicted by the model, as a result, the alloy might solidify with smaller partitioning coefficients than those predicted by the Scheil model [174].

Therefore, for comparison, equilibrium calculations using the same fixed composition set were also performed. The results, available in Figure 102, revealed a similar microstructural prediction by both software/databases. Although not completely emulating the fast-cooling conditions developed during welding, this equilibrium calculation method permits to

infer the formation of the temperature dependent PMZ and HAZ. That is, considering the temperature range at which both liquid and solid state coexist, corresponding to a range of approximately 50°C, the formation of the PMZ is inevitable due to the heat dissipation and consequent melting of the boundaries of the grains near the material in the liquid state. Thus, it is possible to infer that the PMZ is composed mainly of γ phase in the solid state once the liquid phase at the grain boundaries solidifies, the formation of γ' in this case would be tied to how fast the cooling happens on the solid state. Considering in this work the plate is thin, the likelihood of this precipitation in small, as will be shown later.

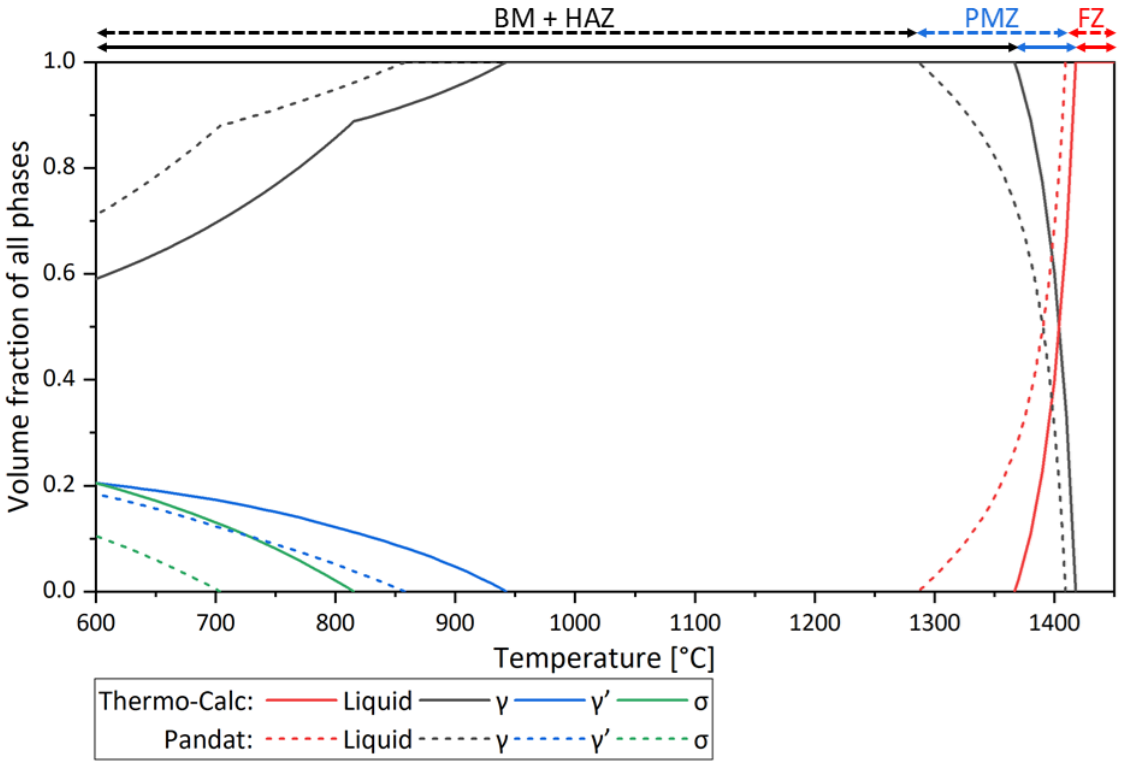


Figure 102 - One axis equilibrium calculation performed on the nominal composition of the MPEA, to evaluate the phase formation in equilibrium conditions. The calculations were computed using TCHEA5 and PanHEA2022 databases.

For further thermodynamical understanding of the solidification behavior of the molten pool, Figure 103 shows the evident difference in phase nucleation temperatures relatively to the composition of the interdendritic liquid. Such results were only computed using Thermo-Calc with the THCEA5 database to avoid overpopulation of data. Only the phases that from at high temperatures are considered. The results displayed here come from single

equilibrium simulations performed using the liquid phase composition obtained from the Scheil-Gulliver simulation (refer to Figure 100). In this way, it is possible to infer on the temperature at which a given phase nucleates, and due to the uneven temperature flow distribution in welding this provides a good overview of what to expect from the weld microstructure. Interpreting this data requires the understanding that the first compositions retrieved from the Scheil simulation correspond to the newly generated dendrites that eventually become dendritic cores as solidification proceeds. The last compositions obtained from the Scheil-Gulliver simulation correspond to the last interdendritic liquid to solidify. As expected, and accordingly to Figure 102, the dendritic core is mainly composed γ phase. With further solidification, the interdendritic liquid becomes more concentrated in all elements apart from Ni, allowing the formation of new phases in the microstructure, namely the BCC, B2, and η phases. At roughly 50% of the solidification curve (refer to Figure 103), the γ matrix stops being the most stable one, as it can be observed when the phase fraction achieves a mole fraction of solid of 0.5. Finally, with further solidification, when the mole fraction of solid approaches 1, it is possible to observe that formation of the B2 phase is expected to occur first, followed by the γ and γ' phases. These phases should be the ones that reign over the microstructure of the interdendritic region, while the dendritic core is mainly composed by the matrix γ phase.

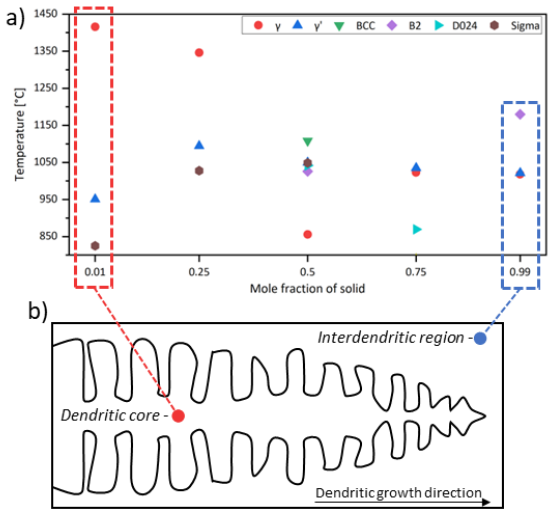


Figure 103 - Understanding the microstructure of the fusion zone using Thermo-Calc software (TCHEA5 database): (a) equilibrium calculations performed on specific compositions retrieved from Scheil-Gulliver simulations and (b) representation of a dendrite and the material that surrounds it, to highligh the microstrcutural differences form the dendrites and the interdedritic material.

This analysis allows to observe that although γ phase is predicted to be the matrix phase of the alloy, other phases may also nucleate at the end of the solidification. Furthermore, it is important to keep in mind that the cooling rate and temperature distribution of the fusion zone are not considered on these Scheil calculations. This, together with variations in composition across the welded joint due to Marangoni currents, can lead to the formation of unexpected phases or even preventing other that would be thermodynamically predicted if an homogenous composition existed within the FZ.

4.5.4 Synchrotron x-ray diffraction

Further evaluation of the microstructure of the welded joints was performed using SXRD, as detailed in Figure 104. Working in transmission mode it is possible to retrieve bulk information on the existing phases in the welded joint. This diffraction data can also be helpful to evaluate the previously detailed thermodynamic predictions, which coupled with EDS analysis can help in improving the reliability of the current thermodynamic databases for MPEAs.

Superposition of the diffraction patterns from one side of the BM to the other side is detailed in Figure 104 (a). Although no significant changes are visible in the diffraction reflections with higher intensity, it is possible to observe, that in the FZ (where the material undergoes major changes), new and low intensity diffraction peaks differing from those visible in the BM are visible. As such, representative diffraction patterns of the BM, HAZ and FZ are further detailed in Figure 104 (b), (c) and (d).

For instance, in Figure 104 (b) representing the diffraction pattern of the BM, it is possible to observe the FCC matrix phase present in this alloy, which corresponds to the higher peaks in the diffraction patterns, represented as γ. Additionally, small peaks of the ordered FCC precipitates, represented as γ’ are also noticeable, alongside the presence of TiN particles and the hexagonal η phase.

Regarding the HAZ and FZ, it is also possible to observe the diffraction peaks corresponding to the matrix γ FCC phase, as well as γ’, which can be easily identified from the diffraction peaks. The γ’ peaks are more intense on the HAZ compared to both other regions. Additionally, beyond the phases already identified in the BM, the presence of small peaks of the σ phase can also be noticeable. It should be noticed that this phase is only visible due to the excellent signal-to-noise ratio typical of synchrotron radiation. If a conventional X-ray

laboratorial source was used, these very low intensity peaks would be hidden in the background since the volume fraction of this phase is reduced. Also, the same can be said for the η phase, which is present in a very low volume fraction, being only visible on the FZ and the BM. The fact that it is not observed in the HAZ can be due to its dissolution in the matrix during the heat dissipation coming from the molten pool. This phenomenon locally translates on phase dissolution from the microstructure of the HAZ, which in turn contributes to the variation of the mechanical properties along the full extension of the weld.

Interestingly, in the FZ it is also possible to see the signature peaks of the B2 phase, although small and partially overlapped by the higher FCC diffraction peaks. Nevertheless, the correlation between the thermodynamic simulations and the X-ray diffraction results, clearly shows that, at the present time, simulations aided in the interpretation of the phases present in this MPEA welded joint microstructure.

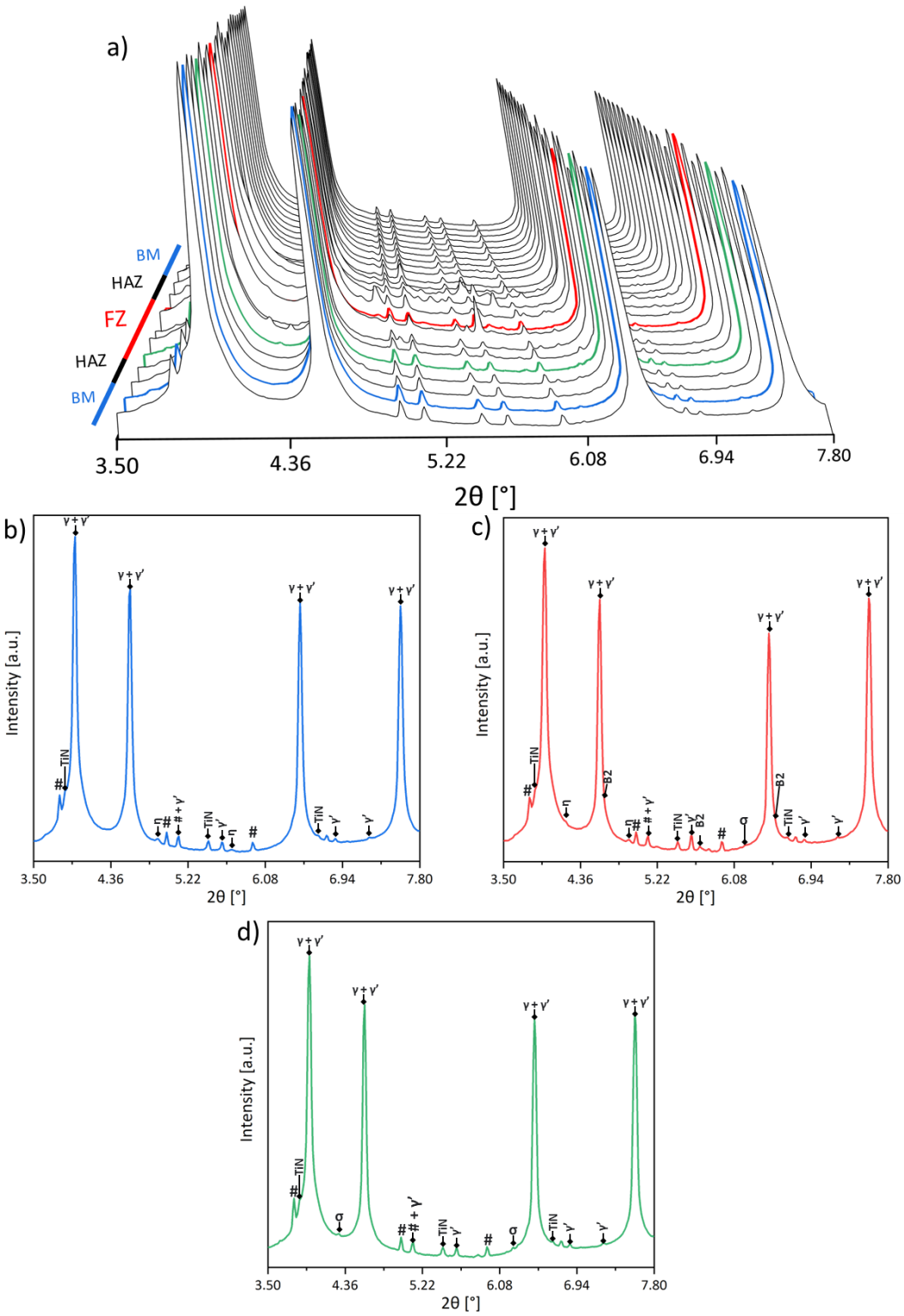


Figure 104 – Synchrotron X-ray data of the Cr29.7Co29.7Ni35.4Al4Ti1.2 MPEA welded joint: (a) Overall superimposition of the diffraction patters highlighting the different regions of the welded joint, namely: (b) Base material, (c) Fusion Zone and (d) Heat affected zone (# corresponds to 2nd harmonic reflections).

4.5.5 Mechanical properties of the welded joints

Performing an insightful microstructural analysis on welded joints, especially on MPEAs can help to explain their behavior and performance and is known to be an important asset when aiming at improving their characteristics for any purpose [103,157,175,176]. Therefore, after evaluating the joint's microstructure, one must address the resulting mechanical properties not only to determine their suitability for the targeted applications but also to determine microstructure/properties relationships.

Figure 105 details a microhardness map obtained across the welded joint. The gradient of hardness present here shows that an increase of hardness occurred from BM to the HAZ. These measurements show that the BM hardness varies in a range of 190.7 to 224.9 $HV_{0.5}$, while the HAZ is varied within 204.2 to 242 $HV_{0.5}$. Such variation can be due to the different microstructural features exhibited by this region when compared to the adjacent ones in terms of grain size, phase constitution and residual stresses. While the BM is in solution-annealed condition with small content and underaged γ' precipitate condition, the weld thermal cycle experienced at the HAZ location of the joint resembles that of a short time aging heat treatment, which can then influence the microstructure features. As such, according to Santana et al. [57] an increase of hardness is to be expected as a function of aging time during heat treatments of the present alloy, which is due to γ' precipitate growth within the microstructure. Moving closer to the FZ but still on the HAZ, there is a region where the temperature of the material surpassed the γ' solvus, shown in Figure 11, and this region already displays a lower hardness due to dissolution of γ'.

Furthermore, as per the X-ray diffraction data, no indication of η phase was observed in the HAZ which can also influence the local hardness of the MPEA in this regard. In fact, the η phase has been found to improve the tensile properties in a medium entropy alloys based in the same CoCrNi matrix [177], but although this does not explain the increase hardness compared with the BM, one can infer that a possible reason for such phenomenon can be due to the tendency for compressive nature of residual stresses in the HAZ, which is well established in the welding literature [32]. The stress condition of the HAZ arises from the thermal conditions occurring this region and can explain the disparity between the hardness of the BM and the HAZ, since the BM has been subjected to a solution annealing processing prior to

welding. Interestingly, the PMZ is not clearly evident in the hardness map, which is related to its small extension and the need to have the minimum recommended distance between two consecutive hardness indents.

The lower values of hardness were obtained in the FZ, reaching 170 $HV_{0.5}$ at its minimum. As previously observed through synchrotron x-ray diffraction, this region has large grains and has the least amount of precipitate phases. Concerning the residual stresses of this region, the FZ is characterized by exhibiting mainly internal tensile stresses, which contributes to the decrease of hardness of the MPEA in this region [32,178]. As such, the presence of such phases in the microstructure is counteracted by the combined influence of the residual stress condition and the large grain size in the FZ (following the Hall-Petch equation), which results in lower hardness values.

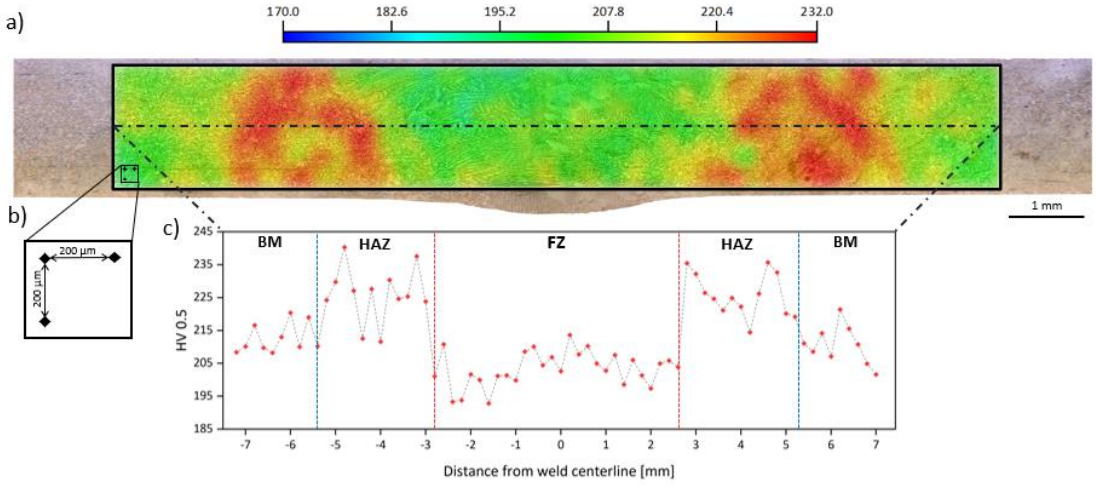


Figure 105 - Microhardness measurements: (A) Microhardness map across the welded joint); (B) representative line scan obtained at the joint mid height.

Tensile testing is the most direct way to evaluate the suitability of a welded joint for a structural application. The mechanical behavior of the joint is typically compared to that of the original BM and the fracture mechanism and location in the welded material can be understood based on existing microstructure features. Representative tensile stress-strain curves of the BM and welded joint are detailed in Figure 106. While the BM had a better mechanical performance, reaching a tensile strength of ≈ 830 MPa (corresponding to a elongation to fracture of 57%), the welded joint reached 91.3% of the BM strength (≈ 750 MPa) and 58%

of the BM elongation (with an elongation to fracture of ≈ 33%). Thus, although less performing, the welded joint still exhibits excellent combination of strength and ductility.

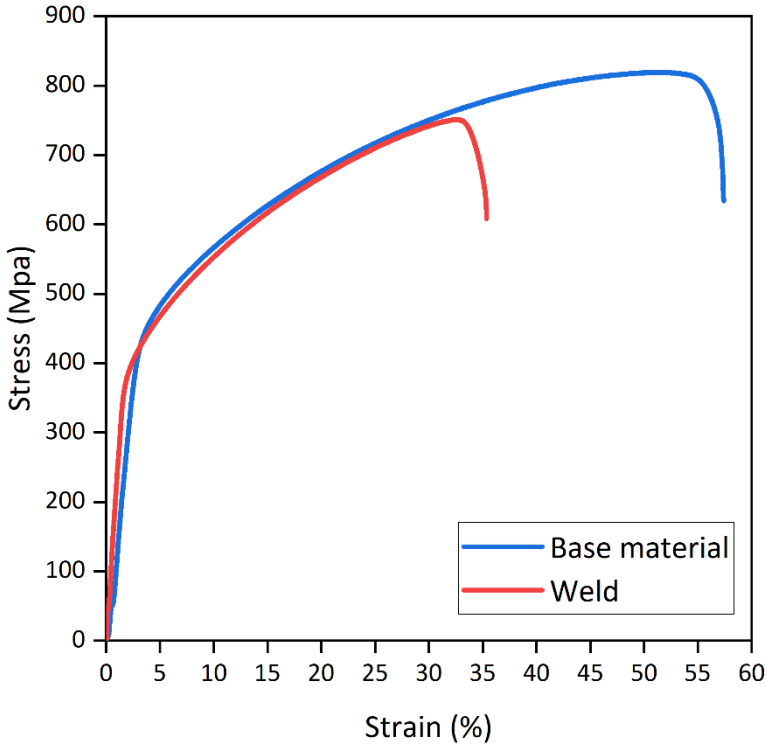


Figure 106 – Comparison of the tensile behavior of the welded $Cr_{29.7}Co_{29.7}Ni_{35.4}Al_4Ti_{1.2}$ MPEA and the BM.

To complement the mechanical characterization of the welded joint, in situ Digital Image Correlation (DIC) was used during tensile testing until failure to further understand the strain partitioning between the regions that comprise the welded joint (refer to Figure 106). Strain partitioning between the three regions can be observed as the tensile test progresses, leading to the eventual fracture of the sample near the HAZ/FZ boundary. Such may have been possible by the microstructural nature of the HAZ compared with the other regions. Due discontinuity of grain size, which occurs due to the changes in the peak temperature across the material and other already mentioned microstructural features, can provide the means for fracture initiation in the HAZ. Also, it is also important to notice that the previous thermomechanical processing undertaken by the BM and the residual stress left by rolling and later welding may, as well as the microstructure gradient within the joint, all play a key role in the final mechanical properties exhibited by the material.

The DIC data showed that the average strain exhibited by the welded sample was 36.5%, which is good agreement with the macroscopic tensile response of the welded joint.

Further analysis of the DIC data considering one representative region of the BM, HAZ and FZ is detailed in Figure 107, which was used to further elucidate on the local mechanical behavior exhibited by each region. As it is possible to observe, the different regions of the weld behaved differently during macroscopic tensile loading.

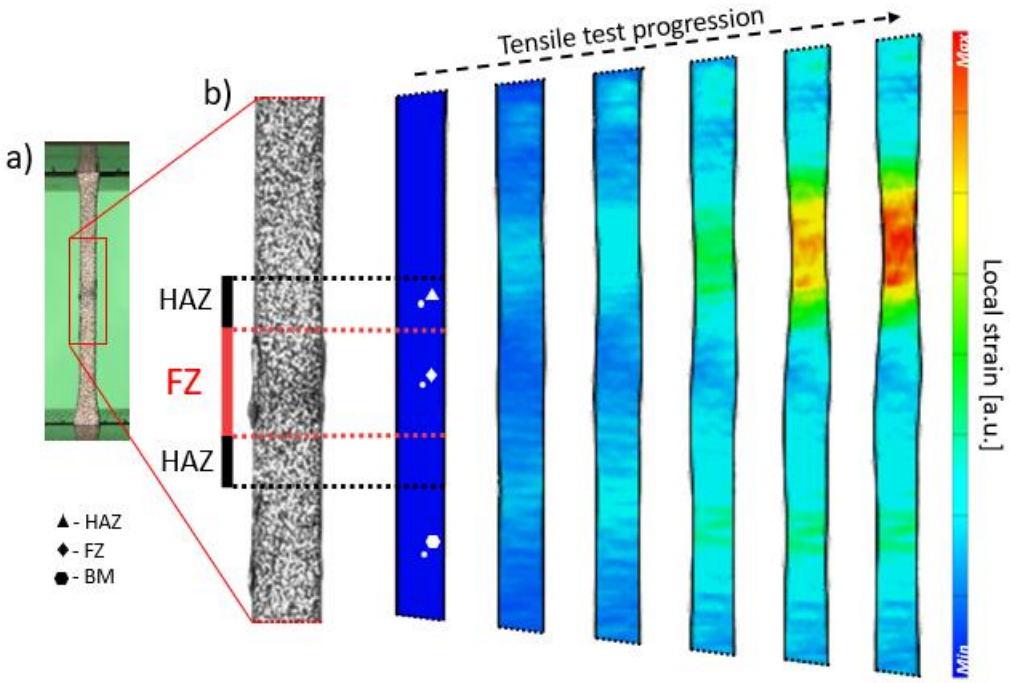


Figure 107 – Weld tensile behavior probed by DIC: (A) Sample condition before loading and (B) Strain partitioning evolution throughout the test. The symbols marked in the underformed material (blue collored snapshot of b) correspond to the locations of the welded joint which were used to obtain the representative stress-strain behaviors of the BM, HAZ and FZ detailed in Figure 108.

A further look on the behavior of specific points in each region of interest (BM, HAZ and FZ) is displayed in Figure 108. Clearly, it can be observed that the BM exhibits the lowest elongation (nearly 26%), followed by the FZ with 54% and finally the HAZ reached 73%. The reason for the HAZ to exhibit such behavior can mainly be due to the larger grain size compared to the BM in the region close to the FZ, yielding a lower strength, especially on the region closer to the FZ where the material was heated above the γ' solvus and a low fraction of precipitates exists. Furthermore, although the FZ possesses larger grains, due to the nature of the welding process the cross section of that region is larger, as shown in Figure 2 a)s, therefore the total stress imparted by the FZ is smaller than in the rest of the material. Comparably, the average strain vs stress curve obtained with DIC was very similar to the one

obtained through the tensile machine, differing mainly on the elastic regime and on the final stages of the tensile test, exhibiting nonetheless a good correlation between both analysis methods.

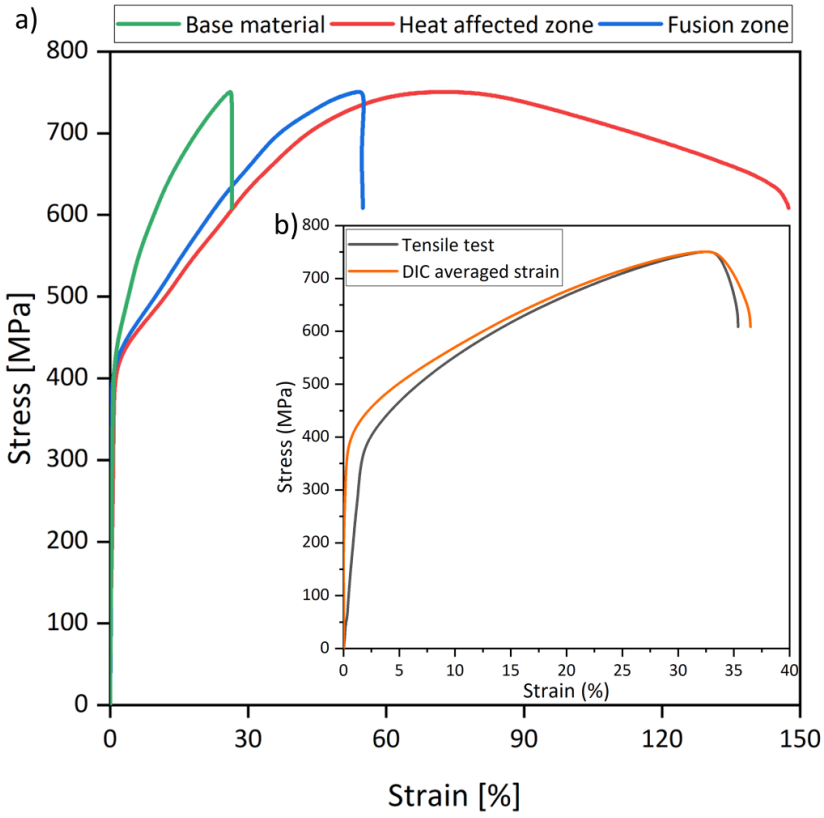


Figure 108 – Stress-strain behavior of representative points located in the BM, HAZ and FZ obtained with DIC during tensile testing of the welded joints. between the analyzed points (marked in Figure 107 (B) sample un-deformed condition). Locations of these regions was previously indicated in Figure 107. The insert details the macroscopic mechanical response of the welded joint (black curve) and the DIC average response (orange curve).

Eventually the sample fractured in the boundary between the HAZ and the FZ. A representative fracture surface of one of the welded joints is detailed in Figure 109. Dimples are observed throughout the weld fracture surface which is indicative of a ductile-like fracture and in good agreement with the high ductility of the welded joint. Even though precipitates existed in the welded material, these were not conducive to a brittle-like fracture mechanism in the welded joint.

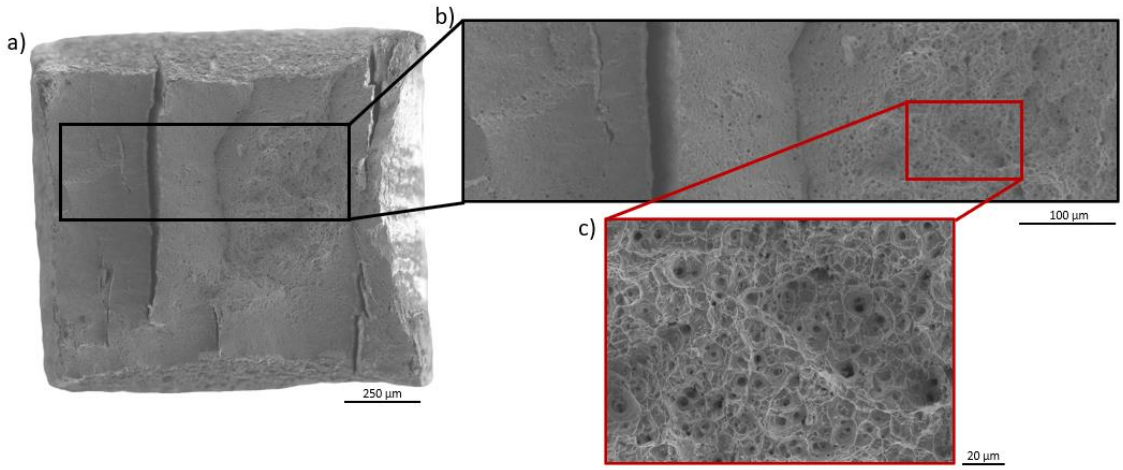


Figure 109 - Fractography of the welded sample: (A) Overview of a fractured sample; (B) Close-up highlighting a ductile-like morphology of the surface; (C) Detail of the dimples in the ductile region of the fracture surface.

4.5.6 Section summary and conclusions

This study details the first report on the weldability of a rolled $Cr_{29.7}Co_{29.7}Ni_{35.4}Al_4Ti_{1.2}$ MPEA obtained using GTAW. With focus on evaluating the effects of welding on this MPEA a correlation between the weld's microstructure and mechanical properties was established. The following conclusions can be drawn:

- Defect free welds were obtained on the $Cr_{29.7}Co_{29.7}Ni_{35.4}Al_4Ti_{1.2}$ MPEA, which exhibit an overall good weldability using GTAW;
- Grain size varies along the observed regions, where, as expected, larger grains were observed on the FZ in contrast to the BM, ultimately impacting the microhardness distribution along the full extension of the weld;
- Synchrotron X-ray diffraction revealed that the microstructure of the material is mostly composed of g and g' phases, although minor fractions of B2, η and σ can be seen in some regions of the welded joint;
- Thermodynamical calculations were useful to index the observed phases, although the partitioning predicted was not experimentally observed;
- In terms of tensile behavior, the welds exhibit lower strength and ductility than the base material, achieving a tensile strength of 751 MPa and elongation at fracture of 35 %.

4.6 Microstructure and mechanical performance analysis of the CoCrFeMnNi HEA

4.6.1 Section highlights

The microstructure and the mechanical performance of the gas tungsten arc welded equiatomic CoCrFeMnNi HEA were accessed using an in-situ tensile test probed using synchrotron x-ray diffraction. The results, as follows, detail the role of local microstructure on the strain partitioning and deformation behavior considering both qualitative and quantitative analysis. Here, the microstructure evolution of each welding region was performed by tracking changes in diffracted peak intensity and lattice strain and orientation-dependent evolution is highlighted. Evidence of strain concentration at specific locations is correlated with the overall macroscopic mechanical behavior. Furthermore, dissimilar welding with Inconel 718 was successfully attempted.

4.6.2 In-situ microstructural evolution during tensile loading of CoCrFeMnNi high entropy alloy welded joint probed by high energy synchrotron X-ray diffraction[6]

For this study, the experimental procedure is depicted in Figure 110 and can be comprehended as follows. With prior knowledge of the stress-strain behavior of the joints (detailed in [103]), the in-situ tensile test (performed at the P07 beamline in DESY) was paused at specific strain stages until eventual fracture of the weld occurred. At each stage, a series of consecutive scans was conducted along the full extension of the joint, where the material, located at 1.396 m from the detector, was exposed to an energy X-ray beam of 87.1 KeV, corresponding to a wavelength of 0.14235 Å. A beam spot size of 0.25x0.25 mm was utilized, and each analyzed spot was located at a distance of 0.25 mm from the previous one. This setup allowed to work in transmission mode permitting to acquire bulk information at each scanned region in the form of the Debye-Scherrer rings (see Figure 110 b)). The obtained raw-data was analyzed using a combination of PyFAI [179] and python-based scripts to retrieve

[6] The results discussed in this sub-section are already published in the Science and Technology of Welding and Joining journal, corresponding to reference [208].

the diffraction peak specific reaction to the externally applied load. The analysis was conducted via full azimuthal integration and by the integration in 10° segments oriented in the loading (LD) and transverse (TD) directions (see Figure 110 b) for the schematic representation).

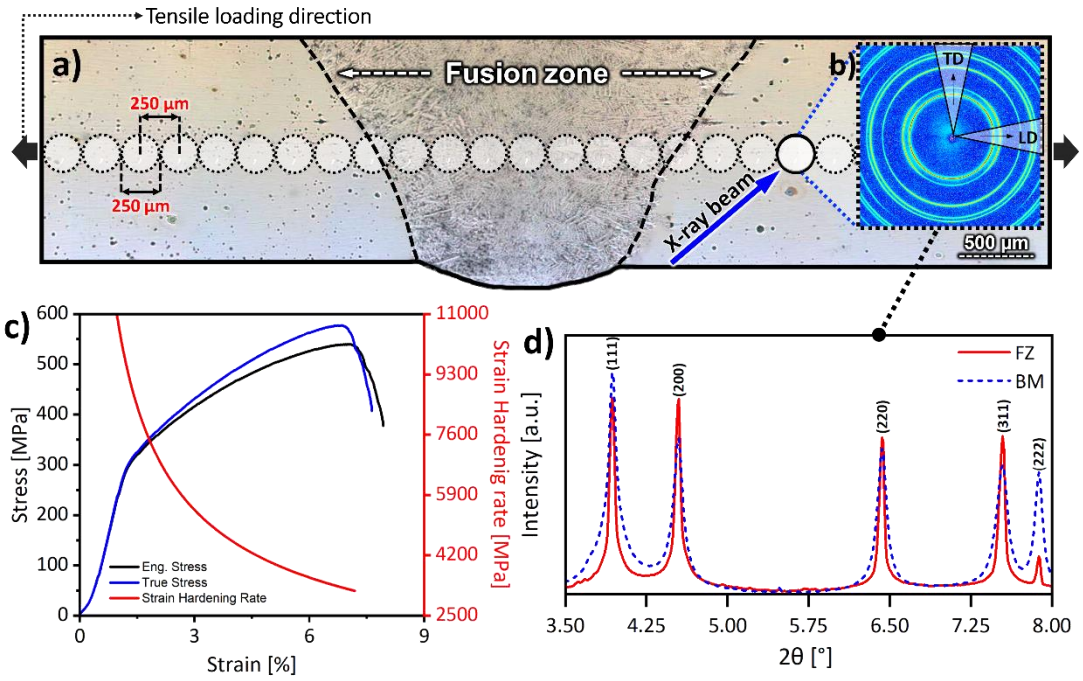


Figure 110 – Depiction of the experimental procedure and conditions: (a) Optical micrograph of the welded joint complementing a graphical explanation of the SXRD in-situ tensile test; (b) Debye-Scherrer rings captured by the 2D detector during one scan of the welded joint; (c) mechanical performance of the welded joint under tensile stress; (d) Representative diffraction patterns of the BM and FZ prior to loading.

In Figure 110 a) we can observe a representative optical micrograph of the welded joint utilized in the in-situ tensile test. The mechanical results obtained during the test are depicted in Figure 110 c). There, the engineering and true stress-strain curves are exhibited alongside the strain hardening rate. Overall, an ultimate tensile strength (UTS) of 541 MPa was achieved, with eventual fracture occurring at 7.93% of strain (all engineering values). Accordingly, the strain hardening rate tends to decrease with increasing levels of stress. This is to be expected, provided that with more deformation, the hardening capacity of the joint is reduced, directly affecting the rate at which hardening caused by increasing strain occurs.

Concerning the diffraction data, in Figure 110 d) it is possible to observe a rough comparison between the resulting diffraction patterns obtained for the BM and FZ prior to load

applied to the joint. There, the diffraction reflections of the FCC phase characteristic of the CoCrFeMnNi alloy, obeying Bragg's law, are visible. As expected, throughout the weld this phase is dominant, although the presence of Cr-Mn oxides can also be observed to occur in the material [103]. However, these particles are not considered in this study due to their low intensity (and relatively low phase fraction). Rather, we turn our focus to the FCC phase diffraction peaks and their evolution.

Figure 111 a) introduces the region-specific behavioral changes with increasing stress through the evaluation of the normalized integrated intensity of the (3 1 1) peak variation (chosen due to its intrinsic insensitivity to intergranular strains [25]). There it is possible to observe the increasing lengths of both the FZ and HAZ during the tensile test, which are also graphically represented in Figure 111 b), as the progression of the tensile test causes the cross section of the weld to increase in the LD and decrease in TD.

Starting from the stress-free condition (0 MPa) to the point where failure occurred, at 540 MPa, it is observed that in the BM practically no changes are observable from the microstructural evolution visible from the normalized integrated intensities. Such is due to its comparatively smaller grain size amidst the weld regions and given that this area is already strain-hardened due to previous cold rolling, causes plastic deformation to be delayed and transferred to other regions of the joint. Given this, the HAZ and the FZ are more prone to undertake several microstructure alterations during tensile testing, given their relatively lower hardness and varying microstructure (i.e. larger grain size), which will impact the diffracted intensity. In fact, although the intensity values of the HAZ also exhibit some variation throughout the test, it is in the FZ that this parameter presents itself with a more unstable behavior. That is, showcasing a more scattered intensity distribution at the beginning than in the later stages. Such is due to the large grain size present in this region. Conversely, with the increasing level of strain such distribution becomes steadier, indicating the realignment of the (3 1 1) grains as the tensile test progresses.

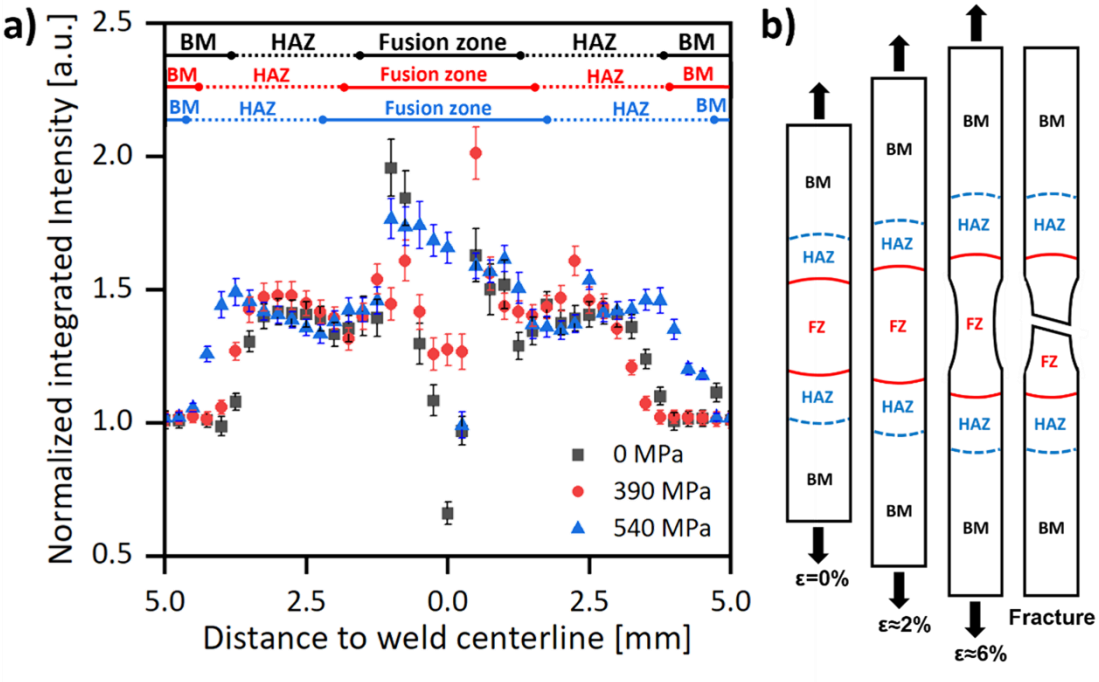


Figure 111 – (a) Normalized integrated intensity variation of the (3 1 1) diffraction reflection obtained throughout the full extension of the weld, at different loading stages. The joint regions (BM, HAZ and FZ) are marked considering the 0 MPa loading condition. Data obtained using full azimuthal integrated data. (b) Schematic representation of the cross-section evolution during tensile testing.

The differences noticeable through the normalized integrated intensity will also be visible in other meaningful peak parameters. Such is the case of peak center which allows to compute the peak-specific lattice strain evolution throughout the joint during the tensile experiment. By using Bragg's law, the lattice strain, ε, can be calculated using $\varepsilon=d/d_0$, where d_0 corresponds to the interplanar spacing at 0 MPa. Given this, Figure 112 displays a comparison in evolution of ε along the TD and LD, for the (2 0 0) and (3 1 1) peaks. Here, it is important to mention that in the FZ, these are the only visible reflections in the LD. Such occurs because the LD is aligned to the favored direction for heat flow extraction during welding. This, combined with the fact that the (2 0 0) peak is the crystallographic equivalent to the easy growth direction of FCC metals (corresponding to the (0 0 1) planes), provides the means for these grains to be oriented in a higher fraction towards the LD [180]. Additionally, beyond the aforementioned characteristics of the (3 1 1) peak, the (2 0 0) reflection corresponds to the softest plane in FCC material [74], meaning that, of all the visible diffraction peaks, it showcases the higher deformation values with increasing levels of stress.

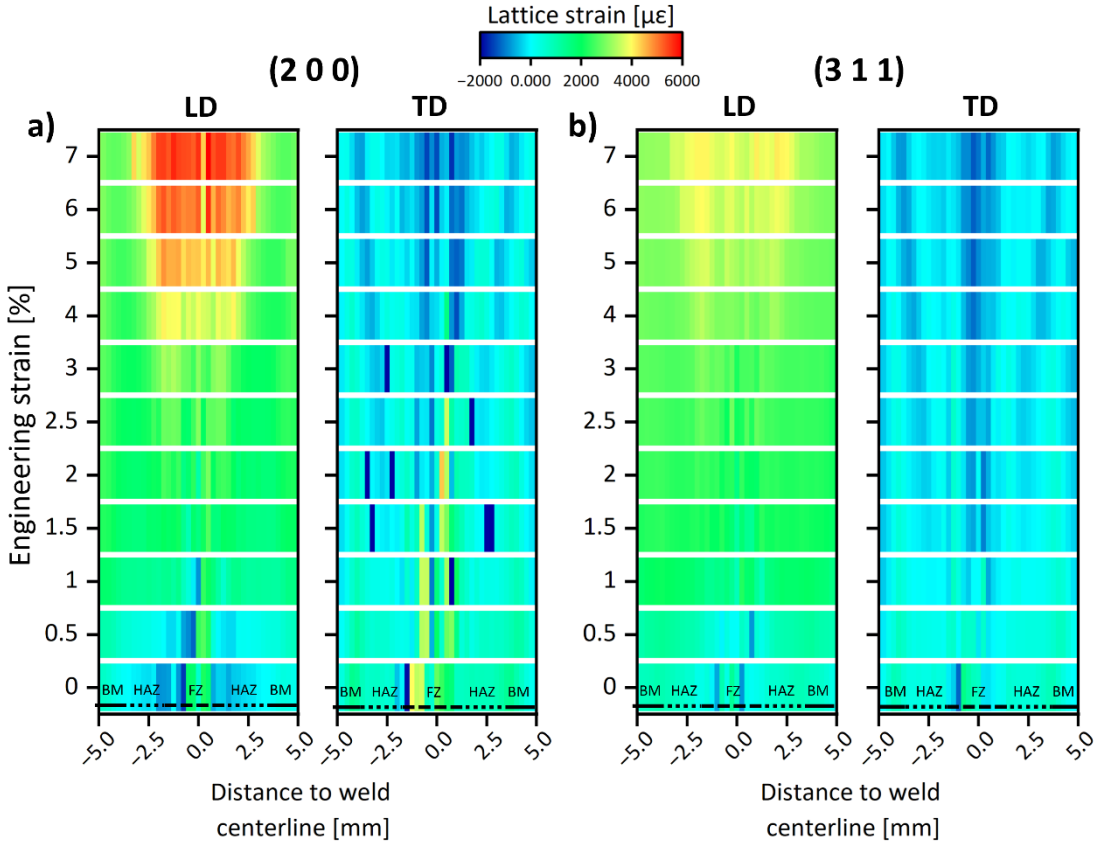


Figure 112 – Lattice strain evolution, measured on the LD and TD, throughout the in-situ tensile test. The diffraction reflections (a) (2 0 0) and (b) (3 1 1), were chosen due to their exclusive availability in the LD of the FZ. The value of d_0 was set to be the value for d-spacing obtained in the BM at the 0 MPa stage serving as the baseline for comparison.

On a qualitative basis, at 0 MPa for the (2 0 0) peak, the LD lattice strain distribution is lower in HAZ tending to increase towards the BM and the FZ. Such can be explained by the internal-stress developed during rolling of the BM and the stress-relieving phenomena associated to the high temperatures attained in the HAZ during GTAW. However, a scattered distribution is observable in the TD, achieving negative values as expected given Poisson's effect. Similarly, concerning the (3 1 1) peak, the lattice strain decreases when going from the BM to the FZ, while a more scattered distribution can be found in the TD.

In both cases, throughout the evolution of the tensile test, the lattice strain can be observed increasing in the LD, while decreasing in the TD. These changes can be especially observed in the HAZ and FZ, where a massive dissimilarity is observed in these regions of the weld, whose dimension in the LD increases throughout the test, due to the applied

unidirectional force. Such is compliant with the microhardness results obtained in the joint [103], where the BM has hardness of ≈350 HV, the HAZ showcases a peak (up to ≈375 HV), drastically reducing from that point on to ≈150 HV in the FZ, enabling us to anticipate that the majority of the strain will be imparted partially by the HAZ and from the whole FZ, the weld's softest region.

Considering the increasing extension of the FZ and the HAZ in the LD, we now focus on the individual response of each region of the weld (BM, HAZ and FZ). Such allows us to delve into the question of how each zone, and consequently each grain family, behaves under loading.

These results are shown in Figure 113, where the lattice strain evolution regarding the increase in macroscopic strain are highlighted. There, as expected, the highest magnitude for lattice strain was achieved at the final loading stages in all cases in the FZ, followed by the HAZ and the BM.

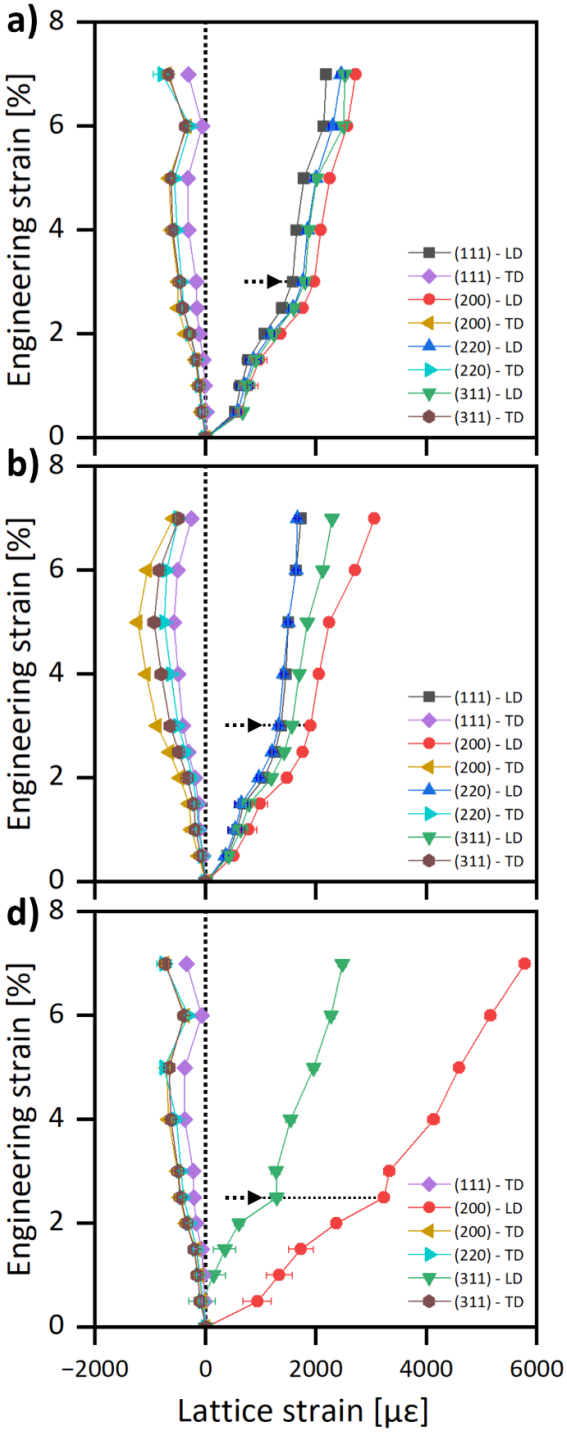


Figure 113 – Region-specific lattice strain evolution during tensile loading along LD and TD with regard to strain. The results shown in (a) and (b) correspond to the BM, (c) and (d) correspond to the HAZ and (e) and (f) correspond to the FZ. Note that in the FZ, the only visible reflections correspond to the (2 0 0) and (3 1 1) planes on the LD, such being due to the large grain size characteristic of this region and the solidification conditions imposed during welding.

Furthermore, it is possible to distinguish the elastic and plastic domains of the tensile test, undertaken by each region, through the variation in slope exhibited by the lattice strain evolution. In this sense, a lower slope indicates that the lattice strain, which is affected by peak shift (and, thus, by the change in interplanar spacing) corresponds to the elastic domain of the tensile test. On the other hand, a steeper slope indicates that the contribution of elastic strain to the overall increase in engineering strain is minimal, therefore, marking the onset of the plastic regime during loading, where strains are mostly accommodated via dislocation slip [181], therefore affecting peak shift in a more negligeable manner.

From this perspective, the change in the lattice strain evolution slope evidences a variation in yielding point regarding each analyzed region. That is, while in the BM and HAZ the slopes (marked with a black dashed arrow) only change when reaching a macroscopic strain level of ≈ 3%, in the change in slope exhibited in the FZ is altered in an earlier stage, at ≈ 2.5 %. Such comparison allows us to observe that, amidst the three regions, the FZ yields first, although showcasing a more ductile behavior than the other regions. From this, it is possible to perceive that the lower sensitivity for changes in lattice strain in the BM is related to its highly deformed, cold-worked microstructure, while in the FZ the soft microstructure led to increasing lattice strain values during tensile testing. The HAZ will have a behavior in between those of the BM and FZ, stemming from its hardness (below that of the BM and above the FZ, except for a localized region where the grain size slightly decreased)."

Moreover, in all cases, the (2 0 0) diffraction reflection exhibits the largest lattice strain in the LD and the lowest in the TD, indicating its lower stiffness and lower hardening ability, when compared to the other analyzed grain families. Conversely, apart from the FZ, the (1 1 1) peak exhibits the stiffest behavior. The data retrieved from the accessible peaks on the FZ allows us to observe that, in this particular case, the stiffest behavior is shown by the (3 1 1) planes.

Having established the amount of lattice strain partaken by each region during the experiment, the next step is to delve deeper at the differences between the initial and final microstructure of the weld, as acknowledged in Figure 114. There, the Debye-Scherrer rings data (see Figure 110 b)) was integrated into 1-degree segments throughout the full azimuthal

range, allowing to observe qualitatively, the peak center displacement and the intensity changes due to the applied stresses, indicating grain rotation.

On a first note, the initial condition of the three regions (BM, HAZ and FZ) highlights a clear distinction on their grain orientation distribution. Nevertheless, before analyzing each region, it should be emphasized that a high intensity on a specific azimuthal angle implies that the grains are preferably oriented towards the direction that such azimuthal angle corresponds in space.

As such, observing Figure 114 a), corresponding to the unloaded condition, we can see that in the BM most grains are oriented in the LD, which also corresponds to the direction of rolling to which it was subjected before welding. Prior to fracture, although no significant changes can be observed in terms of peak intensity, the local lattice strain (see Figure 114 c)) increases up to ≈3 times along the LD. This region shows less differences in comparison with its initial state, which can be associated to small and highly oriented grains.

Next, we have the HAZ, which experienced recrystallization and grain growth processes during welding. At 0 MPa, this region exhibits a more random grain orientation distribution, which translates in a less evident intensity distribution over the full azimuthal range. At 540 MPa, however, a clear rotation of the grains in the LD (90° and 270° angles) can be observed. Quantification of the microstrain indicates that the local lattice strain distribution in this region increases to ≈4 times more than in its initial condition.

Lastly, we turn to the FZ, where the widely sparse intensity distribution is caused by the large grain size. This results in the collection of diffraction data from a relatively lower number of grains, given that the adopted beam spot size remained constant throughout the test. Comparison between the initial and final stages enables to observe that the grains have reoriented/deformed to accommodate the imposed external stress. In this region, at 540 MPa, the intensities are also higher in the LD. This suggests that the FZ is the region that undergoes most microstructural changes to grant the as-welded HEA most of its mechanical performance. In this region the local lattice strain increases up to ≈6 times in the LD and ≈2 times in the TD, in comparison with its original state.

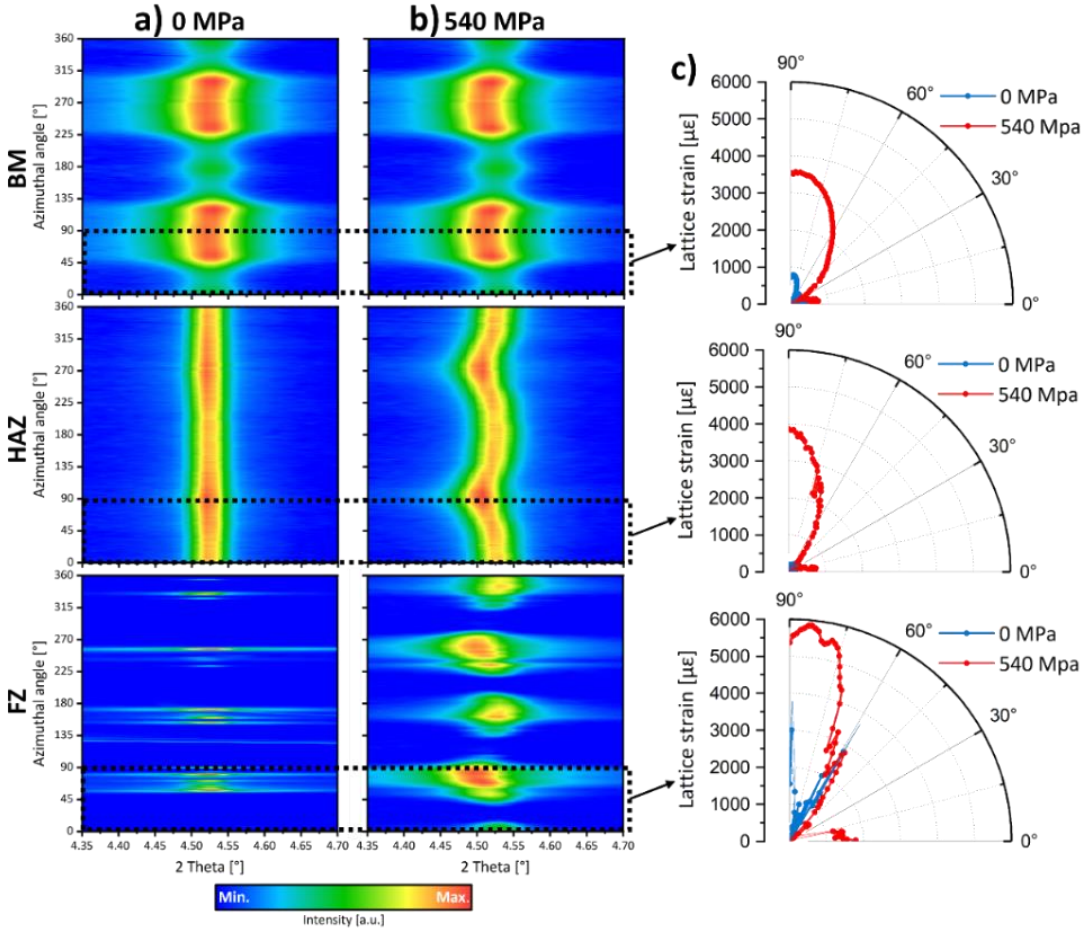


Figure 114 – (a) Initial and (b) last stages of the tensile test probed by SXRD, highlighting, qualitatively, prevalent grain orientations on the BM, HAZ and FZ, obtained by integration of 1-degree segments on the full azimuthal range. (c) corresponds to the obtained lattice strain on each of the segments, quantitatively indicating the amount of localized lattice strain handled by each of the regions.

In conclusion, an in-situ tensile experiment coupled with high energy SXRD was performed on a CoCrFeMnNi high entropy alloy welded joint. It was shown that a UTS of 541 MPa was reached with fracture occurring at an engineering strain of 7.93%. Overall, a qualitative and quantitative comparison between each of the welded regions was performed, allowing to highlight the differences arising from their mechanical response to the tensile loading. More specifically, using the intensity distribution evidenced the location of the welded regions, and site-specific analysis allowed to exhibit the intensity distribution throughout the azimuthal angle on each region, highlighting grain rotation during the tensile solicitation. Regarding the lattice strain, the imparted strain on each region was quantified, indicating that the FZ was

the most impacted region by the external stresses. Overall, the FZ was noted to be the critical region of the GTAW joint.

4.6.3 Dissimilar laser welding of an as-rolled CoCrFeMnNi high entropy alloy to Inconel 718 superalloy

High entropy alloys (HEAs) are novel class of materials known for its revolutionary way to enable new alloy compositions significantly different from those commonly used in conventional engineering alloys [182]. Among the several HEAs that have already been discovered, the equiatomic CoCrFeMnNi HEA, also known as the Cantor alloy, stands as the first HEA to have been reported [2,183]. Throughout the years, the CoCrFeMnNi alloy has shown remarkable properties depending on its processing conditions. The interesting properties associated to these materials include high strength at extreme temperatures [184], notable wear resistance [185] and excellent corrosion resistance [186].

The advancements on CoCrFeMnNi-based HEAs research further potentialize its integration in key engineering applications. Furthermore, such premise can be accomplished by studying the weldability of HEAs, since the possibility of using them to create complex structures is very appealing to industry and welding is a widely used technique for such endeavor [24,34,187]. On this topic, literature shows that an effort to understand (and control) the metallurgical changes occurring in the CoCrFeMnNi HEA during welding have already been conducted in both similar [29,188–191] and dissimilar combinations [26,27,157,192–196]. As such, in this work, we study the weldability of a dissimilar laser welded joint between an as-rolled CoCrFeMnNi alloy and Inconel 718 Ni-based superalloy by detailing its microstructure and unraveling its mechanical behavior.

The choice of Inconel 718 to be coupled to the CoCrFeMnNi HEA is based on its high strength and corrosion resistant characteristics which makes it a competitive choice for several industrial sectors such as aerospace, gas turbines, and oil & gas [197–200]. In this regard, our results address the lack of comprehension regarding the compatibility of the CoCrFeMnNi alloy with Inconel 718 which, to the best of the authors knowledge, has not been addressed to this point in the literature.

For such, as-annealed Inconel 718 plates with a thickness of 1.5 mm were acquired from McMaster-Carr, while an as-rolled equiatomic CrMnFeCoNi high entropy alloy was fabricated from commercially pure elements and subjected to a thickness reduction of ≈50% via cold-rolling (to a final thickness of 1.5 mm). Both materials were then cut via wire electron discharge machining to obtain 30 x 30 mm coupons which were used for laser welding.

Given this, the laser welding procedure was performed using a Miyachi Unitek LW50A pulsed Nd:YAG laser system, with a wavelength of 1.064 µm. A spot diameter of 600 µm and a peak power of 1.0 kW were used to obtain full penetration. Corresponding to a power density of ≈3.54 kW/mm^2 (calculated through the ratio between the peak power and the area of the beam [201,202]). The pulse profile had a duration of 10 ms, including 2 ms of up- and downslopes. Argon gas was applied at a flow rate of 0.57 m^3/h, to create a protective atmosphere surrounding the joint. A butt joint configuration was used.

For microstructural analysis, the joint cross section was analyzed using a JEOL JSM-7800F PRIME high-resolution field emission SEM equipped with backscattered electrons (BSE) and energy-dispersive X-ray spectroscopy (EDS) detectors. Electron backscatter diffraction (EBSD) analysis was performed using a FEI XL- 30S FEG SEM. Phase field mapping predictions using EDS data retrieved from the fusion zone (FZ) were calculated using the Scheil-Gulliver model available in ThermoCalc [203] software, with the TCHEA5 database. Additionally, the full extension of the weld was scanned from one base material (BM) to the other using high energy synchrotron X-ray diffraction (SXRD), performed at the P07 beamline at PETRAIII/DESY. The beam spot size was set to 150 × 150 µm, with a 150 µm distance between consecutively analyzed spots. The X-ray beam had an energy of 87.1 keV (corresponding to a wavelength of 0.14235 Å) and the sample-to-detector distance was 1.365 m. The raw data was integrated using PyFAI [179] and analyzed using in-house developed python-based scripts.

To inspect the (local) mechanical properties, microhardness mapping was performed using a Mitutoyo Micro Hardness Testing Machine HM-112, with an indentation load of 300 g held for 10 seconds. The space between consecutive indentations was set to 125 µm in the longitudinal and transverse directions. Tensile testing was conducted on an Autograph Shimadzu AG50kNG machine, equipped with a 50 kN load cell at a 0.01 mm/s cross-head speed. Three repeats were performed to assess the joints reliability. The fracture surfaces were then analyzed using a Hitachi SU8000 SEM.

Figure 115 depicts SEM imaging coupled with EBSD maps acquired from a representative cross section of the welded joint between Inconel 718 and the CoCrFeMnNi base materials (BMs). As observed, full penetration with no defects such as cracks or pores was obtained, potentially indicating a good weldability between the two alloys.

Comparing both BMs, the Inconel 718 BM has an average grain size of ≈15.1 ± 1.4 µm, while in the case of the CoCrFeMnNi HEA, the highly deformed condition of the grains hiders the acquisition of the Kikuchi patterns, inhibiting the quantification of grain size on this side

(see Figure 115 e)). However, previous work on the same BM revealed that the CoCrFeMnNi HEA possessed pancake-shaped grains with an average grain size approaching ≈2 µm [193].

Going closer from each of the BMs to the FZ, the heat affected zones (HAZ) arise. The HAZ is often associated with solid state transformation phenomena, such as grain growth and recrystallization, due to the relatively high temperatures (below complete melting) experienced by the material [25]. However, laser welding is known for its high cooling rates and reduced heat source dimensions resulting in a narrow HAZ extensions, which when associated to the different thermal conductivities of each BMs, may result in disparities in both grain size and shape of the HAZ on each side of the FZ. Such is the case in the present dissimilar welded joint. On the Inconel 718 side, the HAZ possesses an average grain size of ≈16.4 ± 0.8 µm and an extension of ≈265 ± 22 µm. On the CoCrFeMnNi side, as it is possible to observe in Figure 115 c), the transition from the BM to the FZ is made evident, where a relatively shorter HAZ can be observed (≈195 ± 33 µm µm), with the grain size reaching values up to ≈4.5 ± 0.9 µm. Additionally, the differences in HAZ extension can also be related to the varying thermal conductivity values of both BMs with temperature. In fact, at temperatures under ≈900°C, the thermal conductivity of the CoCrFeMnNi HEA tends to be slightly lower than that of the Inconel 718 BM, as calculated based on the compositions available in Table 15 and ThermoCalc software (refer to the Supplementary Material for the variation of thermal conductivity for both BM with temperature).

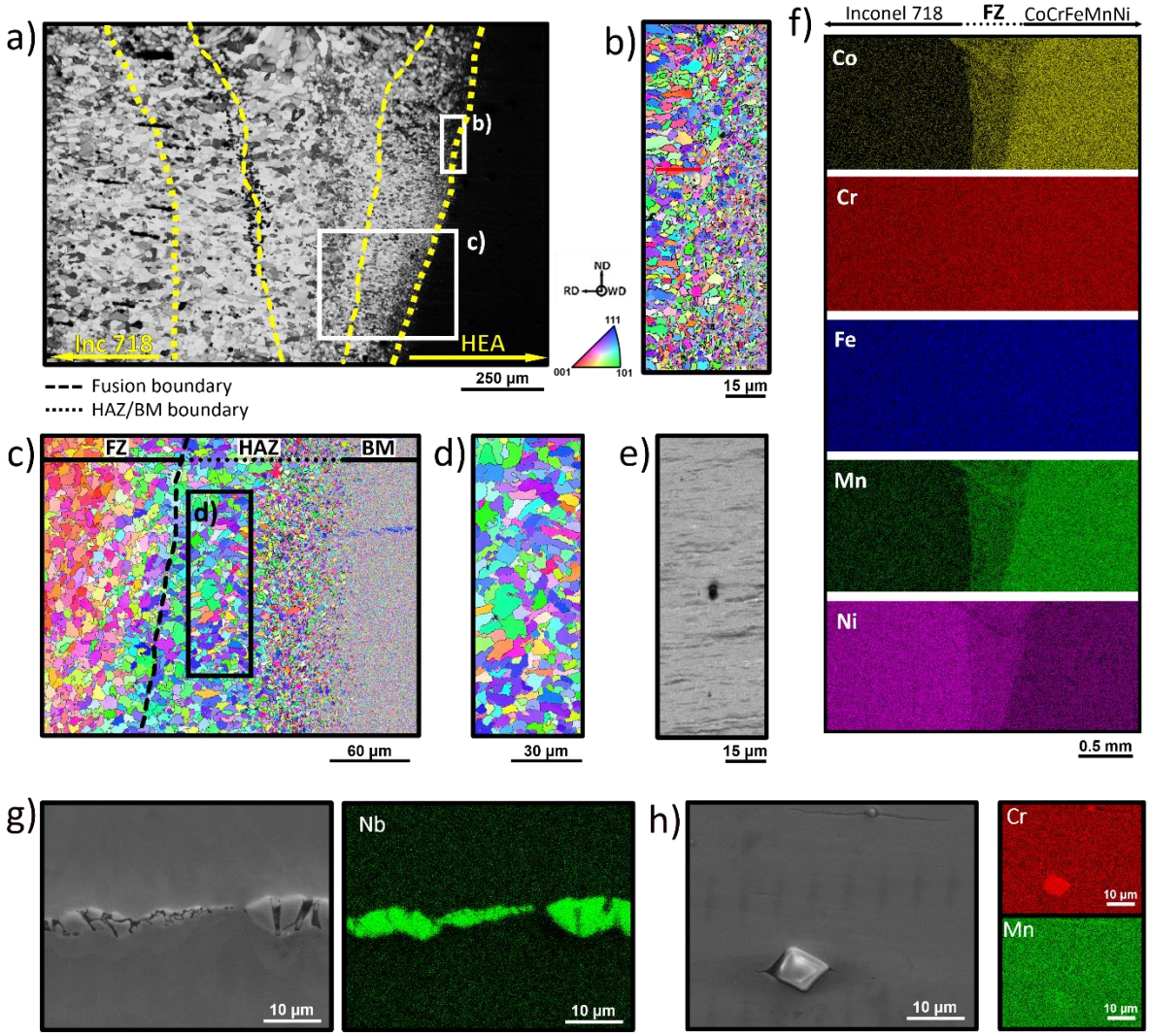


Figure 115 – Microstructure of the welded joint: a) SEM macrograph of the welded joint and corresponding EBSD IPF maps of the transition from the HAZ to the BM (b) and transition from the FZ to the HAZ (c) and detailed view of the HAZ (d); e) SEM micrograph of the BM; f) EDS maps the along the full extension of the welded joint. Additional detailed view and corresponding EDS maps of: g) NbC precipitates on the Inconel 718 BM and h) Cr-Mn oxides on the Cantor HEA BM.

Attention is now directed to the FZ, where both BM experienced full melting and mixing during welding. Given the dissimilar nature of the BMs, this region presents itself as the most prone to generate intermetallic compounds that can hinder the overall performance of the joint. In the present case the shape of the FZ highlights a keyhole welding mode, where the length of the FZ is larger than its width. A keyhole FZ is caused by the high energy laser density applied on the interface of both materials to achieve full penetration [157]. Focusing on the inverse pole figure (IPF) map in Figure 115 c), the color displayed by the FZ present

itself with a red tone indicating grain orientation in the <001>, which indeed corresponds to the easy growth direction of FCC materials [32,180].

Furthermore, EDS maps taken across the welded joint are displayed in Figure 115 f). Comparably, the Cr and Fe maps showcase that the amount of each of these elements is similar in both BMs and in the FZ. The same does not occur for the other elements, where evidently Co and Mn are present in higher amount in the HEA side, while Ni is more evident on the Inconel 718 BM. Such agrees with what is known from the elemental contents of both BMs. Qualitatively, the FZ showcases the presence of all the aforementioned elements, although exhibiting a lower amount of Co and Mn than the HEA BM, and a lower amount of Ni than the Inconel 718 BM. This occurs due to a dilution effect induced by melting and mixing of the two BMs. It is, nonetheless, obvious that the Ni content in the FZ is higher than in the HEA BM. The average composition of both BMs and the FZ is detailed in Table 15.

Table 15 – Average chemical composition of Inconel 718 and CoCrFeMnNi BMs and the FZ, obtained via EDS, considering the elements detailed in Figure 115.

Composition (at%)	Co	Cr	Fe	Mn	Ni	Nb
Inconel 718	≈0	22.5	19.8	≈0	54.5	2.8
CoCrFeMnNi	20.1	21.6	19.3	19.0	20.0	---
FZ	13.4	22.0	19.5	11.3	32.7	1.0

Figure 116 a) displays the results obtained by consecutively probing the full extension of the welds using SXRD. This enabled to highlight the differences occurring in the diffraction patterns (obtained via full azimuthal integration) due to the varying microstructure across the joint.

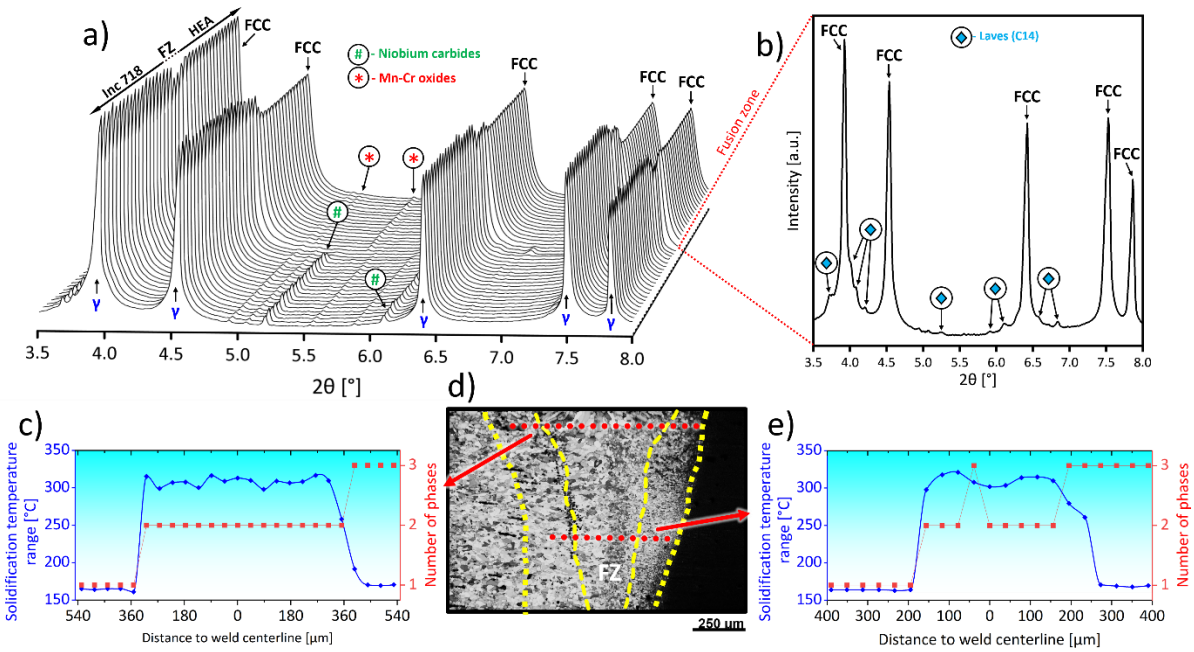


Figure 116 – Phase identification and distribution across the welded joint: a) Superimposition of the SXRD patterns along the whole extension of the weld; b) representative SXRD pattern of the FZ; c) CalPhaD-predicted phase distribution at the top of the joint, which is located in d), alongside with the e) phase distribution prediction at the middle of the joint.

Regarding phase identification, it is possible to see that both BMs are composed of a FCC matrix phase. Furthermore, consistent with Figure 115 g) and h), the presence of Mn-Cr oxides on the CoCrFeMnNi HEA and NbC precipitates in the Inconel 718 BM is also noticeable throughout the diffraction patterns. It is however, in the FZ, that the existence of a Laves (C14) intermetallic phase is visible (refer to Figure 116 b)), indicating that the FZ is not composed of a simple FCC solid solution, as it would be expected from HEAs given their often inherent solid solution effect [6].

To further investigate the phases present within the joint, CalPhaD-based thermodynamic calculations were performed using the non-equilibrium Scheil-Gulliver methodology, as shown in Figure 116 d) and e). For such, a consecutive series of EDS point measurements were gathered along the red dashed lines marked in Figure 116 d). These compositional data points where then used to obtain the temperature interval between the moment when the Liquid phase starts to solidify and when it reaches a total phase fraction of 0.01%, and number of phases present at the final stages of solidification. By analyzing this data, it is possible to perceive that regarding the BMs, the Cantor HEA side is only expected to exhibit a single FCC phase, while the Inconel 718 superalloy showcases a total of three phases within its microstructure, these being the matrix FCC phase, a Laves (C14) phase and an orthorhombic $D0_a$

phase (also known as δ phase [204]) rich in both Nb and Ni. This $D0_a$ structure, however, was not identified via SXRD, which can be explained by the fact that the of Nb content comes from the precipitates that are visible in Figure 115 g) and Figure 116 a).

It is in the FZ that these calculations are more relevant, as it is this region that undergoes fast and non-equilibrium solidification conditions due to the laser welding process, compounded by the complex mixing of the original BMs. As such, in the two measured lines it is possible to perceive that the mixture between the compositions of both alloys results in a higher solidification temperature range (approximately 300 °C) than the two dissimilar bulk BMs. Such differences in composition can be qualitatively viewed in Figure 115 f), and allow to perceive a higher risk for solidification cracking to occur in FZ, although no such defects were observed in the present joints.

Furthermore, considering the number of phases generated in the FZ upon the final stages of solidification, it can be observed that only two phases are formed, these being an FCC phase and a Laves (C14). These results are compliant with the phase identification using SXRD shown in Figure 116 a). Interestingly, in Figure 116 d), one single point indicates the formation of three phases, where the third phase corresponds to the $D0_a$ (δ) phase structure. This indicates that the local composition in this region is closer to the Inconel 718 BM, possibly due to elemental segregation or molten pool dynamics associated with the Marangoni effect [205]. Nevertheless, going further into the evenly dispersed Laves (C14) phase on both the FZ and Inconel 718 BM, the literature indicates that the Nb content (which has a higher atomic radius) is critical in its formation in Inconel 718 [206,207]. Such allows us to assume that the same factor can be expected in the FZ.

Additionally, observing the maximum peak intensity values in Figure 116 a) (corresponding, in this case, to the peak height) of the FZ, the influence of the different grain size and morphology between both BMs is demonstrated. In fact, while the more refined CoCrFeMnNi BM exhibits a constant intensity distribution with increasing distance from the FZ, the Inconel 718 side exhibits a higher variability on the maximum intensity values. Nevertheless, a deeper insight on the effect of grain size and structural defects on the SXRD data will be provided further ahead in Figure 117 when considering the full width at half maximum (FWHM) variation of the (3 1 1) diffraction peak.

As such, the evolution of the FWHM of the (3 1 1) peak was obtained by integrating from 10° segments along the 0° and 90° azimuthal angles, corresponding to the welding direction and the direction perpendicular to it (refer to [29] for more details on the SXRD experimental procedure). These results are shown in Figure 117. This was performed since the

FWHM relates the broadening effect on the diffraction peaks caused by the combined influence of the internal strains, imposed by structural defects (such as dislocations and stacking faults) and the size of the sub-grain structures, which diffract light coherently within a grain and are often referred to as crystallites [25]. Due to the possibility of imperfect alignment between these sub-grain structures due to residual stresses, radiation is reflected on a divergent but nearby 2θ angle, causing the diffraction peaks to broaden, thus affecting peak width. A higher value of FWHM, thus translates to a superior level of structural defects and/or to smaller sized sub-structures within the grains. Given this, analysis of this parameter along the joint can help understand the microstructural variations caused by the process heat input. In this case, although each peak will have its own preferred orientation after solidification of the molten pool, which is reign by epitaxial and competitive grain growth, we only display the distribution of the (3 1 1) peak FWHM due to its insensitivity to intergranular strains [180].

As it is possible to observe the FWHM variation on the Inconel 718 BM is ≈2.8 times lower than the FWHM displayed in the CoCrFeMnNi BM. Such agrees with the microstructural condition of both BMs highlighted in Figure 115 a), where the Inconel 718 is in the annealed condition and the CoCrFeMnNi HEA is in the as-rolled condition. Between the two BMs, the gradual increase in FWHM from the Inconel 718 to the CoCrFeMnNi side evidences the structural modifications in terms of grains morphology, size and structural defects that occurs in both the HAZs and the FZ. Furthermore, it can, once again, be evidenced that the extension of the HAZ is larger in the Inconel 718 side, reaching 0.8 mm indicating that the effects of the high temperatures on the HAZ are larger than those observed by SEM.

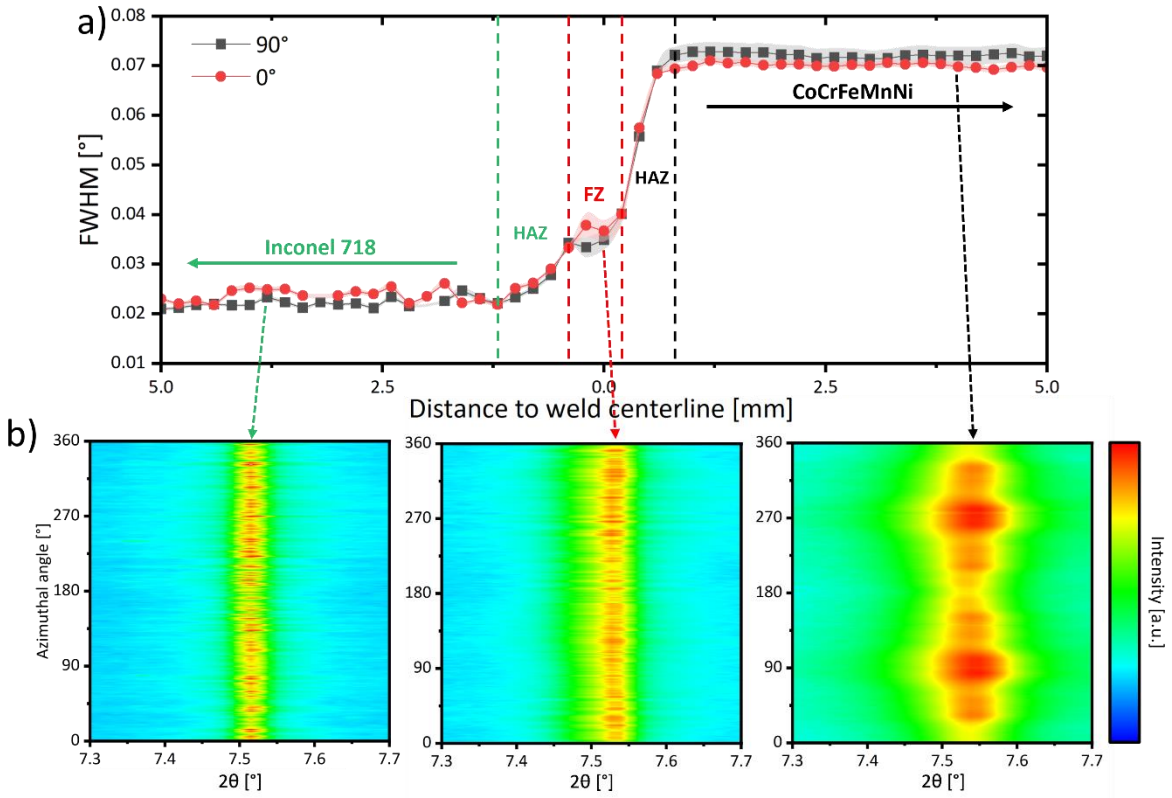


Figure 117 – (a) FWHM variation of the (3 1 1) diffraction peak measured on the 0 º and 90 º azimuthal angles along the welded joint. b) Comparison between the diffraction data obtained on the FZ and both BM, obtained by integrating in 1º segments along the azimuthal angle.

On a different note, the 2θ angle peak distribution of the (3 1 1) peak in regard to the azimuthal angle can be observed in Figure 117 b), which was obtained by integrating the raw diffraction data into 1° segments. For the Inconel 718 case, the consistent distribution of the peaks along the full azimuthal range indicates a relatively stress-free condition of this BM. The same, however, cannot be said regarding the CoCrFeMnNi BM, as it clearly shown that the diffraction peak distribution showcases a preferential orientation towards the 90° and 270° angles, which are aligned with the rolling process direction to which the HEA was submitted prior to welding, thus evidencing a strong texture effect caused by it.

Finally, the FZ evidences a similar diffraction peak distribution to the Inconel 718 BM throughout the azimuthal range, indicating that upon solidification the (3 1 1) grains of the FZ do not evidence any preferential orientation, probably due to the fast-cooling rate of laser welding which restricts the formation of large and highly aligned grains, as opposed to arc-based processes.

With the microstructural condition of the welded joint highlighted, the next step is to evaluate how the local mechanical response of the weld is affected by the microstructure

changes imposed by the weld thermal cycle. For such, Figure 118 displays the variation in microhardness along the joint. While Inconel 718 (in the as-annealed condition) reaches values surrounding 208 ± 12 $HV_{0.3}$, the microhardness of the CoCrFeMnNi BM goes up to 343 ± 9 $HV_{0.3}$, as a result of the impact on of the high dislocation density induced by the cold rolling process. Interestingly, despite the fact that the grain size of the FZ should produce the lowest microhardness values on the joint, the solid solution effect granted by the mixture between the two BMs causes intermediate microhardness values between the two BMs (and above that of as-cast CoCrFeMnNi HEA) to occur in this region, yielding a microhardness of approximately 220 ± 35 $HV_{0.3}$.

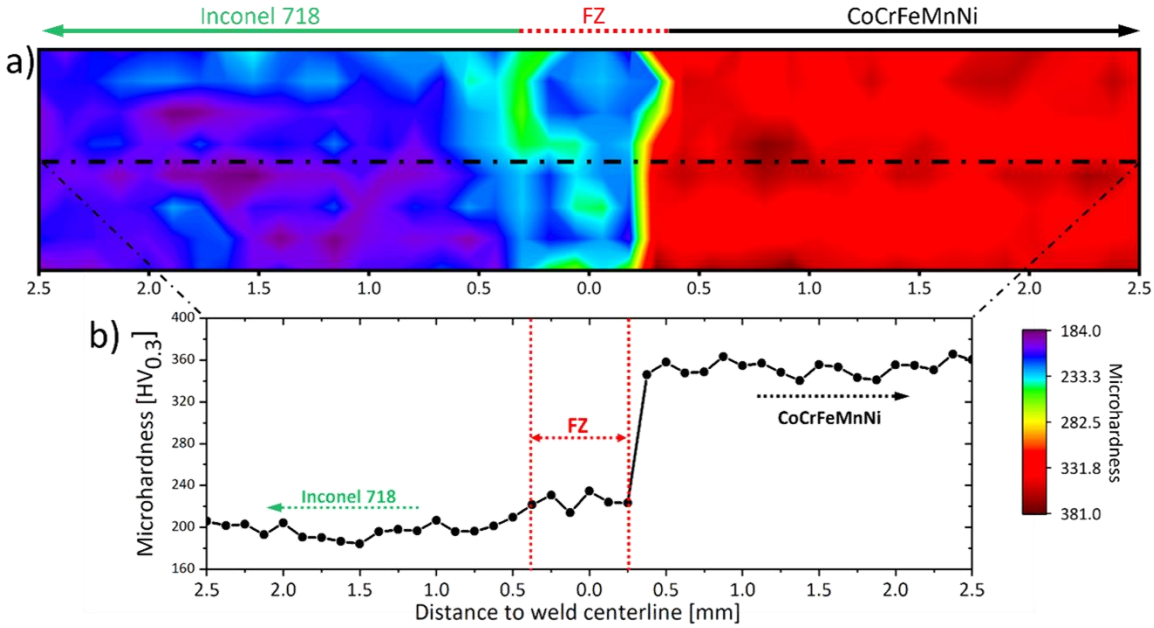


Figure 118 - a) Microhardness distribution along the welded joint and b) corresponding microhardness distribution measured at mid height.

A representative stress/strain curve for the dissimilar joint is shown in Figure 119 a) alongside with the tensile curves of the BMs (see Figure 119 c) and d)). The yield strength (YS), ultimate tensile strength (UTS) and fracture strain values for both BMs and dissimilar joint are summarized in Table 16.

Table 16 - Summary of the welded joint mechanical properties of both BM and dissimilar welded joint.

Material	Yield strength [MPa]	Ultimate tensile strength [MPa]	Fracture strain [%]
CoCrFeMnNi HEA (from [193])	587 ± 7	943 ± 6	9.5 ± 0.2
Inconel 718	461.4 ± 16	743 ± 52	48.4 ± 7.7
Welded joints	614 ± 35	822 ± 63	7.1 ± 0.4

Comparing both BMs, it is possible to observe that the CrMnFeCoNi HEA achieves higher stress levels than the Inconel 718, while exhibiting significantly lower fracture strain values. Additionally, considering the tensile properties of the welded joints, it can be observed that its UTS reaches intermediate values between the two BMs, however showcasing the lowest elongation to fracture amongst all cases. This can be explained by the fact that the chemical composition of its FZ is a combination of the two BMs (see Figure 115 f)), thus allowing the joints to sustain similar levels of stress, which is in line with the hardness distribution in the welded joints. On the other hand, such can also explain the lower elongation to fracture exhibited by the joints, which can be further hindered by the presence of Laves (C14) particles in the FZ.

Regarding the fracture surface, Ni-based superalloys and CrMnFeCoNi HEAs commonly fail by ductile fracture processes [29,188,198,199]. However, from Figure 119 b), e), and f) the fracture surfaces present themselves as a mixture of ductile and brittle-like fracture presented by the dimples and rivers patterns in the analyzed regions. Such is granted by the relatively smaller grains and the presence of intermetallic phases of the FZ. Given this, although the main fracture mechanism is ductile, the presence of the Laves (C14) phase may contribute to the embrittlement of the joint. Such indicates the relatively lower plastic deformation tolerance of the welded joint, although exhibiting excellent mechanical properties for a dissimilar joint.

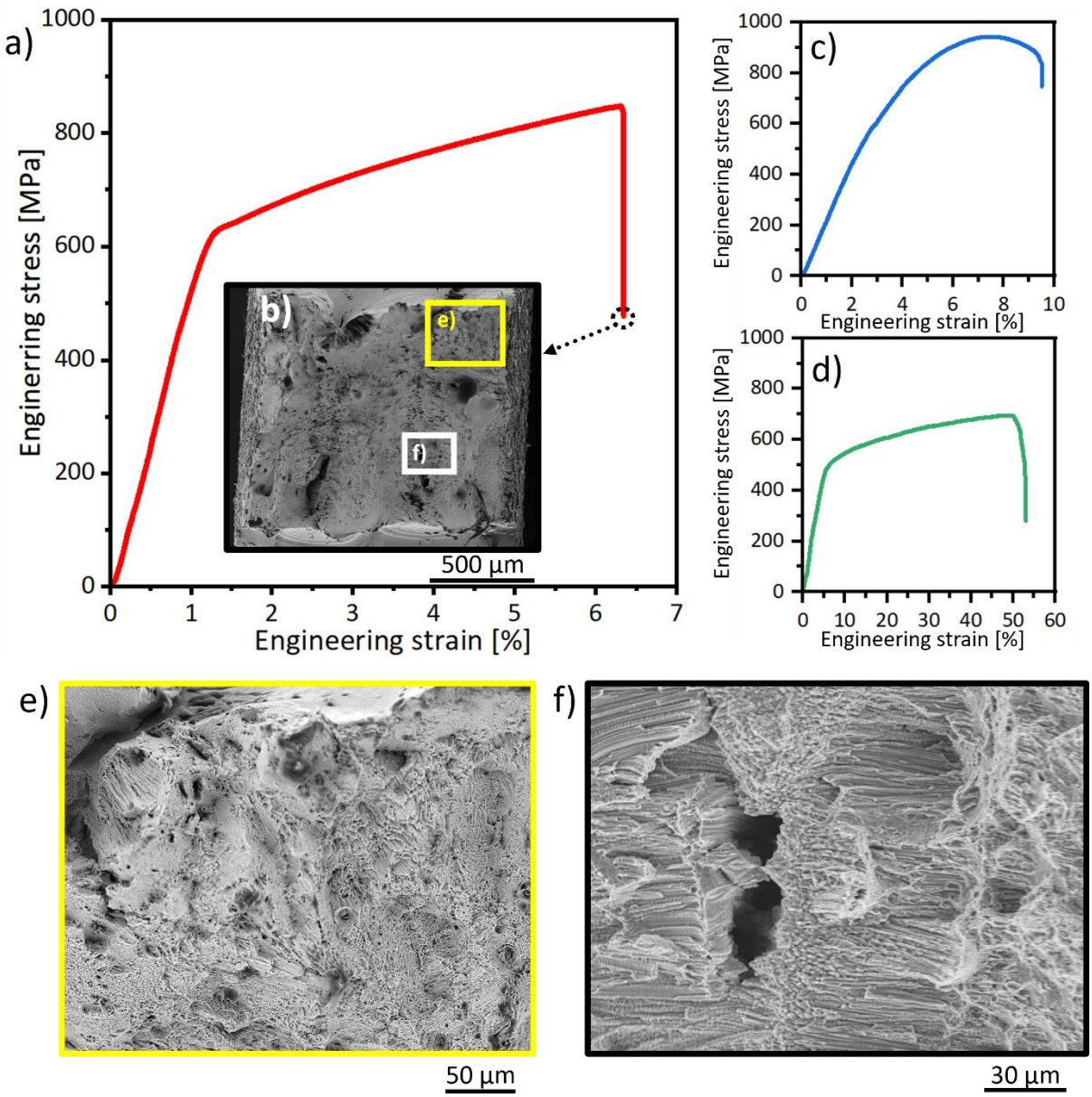


Figure 119 –a) Representative stress-strain curve of the welded joint tensile and macroscopic view of the fracture surface (b); c) and d) are representative stress-strain curves for the rolled CoCrFeMnNi and annealed Inconel 718 BMs, respectively. e) and f) corresponding to detailed views of the macroscopic fracture surface shown in b).

Overall, dissimilar laser welding between an as-rolled CoCrFeMnNi HEA and Inconel 718 was successfully accomplished. Analysis of the microstructure allowed to unveil the microstructural differences between both BMs and the features arising on the HAZ and FZ due to the high temperatures developed during laser welding. Interestingly, the nucleation of a Laves (C14) phase was observed by means of SXRD and confirmed by CalPhaD simulations.

Regarding the mechanical behavior, the FZ exhibited an intermediate microhardness level between both BMs, due to the combined effect of varying grain morphology and the compositional mixture between the BMs. Tensile testing indicated that the welded samples could endure stresses up to ≈822 ± 63 MPa eventually fracturing at strain of ≈7.1 ± 0.4%, showcasing their potential use as part of structural components.

4.6.4 Section summary

In this section a complete analysis of the mechanical behavior during tensile testing under synchrotron X-ray diffraction was conducted. It was possible to infer that orientation-dependent evolution is highlighted by considering partial azimuthal integration. Evidence of strain concentration at specific locations is correlated with the microstructure and overall macroscopic mechanical behavior.

In addition to this, dissimilar laser welding between an as-rolled CoCrFeMnNi high entropy alloy (HEA) and Inconel 718 Ni-base superalloy was successfully performed. Although precipitation of Laves phase was observed within the fusion zone. These results reveal the excellent dissimilar weldability between the two alloys, allowing the deployment of this type of joints for structural applications.

5

CONCLUSIONS AND FUTURE WORK

The purpose of this document and of the research work it contains is to mechanistically evaluate the feasibility of HEAs for potential engineering applications using welding-based technologies. Such an effort was accomplished using GTAW on different HEA systems. As such, although the specific conclusions of each joint were presented in each corresponding section/sub-section of Chapter 4, some overall conclusions can be drawn alongside some proposal for the continuity of the work.

While the FeMnCoCr and the CoCrNiAlTi alloys exhibited excellent mechanical behavior upon welding, there is room for more research regarding their dissimilar weldability with other key engineering alloys. Of special mention on this topic, is the research performed on the dissimilar weldability of the FeMnCoCr and the AlCoCrFeNi HEA with an Fe-based SMA and SS 316 L, highlighting their compatibility with other key engineering alloys and hinting for their assimilation in advanced engineering applications.

Moreover, research on the inoculation of the molten pool of the AlCoCrFeNi HEA is promising and should be further investigated and pursued on other HEAs as well. Regarding the weldability of the $CoCu_xFeMnNi$ (x=20,30), the results revealed that the mechanical properties were hindered by GTAW, thus ensuing the question if inoculation can improve the obtainable mechanical properties of joints or if the application of a different welding technique can help in this endeavor.

Overall, the research conducted in this thesis highlights the wide compositional space, within the framework of HEAs, that can be developed and processed using fusion-based welding techniques for future usage in key engineering applications. These include aerospace, infrastructure and automobile industries, that in turn and depending on their requirements can also become value inputs to further develop mechanistically the welding process on such novel and advanced materials.

Given this, future works will envisage the continuity of the presented results and their subsequent publication in internation peer reviewed scientific journals. Such research will

focus on the similar and dissimilar weldability of different HEAs, including different welding techniques and other approaches for microstructural control upon solidification. With this mentioned, other ideas may still arise to help in the assimilation of HEAs in key engineering applications and their development.

REFERENCES

[1] F.C. Achard, Recherches sur les propriétés des alliages métalliques, 1st Edition, Imprimé chez George Jacques Decker & Fils, 1788.

[2] B. Cantor, I.T.H. Chang, P. Knight, A.J.B. Vincent, Microstructural development in equiatomic multicomponent alloys, Materials Science and Engineering: A 375–377 (2004) 213–218. https://doi.org/10.1016/J.MSEA.2003.10.257.

[3] J.W. Yeh, S.K. Chen, S.J. Lin, J.Y. Gan, T.S. Chin, T.T. Shun, C.H. Tsau, S.Y. Chang, Nanostructured High-Entropy Alloys with Multiple Principal Elements: Novel Alloy Design Concepts and Outcomes, Adv Eng Mater 6 (2004) 299–303. https://doi.org/10.1002/ADEM.200300567.

[4] Y.F. Ye, Q. Wang, J. Lu, C.T. Liu, Y. Yang, High-entropy alloy: challenges and prospects, Materials Today 19 (2016) 349–362. https://doi.org/10.1016/J.MATTOD.2015.11.026.

[5] E.P. George, D. Raabe, R.O. Ritchie, High-entropy alloys, Nature Reviews Materials 2019 4:8 4 (2019) 515–534. https://doi.org/10.1038/s41578-019-0121-4.

[6] D.B. Miracle, O.N. Senkov, A critical review of high entropy alloys and related concepts, Acta Mater 122 (2017) 448–511. https://doi.org/10.1016/j.actamat.2016.08.081.

[7] Y.D. Wu, Y.H. Cai, X.H. Chen, T. Wang, J.J. Si, L. Wang, Y.D. Wang, X.D. Hui, Phase composition and solid solution strengthening effect in TiZrNbMoV high-entropy alloys, Mater Des 83 (2015) 651–660. https://doi.org/10.1016/J.MATDES.2015.06.072.

[8] W. Chen, A. Hilhorst, G. Bokas, S. Gorsse, P.J. Jacques, G. Hautier, A map of single-phase high-entropy alloys, Nature Communications 2023 14:1 14 (2023) 1–10. https://doi.org/10.1038/s41467-023-38423-7.

[9] D.A. Santana, K.R. Santos, C.S. Kiminami, F.G. Coury, Design, phase equilibria, and coarsening kinetics of a new γ/γ′ precipitation-hardened multi-principal element alloy, J Alloys Compd 882 (2021) 160729. https://doi.org/10.1016/J.JALLCOM.2021.160729.

[10] D. de Araujo Santana, C.S. Kiminami, F.G. Coury, Mechanical properties and yield strength modeling of a medium entropy alloy containing L12 precipitates, J Alloys Compd 898 (2022) 162923. https://doi.org/10.1016/J.JALLCOM.2021.162923.

[11] Y. Deng, C.C. Tasan, K.G. Pradeep, H. Springer, A. Kostka, D. Raabe, Design of a twinning-induced plasticity high entropy alloy, Acta Mater 94 (2015) 124–133. https://doi.org/10.1016/J.ACTAMAT.2015.04.014.

[12] Z. Li, K.G. Pradeep, Y. Deng, D. Raabe, C.C. Tasan, Metastable high-entropy dual-phase alloys overcome the strength–ductility trade-off, Nature 2016 534:7606 534 (2016) 227–230. https://doi.org/10.1038/nature17981.

[13] K. Liu, S.S. Nene, M. Frank, S. Sinha, R.S. Mishra, Extremely high fatigue resistance in an ultrafine grained high entropy alloy, Appl Mater Today 15 (2019) 525–530. https://doi.org/10.1016/J.APMT.2019.04.001.

[14] S.S. Nene, M. Frank, K. Liu, S. Sinha, R.S. Mishra, B.A. McWilliams, K.C. Cho, Corrosion-resistant high entropy alloy with high strength and ductility, Scr Mater 166 (2019) 168–172. https://doi.org/10.1016/j.scriptamat.2019.03.028.

[15] Z. Xu, H. Zhang, X. Du, Y. He, H. Luo, G. Song, L. Mao, T. Zhou, L. Wang, Corrosion resistance enhancement of CoCrFeMnNi high-entropy alloy fabricated by additive manufacturing, Corros Sci 177 (2020) 108954. https://doi.org/10.1016/J.CORSCI.2020.108954.

[16] K.R. Lim, K.S. Lee, J.S. Lee, J.Y. Kim, H.J. Chang, Y.S. Na, Dual-phase high-entropy alloys for high-temperature structural applications, J Alloys Compd 728 (2017) 1235–1238. https://doi.org/10.1016/J.JALLCOM.2017.09.089.

[17] N.D. Stepanov, D.G. Shaysultanov, N.Y. Yurchenko, S. V. Zherebtsov, A.N. Ladygin, G.A. Salishchev, M.A. Tikhonovsky, High temperature deformation behavior and dynamic recrystallization in CoCrFeNiMn high entropy alloy, Materials Science and Engineering: A 636 (2015) 188–195. https://doi.org/10.1016/J.MSEA.2015.03.097.

[18] Q. Lin, J. Liu, X. An, H. Wang, Y. Zhang, X. Liao, Cryogenic-deformation-induced phase transformation in an FeCoCrNi high-entropy alloy, Mater Res Lett 6 (2018) 236–243. https://doi.org/10.1080/21663831.2018.1434250.

[19] B. Gludovatz, A. Hohenwarter, D. Catoor, E.H. Chang, E.P. George, R.O. Ritchie, A fracture-resistant high-entropy alloy for cryogenic applications, Science (1979) 345 (2014) 1153–1158. https://doi.org/10.1126/SCIENCE.1254581/SUPPL_FILE/GLUDOVATZ.SM.PDF.

[20] T. Bhattacharjee, R. Zheng, Y. Chong, S. Sheikh, S. Guo, I.T. Clark, T. Okawa, I.S. Wani, P.P. Bhattacharjee, A. Shibata, N. Tsuji, Effect of low temperature on tensile properties of AlCoCrFeNi2.1 eutectic high entropy alloy, Mater Chem Phys 210 (2018) 207–212. https://doi.org/10.1016/J.MATCHEMPHYS.2017.06.023.

[21] A. V. Kuznetsov, D.G. Shaysultanov, N.D. Stepanov, G.A. Salishchev, O.N. Senkov, Tensile properties of an AlCrCuNiFeCo high-entropy alloy in as-cast and wrought

conditions, Materials Science and Engineering: A 533 (2012) 107–118. https://doi.org/10.1016/J.MSEA.2011.11.045.

[22] J. na Liu, Z. guo Xing, H. dou Wang, X. fang Cui, G. Jin, B. shi Xu, Microstructure and fatigue damage mechanism of FeCoNiAlTiZr high-entropy alloy film by nanoscale dynamic mechanical analysis, Vacuum 159 (2019) 516–523. https://doi.org/10.1016/J.VACUUM.2018.10.061.

[23] M.A. Hemphill, T. Yuan, G.Y. Wang, J.W. Yeh, C.W. Tsai, A. Chuang, P.K. Liaw, Fatigue behavior of Al0.5CoCrCuFeNi high entropy alloys, Acta Mater 60 (2012) 5723–5734. https://doi.org/10.1016/J.ACTAMAT.2012.06.046.

[24] J.G. Lopes, J.P. Oliveira, A Short Review on Welding and Joining of High Entropy Alloys, Metals (Basel) 10 (2020) 212. https://doi.org/10.3390/met10020212.

[25] J.G. Lopes, P. Agrawal, J. Shen, N. Schell, R.S. Mishra, J.P. Oliveira, Evolution of microstructure and mechanical properties in gas tungsten arc welded dual-phase Fe50Mn30Co10Cr10 high entropy alloy, Materials Science and Engineering: A 878 (2023) 145233. https://doi.org/10.1016/J.MSEA.2023.145233.

[26] J. Shen, R. Gonçalves, Y.T. Choi, J.G. Lopes, J. Yang, N. Schell, H.S. Kim, J.P. Oliveira, Microstructure and mechanical properties of gas metal arc welded CoCrFeMnNi joints using a 308 stainless steel filler metal, Scr Mater 222 (2023) 115053. https://doi.org/10.1016/J.SCRIPTAMAT.2022.115053.

[27] J. Shen, R. Gonçalves, Y.T. Choi, J.G. Lopes, J. Yang, N. Schell, H.S. Kim, J.P. Oliveira, Microstructure and mechanical properties of gas metal arc welded CoCrFeMnNi joints using a 410 stainless steel filler metal, Materials Science and Engineering: A 857 (2022) 144025. https://doi.org/10.1016/J.MSEA.2022.144025.

[28] J. Shen, P. Agrawal, T.A. Rodrigues, J.G. Lopes, N. Schell, Z. Zeng, R.S. Mishra, J.P. Oliveira, Gas tungsten arc welding of as-cast AlCoCrFeNi2.1 eutectic high entropy alloy, Mater Des 223 (2022) 111176. https://doi.org/10.1016/J.MATDES.2022.111176.

[29] J.P. Oliveira, T.M. Curado, Z. Zeng, J.G. Lopes, E. Rossinyol, J.M. Park, N. Schell, F.M. Braz Fernandes, H.S. Kim, Gas tungsten arc welding of as-rolled CrMnFeCoNi high entropy alloy, Mater Des 189 (2020). https://doi.org/10.1016/j.matdes.2020.108505.

[30] J.G. Lopes, P. Rocha, D.A. Santana, J. Shen, E. Maawad, N. Schell, F.G. Coury, J.P. Oliveira, Impact of Arc-Based Welding on the Microstructure Evolution and Mechanical Properties in Newly Developed Cr29.7Co29.7Ni35.4Al4Ti1.2 Multi-Principal Element Alloy, Adv Eng Mater 25 (2023) 2300109. https://doi.org/10.1002/ADEM.202300109.

[31] J. Shen, P. Agrawal, T.A. Rodrigues, J.G. Lopes, N. Schell, J. He, Z. Zeng, R.S. Mishra, J.P. Oliveira, Microstructure evolution and mechanical properties in a gas tungsten arc welded Fe42Mn28Co10Cr15Si5 metastable high entropy alloy, Materials Science and Engineering: A 867 (2023) 144722. https://doi.org/10.1016/J.MSEA.2023.144722.

[32] S. Kou, Welding Metallurgy, Welding Metallurgy (2002). https://doi.org/10.1002/0471434027.

[33] ISO 4063:2023 - Welding, brazing, soldering and cutting - Nomenclature of processes and reference numbers, (2023).

[34] J.P. Oliveira, T.G. Santos, R.M. Miranda, Revisiting fundamental welding concepts to improve additive manufacturing: From theory to practice, Prog Mater Sci 107 (2020) 100590. https://doi.org/10.1016/J.PMATSCI.2019.100590.

[35] R.E. Reed-hill, PHYSICAL METALLURGY PWS-KENT, (2015). https://archive.org/details/physicalmetallur0000reed (accessed February 27, 2023).

[36] Z. Li, C.C. Tasan, K.G. Pradeep, D. Raabe, A TRIP-assisted dual-phase high-entropy alloy: Grain size and phase fraction effects on deformation behavior, Acta Mater 131 (2017) 323–335. https://doi.org/10.1016/J.ACTAMAT.2017.03.069.

[37] Y. Lu, Y. Dong, S. Guo, L. Jiang, H. Kang, T. Wang, B. Wen, Z. Wang, J. Jie, Z. Cao, H. Ruan, T. Li, A Promising New Class of High-Temperature Alloys: Eutectic High-Entropy Alloys, Scientific Reports 2014 4:1 4 (2014) 1–5. https://doi.org/10.1038/srep06200.

[38] J. Zhu, S. Lu, Y. Jin, L. Xu, X. Xu, C. Yin, Y. Jia, High-Temperature Oxidation Behaviours of AlCoCrFeNi High-Entropy Alloy at 1073–1273 K, Oxidation of Metals 94 (2020) 265–281. https://doi.org/10.1007/S11085-020-09991-6/FIGURES/14.

[39] R. Gawel, Ł. Rogal, J. Dąbek, M. Wójcik-Bania, K. Przybylski, High temperature oxidation behaviour of non-equimolar AlCoCrFeNi high entropy alloys, Vacuum 184 (2021) 109969. https://doi.org/10.1016/J.VACUUM.2020.109969.

[40] D. Li, C. Li, T. Feng, Y. Zhang, G. Sha, J.J. Lewandowski, P.K. Liaw, Y. Zhang, High-entropy Al0.3CoCrFeNi alloy fibers with high tensile strength and ductility at ambient and cryogenic temperatures, Acta Mater 123 (2017) 285–294. https://doi.org/10.1016/J.ACTAMAT.2016.10.038.

[41] J.W. Qiao, S.G. Ma, E.W. Huang, C.P. Chuang, P.K. Liaw, Y. Zhang, Microstructural Characteristics and Mechanical Behaviors of AlCoCrFeNi High-Entropy Alloys at Ambient and Cryogenic Temperatures, Materials Science Forum 688 (2011) 419–425. https://doi.org/10.4028/WWW.SCIENTIFIC.NET/MSF.688.419.

[42] T. Wang, M. Komarasamy, S. Shukla, R.S. Mishra, Simultaneous enhancement of strength and ductility in an AlCoCrFeNi2.1 eutectic high-entropy alloy via friction stir processing, J Alloys Compd 766 (2018) 312–317. https://doi.org/10.1016/J.JALLCOM.2018.06.337.

[43] P. Li, H. Sun, S. Wang, X. Hao, H. Dong, Rotary friction welding of AlCoCrFeNi2.1 eutectic high entropy alloy, J Alloys Compd 814 (2020) 152322. https://doi.org/10.1016/J.JALLCOM.2019.152322.

[44] P. Li, S. Wang, Y. Xia, X. Hao, H. Dong, Diffusion bonding of AlCoCrFeNi2.1 eutectic high entropy alloy to TiAl alloy, J Mater Sci Technol 45 (2020) 59–69. https://doi.org/10.1016/J.JMST.2019.10.041.

[45] P. Li, H. Sun, S. Wang, Y. Xia, H. Dong, G. Wen, H. Zhang, Diffusion bonding of AlCoCrFeNi2.1 eutectic high entropy alloy to GH4169 superalloy, Materials Science and Engineering: A 793 (2020) 139843. https://doi.org/10.1016/J.MSEA.2020.139843.

[46] M. Zhang, D. Wang, L. He, X. Ye, W. Zhang, Laser beam welding of AlCoCrFeNi2.1 eutectic high-entropy alloy, Mater Lett 308 (2022) 131137. https://doi.org/10.1016/J.MATLET.2021.131137.

[47] Tazuddin, N.P. Gurao, K. Biswas, In the quest of single phase multi-component multiprincipal high entropy alloys, J Alloys Compd 697 (2017) 434–442. https://doi.org/10.1016/J.JALLCOM.2016.11.383.

[48] R. Sonkusare, P. Divya Janani, N.P. Gurao, S. Sarkar, S. Sen, K.G. Pradeep, K. Biswas, (K Biswas, Phase equilibria in equiatomic CoCuFeMnNi high entropy alloy, (2017). https://doi.org/10.1016/j.matchemphys.2017.08.051.

[49] S. Hun Shim, H. Pouraliakbar, S. Ig Hong, High strength dual fcc phase CoCuFeMnNi high-entropy alloy wires with dislocation wall boundaries stabilized by phase boundaries, (2021). https://doi.org/10.1016/j.msea.2021.141875.

[50] Y. Bin Kang, S. Hoon Shim, K. Ho Lee, S. Ig Hong, Dislocation creep behavior of CoCrFeMnNi high entropy alloy at intermediate temperatures, (2018). https://doi.org/10.1080/21663831.2018.1543731.

[51] Y.-G. Tong, N. Tian, H. Chen, X.-C. Zhang, Y.-L. Hu, X.-X. Ji, M.-J. Zhang, C.-J. Zhao, Real-time atomic deformation behavior of nano CoCrCuFeNi high-entropy alloy, Trans. Nonferrous Met. Soc. China 33 (2023) 1156–1163. https://doi.org/10.1016/S1003-6326(23)66172-2.

[52] S. Hun Shim, S. Min Oh, J. Lee, S.-K. Hong, S. Ig Hong, Nanoscale modulated structures by balanced distribution of atoms and mechanical/structural stabilities in CoCuFeMnNi high entropy alloys, (2019). https://doi.org/10.1016/j.msea.2019.138120.

[53] Y. Keun Kim, B. Ju Lee, S.-K. Hong, S. Ig Hong, Strengthening and fracture of deformation-processed dual fcc-phase CoCrFeCuNi and CoCrFeCu 1.71 Ni high entropy alloys, (2020). https://doi.org/10.1016/j.msea.2020.139241.

[54] Y. Keun Kim, S. Hun Shim, B. Ju Lee, S. Ig Hong, Correlation between mechanical properties and thermodynamic parameters of dual-fcc-phase CoCrFeCu x Ni (x = 1, 1.71) and CoCu 1.71 FeMnNi, (n.d.). https://doi.org/10.1016/j.matlet.2020.127866.

[55] J. Fiocchi, R. Casati, A. Tuissi, C.A. Biffi, Laser Beam Welding of CoCuFeMnNi High Entropy Alloy: Processing, Microstructure, and Mechanical Properties, Adv Eng Mater 24 (2022). https://doi.org/10.1002/ADEM.202200523.

[56] M.A. Karimi, M. Shamanian, M.H. Enayati, Microstructural and mechanical properties assessment of transient liquid phase bonding of CoCuFeMnNi high entropy alloy, Trans. Nonferrous Met. Soc. China 31 (2021) 3063–3074. https://doi.org/10.1016/S1003-6326(21)65715-1.

[57] D.A. Santana, K.R. Santos, C.S. Kiminami, F.G. Coury, Design, phase equilibria, and coarsening kinetics of a new γ/γ′ precipitation-hardened multi-principal element alloy, J Alloys Compd 882 (2021) 160729. https://doi.org/10.1016/J.JALLCOM.2021.160729.

[58] B. Cantor, I.T.H. Chang, P. Knight, A.J.B. Vincent, Microstructural development in equiatomic multicomponent alloys, Materials Science and Engineering A 375–377 (2004) 213–218. https://doi.org/10.1016/j.msea.2003.10.257.

[59] S. Gorsse, J.P. Couzinié, D.B. Miracle, From high-entropy alloys to complex concentrated alloys, C R Phys 19 (2018) 721–736. https://doi.org/10.1016/J.CRHY.2018.09.004.

[60] J.W. Yeh, S.J. Lin, Breakthrough applications of high-entropy materials, J Mater Res 33 (2018) 3129–3137. https://doi.org/10.1557/jmr.2018.283.

[61] H. Feng, H.B. Li, J. Dai, Y. Han, J.D. Qu, Z.H. Jiang, Y. Zhao, T. Zhang, Why CoCrFeMnNi HEA could not passivate in chloride solution? – A novel strategy to significantly improve corrosion resistance of CoCrFeMnNi HEA by N-alloying, Corros Sci 204 (2022) 110396. https://doi.org/10.1016/J.CORSCI.2022.110396.

[62] H. Luo, Z. Li, A.M. Mingers, D. Raabe, Corrosion behavior of an equiatomic CoCrFeMnNi high-entropy alloy compared with 304 stainless steel in sulfuric acid solution, Corros Sci 134 (2018) 131–139. https://doi.org/10.1016/J.CORSCI.2018.02.031.

[63] M. V. Klimova, A.O. Semenyuk, D.G. Shaysultanov, G.A. Salishchev, S. V. Zherebtsov, N.D. Stepanov, Effect of carbon on cryogenic tensile behavior of CoCrFeMnNi-type high entropy alloys, J Alloys Compd 811 (2019) 152000. https://doi.org/10.1016/J.JALLCOM.2019.152000.

[64] A.S. Tirunilai, T. Hanemann, C. Reinhart, V. Tschan, K.P. Weiss, G. Laplanche, J. Freudenberger, M. Heilmaier, A. Kauffmann, Comparison of cryogenic deformation of the concentrated solid solutions CoCrFeMnNi, CoCrNi and CoNi, Materials Science and Engineering: A 783 (2020) 139290. https://doi.org/10.1016/J.MSEA.2020.139290.

[65] H.G. Li, Y.J. Huang, W.J. Zhao, T. Chen, J.F. Sun, D.Q. Wei, Q. Du, Y.C. Zou, Y.Z. Lu, P. Zhu, X. Lu, A.H.W. Ngan, Overcoming the strength-ductility trade-off in an additively manufactured CoCrFeMnNi high entropy alloy via deep cryogenic treatment, Addit Manuf 50 (2022) 102546. https://doi.org/10.1016/J.ADDMA.2021.102546.

[66] S. Park, H. Nam, J. Park, Y. Na, H. Kim, N. Kang, Superior-tensile property of CoCrFeMnNi alloys achieved using friction-stir welding for cryogenic applications, (2020). https://doi.org/10.1016/j.msea.2020.139547.

[67] N.K. Adomako, G. Shin, N. Park, K. Park, J.H. Kim, Laser dissimilar welding of CoCrFeMnNi-high entropy alloy and duplex stainless steel, J Mater Sci Technol 85 (2021) 95–105. https://doi.org/10.1016/j.jmst.2021.02.003.

[68] H. Nam, S. Yoo, J. Won Ha, B.-J. Lee, S. Song, Y. Na, N. Kang, Enhancement of tensile properties of gas tungsten arc welds using Cu-coated CoCrFeMnNi filler and posteweld heat treatment, (2022). https://doi.org/10.1016/j.jmrt.2022.07.023.

[69] H. Nam, S. Park, N. Park, Y. Na, H. Kim, S.-J. Yoo, Y.-H. Moon, N. Kang, Weldability of cast CoCrFeMnNi high-entropy alloys using various filler metals for cryogenic applications, (2019). https://doi.org/10.1016/j.jallcom.2019.153278.

[70] H. Nam, S. Park, S.W. Kim, S.H. Shim, Y. Na, N. Kim, S. Song, S.I. Hong, N. Kang, Enhancement of tensile properties applying phase separation with Cu addition in gas tungsten arc welds of CoCrFeMnNi high entropy alloys, Scr Mater 220 (2022) 114897. https://doi.org/10.1016/J.SCRIPTAMAT.2022.114897.

[71] J. Kieffer, V. Valls, N. Blanc, C. Hennig, New tools for calibrating diffraction setups, Urn:Issn:1600-5775 27 (2020) 558–566. https://doi.org/10.1107/S1600577520000776.

[72] A.P. Hammersley, FIT2D: a multi-purpose data reduction, analysis and visualization program, Urn:Issn:1600-5767 49 (2016) 646–652. https://doi.org/10.1107/S1600576716000455.

[73] B.B. He, Two-Dimensional X-Ray Diffraction, Two-Dimensional X-Ray Diffraction (2009) 1–426. https://doi.org/10.1002/9780470502648.

[74] J. Shen, J.G. Lopes, Z. Zeng, Y.T. Choi, E. Maawad, N. Schell, H.S. Kim, R.S. Mishra, J.P. Oliveira, Deformation behavior and strengthening effects of an eutectic AlCoCrFeNi2.1 high entropy alloy probed by in-situ synchrotron X-ray diffraction and post-mortem EBSD, Materials Science and Engineering: A 872 (2023) 144946. https://doi.org/10.1016/J.MSEA.2023.144946.

[75] D. Hull, D.J. Bacon, Introduction to Dislocations, Fifth Edition, Introduction to Dislocations, Fifth Edition (2011) 1–257. https://doi.org/10.1016/C2009-0-64358-0.

[76] R. Verma, R. Jayaganthan, S.K. Nath, A. Srinivasan, Effect of multiaxial forging followed by hot rolling on non-basal planes and its influence on tensile and fracture toughness behaviour of Mg–4Zn–4Gd alloy, Materials Science and Engineering: A 774 (2020) 138890. https://doi.org/10.1016/J.MSEA.2019.138890.

[77] Y. Lin, B. Wu, S. Li, S. Mao, X. Liu, Y. Zhang, L. Wang, The quantitative relationship between microstructure and mechanical property of a melt spun Al–Mg alloy, Materials Science and Engineering: A 621 (2015) 212–217. https://doi.org/10.1016/J.MSEA.2014.10.047.

[78] J. Su, D. Raabe, Z. Li, Hierarchical microstructure design to tune the mechanical behavior of an interstitial TRIP-TWIP high-entropy alloy, Acta Mater 163 (2019) 40–54. https://doi.org/10.1016/J.ACTAMAT.2018.10.017.

[79] H.W. Deng, M.M. Wang, Z.M. Xie, T. Zhang, X.P. Wang, Q.F. Fang, Y. Xiong, Enhancement of strength and ductility in non-equiatomic CoCrNi medium-entropy alloy at room temperature via transformation-induced plasticity, Materials Science and Engineering: A 804 (2021) 140516. https://doi.org/10.1016/J.MSEA.2020.140516.

[80] M. Frank, S.S. Nene, Y. Chen, B. Gwalani, E.J. Kautz, A. Devaraj, K. An, R.S. Mishra, Correlating work hardening with co-activation of stacking fault strengthening and transformation in a high entropy alloy using in-situ neutron diffraction, Scientific Reports 2020 10:1 10 (2020) 1–10. https://doi.org/10.1038/s41598-020-79492-8.

[81] J. Zhang, Y. Xu, D. Han, Z. Tong, Improving yield strength and elongation combination by tailoring austenite characteristics and deformation mechanism in medium Mn steel, Scr Mater 218 (2022) 114790. https://doi.org/10.1016/J.SCRIPTAMAT.2022.114790.

[82] S. Basu, Z. Li, K.G. Pradeep, D. Raabe, Strain Rate Sensitivity of a TRIP-Assisted Dual-Phase High-Entropy Alloy, Front Mater 5 (2018) 30. https://doi.org/10.3389/fmats.2018.00030.

[83] Z.F. He, N. Jia, H.W. Wang, Y. Liu, D.Y. Li, Y.F. Shen, The effect of strain rate on mechanical properties and microstructure of a metastable FeMnCoCr high entropy alloy, Materials Science and Engineering: A 776 (2020) 138982. https://doi.org/10.1016/J.MSEA.2020.138982.

[84] S. Fu, H. Bei, Y. Chen, T.K. Liu, D. Yu, K. An, Deformation mechanisms and work-hardening behavior of transformation-induced plasticity high entropy alloys by in -situ neutron diffraction, Mater Res Lett 6 (2018) 620–626. https://doi.org/10.1080/21663831.2018.1523239.

[85] A.M. Hossain, N. Kumar, Microstructure and mechanical properties of a dual phase transformation induced plasticity Fe-Mn-Co-Cr high entropy alloy, J Alloys Compd 893 (2022) 162152. https://doi.org/10.1016/J.JALLCOM.2021.162152.

[86] S. Sinha, S.S. Nene, M. Frank, K. Liu, P. Agrawal, R.S. Mishra, On the evolving nature of c/a ratio in a hexagonal close-packed epsilon martensite phase in transformative high entropy alloys, Scientific Reports 2019 9:1 9 (2019) 1–14. https://doi.org/10.1038/s41598-019-49904-5.

[87] A.I. Saville, A. Creuziger, E.B. Mitchell, S.C. Vogel, J.T. Benzing, J. Klemm-Toole, K.D. Clarke, A.J. Clarke, MAUD Rietveld Refinement Software for Neutron Diffraction Texture Studies of Single- and Dual-Phase Materials, Integr Mater Manuf Innov 10 (2021) 461–487. https://doi.org/10.1007/s40192-021-00224-5.

[88] J. Shen, W. Zhang, J.G. Lopes, Y. Pei, Z. Zeng, E. Maawad, N. Schell, A.C. Baptista, R.S. Mishra, J.P. Oliveira, Evolution of microstructure and deformation mechanisms in a metastable Fe42Mn28Co10Cr15Si5 high entropy alloy: A combined in-situ synchrotron X-ray diffraction and EBSD analysis, Mater Des 238 (2024) 112662. https://doi.org/10.1016/j.matdes.2024.112662.

[89] N. Xu, S. Li, R. Li, M. Zhang, Z. Yan, Y. Cao, Z. Nie, Y. Ren, Y.D. Wang, In situ investigation of the deformation behaviors of Fe20Co30Cr25Ni25 and Fe20Co30Cr30Ni20 high entropy alloys by high-energy X-ray diffraction, Materials Science and Engineering: A 795 (2020) 139936. https://doi.org/10.1016/J.MSEA.2020.139936.

[90] T. Shintani, Y. Murata, Evaluation of the dislocation density and dislocation character in cold rolled Type 304 steel determined by profile analysis of X-ray diffraction, Acta Mater 59 (2011) 4314–4322. https://doi.org/10.1016/J.ACTAMAT.2011.03.055.

[91] Z. Nishiyama, M.E. Fine, M. Meshii, C.M. Wayman, Martensitic transformation, Academic Press, 1978.

[92] M. Saboktakin Rizi, H. Minouei, B.J. Lee, M.R. Toroghinejad, S.I. Hong, Effects of carbon and molybdenum on the nanostructural evolution and strength/ductility trade-off in Fe40Mn40Co10Cr10 high-entropy alloys, J Alloys Compd 911 (2022) 165108. https://doi.org/10.1016/J.JALLCOM.2022.165108.

[93] Y. Liu, J. Tu, L. Deng, C. hao Wang, Z. ming Zhou, Z. tao Jiang, J. ru Luo, Characteristics of thermal- and strain-induced ε-martensite in Fe50Mn30Co10Cr10 multi-component alloy: Effect of grain size, Mater Charact 171 (2021) 110817. https://doi.org/10.1016/J.MATCHAR.2020.110817.

[94] Z. Li, K.G. Pradeep, Y. Deng, D. Raabe, C.C. Tasan, Metastable high-entropy dual-phase alloys overcome the strength–ductility trade-off, Nature 2016 534:7606 534 (2016) 227–230. https://doi.org/10.1038/nature17981.

[95] P. Erdely, P. Staron, E. Maawad, N. Schell, H. Clemens, S. Mayer, Lattice and phase strain evolution during tensile loading of an intermetallic, multi-phase γ-TiAl based alloy, Acta Mater 158 (2018) 193–205. https://doi.org/10.1016/J.ACTAMAT.2018.07.062.

[96] Y. Bu, Z. Li, J. Liu, H. Wang, D. Raabe, W. Yang, Nonbasal Slip Systems Enable a Strong and Ductile Hexagonal-Close-Packed High-Entropy Phase, Phys Rev Lett 122 (2019) 075502. https://doi.org/10.1103/PHYSREVLETT.122.075502.

[97] F. Mokdad, D.L. Chen, D.Y. Li, Twin-twin interactions and contraction twin formation in an extruded magnesium alloy subjected to an alteration of compressive direction, J Alloys Compd 737 (2018) 549–560. https://doi.org/10.1016/J.JALLCOM.2017.12.043.

[98] Y. Liu, J. Tu, L. Deng, C. hao Wang, Z. ming Zhou, Z. tao Jiang, J. ru Luo, Characteristics of thermal- and strain-induced ε-martensite in Fe50Mn30Co10Cr10 multi-component alloy: Effect of grain size, Mater Charact 171 (2021) 110817. https://doi.org/10.1016/J.MATCHAR.2020.110817.

[99] A.M. Hossain, N. Kumar, Microstructure and mechanical properties of a dual phase transformation induced plasticity Fe-Mn-Co-Cr high entropy alloy, J Alloys Compd 893 (2022) 162152. https://doi.org/10.1016/J.JALLCOM.2021.162152.

[100] Y. Liu, J. Tu, L. Deng, C. hao Wang, Z. ming Zhou, Z. tao Jiang, J. ru Luo, Characteristics of thermal- and strain-induced ε-martensite in Fe50Mn30Co10Cr10 multi-component alloy: Effect of grain size, Mater Charact 171 (2021) 110817. https://doi.org/10.1016/J.MATCHAR.2020.110817.

[101] S.I. Wright, M.M. Nowell, D.P. Field, A Review of Strain Analysis Using Electron Backscatter Diffraction, Microscopy and Microanalysis 17 (2011) 316–329. https://doi.org/10.1017/S1431927611000055.

[102] S.S. Rui, Q.N. Han, X. Wang, S. Li, X. Ma, Y. Su, Z. Cai, D. Du, H.J. Shi, Correlations between two EBSD-based metrics Kernel Average Misorientation and Image Quality on indicating dislocations of near-failure low alloy steels induced by tensile and cyclic deformations, Mater Today Commun 27 (2021) 102445. https://doi.org/10.1016/J.MTCOMM.2021.102445.

[103] J.P. Oliveira, T.M. Curado, Z. Zeng, J.G. Lopes, E. Rossinyol, J.M. Park, N. Schell, F.M.B. Fernandes, H.S. Kim, Gas tungsten arc welding of as-rolled CrMnFeCoNi high entropy alloy, Mater Des 189 (2020) 108505. https://doi.org/10.1016/j.matdes.2020.108505.

[104] J. Shen, J.G. Lopes, Z. Zeng, Y.T. Choi, E. Maawad, N. Schell, H.S. Kim, R.S. Mishra, J.P. Oliveira, Deformation behavior and strengthening effects of an eutectic AlCoCrFeNi2.1 high entropy alloy probed by in-situ synchrotron X-ray diffraction and post-mortem EBSD, Materials Science and Engineering: A 872 (2023) 144946. https://doi.org/10.1016/J.MSEA.2023.144946.

[105] Y. Zhao, J. Zhang, Microstrain and grain-size analysis from diffraction peak width and graphical derivation of high-pressure thermomechanics, Urn:Issn:0021-8898 41 (2008) 1095–1108. https://doi.org/10.1107/S0021889808031762.

[106] B. Bocklund, L.D. Bobbio, R.A. Otis, A.M. Beese, Z.K. Liu, Experimental validation of Scheil–Gulliver simulations for gradient path planning in additively manufactured functionally graded materials, Materialia (Oxf) 11 (2020) 100689. https://doi.org/10.1016/J.MTLA.2020.100689.

[107] A. Röttger, J. Boes, F. Großwendt, S. Weber, Description of a new concept for the development of adapted hot-work tool steels for laser-powder bed fusion, Addit Manuf 61 (2023) 103292. https://doi.org/10.1016/J.ADDMA.2022.103292.

[108] M. v. Klimova, D.G. Shaysultanov, S. v. Zherebtsov, N.D. Stepanov, Effect of second phase particles on mechanical properties and grain growth in a CoCrFeMnNi high entropy alloy, Materials Science and Engineering: A 748 (2019) 228–235. https://doi.org/10.1016/J.MSEA.2019.01.112.

[109] A.M. Hossain, N. Kumar, Microstructure and mechanical properties of a dual phase transformation induced plasticity Fe-Mn-Co-Cr high entropy alloy, J Alloys Compd 893 (2022) 162152. https://doi.org/10.1016/J.JALLCOM.2021.162152.

[110] Y.N. Hu, S.C. Wu, L. Chen, Review on failure behaviors of fusion welded high-strength Al alloys due to fine equiaxed zone, Eng Fract Mech 208 (2019) 45–71. https://doi.org/10.1016/J.ENGFRACMECH.2019.01.013.

[111] Y. Shao, X. Li, L. Chen, E. He, New insights into fine equiaxed zone of laser-welded 2A97 Al-Li alloy, J Alloys Compd 895 (2022) 162717. https://doi.org/10.1016/J.JALLCOM.2021.162717.

[112] K. Rajasekhar, C.S. Harendranath, R. Raman, S.D. Kulkarni, Microstructural evolution during solidification of austenitic stainless steel weld metals: A color metallographic and electron microprobe analysis study, Mater Charact 38 (1997) 53–65. https://doi.org/10.1016/S1044-5803(97)80024-1.

[113] H. Peng, Y. Wen, Y. Du, J. Chen, Q. Yang, A new set of Creq and Nieq equations for predicting solidification modes of cast austenitic Fe-Mn-Si-Cr-Ni shape memory alloys, Metallurgical and Materials Transactions B: Process Metallurgy and Materials Processing Science 45 (2014) 6–11. https://doi.org/10.1007/S11663-013-0005-8.

[114] V. Fuster, A. V. Druker, A. Baruj, J. Malarría, R. Bolmaro, Characterization of phases in an Fe–Mn–Si–Cr–Ni shape memory alloy processed by different thermomechanical methods, Mater Charact 109 (2015) 128–137. https://doi.org/10.1016/J.MATCHAR.2015.09.026.

[115] A. Druker, P. La Roca, P. Vermaut, P. Ochin, J. Malarría, Microstructure and shape memory properties of Fe–15Mn–5Si–9Cr–5Ni melt-spun ribbons, Materials Science and Engineering: A 556 (2012) 936–945. https://doi.org/10.1016/J.MSEA.2012.07.097.

[116] B.C. Maji, M. Krishnan, A. Verma, R. Basu, I. Samajdar, R.K. Ray, Effect of Pre-straining on the Shape Recovery of Fe-Mn-Si-Cr-Ni Shape Memory Alloys, Metall Mater Trans A Phys Metall Mater Sci 46 (2015) 639–655. https://doi.org/10.1007/S11661-014-2645-Y.

[117] T. Kirindi, E. Güler, M. Dikici, Effects of homogenization time on the both martensitic transformations and mechanical properties of Fe–Mn–Si–Cr–Ni shape memory alloy, J Alloys Compd 433 (2007) 202–206. https://doi.org/10.1016/J.JALLCOM.2006.06.091.

[118] B.C. Maji, M. Krishnan, Gouthama, R.K. Ray, Role of Si in improving the shape recovery of FeMnSiCrNi shape memory alloys, Metall Mater Trans A Phys Metall Mater Sci 42 (2011) 2153–2165. https://doi.org/10.1007/S11661-011-0651-X.

[119] B.C. Maji, M. Krishnan, Effect of copper addition on the microstructure and shape recovery of Fe–Mn–Si–Cr–Ni shape memory alloys, Materials Science and Engineering: A 570 (2013) 13–26. https://doi.org/10.1016/J.MSEA.2013.01.061.

[120] F. Malamud, L.M. Guerrero, P. La Roca, M. Sade, A. Baruj, Role of Mn and Cr on structural parameters and strain energy during FCC-HCP martensitic transformation in Fe-

Mn-Cr shape memory alloys, Mater Des 139 (2018) 314–323. https://doi.org/10.1016/J.MATDES.2017.11.017.

[121] B.C. Maji, M. Krishnan, The effect of microstructure on the shape recovery of a Fe–Mn–Si–Cr–Ni stainless steel shape memory alloy, Scr Mater 48 (2003) 71–77. https://doi.org/10.1016/S1359-6462(02)00348-2.

[122] A. Cladera, B. Weber, C. Leinenbach, C. Czaderski, M. Shahverdi, M. Motavalli, Iron-based shape memory alloys for civil engineering structures: An overview, Constr Build Mater 63 (2014) 281–293. https://doi.org/10.1016/J.CONBUILDMAT.2014.04.032.

[123] M.M. Pan, X.M. Zhang, D. Zhou, R.D.K. Misra, P. Chen, Fe–Mn–Si–Cr–Ni based shape memory alloy: Thermal and stress-induced martensite, Materials Science and Engineering: A 797 (2020) 140107. https://doi.org/10.1016/J.MSEA.2020.140107.

[124] W.Y. Jang, Q. Gu, J. Van Humbeeck, L. Delaey, Microscopic observation of γ-phase and ε- and α′-martensite in Fe□Mn□Si-based shape memory alloys, Mater Charact 34 (1995) 67–72. https://doi.org/https://doi.org/10.1016/1044-5803(94)00054-O.

[125] H. Khodaverdi, M. Mohri, E. Ghafoori, A.S. Ghorabaei, M. Nili-Ahmadabadi, Enhanced pseudoelasticity of an Fe–Mn–Si-based shape memory alloy by applying microstructural engineering through recrystallization and precipitation, Journal of Materials Research and Technology 21 (2022) 2999–3013. https://doi.org/10.1016/J.JMRT.2022.10.092.

[126] M. Mohri, I. Ferretto, C. Leinenbach, D. Kim, D.G. Lignos, E. Ghafoori, Effect of thermo-mechanical treatment and microstructure on pseudo-elastic behavior of Fe–Mn–Si–Cr–Ni-(V, C) shape memory alloy, Materials Science and Engineering: A 855 (2022) 143917. https://doi.org/10.1016/J.MSEA.2022.143917.

[127] C. Song, H. Yu, J. Lu, T. Zhou, S. Yang, Stress partitioning among ferrite, martensite and retained austenite of a TRIP-assisted multiphase steel: An in-situ high-energy X-ray diffraction study, Materials Science and Engineering: A 726 (2018) 1–9. https://doi.org/10.1016/J.MSEA.2018.04.066.

[128] H.J. Flitt, D.P. Schweinsberg, Evaluation of corrosion rate from polarisation curves not exhibiting a Tafel region, Corros Sci 47 (2005) 3034–3052. https://doi.org/10.1016/J.CORSCI.2005.06.014.

[129] I. Barauskienė, G. Laukaitis, E. Valatka, Stainless steel as an electrocatalyst for overall water splitting under alkaline and neutral conditions, Journal of Electroanalytical Chemistry 950 (2023) 117880. https://doi.org/10.1016/J.JELECHEM.2023.117880.

[130] E. Ghafoori, E. Hosseini, C. Leinenbach, J. Michels, M. Motavalli, Fatigue behavior of a Fe-Mn-Si shape memory alloy used for prestressed strengthening, Mater Des 133 (2017) 349–362. https://doi.org/10.1016/J.MATDES.2017.07.055.

[131] D.I.H. Rosa, A. Hartloper, A. de Castro e Sousa, D.G. Lignos, M. Motavalli, E. Ghafoori, Experimental behavior of iron-based shape memory alloys under cyclic loading histories, Constr Build Mater 272 (2021) 121712. https://doi.org/10.1016/J.CONBUILDMAT.2020.121712.

[132] X.-L. Gu, Z.-Y. Chen, Q.-Q. Yu, E. Ghafoori, Stress recovery behavior of an Fe-Mn-Si shape memory alloy, (2021). https://doi.org/10.1016/j.engstruct.2021.112710.

[133] M. Koster, W.J. Lee, M. Schwarzenberger, C. Leinenbach, Cyclic deformation and structural fatigue behavior of an FE–Mn–Si shape memory alloy, Materials Science and Engineering: A 637 (2015) 29–39. https://doi.org/10.1016/J.MSEA.2015.04.028.

[134] S.K. Paul, A critical review of experimental aspects in ratcheting fatigue: microstructure to specimen to component, Journal of Materials Research and Technology 8 (2019) 4894–4914. https://doi.org/10.1016/J.JMRT.2019.06.014.

[135] J.G. Lopes, D. Martins, K. Zhang, B. Li, B. Wang, X. Wang, N. Schell, E. Ghafoori, A.C. Baptista, J.P. Oliveira, Unveiling the microstructure evolution and mechanical properties in a gas tungsten arc-welded Fe–Mn–Si–Cr–Ni shape memory alloy, Journal of Materials Science 2024 (2024) 1–22. https://doi.org/10.1007/S10853-024-09606-4.

[136] J.G. Lopes, J. Shen, E. Maawad, P. Agrawal, N. Schell, R.S. Mishra, J.P. Oliveira, Time-resolved evolution of the deformation mechanisms in a TRIP/TWIP Fe50Mn30Co10Cr10 high entropy during tensile loading probed with synchrotron X-ray diffraction, Int J Plast 179 (2024) 104048. https://doi.org/10.1016/J.IJPLAS.2024.104048.

[137] Y.L. Krutskii, T.S. Gudyma, I.D. Kuchumova, R.R. Khabirov, K.A. Antropova, Carbides of Transition Metals: Properties, Application and Production. Review. Part 1. Titanium and Vanadium Carbides, Steel in Translation 52 (2022) 465–478. https://doi.org/10.3103/S0967091222050059/TABLES/1.

[138] E.K. Storms, R.J. McNeal, The vanadium-vanadium carbide system, Journal of Physical Chemistry 66 (1962) 1401–1408. https://doi.org/10.1021/J100814A007/ASSET/J100814A007.FP.PNG_V03.

[139] T.S.R.C. Murthy, J.K. Sonber, C. Subramanian, R.K. Fotedar, M.R. Gonal, A.K. Suri, Effect of CrB2 addition on densification, properties and oxidation resistance of TiB2, Int J Refract Metals Hard Mater 27 (2009) 976–984. https://doi.org/10.1016/J.IJRMHM.2009.06.004.

[140] B.R. Golla, T. Bhandari, A. Mukhopadhyay, B. Basu, Titanium Diboride, Ultra-High Temperature Ceramics: Materials for Extreme Environment Applications 9781118700785 (2014) 316–360. https://doi.org/10.1002/9781118700853.CH13.

[141] J. Shen, P. Agrawal, T.A. Rodrigues, J.G. Lopes, N. Schell, Z. Zeng, R.S. Mishra, J.P. Oliveira, Gas tungsten arc welding of as-cast AlCoCrFeNi2.1 eutectic high entropy alloy, Mater Des 223 (2022) 111176. https://doi.org/10.1016/J.MATDES.2022.111176.

[142] J. Miao, H. Yao, J. Wang, Y. Lu, T. Wang, T. Li, Surface modification for AlCoCrFeNi2.1 eutectic high-entropy alloy via laser remelting technology and subsequent aging heat treatment, J Alloys Compd 894 (2022) 162380. https://doi.org/10.1016/J.JALLCOM.2021.162380.

[143] A. Lozinko, O. V. Mishin, T. Yu, U. Klement, S. Guo, Y. Zhang, Quantification of microstructure in a eutectic high entropy alloy AlCoCrFeNi2.1, IOP Conf Ser Mater Sci Eng 580 (2019) 012039. https://doi.org/10.1088/1757-899X/580/1/012039.

[144] I.S. Wani, T. Bhattacharjee, S. Sheikh, P.P. Bhattacharjee, S. Guo, N. Tsuji, Tailoring nanostructures and mechanical properties of AlCoCrFeNi2.1 eutectic high entropy alloy using thermo-mechanical processing, Materials Science and Engineering: A 675 (2016) 99–109. https://doi.org/10.1016/J.MSEA.2016.08.048.

[145] D. Choudhuri, S. Shukla, P.A. Jannotti, S. Muskeri, S. Mukherjee, J.T. Lloyd, R.S. Mishra, Characterization of as-cast microstructural heterogeneities and damage mechanisms in eutectic AlCoCrFeNi2.1 high entropy alloy, Mater Charact 158 (2019) 109955. https://doi.org/10.1016/J.MATCHAR.2019.109955.

[146] C.C. Tung, J.W. Yeh, T. tsung Shun, S.K. Chen, Y.S. Huang, H.C. Chen, On the elemental effect of AlCoCrCuFeNi high-entropy alloy system, Mater Lett 61 (2007) 1–5. https://doi.org/10.1016/J.MATLET.2006.03.140.

[147] Y.N. Hu, S.C. Wu, L. Chen, Review on failure behaviors of fusion welded high-strength Al alloys due to fine equiaxed zone, Eng Fract Mech 208 (2019) 45–71. https://doi.org/10.1016/J.ENGFRACMECH.2019.01.013.

[148] I. Cazic, J. Zollinger, S. Mathieu, M. El Kandaoui, P. Plapper, B. Appolaire, New insights into the origin of fine equiaxed microstructures in additively manufactured Inconel 718, Scr Mater 195 (2021) 113740. https://doi.org/10.1016/J.SCRIPTAMAT.2021.113740.

[149] L. Liu, T. Minasyan, R. Ivanov, S. Aydinyan, I. Hussainova, Selective laser melting of TiB2-Ti composite with high content of ceramic phase, Ceram Int 46 (2020) 21128–21135. https://doi.org/10.1016/J.CERAMINT.2020.05.189.

[150] J. Haidar, A theoretical model for gas metal arc welding and gas tungsten arc welding. I., J Appl Phys 84 (1998) 3518–3529. https://doi.org/10.1063/1.368527.

[151] J. Miao, H. Yao, J. Wang, Y. Lu, T. Wang, T. Li, Surface modification for AlCoCrFeNi 2.1 eutectic high-entropy alloy via laser remelting technology and subsequent aging heat treatment, (2021). https://doi.org/10.1016/j.jallcom.2021.162380.

[152] X.J. Wang, M. Xu, N. Liu, L.X. Liu, The formation of sigma phase in the CoCrFeNi high-entropy alloys, Mater Res Express 8 (2021) 76514. https://doi.org/10.1088/2053-1591/ac0a5c.

[153] K. Kishore, S. Kushwaha, K. Sai, P. Teja, A.K. Chandan, M. Mukherjee, M. Adhikary, A. Kumar, Sigma phase embrittlement-induced failures of heat-resistant stainless steel traveling grate links, Eng Fail Anal 144 (2023) 106979. https://doi.org/10.1016/j.engfailanal.2022.106979.

[154] J.G. Lopes, J.P. Oliveira, A short review on welding and joining of high entropy alloys, Metals (Basel) 10 (2020) 212. https://doi.org/10.3390/met10020212.

[155] J.G. Lopes, A. Candeias, P. Agrawal, J. Shen, N. Schell, R.S. Mishra, J.P. Oliveira, Role of TiB2 inoculation particles during welding of a AlCoCrFeNi high entropy alloy, J Alloys Compd 995 (2024) 174694. https://doi.org/10.1016/J.JALLCOM.2024.174694.

[156] W. Kurz, D. Fisher, Fundamentals of Solidification, 1998.

[157] J.P. Oliveira, A. Shamsolhodaei, J. Shen, J.G. Lopes, R.M. Gonçalves, M. de Brito Ferraz, L. Piçarra, Z. Zeng, N. Schell, N. Zhou, H. Seop Kim, Improving the ductility in laser welded joints of CoCrFeMnNi high entropy alloy to 316 stainless steel, Mater Des 219 (2022) 110717. https://doi.org/10.1016/J.MATDES.2022.110717.

[158] D. Choudhuri, S. Shukla, P.A. Jannotti, S. Muskeri, S. Mukherjee, J.T. Lloyd, R.S. Mishra, Characterization of as-cast microstructural heterogeneities and damage mechanisms in eutectic AlCoCrFeNi2.1 high entropy alloy, Mater Charact 158 (2019) 109955. https://doi.org/10.1016/J.MATCHAR.2019.109955.

[159] T. Xiong, S. Zheng, J. Pang, X. Ma, High-strength and high-ductility AlCoCrFeNi2.1 eutectic high-entropy alloy achieved via precipitation strengthening in a heterogeneous structure, Scr Mater 186 (2020) 336–340. https://doi.org/10.1016/J.SCRIPTAMAT.2020.04.035.

[160] B.E. Macdonald, Z. Fu, X. Wang, Z. Li, W. Chen, Y. Zhou, D. Raabe, J. Schoenung, H. Hahn, E.J. Lavernia, Influence of phase decomposition on mechanical behavior of an equiatomic CoCuFeMnNi high entropy alloy, Acta Mater 181 (2019) 25–35. https://doi.org/10.1016/j.actamat.2019.09.030.

[161] S.H. Shim, H. Pouraliakbar, H. Minouei, M.S. Rizi, V. Fallah, Y.-S. Na, H. Han, S.I. Hong, Characterization of the microscale/nanoscale hierarchical microstructure of an as-cast CrMnFeNiCu high-entropy alloy with promising mechanical properties, (2023). https://doi.org/10.1016/j.jallcom.2023.170091.

[162] S. Singh, C. Srivastava, Effect of carbon nanotube incorporation on the evolution of morphology, phase and compositional homogeneity, surface oxide chemistry and corrosion behaviour of electrodeposited FeCuMnNiCo-carbon nanotube composite coatings, Electrochim Acta 439 (2023) 141639. https://doi.org/10.1016/J.ELECTACTA.2022.141639.

[163] S. Mahajan, C.S. Pande, M.A. Imam, B.B. Rath, Formation of annealing twins in f.c.c. crystals, Acta Mater 45 (1997) 2633–2638. https://doi.org/10.1016/S1359-6454(96)00336-9.

[164] D.P. Field, L.T. Bradford, M.M. Nowell, T.M. Lillo, The role of annealing twins during recrystallization of Cu, Acta Mater 55 (2007) 4233–4241. https://doi.org/10.1016/J.ACTAMAT.2007.03.021.

[165] S.K. Michelic, D. Loder, T. Reip, A.A. Barani, C. Bernhard, Characterization of TiN, TiC and Ti(C,N) in titanium-alloyed ferritic chromium steels focusing on the significance of different particle morphologies, Mater Charact 100 (2015) 61–67. https://doi.org/10.1016/J.MATCHAR.2014.12.014.

[166] Y. Hou, G. Cheng, K. Kadoi, H. Inoue, Acceleration mechanism of Ti2O3 on TiN formation and δ-ferrite nucleation of ferritic stainless steel, J Alloys Compd 912 (2022) 165221. https://doi.org/10.1016/J.JALLCOM.2022.165221.

[167] P.C. Gasson, The Superalloys: Fundamentals and Applications R. C. Reed Cambridge University Press, The Edinburgh Building, Shaftesbury Road, Cambridge, CB2 2RU, UK, 2006. 372pp. Illustrated. £80. ISBN 0-521-85904-2., The Aeronautical Journal 112 (2008) 291–291. https://doi.org/10.1017/S0001924000087509.

[168] O.G. Rivera, P.G. Allison, J.B. Jordon, O.L. Rodriguez, L.N. Brewer, Z. McClelland, W.R. Whittington, D. Francis, J. Su, R.L. Martens, N. Hardwick, Microstructures and mechanical behavior of Inconel 625 fabricated by solid-state additive manufacturing, Materials Science and Engineering: A 694 (2017) 1–9. https://doi.org/10.1016/J.MSEA.2017.03.105.

[169] Y. Hu, S. Wu, Y. Guo, Z. Shen, A.M. Korsunsky, Y. Yu, X. Zhang, Y. Fu, Z. Che, T. Xiao, S. Lozano-Perez, Q. Yuan, X. Zhong, X. Zeng, G. Kang, P.J. Withers, Inhibiting weld cracking

in high-strength aluminium alloys, Nature Communications 2022 13:1 13 (2022) 1–9. https://doi.org/10.1038/s41467-022-33188-x.

[170] S. Eshkabilov, I. Ara, I. Sevostianov, F. Azarmi, X. Tangpong, Mechanical and thermal properties of stainless steel parts, manufactured by various technologies, in relation to their microstructure, Int J Eng Sci 159 (2021) 103398. https://doi.org/10.1016/J.IJENGSCI.2020.103398.

[171] B. Bocklund, L.D. Bobbio, R.A. Otis, A.M. Beese, Z.K. Liu, Experimental validation of Scheil–Gulliver simulations for gradient path planning in additively manufactured functionally graded materials, Materialia (Oxf) 11 (2020) 100689. https://doi.org/10.1016/J.MTLA.2020.100689.

[172] T. Keller, G. Lindwall, S. Ghosh, L. Ma, B.M. Lane, F. Zhang, U.R. Kattner, E.A. Lass, J.C. Heigel, Y. Idell, M.E. Williams, A.J. Allen, J.E. Guyer, L.E. Levine, Application of finite element, phase-field, and CALPHAD-based methods to additive manufacturing of Ni-based superalloys, Acta Mater 139 (2017) 244–253. https://doi.org/10.1016/J.ACTAMAT.2017.05.003.

[173] J.P. Oliveira, T.G. Santos, R.M. Miranda, Revisiting fundamental welding concepts to improve additive manufacturing: From theory to practice, Prog Mater Sci 107 (2020) 100590. https://doi.org/10.1016/j.pmatsci.2019.100590.

[174] D.A. Porter, K.E. Easterling, M.Y. Sherif, Phase transformations in metals and alloys., (n.d.) 520.

[175] J. Shen, R. Gonçalves, Y.T. Choi, J.G. Lopes, J. Yang, N. Schell, H.S. Kim, J.P. Oliveira, Microstructure and mechanical properties of gas metal arc welded CoCrFeMnNi joints using a 308 stainless steel filler metal, Scr Mater 222 (2023) 115053. https://doi.org/10.1016/J.SCRIPTAMAT.2022.115053.

[176] Z. Wu, S.A. David, D.N. Leonard, Z. Feng, H. Bei, Microstructures and mechanical properties of a welded CoCrFeMnNi high-entropy alloy, Https://Doi.Org/10.1080/13621718.2018.1430114 23 (2018) 585–595. https://doi.org/10.1080/13621718.2018.1430114.

[177] P.K. Shen, H.C. Liu, C.Y. Huang, H.W. Yen, J.W. Yeh, C.W. Tsai, Microstructure and mechanical properties of medium-entropy alloys with a high-density η-D024 phase, Mater Charact 185 (2022) 111713. https://doi.org/10.1016/J.MATCHAR.2021.111713.

[178] N. Huber, J. Heerens, On the effect of a general residual stress state on indentation and hardness testing, Acta Mater 56 (2008) 6205–6213. https://doi.org/10.1016/J.ACTAMAT.2008.08.029.

[179] J. Kieffer, V. Valls, N. Blanc, C. Hennig, New tools for calibrating diffraction setups, Urn:Issn:1600-5775 27 (2020) 558–566. https://doi.org/10.1107/S1600577520000776.

[180] J.G. Lopes, P. Rocha, D.A. Santana, J. Shen, E. Maawad, N. Schell, F.G. Coury, J.P. Oliveira, Impact of Arc-Based Welding on the Microstructure Evolution and Mechanical Properties in Newly Developed Cr29.7Co29.7Ni35.4Al4Ti1.2 Multi-Principal Element Alloy, Adv Eng Mater (2023) 2300109. https://doi.org/10.1002/ADEM.202300109.

[181] F. Otto, A. Dlouhý, C. Somsen, H. Bei, G. Eggeler, E.P. George, The influences of temperature and microstructure on the tensile properties of a CoCrFeMnNi high-entropy alloy, Acta Mater 61 (2013) 5743–5755. https://doi.org/10.1016/J.ACTAMAT.2013.06.018.

[182] I. Baker, B. Cantor, J.-W. Yeh, High Entropy Alloys and Materials, High Entropy Alloys & Materials 2023 1 (2023) 1–3. https://doi.org/10.1007/S44210-023-00019-7.

[183] J.W. Yeh, S.K. Chen, S.J. Lin, J.Y. Gan, T.S. Chin, T.T. Shun, C.H. Tsau, S.Y. Chang, Nanostructured High-Entropy Alloys with Multiple Principal Elements: Novel Alloy Design Concepts and Outcomes, Adv Eng Mater 6 (2004) 299–303. https://doi.org/10.1002/ADEM.200300567.

[184] Z. Han, W. Ren, J. Yang, Y. Du, R. Wei, C. Zhang, Y. Chen, G. Zhang, The deformation behavior and strain rate sensitivity of ultra-fine grained CoNiFeCrMn high-entropy alloys at temperatures ranging from 77 K to 573 K, J Alloys Compd 791 (2019) 962–970. https://doi.org/10.1016/J.JALLCOM.2019.03.373.

[185] J. Joseph, N. Haghdadi, M. Annasamy, S. Kada, P.D. Hodgson, M.R. Barnett, D.M. Fabijanic, On the enhanced wear resistance of CoCrFeMnNi high entropy alloy at intermediate temperature, Scr Mater 186 (2020) 230–235. https://doi.org/10.1016/J.SCRIPTAMAT.2020.05.053.

[186] H. Thota, R. Jeyaraam, L.R. Bairi, A.S. Tirunilai, A. Kauffmann, J. Freudenberger, M. Heilmaier, S. Mandal, S.S. Vadlamani, Grain boundary engineering and its implications on corrosion behavior of equiatomic CoCrFeMnNi high entropy alloy, J Alloys Compd 888 (2021) 161500. https://doi.org/10.1016/J.JALLCOM.2021.161500.

[187] A. Hamada, S. Ghosh, M. Ali, M. Jaskari, A. Järvenpää, Studying the strengthening mechanisms and mechanical properties of dissimilar laser-welded butt joints of medium-Mn stainless steel and automotive high-strength carbon steel, Materials Science and Engineering: A 856 (2022) 143936. https://doi.org/10.1016/J.MSEA.2022.143936.

[188] Z. Wu, S.A. David, D.N. Leonard, Z. Feng, H. Bei, Microstructures and mechanical properties of a welded CoCrFeMnNi high-entropy alloy, Science and Technology of Welding and Joining 23 (2018) 585–595. https://doi.org/10.1080/13621718.2018.1430114.

[189] J.Y. Lin, Z.H. Lai, T. Otsuki, H.W. Yen, S. Nambu, Gradient microstructure and interfacial strength of CoCrFeMnNi high-entropy alloy in solid-state ultrasonic welding, Materials Science and Engineering: A 825 (2021) 141885. https://doi.org/10.1016/J.MSEA.2021.141885.

[190] R. Li, P. Niu, T. Yuan, P. Cao, C. Chen, K. Zhou, Selective laser melting of an equiatomic CoCrFeMnNi high-entropy alloy: Processability, non-equilibrium microstructure and mechanical property, J Alloys Compd 746 (2018) 125–134. https://doi.org/10.1016/J.JALLCOM.2018.02.298.

[191] S. Park, H. Nam, J. Park, Y. Na, H. Kim, N. Kang, Superior-tensile property of CoCrFeMnNi alloys achieved using friction-stir welding for cryogenic applications, Materials Science and Engineering: A 788 (2020) 139547. https://doi.org/10.1016/J.MSEA.2020.139547.

[192] H. Do, S. Asadi, N. Park, Microstructural and mechanical properties of dissimilar friction stir welded CoCrFeMnNi high entropy alloy to STS304 stainless steel, Materials Science and Engineering: A 840 (2022) 142979. https://doi.org/10.1016/J.MSEA.2022.142979.

[193] J.P. Oliveira, J. Shen, Z. Zeng, J.M. Park, Y.T. Choi, N. Schell, E. Maawad, N. Zhou, H.S. Kim, Dissimilar laser welding of a CoCrFeMnNi high entropy alloy to 316 stainless steel, Scr Mater 206 (2022) 114219. https://doi.org/10.1016/J.SCRIPTAMAT.2021.114219.

[194] N.K. Adomako, G. Shin, N. Park, K. Park, J.H. Kim, Laser dissimilar welding of CoCrFeMnNi-high entropy alloy and duplex stainless steel, J Mater Sci Technol 85 (2021) 95–105. https://doi.org/10.1016/J.JMST.2021.02.003.

[195] H. Nam, S. Park, N. Park, Y. Na, H. Kim, S.J. Yoo, Y.H. Moon, N. Kang, Weldability of cast CoCrFeMnNi high-entropy alloys using various filler metals for cryogenic applications, J Alloys Compd 819 (2020) 153278. https://doi.org/10.1016/J.JALLCOM.2019.153278.

[196] H. Nam, S. Park, E.-J. Chun, H. Kim, Y. Na, N. Kang, Laser dissimilar weldability of cast and rolled CoCrFeMnNi high-entropy alloys for cryogenic applications, Science and Technology of Welding and Joining (2019) 1–8. https://doi.org/10.1080/13621718.2019.1644471.

[197] T. Sonar, V. Balasubramanian, S. Malarvizhi, T. Venkateswaran, D. Sivakumar, An overview on welding of Inconel 718 alloy - Effect of welding processes on microstructural evolution and mechanical properties of joints, Mater Charact 174 (2021) 110997. https://doi.org/10.1016/J.MATCHAR.2021.110997.

[198] B. Kagay, K. Findley, S. Coryell, A.B. Nissan, Effects of alloy 718 microstructure on hydrogen embrittlement susceptibility for oil and gas environments, Materials Science and Technology 32 (2016) 697–707. https://doi.org/10.1080/02670836.2016.1139225.

[199] K. Sajun Prasad, S.K. Panda, S.K. Kar, M. Sen, S.V.S.N. Murty, S.C. Sharma, Microstructures, Forming Limit and Failure Analyses of Inconel 718 Sheets for Fabrication of Aerospace Components, J Mater Eng Perform 26 (2017) 1513–1530. https://doi.org/10.1007/S11665-017-2547-4.

[200] M.A. Kattimani, P.R. Venkatesh, H. Masum, M.M. Math, V.N. Bahadurdesai, S. Mustafkhadri, C.D. Prasad, H. Vasudev, Design and numerical analysis of tensile deformation and fracture properties of induction hardened inconel 718 superalloy for gas turbine applications, International Journal on Interactive Design and Manufacturing (2023) 1–11. https://doi.org/10.1007/S12008-023-01452-Z.

[201] E. Assuncao, S. Williams, D. Yapp, Interaction time and beam diameter effects on the conduction mode limit, Opt Lasers Eng 50 (2012) 823–828. https://doi.org/10.1016/J.OPTLASENG.2012.02.001.

[202] W.A. Ayoola, W.J. Suder, S.W. Williams, Parameters controlling weld bead profile in conduction laser welding, J Mater Process Technol 249 (2017) 522–530. https://doi.org/10.1016/J.JMATPROTEC.2017.06.026.

[203] J.O. Andersson, T. Helander, L. Höglund, P. Shi, B. Sundman, Thermo-Calc & DICTRA, computational tools for materials science, Calphad 26 (2002) 273–312. https://doi.org/10.1016/S0364-5916(02)00037-8.

[204] S. Mahadevan, S. Nalawade, J.B. Singh, A. Verma, B. Paul, K. Ramaswamy, Evolution of δ Phase Microstructure in Alloy 718, 7th International Symposium on Superalloy 718 and Derivatives 2010 2 (2010) 737–750. https://doi.org/10.1002/9781118495223.CH57.

[205] J.P. Oliveira, Z. Zeng, C. Andrei, F.M. Braz Fernandes, R.M. Miranda, A.J. Ramirez, T. Omori, N. Zhou, Dissimilar laser welding of superelastic NiTi and CuAlMn shape memory alloys, Mater Des 128 (2017) 166–175. https://doi.org/10.1016/J.MATDES.2017.05.011.

[206] S. Sui, H. Tan, J. Chen, C. Zhong, Z. Li, W. Fan, A. Gasser, W. Huang, The influence of Laves phases on the room temperature tensile properties of Inconel 718 fabricated by powder feeding laser additive manufacturing, Acta Mater 164 (2019) 413–427. https://doi.org/10.1016/J.ACTAMAT.2018.10.032.

[207] Y. Zhang, Z. Li, P. Nie, Y. Wu, Effect of cooling rate on the microstructure of laser-remelted INCONEL 718 coating, Metall Mater Trans A Phys Metall Mater Sci 44 (2013) 5513–5521. https://doi.org/10.1007/S11661-013-1903-8.

[208] P. Dias, J.G. Lopes, T. Curado, E. Maawad, N. Schell, H.S. Kim, J.P. Oliveira, In-situ micro-structural evolution during tensile loading of CoCrFeMnNi high entropy alloy welded joint probed by high energy synchrotron X-ray diffraction, Science and Technology of Welding and Joining (2024). https://doi.org/10.1177/13621718241259349.

2024

JOÃO LOPES

INVESTIGATION ON WELDING OF HIGH ENTROPY ALLOYS IN SIMILAR AND DISSIMILAR COMBINATIONS.